The dynamics of the Lambert-Amery glacial system and its response to climatic variations

Mark Llewellyn Pittard
Bachelor of Global and Ocean Sciences (Honours)

Institute for Marine and Antarctic Studies
Antarctic Climate & Ecosystems Cooperative Research Centre
University of Tasmania

Submitted in fulfilment of the requirements for the degree of Doctor of Philosophy
November, 2016

Declaration of Originality

This thesis contains no material which has been accepted for a degree or diploma by the University or any other institution, except by way of background information and duly acknowledged in the thesis, and to the best of my knowledge and belief no material previously published or written by another person except where due acknowledgement is made in the text of the thesis, nor does the thesis contain any material that infringes copyright.

Matt Pittard April 26, 2016

Authority of Access

Statement of Co-Authorship

The following people and institutions contributed to the publication of work undertaken as part of this thesis:

Mark L Pittard (Candidate)
Institute for Marine and Antarctic Studies, University of Tasmania, Antarctic Climate & Ecosystems Cooperative Research Centre, University of Tasmania

Benjamin Galton-Fenzi (Primary Supervisor)
Australia Antarctic Division, Antarctic Climate & Ecosystems Cooperative Research Centre, University of Tasmania

Jason Roberts (Supervisor)
Australia Antarctic Division, Antarctic Climate & Ecosystems Cooperative Research Centre, University of Tasmania

Christopher Watson (Supervisor)
School of Land and Food, University of Tasmania

Roland Warner (Co-Author)
Australia Antarctic Division, Antarctic Climate & Ecosystems Cooperative Research Centre

Richard Coleman (Co-Author)
Institute for Marine and Antarctic Studies, University of Tasmania

Conference Manuscript 1: *Flow of the Amery Ice Shelf and its Tributary Glaciers*, Pittard (70%), Galton-Fenzi (5%), Roberts (10%), Watson (5%), Warner (5%), Coleman (5%):

All authors contributed to the experimental design and the editorial process. Roberts provided technical advice for the methodology and aided with figure creation. Pittard performed all data processing, analysis and writing.

Manuscript 1, *Velocities of the Amery Ice Shelf's primary tributary glaciers, 2004–12*, Pittard (70%), Galton-Fenzi (5%), Roberts (10%), Watson (5%), Warner (5%), Coleman (5%):
All authors contributed to the experimental design and the editorial process. Roberts provided technical advice for the methodology and aided with figure creation. Pittard performed all data processing, analysis and writing.

Manuscript 2, *Sensitivity of the Lambert-Amery glacial system to geothermal heat flux*, Pittard (75%), Galton-Fenzi (7.5%), Roberts (10%), Watson (7.5%):
All authors contributed to the experimental design and the editorial process. Pittard performed all data processing, analysis and writing.

Manuscript 3, *Organization of ice flow by localized regions of elevated geothermal heat flux*, Pittard (80%), Galton-Fenzi (7.5%), Roberts (5%), Watson (7.5%):
All authors contributed to the experimental design and editorial process. Pittard performed all data processing, analysis and writing.

Manuscript 4, *Future sea level change from Antarctica's Lambert-Amery glacial system*, Pittard (80%), Galton-Fenzi (10%), Roberts (5%), Watson (5%):
All authors contributed to the experimental design and editorial process. Pittard performed all data processing, analysis and writing.

I the undersigned agree with the above stated 'proportion of work undertaken' for each of the above published (or submitted) peer-reviewed manuscripts contributing to this thesis.

Benjamin Galton-Fenzi, April 26, 2016
Primary Supervisor
Australian Antarctic Division
Antarctic Climate & Ecosystems Cooperative Research Centre

Abstract

Antarctica's current and future contribution to sea level rise is uncertain, with changes in ice dynamics along the coast leading to mass loss while increasing precipitation in the interior is leading to mass gain. The Lambert-Amery glacial system drains a large region of East Antarctica, with the two largest glaciers within the glacial system, the Lambert and Mellor glaciers, having a substantial volume of ice grounded below sea level, suggesting a risk of marine ice sheet instability. The velocities of Lambert-Amery glacial system have been observed to be stable between 1968 and 1999, albeit with limited sampling. Recent mass balance and gravimetry studies also suggest a system in near balance. Here, visible spectrum satellite images between 2004 to 2012 have been used to compute surface ice velocities using a feature tracking approach. No significant changes in velocity were observed over the study region that included the Amery Ice Shelf adjacent to the grounding line and its three main tributary glaciers, the Lambert, Mellor and Fisher Glaciers. The stability of the Lambert-Amery glacial system allows for the initialisation of an ice sheet model by minimising the misfit between the simulated and observed system.

A regional domain of the Lambert-Amery glacial system is simulated with the Parallel Ice Sheet Model. The control solution of the regional model is initialised by minimising the misfit to observations through an optimisation process. We investigate the importance of a primary boundary condition, geothermal heat flux to ice flow. Existing broad scale geothermal heat flux datasets fail to capture small scale localised variations in geothermal heat flux, such as estimates of geothermal heat flux in Prydz Bay suggesting that radiogenic crustal heat production can locally elevate geothermal heat flux by at least 100% compared to the background field. We insert high heat flow regions into a broad scale background geothermal heat flux field, and find that the presence of a high heat flow region can change the flow behaviour in regions from slow sheet flow to stream-like flow, while making no difference to regions of fast flow. This mechanism may contribute to the long term organisation of ice flow. Additionally, we use a range of different geothermal heat flux datasets, and compare simulation using them in place of our control geothermal heat flux. The simulations which use a relatively high GHF compared to the control solution increase the volume and area of temperate ice, which causes higher surface velocities at higher elevations, which leads to the advance of the grounding line. The grounding line advance leads to changes in the local flow

configuration, which dominates the changes within the glacial system. To investigate the difference in spatial patterns within the geothermal datasets, they were scaled to have the same median value as the control dataset. These scaled geothermal heat flux simulations showed that the ice flow was most sensitive to the spatial variation in the underlying geothermal heat flux near the ice divides and on the edges of the ice streams.

The Lambert-Amery glacial system is evidenced to change significantly during glacial cycles, with the grounding line advancing and retreating up to 700 km. This contrasts with the current stability of the glacial system. The Antarctic Ice Sheet responds to climate through several factors, including the temperature at the surface of the ice, the accumulation on the surface, the oceanic forcing at the base of the floating ice, and sea level change. We test the response of the Lambert-Amery glacial system to climatic variations by simulating the effects of a global air temperature change of $\pm$ 3°C. Each climate variable is simulated in isolation to test the sensitivity to each climatic variation, before a combined simulation. We find that the Lambert-Amery glacial system responds most rapidly to accumulation on the surface and the oceanic forcing at the base of the floating ice, while surface temperature eventually lead to the largest change, but on time scales longer than the recent glacial-inter-glacial cycles. The advance of the grounding line moves rapidly between negative sloping beds, where it then stabilises on a positive bed slope, with the ice sheet growing until a threshold is reached and the grounding line advances again. The model simulations are unable to recreate an advance simulation which was similar to the last glacial maximum, with the grounding line either not advancing to the continental shelf, or the ice sheet growing rapidly when the grounding line does advance.

The contribution of Lambert-Amery glacial system to future sea level change is investigated through a range of future scenarios. Within our simulations, we find that under a range of plausible and extreme scenarios, the grounding line is unlikely to become unstable and retreat into the deep marine basins. This causes increases in precipitation to exceed mass loss through ice discharge within our simulations as long as a minimal ice shelf remains. This suggests that the Lambert-Amery glacial system has the potential to gain mass and mitigate the severity of sea level rise from Antarctica for the next 500 years.

Acknowledgements

The completion of this thesis would not have been possible without the help of my supervisory team, Ben Galton-Fenzi, Jason Roberts and Christopher Watson. Each has provided me with considerable time and attention, and without their guidance, patience and advice this thesis would not have been completed. I was particularly lucky in that each of my supervisors were different in their approach to research and writing, providing me with well-rounded feedback which greatly balanced my manuscripts and thesis, in addition to expanding my perspective on how to approach research.

This research was supported by the University of Tasmania, the Institute for Marine and Antarctic Science and the Antarctic Climate & Ecosystems Cooperative Research Centre. I would like to thank the Antarctic Climate & Ecosystems Cooperative Research Centre for managing my candidature and with the financial travel support they have provided me. I would also like to thank Richard Coleman, for being an advocate for me to the higher administration which allowed for me apply for personal leave for a tough period, which helped give me the time to complete this thesis.

I would like to thank Nicole, Aaron and Jacob. The warmth and friendship you always offered me made my years in Hobart so much more enjoyable. Finally, a big thank you to my parents for encouraging and supporting me throughout my studies, as well as looking after me throughout the final few months.

Contents

Chapter 1

Introduction

1.1 Motivation

1.1.1 Antarctica's contribution to sea level rise

Accurately forecasting the contribution of the Antarctic Ice Sheet remains one of the biggest unknowns in both closing the current sea level budget and for future sea level rise predictions (e.g. *Church and White*, 2011; *Pachauri et al.*, 2014). It is estimated that Antarctica's contribution to sea level rise increased from 0.27 (0.16 to 0.37) mm year^{-1} (1993-2010) to 0.41 (0.2 to 0.61) mm year^{-1} (2005-2010) (*Pachauri et al.*, 2014), with the acceleration primarily occurring from the West Antarctica Ice Sheet and the Antarctic Peninsula. This contrasts with East Antarctica, where there is evidence to suggest some regions are gaining mass (*Clark et al.*, 2015; *Church et al.*, 2013; *Shepherd et al.*, 2012). There is a positive relationship between warming temperatures and increasing precipitation, which some research suggests could lead to surface mass balance increases being greater than the accelerating mass loss over the next century (*Clark et al.*, 2015). These results assume that Antarctic does not experience rapid mass loss from the Marine Ice Sheet Instability theory (*Church et al.*, 2013; *Clark et al.*, 2015), which, suggests that a feedback loop caused as the grounding line retreats into a deeper bedrock can occur rapidly (*Weertman*, 1974). If rapid mass loss via the Marine Ice Sheet Instability mechanism occurs, it could lead to increases in sea level rise on the order of tens of mm (*Clark et al.*, 2015). *Ritz et al.* (2015) concludes that sea level rise of up to 1 m by 2100 and 1.5 m by 2200 is implausible even with the Marine Ice Sheet Instability mechanism occurring, limiting Antarctica's upper contribution. The broad range of possible future sea level contributions found within the current literature highlights the need for further research on how Antarctica will respond to a changing climate.

Additionally to global sea level change, gravitational changes due to the change in mass in Antarctica will influence regional sea level variations, which are important for understanding the impact sea level rise will have on human civilisation (e.g. *Nicholls and Cazenave*, 2010; *Carson et al.*, 2016). The Antarctic Ice Sheet gains mass pri-

marily through precipitation, and loses the majority of its mass as ice flows across the grounding line. Other sources of mass gain and loss are not a major contributor to the Antarctica mass budget, although surface melt may become a significant source of mass loss in the future. The balance between this mass gain and loss is the mass balance, which measures the net contribution to sea level from the region under consideration. The mass balance can be calculated through a variety of methods such as gravimetry (e.g. *Velicogna*, 2009; *King et al.*, 2012), satellite altimetry (e.g. *Davis et al.*, 2005; *Zwally et al.*, 2015) and mass budget methods (e.g. *Rignot et al.*, 2008). A combined study by *Shepherd et al.* (2012) attempted to reconcile the various techniques to give an estimate of the current mass balance of the Antarctic and Greenland ice sheets. Their best estimate of mass change from Antarctica was -71 ± 53 Gt/year between 1992 and 2011, with $+14 \pm 43$ Gt/year from the East Antarctic Ice Sheet (EAIS), -65 ± 26 Gt/year from the West Antarctic Ice Sheet (WAIS) and -20 ± 14 Gt/year from the Antarctic Peninsula (AP). There is still debate surrounding the sign of Antarctica's current contribution to sea level rise, with some radar altimetry methods suggesting the EAIS growth is greater than current losses from WAIS and AP (*Davis et al.*, 2005; *Zwally et al.*, 2015). Each of these methods have uncertainties associated with them, but a positive contribution to sea level rise from Antarctica helps close the sea level budget over 1993–2007 (*Cazenave and Llovel*, 2010), supporting the idea that Antarctica is currently losing mass.

The mass loss from Antarctica has been driven by the increase in velocity of grounded ice flow following changes in their bordering ice shelves (e.g. *Rott et al.*, 2002; *Scambos et al.*, 2004; *Rignot et al.*, 2008; *Warner and Roberts*, 2013). This acceleration is caused by a reduction in the buttressing provided by the ice shelf through processes such as shearing with slower-moving ice, re-grounding on shallow bed topography and through friction along bay walls (*Dupont and Alley*, 2005). The changes that ice shelves have experienced are thinning, calving front retreat, grounding line retreat and complete disintegration. These have been driven by surface warming (e.g. *Scambos et al.*, 2004), oceanic warming (e.g. *Rignot et al.*, 2008; *Pritchard et al.*, 2012) and changes in ocean circulation bringing warmer circumpolar deep water onto the continental shelves (e.g. *Hellmer et al.*, 2012). For example, the complete collapse of ice shelves in the AP, such as the Larsen A and B ice shelves, have been linked to a mixture of ocean warming, atmospheric changes and hydro-fracturing of the ice shelf (e.g. *Rignot et al.*, 2004; *Rack and Rott*, 2004; *Glasser and Scambos*, 2008). This contrasts with changes in WAIS where the intrusion of warm circumpolar deep water onto the Amundsen Bay continental shelf (e.g. *Thoma et al.*, 2008; *Steig et al.*, 2012) has led to widespread thinning of the local ice shelves and grounding line retreat. The ice shelves have not disintegrated completely like in the AP, but the upstream grounded velocities have still increased, leading to increasing mass loss in the Amundsen Sea sector (e.g. *Rignot et al.*, 2014). This sensitivity of the ice shelves to oceanic forcing, and consequential grounding line retreat is the basis of the marine instability hypothe-

sis (*Weertman*, 1974; *Thomas*, 1979; *Schoof*, 2007). The marine instability hypothesis suggests that for regions grounded below sea level (marine ice sheet basins), when the grounding line retreats down a bed which becomes deeper the further inland it progresses, it will continuously retreat until the bed becomes shallower. Antarctica has substantial areas of ice grounded below sea level (marine basins) which may have the potential to lose mass rapidly via the marine instability mechanism, such as most of the WAIS and the Wilkes Basin in EAIS (e.g. *Bamber et al.*, 2009). The observations of ice flow on glaciers accelerating following changes in their bordering ice shelves highlight the important role ice shelves play in buttressing the ice flow from the continent. Understanding what leads to changes in the ice shelf, and how those changes impact upstream flow is vital to understanding how the major ice sheets will respond to climate change in the future.

While the mass loss is accelerating in many regions of Antarctica, there is evidence through both gravimetry and radar altimetry that regions of Antarctic may also be gaining mass (*King et al.*, 2012; *Shepherd et al.*, 2012; *Zwally et al.*, 2015). The measured mass gains could be driven by recent, long term, or decadal variation in precipitation, although the uncertainty in the interpretations is still high due to the limited observations and possibly invalid assumptions. There is a very short observational record of precipitation for all of Antarctica, with large variations in precipitation expected due to natural variability rather than climate change (*Monaghan et al.*, 2006). The existing observations limit our ability to assess changes as we have such a short, and regionally sparse record of change. The mass gain seen in recent records could be from ongoing changes due to continuing deglaciation (*Wright et al.*, 2008; *Mackintosh et al.*, 2014) in which the ice sheets have been gradually (over thousands of years) responding to, rather than any changes driven from anthropogenic sources. In a warming climate, precipitation is expected to increase, with the Clausius–Clapeyron relation suggesting that for every degree Celsius of temperature increase, there will be an approximately 7.3% increase in precipitation with regional variations (*O'Gorman and Muller*, 2010). Global climate models estimate that the global average temperature may rise as much as 10 degrees Celsius over the next 500 years, which would lead to significant increases in precipitation over Antarctica (*Krinner et al.*, 2007; *Pachauri et al.*, 2014). The increase in precipitation indicates a transfer of mass from the ocean to the ice sheet, which will act to mitigate sea level rise. There is reasonable certainty that Antarctica will and might already be contributing to sea level rise (*Shepherd et al.*, 2012; *Pachauri et al.*, 2014), but the two competing mechanisms of mass loss at the coast and mass gain in the interior makes estimating the net contribution difficult. There is a need to further understand the mechanisms that led to changes in mass loss, and how the ice sheet will respond to mass gain in order to improve calculations of Antarctica's current and future contribution to sea level rise. Understanding the rate at which sea level is rising, and how much it will rise into the future is critical so that appropriate policy can be put in place to minimise the impact on both human society and natural ecosys-

tems (e.g. *McGranahan et al.*, 2007; *Parry et al.*, 2007; *Nicholls and Cazenave*, 2010). Numerical ice sheet modelling provides a valuable method for exploring Antarctica's evolution, and ultimately its net contribution to sea level rise both currently and into the future.

1.1.2 Numerical ice sheet modelling

Numerical ice sheet modelling provides the ability to predict past, present and future sea level rise by simulating the evolution and flow of the ice sheets. Ice sheet models require a range of physical parameters, boundary conditions and forcing conditions to simulate the flow of ice, including both flow and thermal physics. Boundary conditions include the bed topography, initial ice thickness, geothermal heat flux and properties at the base of the ice. Forcing conditions control the evolution of the ice sheet, such as surface mass balance and the basal mass balance of both the ice sheet and the ice shelves.

The flow of ice can be described as a highly viscous fluid, which flows through deformation from gravity under its own weight. This flow can be described by the full Stokes equations (Equation 1.1-1.3), which are a linearisation of the Navier-Stokes equations for small Reynolds number, including the conservation of momentum equation, Glen's flow law (*Glen*, 1958) and the incompressibility equation (Equation 1.4). Glen's flow law describes the relationship between stress and strain rates which controls the internal deformation and flow of ice (Equation 1.5)(*Glen*, 1958). Ice flow is considered a slow flow and as such the Coriolis force is neglected. The ice flow equation can be described in a Cartesian system (x, y, z) where the velocity components in Cartesian space are (v_x, v_y, v_z) as:

$$\frac{\partial}{\partial x}(2\mu\frac{\partial v_x}{\partial x}) + \frac{\partial}{\partial y}(\mu\frac{\partial v_x}{\partial y} + \mu\frac{\partial v_y}{\partial x}) + \frac{\partial}{\partial z}(\mu\frac{\partial v_x}{\partial x} + \mu\frac{\partial v_z}{\partial z}) - \frac{\partial p}{\partial x} = 0 \tag{1.1}$$

$$\frac{\partial}{\partial x}(\mu\frac{\partial v_x}{\partial y} + \mu\frac{\partial v_y}{\partial x}) + \frac{\partial}{\partial y}(2\mu\frac{\partial v_y}{\partial y}) + \frac{\partial}{\partial z}(\mu\frac{\partial v_y}{\partial z} + \mu\frac{\partial v_z}{\partial y}) - \frac{\partial p}{\partial y} = 0 \tag{1.2}$$

$$\frac{\partial}{\partial x}(\mu\frac{\partial v_x}{\partial z} + \mu\frac{\partial v_z}{\partial x}) + \frac{\partial}{\partial y}(\mu\frac{\partial v_y}{\partial z} + \mu\frac{\partial v_z}{\partial y}) + \frac{\partial}{\partial z}(2\mu\frac{\partial v_z}{\partial z}) - \frac{\partial p}{\partial z} - \rho g = 0 \tag{1.3}$$

$$\frac{\partial v_x}{\partial x} + \frac{\partial v_y}{\partial y} + \frac{\partial v_z}{\partial z} = 0 \tag{1.4}$$

where μ is the ice effective viscosity:

$$\mu = \frac{B}{2\dot{\epsilon}_e^{1-\frac{1}{n}}} \tag{1.5}$$

and

- B is the ice hardness (Pa $s^{1/3}$)
- ϵ_e is the second invariant of effective strain rate (s^{-1})

- n is the Glen exponent in the ice flow law (-)
- ρ is the density of the ice (kg m^{-3})
- g is the acceleration due to gravity (m s^{-2})

While some models exist that implement the full Stokes equations (Equation 1.1-1.5), it is computationally expensive and therefore it is common for models to use approximations to this flow (e.g. *Hindmarsh*, 2004; *Pattyn et al.*, 2012). The simplest approximations commonly used are the shallow ice approximation (SIA)(*Hutter*, 1983) and the shallow shelf approximation (SSA)(*MacAyeal*, 1989). Both models assume that the height of the ice is small compared to the length, hence the 'shallow' description. The SIA assumes that the horizontal shear stress component of flow is small, and therefore the flow is dependent on the vertical shear stress gradients that oppose the gravitational drive. This approximation is considered valid for regions of the ice sheet where the thickness scale is much smaller than the length scale, and where basal sliding is minimal. It represents an ice flow which is deforming under its own weight, where the surface slope is important to determining the flow rate. It is used to describe slow moving grounded ice. The shallow ice approximation makes the assumption that the gravitational driving force is exclusively balanced by the shear within the ice, leading to the simplification of the full Stokes equations by neglecting the horizontal shear. The SIA is a single equation system:

$$(\frac{\partial v_x}{\partial z}, \frac{\partial v_y}{\partial z}) = -2(\rho g)^n A(T^*)(h-z)^n |\nabla \cdot h|^{n-1} h \tag{1.6}$$

where

- $A(T^*)$ is the temperature dependant factor in the ice flow law (Pa s$^{1/3}$)
- h is the surface elevation of the ice (m)

The SSA assumes that the vertical shear is insignificant compared to the horizontal shear, representing block flow of the ice that will occur in ice shelves, or in very fast flowing ice streams (*MacAyeal*, 1989). The SSA is a simplification of the full Stokes equations where gravity causes the spreading of a variable thickness ice. This reduces the flow equations to a pair of equations (Equations 1.7-1.8). When applied to an ice stream, shear force components applied at the base of the ice, $(\tau_{b,1}, \tau_{b,2})$, are included in the description. For floating ice these terms are zero. The pair of equations for the SSA are:

$$\frac{\partial}{\partial x}[2\bar{\mu}H(2\frac{\partial v_x}{\partial x} + \frac{\partial v_y}{\partial y})] + \frac{\partial}{\partial y}[\bar{\mu}H(\frac{\partial v_x}{\partial y} + \frac{\partial v_y}{\partial x})] + \tau_{b,1} = \rho g H \frac{\partial h}{\partial x} \tag{1.7}$$

$$\frac{\partial}{\partial x}[\bar{\mu}H(\frac{\partial v_x}{\partial y} + \frac{\partial v_y}{\partial x})] + \frac{\partial}{\partial y}[2\bar{\mu}H(\frac{\partial v_x}{\partial x} + 2\frac{\partial v_y}{\partial y})] + \tau_{b,2} = \rho g H \frac{\partial h}{\partial y} \tag{1.8}$$

where

- H is the ice thickness (m)
- $\bar{\mu}$ is the vertically integrated ice viscosity (Pa s)

The shallow approximations are not particularly valid in regions where basal sliding is a significant portion of the ice velocity, such as fast ice streams or the region near the grounding line, where both vertical and horizontal shear affect the ice flow. This is particularly important for accurately modelling the grounding line movement which is fundamental to understanding the response of the ice sheet to climate forcing (*Vieli and Payne*, 2005; *Schoof*, 2007; *Goldberg et al.*, 2009). Some models use parametrisations to help bridge this gap (*Pattyn et al.*, 2012), while others use a hybrid scheme where the SSA is used as a sliding law for the SIA, with the sliding velocities abiding to the SSA (*Bueler and Brown*, 2009). There are a range of higher order models (*Pattyn et al.*, 2006; *Schoof and Hindmarsh*, 2010; *Cornford et al.*, 2013) which re-introduce vertical components of stress into the shallow shelf approximation via consideration of the hydrostatic approximation in the vertical direction and neglecting vertical resistance stresses (*Pattyn et al.*, 2012).

An extra uncertainty in the flow of ice is the alteration of rheology due to anisotropic crystalline structure of ice. It has been shown that the anisotropic crystalline structure of the ice can lead to the enhancement of flow (*Budd and Jacka*, 1989), which varies both horizontal and vertically through the ice column. There are very few observations of *in situ* crystalline structure of with which to guide ice sheet models (for example, *Treverrow et al.* (2015)), with the enhancement due to the anisotropy typically applied as a single ice sheet wide enhancement factor in both the SIA and SSA equations. Improvements in our understanding of the importance, spatial variability and relevance of these enhancement factors will be vital to improving the performance of ice sheet models and their ability to predict the behaviour of the ice sheet.

One of the largest limitations to accurately modelling the Antarctic Ice Sheet is the lack of observations and knowledge of some key boundary and forcing conditions. The key boundary inputs to an ice sheet model are the bed topography and the initial ice thickness. These are observed through a variety of methods such as local seismic and airborne radar (e.g. *Fretwell et al.*, 2013)), but still have significant data gaps and error in their determination which is a limiting factor in the application of ice sheet models. Furthermore, the conditions at the bed of the ice, a region which is very difficult to observe, have an important influence on the flow of the ice. For example, the geothermal heat flux plays an important role in determining the heat input into the base of the ice which will contribute to the overall temperature profile of the ice sheet and its viscosity. The temperature at the bed directly influences where melting may occur, which can lubricate the bed of the ice sheet and allow for sliding to occur, which greatly enhances the flow of the ice. Geothermal heat flux has been estimated through seismic (*Shapiro and Ritzwoller*, 2004; *An et al.*, 2015) and magnetic field (*Fox Maule et al.*, 2005) models, but these are broad scale datasets with large local errors. There is growing evidence that regional geothermal heat flux can vary greatly compared to the

low resolution background fields, with local radiogenic crustal heat production (*Carson and Pittard*, 2012; *Carson et al.*, 2014) and groundwater flow (*Gooch et al.*, 2016) leading to elevated regions of high heat flux. A direct measurement of the geothermal heat flux at the base of a borehole within the West Antarctic Ice Sheet above a subglacial lake was over twice as high as expected, supporting the idea that local variations may be important (*Fisher et al.*, 2015).

The geology of the bed is also important, with weak sedimentary basins potentially allowing for easier sliding than regions on top of exposed bedrock (*MacAyeal*, 1989). The way in which the basal melt connects within a greater sub-glacial hydrological network, including sub-glacial lakes and complex drainage systems is unknown and their influence on the flow of the ice is uncertain (*Bell*, 2008). This uncertainty at the bed of the ice leads to parametrisations of the local conditions, or inversions of basal resistance and viscosity within ice sheet models (*Pattyn*, 2010; *Cornford et al.*, 2013; *Morlighem et al.*, 2013). Both of these methods have a range of uncertainties. The parametrisation method lacks sufficient direct observations for validation, while the inversion methods are dependant on accurate temperature distributions which are also largely unobserved, and combine a large range of factors, each with associated uncertainties into a single basal resistance term. These factors help control the flow of the ice, but overall climate forcing is the primary driver of ice sheet evolution.

The forcing conditions of ice sheets determine their stability and ultimately our ability to predict sea level change. The mass balance of an ice sheet is dependent on the mass flux into the ice sheet primarily through precipitation, balanced against the mass of ice that is transported across the grounding line into the ocean. The mass flux across the grounding line is controlled largely by the conditions of the fringing ice shelves. The oceanic forcing on the underside of the ice shelf, along with the mechanics that lead to enhanced calving, fracturing or collapse of the ice shelf are important in controlling mass flux. Ice sheet models rely on either parametrisations or output from other models to input these forcing parameters into simulations (e.g. *Winkelmann et al.*, 2011; *Levermann et al.*, 2012; *Gong et al.*, 2014). Using output from other models as input has limitations in that the uncertainty of both models is combined, and changes in the ice sheet could change the behaviour of the input model. For example, using the output of an ocean model that simulates the melt rates on the underside of the ice shelf as an input into a simulation will provide realistic distribution at the start of the simulation, yet as the ice shelf cavity changes in geometry the melt rates would likely change. This has led to the push for coupled models (*Asay-Davis et al.*, 2015), but this can be both computationally difficult to implement and computationally expensive to simulate. Numerical ice sheet models have a large range of uncertainties, and further refinement and exploration of the effects these have on ice sheet simulations is needed to improve overall estimates of ice sheet evolution.

1.1.3 The Lambert-Amery glacial system

The Lambert-Amery glacial system is located in East Antarctica (Figure 1.1a). A glacial system describes the entire catchment, including the regions of sheet flow, glaciers, ice streams and ice shelves. The Lambert-Amery glacial system drains a volume of ice greater than the entire WAIS, with an ice volume of $\approx$ 9.5 m sea level equivalent (calculated by combining the bedmap2 thickness (*Fretwell et al.*, 2013) and a drainage basin calculated by the PISM drainage basin tool (http://www.pism-docs.orgwiki/doku.php, date accessed 20/02/2015)). The Amery Ice Shelf is the third largest ice shelf in Antarctica, but is unique in its configuration. It is a long and relatively thin ice shelf, with a grounding line at least 2500 m deep (*Fricker et al.*, 2002; *Galton-Fenzi*, 2009). It's three primary tributaries, the Lambert, Mellor and Fisher glaciers flow into the a relatively thin region at the back of the ice shelf, where the three ice streams merge as they begin to float (Figure 1.1b). Of these tributaries, the Lambert and Mellor Glaciers have significant regions of ice grounded below sea level (Figure 1.1c). The Amery Ice Shelf has a number of points where the flow is restricted, with the narrowest point of the ice shelf approximately 100 km downstream from the grounding line, which leads to the ice shelf velocity having a minima before it gradually begins to increase again. There are a number of pinning points where the ice shelf re-grounds, in addition to islands which protrude through the ice shelf, causing ice to deviate in its flow (*Galton-Fenzi et al.*, 2008). There is observational evidence of frazil ice refreezing on the underside of the ice shelf (*Craven et al.*, 2004), supported by results from a numerical ocean model of the ice shelf cavity (*Galton-Fenzi et al.*, 2012).

The unique nature of the Lambert-Amery glacial system, along with observations that suggest the ice shelf and grounding line are currently stable (*King et al.*, 2007, 2012; *Wen et al.*, 2008; *Yu et al.*, 2010), allow for the possibility of mass gain in the region under future climate scenarios. However, the significant region of ice grounded below sea level and current oceanic driven change seen in other regions throughout Antarctica could lead to significant mass loss. Changes in oceanic circulation might force warmer circumpolar deep water under the ice shelf, which could lead to the widespread thinning of the ice shelf and the retreat of the grounding line. This would likely mean the grounding line would retreat from its present position (Figure 1.1b), and if it retreated into the region grounded below sea level, it is possible that the Lambert-Amery glacial system would rapidly lose mass and contribute a significant amount to sea level rise. Conversely, if the ice shelf remains stable over the next few centuries, an increase in precipitation may lead to the Lambert-Amery glacial system gaining mass and being a sink for sea level. It is important to understand the contribution of the Lambert-Amery glacial system may have towards sea level change, as it has the potential to either mitigate, or contribute, to sea level, pending the stability of the ice shelf. Rapid collapse of the ice shelf and possible retreat of the grounding line into the deep marine basins could lead to rapid sea level rise, which is a process important to understand for timely societal adaptation to sea level change.

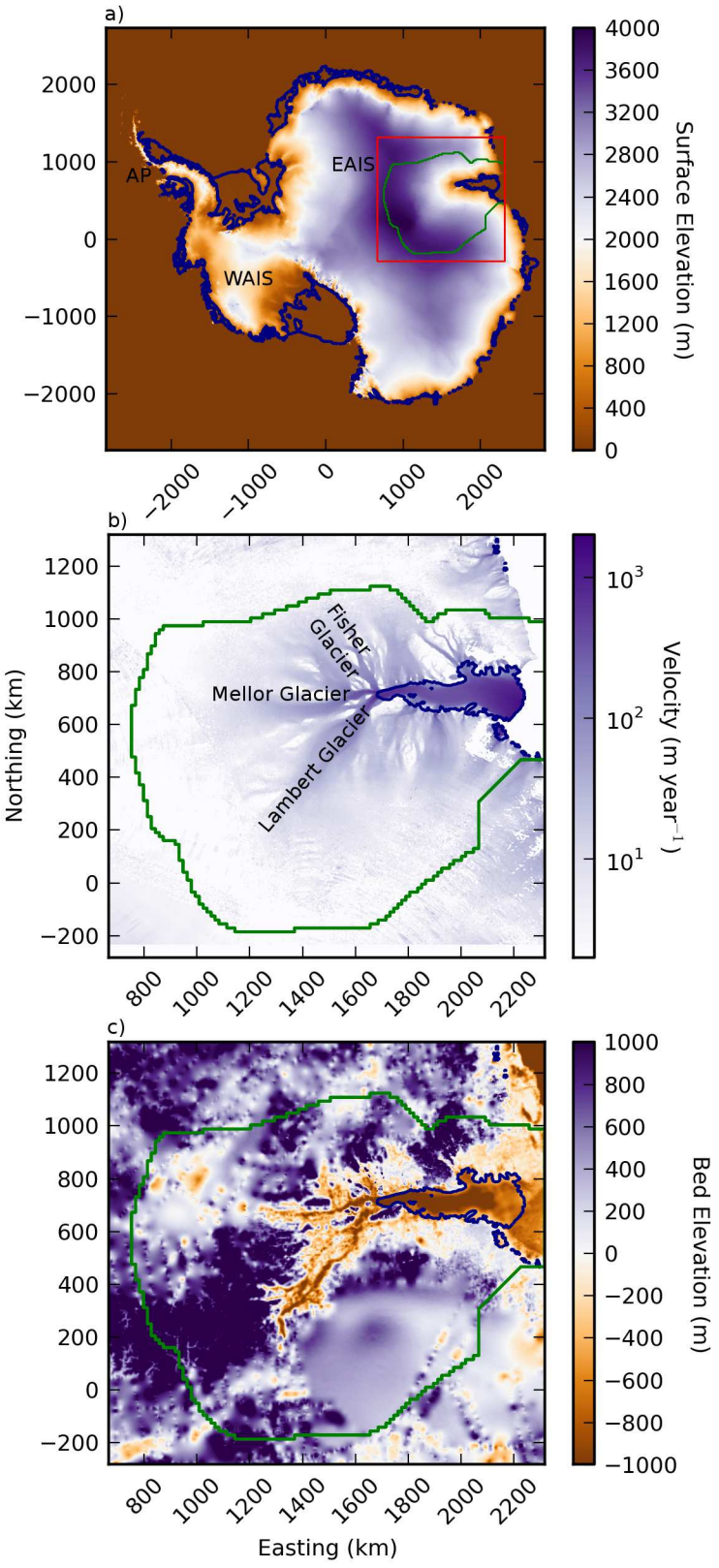

Figure 1.1: a) Antarctica's surface elevation from BEDMAP2 (*Fretwell et al.*, 2013). Green outline indicates the Lambert-Amery glacial system. Red inset indicates the location of b) and c). b) Surface velocities from MEaSUREs (*Rignot et al.*, 2011a). c) Bed elevation from BEDMAP2. (*Fretwell et al.*, 2013).

1.2 Thesis Aims

The goals of this thesis are to observe the dynamics of the Lambert-Amery glacial system, assess its current state and determine its response to a suite of potential climatic variations. The thesis will use remote sensing and numerical ice modelling methods, and contribute to the further development of these techniques in the process of understanding the Lambert-Amery glacial system. To achieve these aims, the thesis has three main objectives, with each having their own aims (dot points):

Objective 1: Assess the current dynamic state of the Lambert-Amery glacial system

- observing the current ice dynamics of the Lambert-Amery glacial system
- determining if the Lambert-Amery glacial system has undergone recent dynamic changes

Objective 2: Develop a regional model of the Lambert-Amery glacial system and contribute to improving the field of ice sheet modelling by investigating the importance of geothermal heat flux on ice flow

- create a regional domain and identify appropriate boundary and forcing parameters
- optimise the model for observations of grounding line location, surface velocity and ice thickness
- perform a sensitivity study to show how different geothermal heat flux datasets affect the solution
- test the importance of regions of localised elevated geothermal heat flux on ice flow

Objective 3: Investigate the sensitivity of the Lambert-Amery glacial system to climatic variations

- investigate the response of the Lambert-Amery glacial system to the primary climate forcing parameters: surface temperature, oceanic driven basal mass balance, surface mass balance and sea level change
- test the mechanisms that lead to the advance and retreat of the Lambert-Amery glacial system over glacial cycles
- assess the risk of marine-ice sheet instability leading to rapid retreat of Lambert and Mellor glaciers
- calculate the likely range of future sea level rise from the Lambert-Amery glacial system

1.3 Thesis Overview

The thesis is presented as a thesis by publication, with the following chapters addressing the thesis objectives:

Chapter 1 - Introduction

Chapter 2 - Flow of the Amery Ice Shelf and its tributary glaciers

This chapter contributes to Objective 1 by assessing the current dynamic state of the Lambert-Amery glacial system using a surface feature tracking technique on visual spectrum satellite images. The surface velocity, strain rates and vorticity fields are presented and discussed. Preliminary results show acceleration in the surface flow on the Mellor glacier between 2006 and 2010. This chapter is published as *Pittard et al.* (2013):

Pittard, M. L., J. L. Roberts, R. C. Warner, B. K. Galton-Fenzi, C. S. Watson, and R. Coleman (2013), Flow of the Amery Ice Shelf and its tributary glaciers, in *18th Australasian Fluid Mechanics Conference*, vol. 1, pp. 605-608.

Chapter 3 - Velocities of the Amery Ice Shelf's primary tributary glaciers, 2004–12

This chapter builds on the work from Chapter 2 and also addresses Objective 1. A new methodology is developed, allowing for more accurate surface velocity observations from surface feature tracking and a detailed error analysis. The temporal span investigated for change is expanded to 2004-2012. It is found that the surface velocities have not significantly changed over the period 2004 to 2012, which in conjunction with other observational studies suggests ongoing stability of the Lambert-Amery glacial system. This chapter is published in *Pittard et al.* (2015):

Pittard, M. L., J. L. Roberts, C. S. Watson, B. K. Galton-Fenzi, R. C. Warner, and R. Coleman (2015), Velocities of the Amery Ice Shelf's primary tributary glaciers, 2004-12, *Antarctic Science*, 27, 511-523, doi: 10.1017/S0954102015000231.

Chapter 4 - Organization of ice flow by localized regions of elevated geothermal heat flux

This chapter contributes to Objective 2, presenting the construction of the regional ice sheet model of the Lambert-Amery glacial system utilising the Parallel Ice Sheet Model (*Bueler et al.*, 2007; *Bueler and Brown*, 2009; *Winkelmann et al.*, 2011). The stability of the ice sheet in this region (Chapters 2 and 3) allow for the initialisation of the ice sheet system through minimising the difference between the simulated and

observed grounding line location, surface velocities and surface elevations. This chapter investigates the importance of localised high heat flow regions of geothermal heat flux that have been identified to exist within the Lambert-Amery glacial system (*Carson et al.*, 2014). We find that high heat flow regions can change the flow behaviour in slow flowing regions, causing the formation of local ice streams that suggests high heat flow regions may affect the organisation of ice flow over long time periods. This chapter is published as *Pittard et al.* (2016a):

Pittard, M. L., B. K. Galton-Fenzi, J. L. Roberts, and C. S. Watson (2016), Organization of ice flow by localized regions of elevated geothermal heat flux, *Geophysical Research Letters*, 43, doi:10.1002/2016GL068436.

Chapter 5 - Sensitivity of the Lambert-Amery glacial system to geothermal heat flux

This chapter contributes to Objective 2, presenting the thermal regime of the Lambert-Amery glacial system, and its sensitivity to choice of geothermal heat flux datasets. This chapter is published as *Pittard et al.* (2016b):

Pittard, M. L., J. L. Roberts, B. K. Galton-Fenzi, and C. S. Watson (2016), Sensitivity of the Lambert-Amery glacial system to geothermal heat flux, *Annals of Glaciology*, 57, doi: 10.1017/aog.2016.26.

Chapter 6 - Response time of Lambert-Amery glacial system to climatic variations

This chapter contributes to Objective 3 by investigating the response of the Lambert-Amery glacial system to long term changes in climatic variations. The focus of this chapter is on the mechanisms which lead to the advance and retreat of the grounding line over glacial cycles. As the ice sheet gains mass, the grounding line rapidly advances along bed slopes which become shallower as it advances, until it the bed slope begins to deepen again. It then stabilises and gains mass before advancing again. The advance of the grounding line and the consequent increases in mass cannot match observations, which suggests mechanisms which cannot be reproduced within our model played a role during the last glacial maximum. We find that the seaward portion of the ice shelf grounded faster than the poleward portion of the ice shelf, creating an enclosed ocean cavity. Retreat from the advanced positions occurs rapidly via the marine instability theory to the current grounding line, where the high sill restricts further retreat. This chapter is not presently under consideration for publication.

Chapter 7 - Future sea level change from Antarctica's Lambert-Amery glacial system

This chapter contributes to Objective 3 by investigating the possible contribution of Lambert-Amery glacial system to sea level rise over the next 500 years. The Lambert-Amery glacial system is resistant to rapid mass loss, as even a small ice shelf provides considerable buttressing to the ice flow. The grounding line is unable to retreat up the steep positive slope where it is currently grounded, allowing for increases in precipitation which led to the region being a sink for sea level in our simulations. This chapter is under preparation for submission to *Geophysical Research Letters*.

Pittard, M. L., B. K. Galton-Fenzi, C. S. Watson, and J. L. Roberts(2016), Future sea level change from Antarctica's Lambert-Amery glacial system, *Geophysical Research Letters*, (In Preparation).

Chapter 8 - Conclusions and Future Directions

This chapter has been removed for copyright or proprietary reasons.

Pittard, M. L., Roberts, J. L., Warner, R. C., Galton-Fenzi, B. K., Watson, C. S., Coleman, R., Flow of the Amery Ice Shelf and its tributary glaciers, Proceedings of the 18th Australasian Fluid Mechanics Conference, 3-7 December 2012, Launceston, Tasmania, pp. 605-608. ISBN 978-0-646-58373-0 (2013) [Refereed Conference Paper]

Chapter 3

Velocities of the Amery Ice Shelf's primary tributary glaciers, 2004–12

This chapter presents observations of the Lambert-Amery glacial system's surface velocity field focussing on the regions adjacent to the grounding zones of the Amery Ice Shelf's primary tributary glaciers for the period of 2004-2012. This work improved the methodology from the previous chapter by using a weighted correction approach which allows for the calculation of an error field. The content of this chapter is published as *Pittard et al.* (2015) and is re-formatted for this thesis but otherwise presented as published in:

Pittard, M. L., J. L. Roberts, C. S. Watson, B. K. Galton-Fenzi, R. C. Warner, and R. Coleman (2015), Velocities of the Amery Ice Shelf's primary tributary glaciers, 2004-12, *Antarctic Science*, 27, 511-523, doi: 10.1017/S0954102015000231.

3.1 Abstract

Monitoring the rate of ice flow into ice shelves is vital to understanding how, where and when mass changes occur in Antarctica. Previous observations of ice surface velocity indicated that the Amery Ice Shelf and tributary glaciers have been relatively stable over the period 1968 until 1999. This study measures the displacement of features on the ice surface over a sequence of Landsat 7 images separated by approximately one year and spanning 2004 to 2012 using the surface feature tracking software IMCORR. The focus is on the region surrounding the southern grounding zone of the Amery Ice Shelf and its primary tributary glaciers: the Fisher, Lambert, and Mellor glaciers. No significant changes in surface velocity are observed over this period. Accordingly, we use the velocity fields from each image pair between 2004 and 2012 to synthesise an average velocity dataset of the Amery Ice Shelf region and compare it to previously

published velocity datasets and *in situ* Global Positioning System velocity observations. We find no significant change in ice surface velocities between 2004 and 2012 in the Amery Ice Shelf region which suggests it continues to remain stable.

3.2 Introduction

There is still large uncertainty regarding how ongoing climate change is impacting the Antarctic Ice Sheet. Current estimates of the mass balance indicate that the Antarctic Ice Sheet is currently losing mass and contributing to sea level rise, but with significant regional variability (*Shepherd et al.*, 2012). The Antarctic Peninsula and the West Antarctic Ice Sheet have been observed to be losing mass at an accelerated rate (e.g. *Scambos et al.*, 2004; *Shepherd et al.*, 2004; *Holland et al.*, 2008). This is partially offset by mass gains over large expanses of the East Antarctic Ice Sheet (EAIS) (e.g. *Shepherd et al.*, 2012). In a warming climate, there are mechanisms that drive increasing mass loss through changes in ice dynamics, and conversely processes that drive increases in accumulation and associated mass gain.

The current and future mass loss from the Antarctic Ice Sheet is likely to be governed by accelerations in ice flow following changes in the dynamics of ice shelves that border the ice sheet, partially balanced by increasing precipitation. Observations of increased ice flow following changes in the ice shelves are linked to increasing ocean temperatures, increases in surface melt days, the intrusion of warmer water masses onto the continental shelf and changes in ocean currents underneath ice shelves (e.g. *Rignot et al.*, 2002; *Holland et al.*, 2008). These changes cause a reduction in the buttressing backforce exerted by the ice shelf on its tributary glaciers (*Dupont and Alley*, 2005; *Pritchard et al.*, 2012), which subsequently leads to accelerations in their flow (e.g. *Holland et al.*, 2008). Increasing mass losses from accelerating glaciers are partially offset by mass gain over the EAIS due to increased precipitation (*Shepherd et al.*, 2012). Global climate models predict an increase in precipitation over Antarctica that may potentially offset the mass loss caused by ice dynamic changes in the future (e.g. *Krinner et al.*, 2007). Recently there have been a number of high snowfall years that may indicate an upward trend in precipitation (*Boening et al.*, 2012), however, the short observational time series makes this conclusion equivocal. Large natural climate variability (*Monaghan et al.*, 2006) combined with spatially extensive monitoring being limited to the satellite era restricts our ability to assess what changes are occurring, what the impacts may be and how they will vary over the next century. The difficulty in estimating future contributions of the Antarctic Ice Sheet to sea level rise is that both the amount of mass loss due to ice dynamical changes and changes in precipitation are uncertain.

While the regions of Antarctica that are demonstrating rapid change have been the focus of high spatial and temporal resolution velocity observations, it is also important to monitor large outlet glaciers currently thought to be stable. The Amery Ice Shelf (AIS) is the third largest ice shelf in Antarctica (*Allison*, 1979) and its drainage basin is a significant contributor to the mass budget of the EAIS (e.g. *Yu et al.*, 2010).

Understanding the present and future climate change response of the EAIS is important to understanding whether the Antarctic will be a net source or sink of sea level rise, making the AIS and its tributary glaciers an important study region.

This study calculates the velocities of the AIS and its three main tributary glaciers: the Fisher, Lambert and Mellor glaciers, concentrating on the AIS grounding zone. The feature tracking software IMCORR was applied on a sequence of Landsat 7 images selected at approximately yearly intervals between 2004 and 2012. The velocities for each yearly image pair between 2004 and 2012 were calculated, as was the overall change between 2004 and 2012. Velocities were compared with limited available *in situ* Global Position System (GPS) measurements and published satellite-based velocity measurements for the region.

3.3 Background

3.3.1 The Amery Ice Shelf Region

The AIS is the largest embayed ice shelf in East Antarctica, with an area of $\approx 60,000$ km^2 (*Galton-Fenzi et al.*, 2008). The Mellor, Fisher and Lambert glaciers account for 60.5% of the mass that flows into the AIS (*Yu et al.*, 2010). The ocean cavity underneath the AIS has one of the deepest contact points with ice in Antarctica (*Fricker et al.*, 2002) with the circulation underneath the AIS dominated by the ice pump process (*Galton-Fenzi*, 2009). The recent BEDMAP2 bedrock topography compilation (*Fretwell et al.*, 2013) shows substantially more marine based ice sheet in the AIS region than was previously known.

There is a long history of measurements on the AIS, with the first *in situ* measurements of elevation and velocity recorded between 1968 - 1970 (*Budd et al.*, 1982). Global Positioning Systems (GPS) were deployed during 1988 and continued episodically until 1999 (*King et al.*, 2007). These observations are limited by their single location nature, and observations focussed on the northern part of AIS (*King et al.*, 2007). The first spatially extensive satellite observations used to analyse velocities in the AIS region were Synthetic Aperture Radar (SAR) images from 1997 (*Joughin*, 2002; *Young and Hyland*, 2002). In addition, gravimetry studies (e.g. *King et al.*, 2012) have been monitoring large scale mass change across Antarctica, with the Amery drainage basin a region of continued interest. Altogether, there exist records around four decades long to review both velocity and elevation change in the AIS region. The velocity of the northern region of the AIS was shown to decrease by 0.5% between 1968 and 1999 (*King et al.*, 2007) with the elevation being stable over the period from 1968 to 2007 (*King et al.*, 2009). A number of different estimates of the velocity field have been calculated for the AIS (*Joughin*, 2002; *Jezek*, 2003; *Rignot et al.*, 2011a; *Young and Hyland*, 2002), however, due to different assumptions in their calculations, these estimates cannot be directly compared. Recently, *Wen et al.* (2008) estimated that the mass of the entire grounded ice catchment feeding the AIS was approximately in bal-

ance with a net flux of -4.2 ± 9.8 Gt year^{-1}, which, contrasts with *Yu et al.* (2010) who estimated an increase in mass of 22.9 ± 4.4 Gt for the same region. Different estimates of ice thickness at the grounding zone appear to be the source of the discrepancy, and of consequent differences in estimates of ice shelf basal mass loss *Galton-Fenzi et al.* (2012).): A gravimetry study found that the region which contains the drainage basins of the Mellor, Fisher and Lambert Glaciers gained 5-15 Gt year^{-1} of mass over a period 2002-2010 (*King et al.*, 2012). The observations outlined above indicate that the AIS and its southern drainage basin are probably in steady state.

3.3.2 Glacier Velocity Measurement Techniques

Surface ice velocities can be measured by *in situ* GPS and a variety of different remote sensing techniques, such as feature tracking, InSAR (*König et al.*, 2001) and speckle tracking (*Gray et al.*, 2001). The point nature of GPS data limit their applications for measurement of large regions, however, they are ideal for the validation of velocity datasets obtained using remote sensing methods.

Feature tracking techniques use optical or radar images, tracking persistent features between two images separated by a known time interval to obtain velocities. This technique was automated by *Scambos et al.* (1992) among others and has been applied to many regions of Antarctica (e.g. *Lucchitta et al.*, 1993; *Scambos and Bindschadler*, 1993; *Warner and Roberts*, 2013). The implementation by *Scambos et al.* (1992) utilises Fast Fourier Transform cross-correlation algorithms to match features between images. The resulting displacements, which maximise the correlations, can be converted into velocities by dividing the displacement by the time interval between image acquisitions. The optimal time interval between an image pair used for this technique will vary between individual study regions. The time should be chosen based on how long surface features will survive in a given area. The longer the time period between image pairs, the larger the signal to noise ratio. However, the longer the time period, the higher the chance of the features changing shape or character sufficiently that a correlation between images cannot be identified. Three main sources of error within this method include inherent error in the feature tracking method, residual geo-location errors in each image and errors due to failure to consider ice flow curvature. The inherent error in the software process is due to limitations of the sub-pixel interpolation (*Scambos et al.*, 1992). The geo-location error is caused by errors in the geo-rectification process, where small errors in sensor location and altitude, combined with an inaccurate Digital Elevation Model (DEM) used in the image ortho-rectification process lead to a complicated spatially variable error across the image, preventing even stationary features being perfectly aligned between two images. Stationary features can be used as control points to correct for this problem, with *Frezzotti et al.* (1998) showing that for Landsat 4 images (30m resolution), when viable control points exist the errors in displacements are approximately 0.5 pixels. The error due to curvature of ice flow is caused by the feature tracking technique only measuring the distance between a feature on two im-

ages, and not the actual path the feature takes, leading to possible underestimates of ice velocity.

3.4 Methods

3.4.1 Data

The Landsat 7 satellite, launched in 1999, produces images within the panchromatic band with a 15m spatial resolution with a 16-day repeat cycle. It has a near polar orbit which is repetitive, circular and sun-synchronous. In 2003 an on-board instrument, the Scan Line Corrector (SLC), failed. All images captured thereafter have data gaps that appear as black stripes that originate towards the middle of the image and are spread in the across track direction. The data gaps caused by the SLC failure account for approximately 25% of each image. The images used in this study have undergone cubic convolution re-sampling to a polar stereographic projection and the lack of ground control points limited correction to Systematic Terrain Correction (Level 1Gt) by the U.S. Geological Survey. This provides systematic, radiometric and geometric accuracy, while utilising the RAMP v2 DEM for elevation correction.

The images used are from Landsat 7 row 127 and path 112 (Figure 3.1). For each year, the image with the lowest percent of cloud cover during the month of February was selected, since having images from different months could introduce errors from different shadow lengths. We undertook our analysis on Landsat 7 images on a polar stereographic projection with standard latitude of 71 °S and central meridian of 0 °E. All our comparison velocity data share this projection.

Two Antarctic-wide velocity datasets were chosen to compare against our results. These datasets are the RADARSAT-1 Antarctic Mapping Project Modified Antarctic Mapping Mission (RAMP-MAMM) (*Jezek*, 2003) and the NASA Making Earth System Data Records for Use in Research Environments Antarctic ice velocity dataset (MEaSUREs (*Rignot et al.*, 2011b)). The RAMP-MAMM velocity dataset was derived from RADARSAT-1 satellite passes between September 3, 2000 and November 17, 2000 and calculated by InSAR. MEaSUREs is derived using a combination of InSAR measurements and speckle tracking (*Mouginot et al.*, 2012) from data taken between 2007 and 2009. The MEaSUREs dataset is provided on a 900m grid (*Rignot et al.*, 2011b) and was re-gridded using linear interpolation to a 1km grid for comparison with our study.

Three GPS measurement sites exist in our study region (Figure 3.2) that can also be used for comparison. The GPS measurements span a different epoch (1998-2001) to the MEaSUREs satellite velocity measurements, but overlap with the RAMP-MAMM dataset. One of the GPS sites is located on the grounded portion of the Mellor Glacier, and two on the floating portion of the AIS (Figure 3.2).

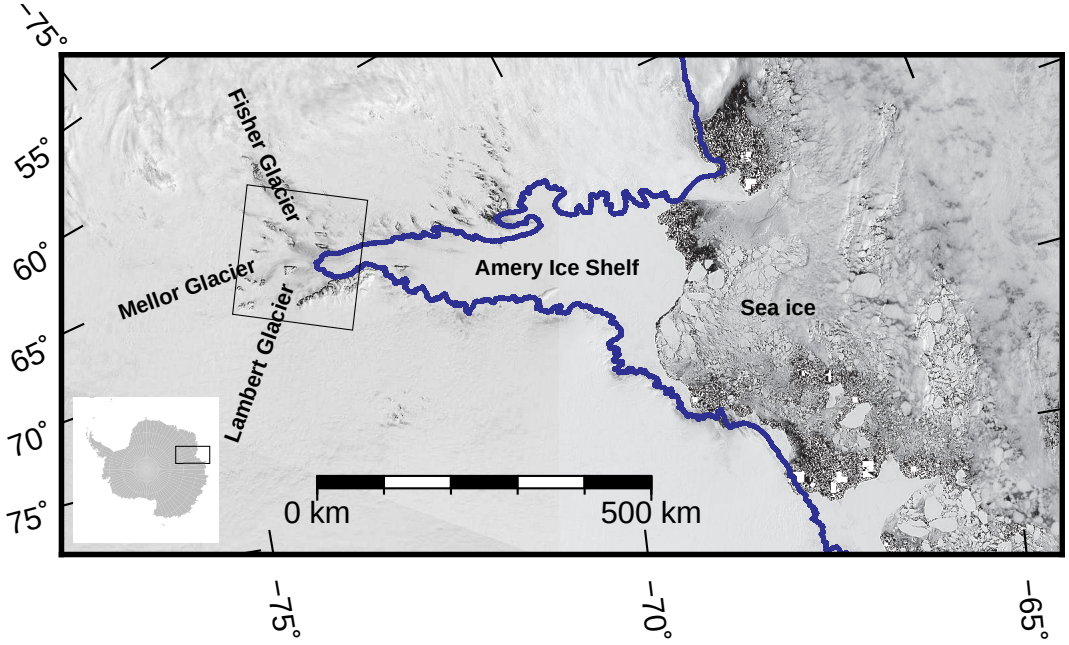

Figure 3.1: Study site locality. The black box shows extent of the Landsat 7 (Row 127, path 112) images and study region. The blue line is the Antarctic surface accumulation and ice discharge grounding line (*Bindschadler et al.*, 2011). Background is from Moderate Resolution Imaging Spectroradiometer image, courtesy NASA Goddard Space Flight Center, Rapid Response.

3.4.2 Velocity Calculations

Velocities are calculated using the feature tracking software, IMCORR, which was developed by *Scambos et al.* (1992) to track features in optical images, such as provided by the Landsat satellites. We use a version of IMCORR modified by *Warner and Roberts* (2013) in order to successfully overcome a limitation of the original software that prevented its use with Landsat 7 data affected by the SLC failure.

The images used in this study were contrast enhanced before analysis to improve the signal to noise ratio. The correlation analysis used a search window of 256x256 pixels and a reference window of 64x64 pixels. The search window and reference window sizes are calibrated to the size of the expected displacements in the study region. The displacements calculated from the IMCORR process were binned into 1km x 1km areas using a least trimmed squares method, requiring three data points to be in each bin, before undergoing a nearest-neighbours culling. A data point was only accepted if four of the nine data points in a 3 x 3 bin window had displacement components within 150m. The displacements were then corrected for geo-location errors (discussed below), and then converted into velocities by dividing by the time between the two images. The measured velocities are horizontal projections of the true velocity, but in this region the vertical velocity is less than 1% of the overall flow, so not considered significant. The velocities are plotted at the start point of the displacement vector. Velocities below 150 m year^{-1} were removed due to low confidence in correlations, largely as a function of minimal surface crevassing and feature expression at low velocities in this region. The

method used is discussed fully in *Warner and Roberts* (2013).

3.4.3 Geo-Location Error Corrections

There is a spatially variable offset between each pair of images, caused by geo-location error, which becomes apparent in the initial displacements that are generated by IMCORR. The displacement direction and magnitude vary for each control point and for each image pair. We assume that the error caused by geo-location error has both a systematic offset component, as well as a random component. Features that are known to be stationary over the given time period, such as mountains and nunataks, are used as control points to correct for the spatially non-uniform systematic offset component, with the remaining random component being treated as an error term in the subsequent computation of the velocity uncertainty.

The six most central groups of mountains/nunataks in the region, N_1 through N_6 (Figure 3.2) that surround the Fisher, Lambert and Mellor glaciers in the imagery were used as control points to account for systematic geo-location offsets. For each image pair, the mountains/nunataks groups, i ($i = 1, ..., 6$), were taken in isolation and a position $\mathbf{n}_i(= \{n_{ix}, n_{iy}\})$, where x is the easting and y is the northing assigned to the centre of each mountain/nunataks group. The IMCORR process generates non-zero displacement vectors across the mountain/nunataks, indicating the offset in the image, since these displacement vectors should be zero. The displacement vectors in the centre of each group of mountains/nunataks are discarded in this calculation to minimise any error due to elevation difference relative to the ice surface and illumination changes. Any other anomalous vectors (those that clearly did not match any features) were manually removed. The median of the remaining displacements, $\mathbf{M}_i(= \{M_{ix}, M_{iy}\})$, and the normalised median absolute deviations (NMAD) at 95% confidence interval of the spread of these displacements, $\mathbf{NMAD}_i(= \{NMAD_{ix}, NMAD_{iy}\})$ was calculated for each group of mountains/nunataks (Table 3.1). The NMAD has been shown to provide appropriate error bounds compared to other techniques (*Höhle and Höhle*, 2009). We then assumed that the median displacements are locally representative of the offset caused by the geo-location error and that it changes smoothly between each group of mountains/nunataks. This allows us to weight the medians of each mountains/nunataks group by distance using an inverse distance squared weighting, and make a correction, $\mathbf{C}(= \{C_x, C_y\})$ (Equation 3.1), to the displacement at any point, $\{p_x, p_y\}$:

$$\mathbf{C}(p_x, p_y) = \frac{1}{d} \sum_{i=1}^{6} \frac{\{M_{ix}, M_{iy}\}}{(p_x - n_{ix})^2 + (p_y - n_{iy})^2} \tag{3.1}$$

where $d = \sum_{i=1}^{6} \frac{1}{(p_x - n_{ix})^2 + (p_y - n_{iy})^2}$

The initial displacements, $\mathbf{D}^I(= \{D_x^I, D_y^I\})$, have $\mathbf{C}$ subtracted to obtain the final displacement vectors, $\mathbf{D}^F(= \{D_x^F, D_y^F\})$ (Equation 3.2).

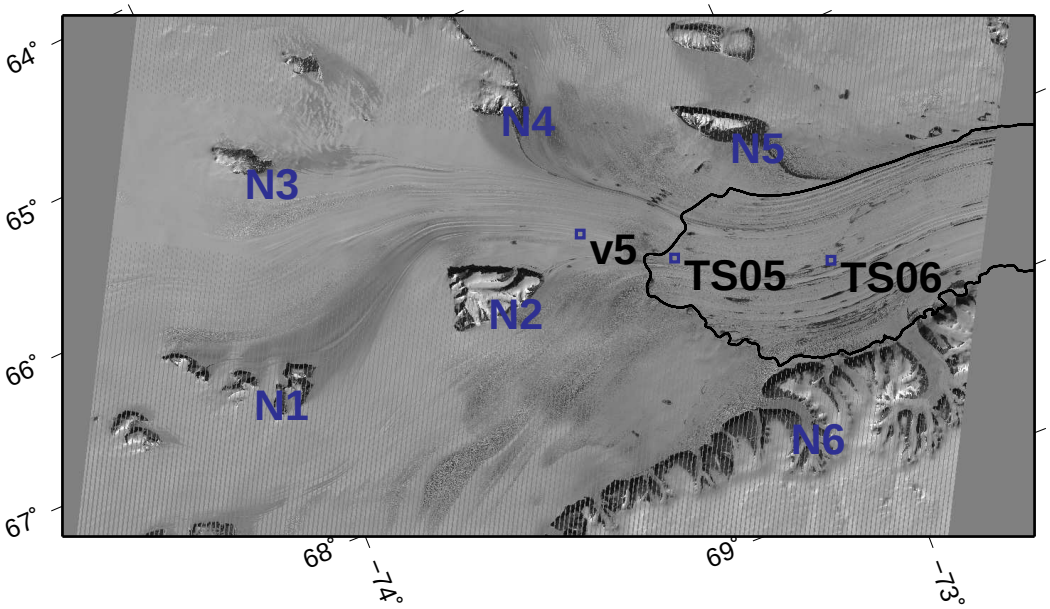

Figure 3.2: The location of the Nunataks used for geo-location corrections and GPS locations. Grounding line as per Figure 1.

Table 3.1: An example of calculated values for image pair of 2004 and 2005, where M_x,M_y, are the median displacements and $NMAD_x$, $NMAD_y$ are the NMAD value at 68.3% confidence interval of the vector components (m) at the given nunatak N1-N6.

Location	Longitude ($^\circ E$)	Latitude ($^\circ S$)	M_x	M_y	$NMAD_x$	$NMAD_y$
N_1	66.74	73.08	25.5	9.3	4.6	4.4
N_2	66.80	73.60	31.05	13.05	4.9	4.7
N_3	65.31	73.93	34.05	10.35	1.8	1.4
N_4	65.65	73.44	38.85	4.8	3.3	2.7
N_5	66.42	73.06	33.15	18.9	2.4	2.3
N_6	68.38	73.16	28.65	16.2	5.7	4.7

$$\mathbf{D}^F = \mathbf{D}^I - \mathbf{C} \tag{3.2}$$

3.4.4 Error Calculation

The error in the calculated velocities, $\mathbf{D}^F$, is made up of the error in $\mathbf{D}^I$ and $\mathbf{C}$. $\mathbf{D}^I$ has three sources of error: one systematic and two independent random errors. The systematic error is from the geo-location systematic offset, which $\mathbf{C}$ is used to correct. The first independent error is associated with the correlation calculated within the IMCORR program (*Scambos et al.*, 1992), and the second is the remaining random error component associated with any residual geo-location error after the offset has been applied. The correction $\mathbf{C}$ has only the two independent sources of error. The correlation method outlined in *Scambos et al.* (1992) reports an error of 0.1 of a pixel, with the modifications by *Warner and Roberts* (2013) reporting an error typically

around 0.25 of a pixel. The residual geo-location error cannot be separated from the IMCORR specific error, and hence we treat them as a single combined error term that can be applied to both $\mathbf{D}^I$and $\mathbf{C}$ respectively. To estimate this error, we use the displacements at the $\mathbf{n}_i$. We know the velocity should be zero at this point, so the remaining spread of displacements should provide an estimate of random errors. This estimate is calculated by using the values from **NMAD**. To estimate the random errors for the displacements on the ice, we assume that the error varies between each nunatak/mountains group in the same way as the computed offset correction field $\mathbf{C}$. This allows us to use the inverse squared weighting applied in equation 1 to assign an error for each point, $\{p_x, p_y\}$, which gives an error field, $\mathbf{E}(= \{E_x, E_y\})$ (Equation 3.3), that gives the error in both $\mathbf{D}^I$ and $\mathbf{C}$ ($\mathbf{E}_{D^I}$ and $\mathbf{E}_C$ respectively).

$$E_x^2 = \frac{1}{d^2} \sum_{i=1}^{6} \frac{NMAD_{ix}^2}{[(p_x - N_{ix})^2 + (p_y - N_{iy})^2]^2} \qquad (3.3)$$

and similarly for E_y

When the offset to correct for the geo-location is applied, the error is propagated in quadrature to give $\mathbf{E}_{D^F}$ (equation 3.4).

$$\mathbf{E}_{D^F} = \sqrt{(\mathbf{E}_{D^I})^2 + (\mathbf{E}_C)^2} \qquad (3.4)$$

Additionally, when a velocity field from one year was compared to another year, the associated errors for each $\mathbf{D}^F$ are propagated in quadrature similarly to equation 3.4.

3.5 Results

The velocity field and error field is calculated for each pair of sequential images between 2004 and 2012. The velocity magnitude and error field comparing 2004 to 2005 (Figure 3.3) shows the spatial variation of the datasets and the base error fields. This is the only comparison for a single year presented herein, the other velocity and error fields are provided in supplementary information (See Figures S3.1-S3.7 in Appendix A).

The velocity fields from 2004/2005 and 2011/2012 are differenced to examine the acceleration of the ice velocity between these two time periods (Figure 3.4a). While there appears to be a coherent pattern of change in the Mellor glacier as it approaches the grounding zone, we have low confidence that a change is significant unless it exceeds the error in the region (Figure 3.4b). Figure 3.4c shows the ratio of change to error, with only values lying outside [-1,1] considered significant. We find there are no coherent patterns of significant change. This is highlighted in Figure 3.5a, as the distribution of velocity differences is approximately Gaussian and is centred on a median just below zero. There is also a potential bias from certain groups of mountains/nunataks used in

the geolocation process as can be seen by the distribution of the error field (Figure 3.4b). Figure 3.5b shows that there were no major velocity changes on a yearly scale over any annual increment within the time periods, with the symmetrical distributions all centred on a median of approximately zero. Each velocity map used in the differencing has an associated error field, which are propagated by quadrature (Figure 3.4) that results in a new error field associated with the velocity difference field. The outlying points on the figures are artefacts of the IMCORR process caused by anomalous highly correlated features that are not representative of ice flow.

A temporally averaged velocity field for the AIS (given the acronym VAIS) was produced by averaging seven of the eight different image pairs (Figure 3.6). The velocity pair from 2009/2010 was excluded due to cloud cover overlap such that 3 out of the 6 control points were covered in cloud across the two images. If a given grid location only had valid data for less than three years it was not included in the average.

The VAIS dataset was compared to the MEaSUREs, RAMP-MAMM and GPS datasets. The MEaSUREs field appears slower across almost the entire region (Figure 3.7a), with a slight patch of slower flow on the eastern side of the Lambert Glacier. The RAMP-MAMM data was shifted by 1km in the easting before comparison due to an offset found when comparing the rms error between RAMP-MAMM and our dataset. The RAMP-MAMM dataset is faster on the ice shelf but the grounded portion of the AIS region shows considerable variations across the tributaries. RAMP-MAMM is faster in the lower section of the grounded Fisher Glacier, the Mellor Glacier is uniformally slower than the VAIS and the Lambert Glacier is faster in the western side and slower on the eastern side (Figure 3.7b). The speed difference between VAIS and MEaSUREs (VAIS-MEaSUREs) and VAIS and RAMP-MAMM (VAIS-RAMP)(Figure 3.8) both show an approximately Gaussian distribution. VAIS-MEaSUREs has a median speed difference of 8.81 m year^{-1} and VAIS-RAMP has a median speed difference of 0.75 m year^{-1}. VAIS-MEaSUREs has a flow angle difference of 0.13 degrees and VAIS-RAMP a median flow angle difference of 0.69 degrees.

The GPS velocities are typically faster than the VAIS (average of 5 closest points), MEaSUREs and RAMP-MAMM datasets (Table 3.2). The GPS site located on the Mellor Glacier (v5, Figure 3.2), showed closest agreement with the RAMP-MAMM dataset, with GPS still significantly faster by 19 m year^{-1}. When compared to VAIS and MEaSUREs, the same site is faster by 29 and 43 m year^{-1} respectively. TS05 was located near the grounding zone of the Mellor Glacier, and showed closest agreement with VAIS, with TS05 only 9 m year^{-1} faster in speed. This compares to 34 and 19 m year^{-1} against the MEaSUREs and RAMP-MAMM fields respectively. The final GPS site, TS06, is located on the ice shelf and shows closest agreement with VAIS, with TS06 being faster by 11 m year^{-1}. However, MEaSUREs and RAMP-MAMM also show close agreement with TS06, although with a difference in sign, with TS06 being 13 m year^{-1} faster than MEaSUREs but 13 m year^{-1} slower than RAMP-MAMM.

Table 3.2: Comparison between this study (VAIS), MEaSUREs, RAMP-MAMM and in situ GPS velocities (All velocities in m year^{-1}). GPS locations are: v5, 67.48°E, 72.98°S, TS05, 67.07°E, 73.25°S, TS06, 66.68°E, 73.40°S.*Some regions in the MEaSUREs dataset may have data from other epochs given the computation approach adopted by *Rignot et al.* (2011a)

GPS Sites	GPS Location	GPS	VAIS (2004-12)	MEaSUREs (2007-09*)	RAMP-MAMM (2000)
v5 (1997/98)	$67.48°E, 72.98°S$	715 ±2	686 ±18	672 ±2	696 ±0.4
TS05 (2000/01)	$67.07°E, 73.25°S$	768 ±2	759 ±14.8	734 ±2	749 ±3.4
TS06 (2000/01)	$66.68°E, 73.40°S$	496 ±2	485 ±12.1	483 ±2	509 ±2.3

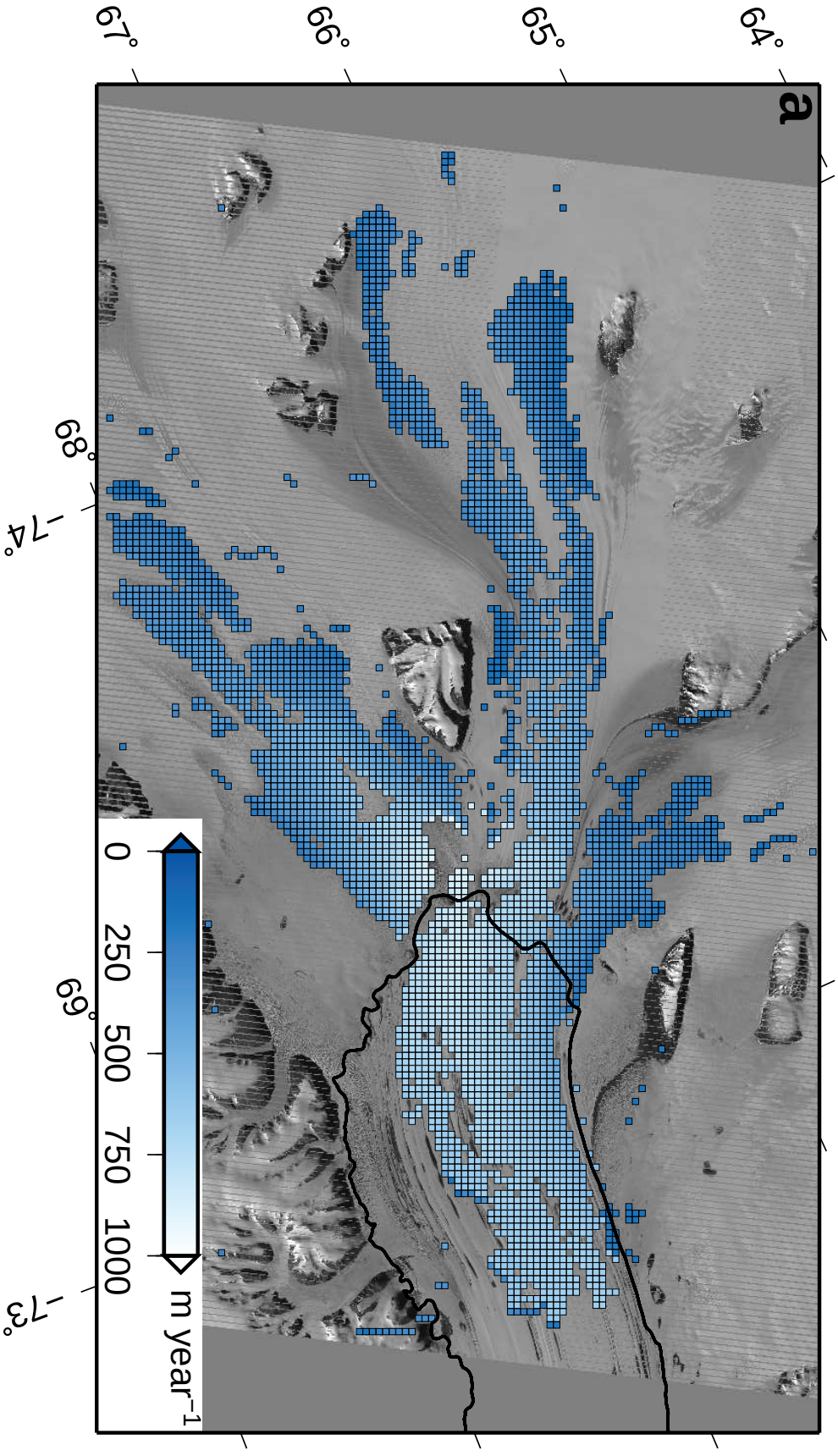

Figure 3.3: a) Magnitude of velocity field for image pair 2004/2005 and b) errors (NMAD 95% confidence interval) for the 2004/2005 image pair.

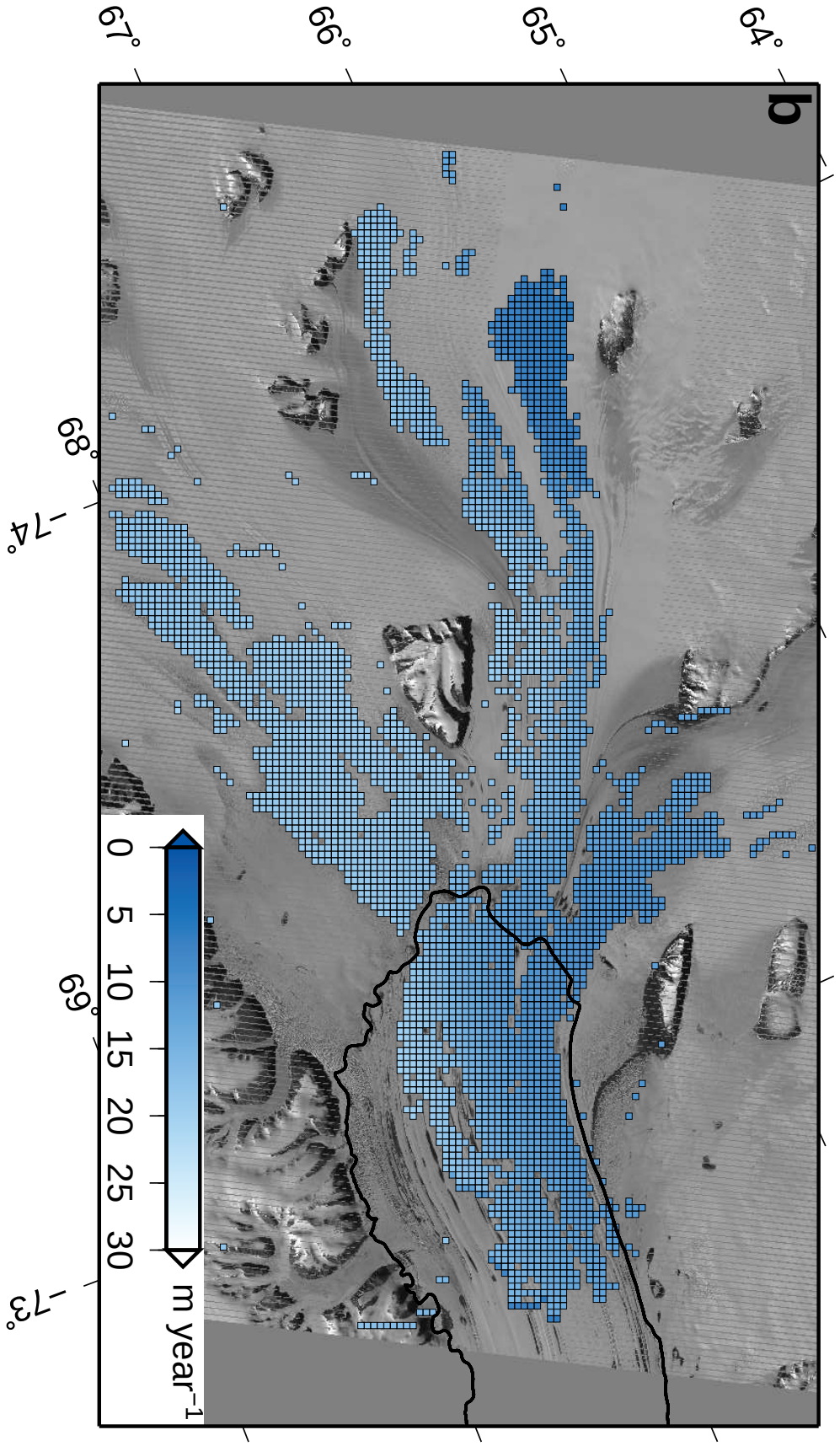

Figure 3.3: a) Magnitude of velocity field for image pair 2004/2005 and b) errors (NMAD 95% confidence interval) for the 2004/2005 image pair.

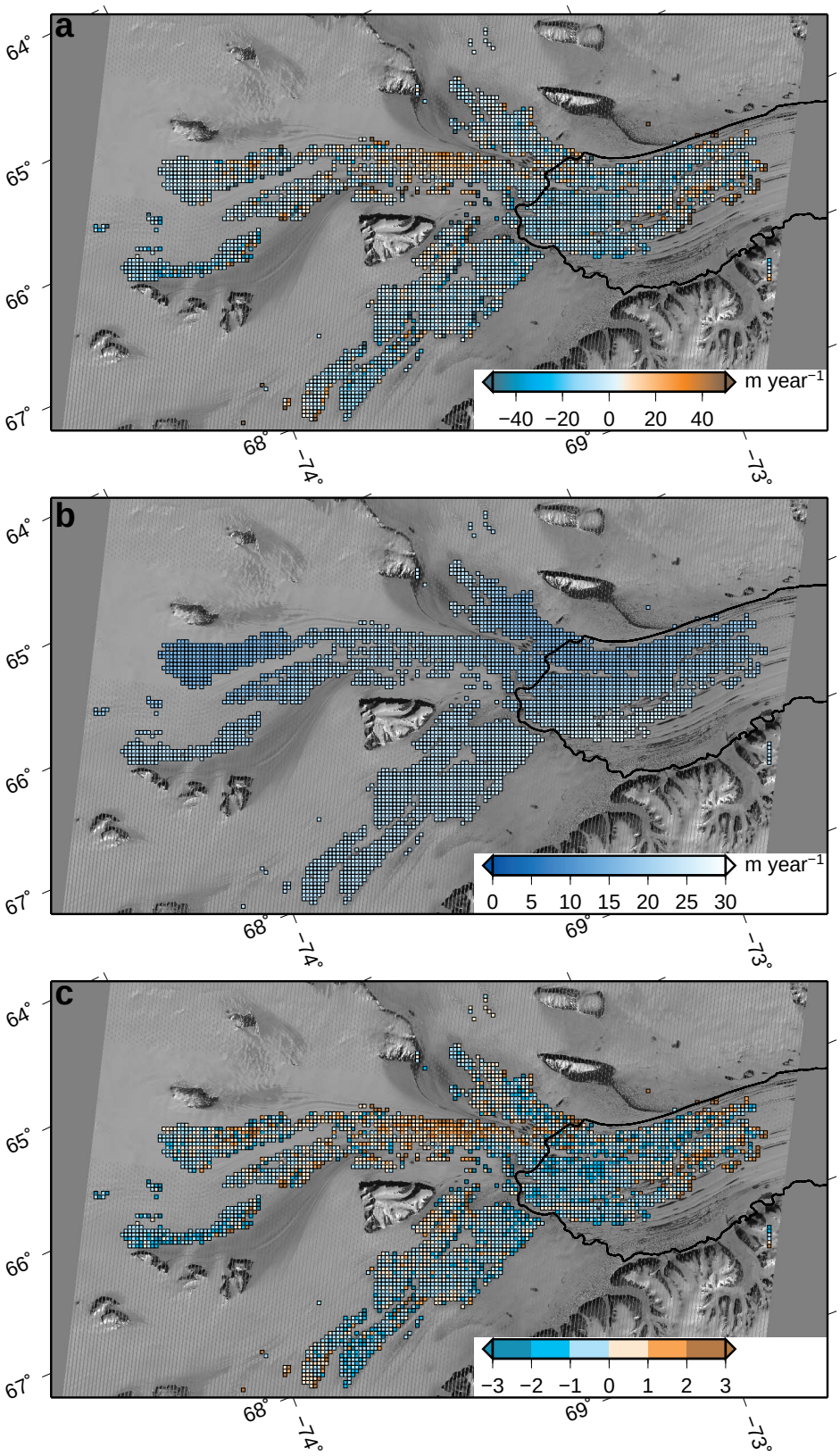

Figure 3.4: a) The change in speed between the year pair of 2004/2005 and 2011/2012. b) The combined area weighted error field (NMAD 95% confidence interval) for the change in speed. c) The ratio of change to error (NMAD), with (-1 to 1) representing the 68.3% confidence interval and (-2 to -1, 1 to 2) representing 95% confidence intervals. There is a signal at the 68.3% confidence level on the Mellor Glacier, but is not at the 95% confidence level.

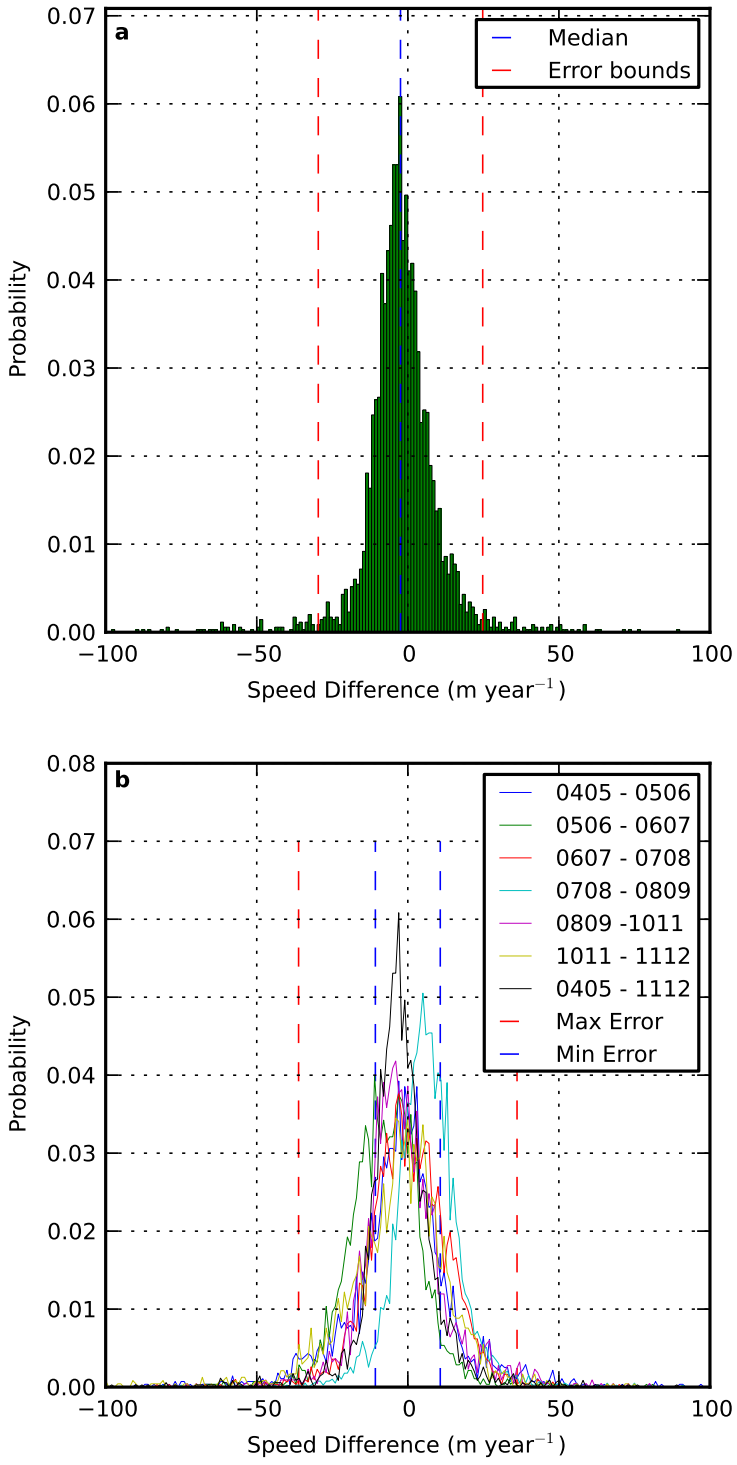

Figure 3.5: a) Histogram of the speed difference between 2004/2005 and 2011/2012. Error bounds are the highest 95% confidence interval from the calculated NMAD values across the study, centred on the median. b) Histogram compilation of all speed differences on a year to year basis between 2004 and 2012. The maximum and minimum error bound is centred around 0 given the assumption of no change, and based on the highest and lowest error (NMAD 95% confidence interval) across all comparisons. The peaks of the comparisons fall well within the error bounds, indicating that no years of anomalously high change occurred across our dataset.

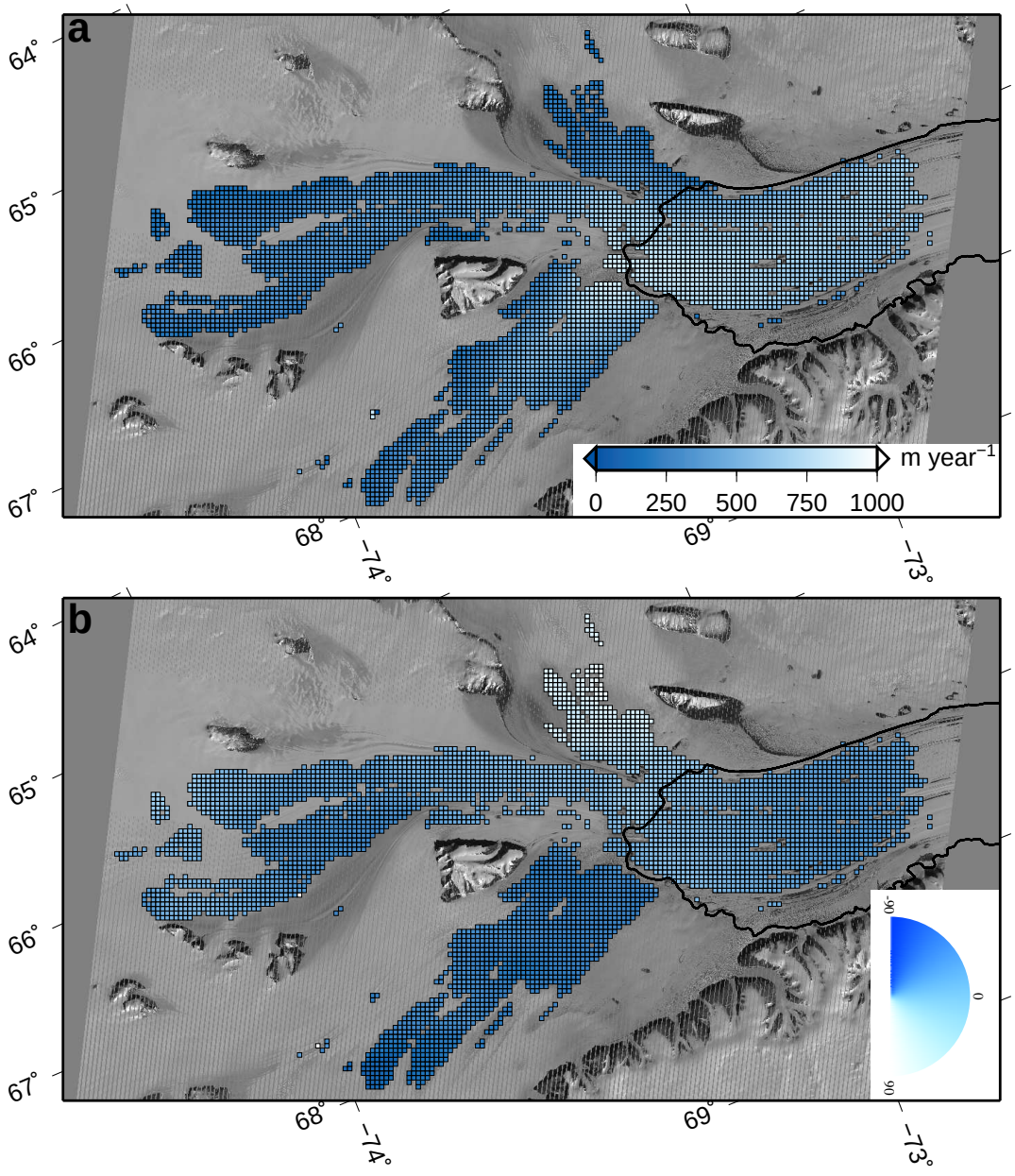

Figure 3.6: a) Mean VAIS flow calculated between 2004 and 2012, where there were at least three valid velocity calculations. b) The mean flow directions of the VAIS relative to the grid easting direction.

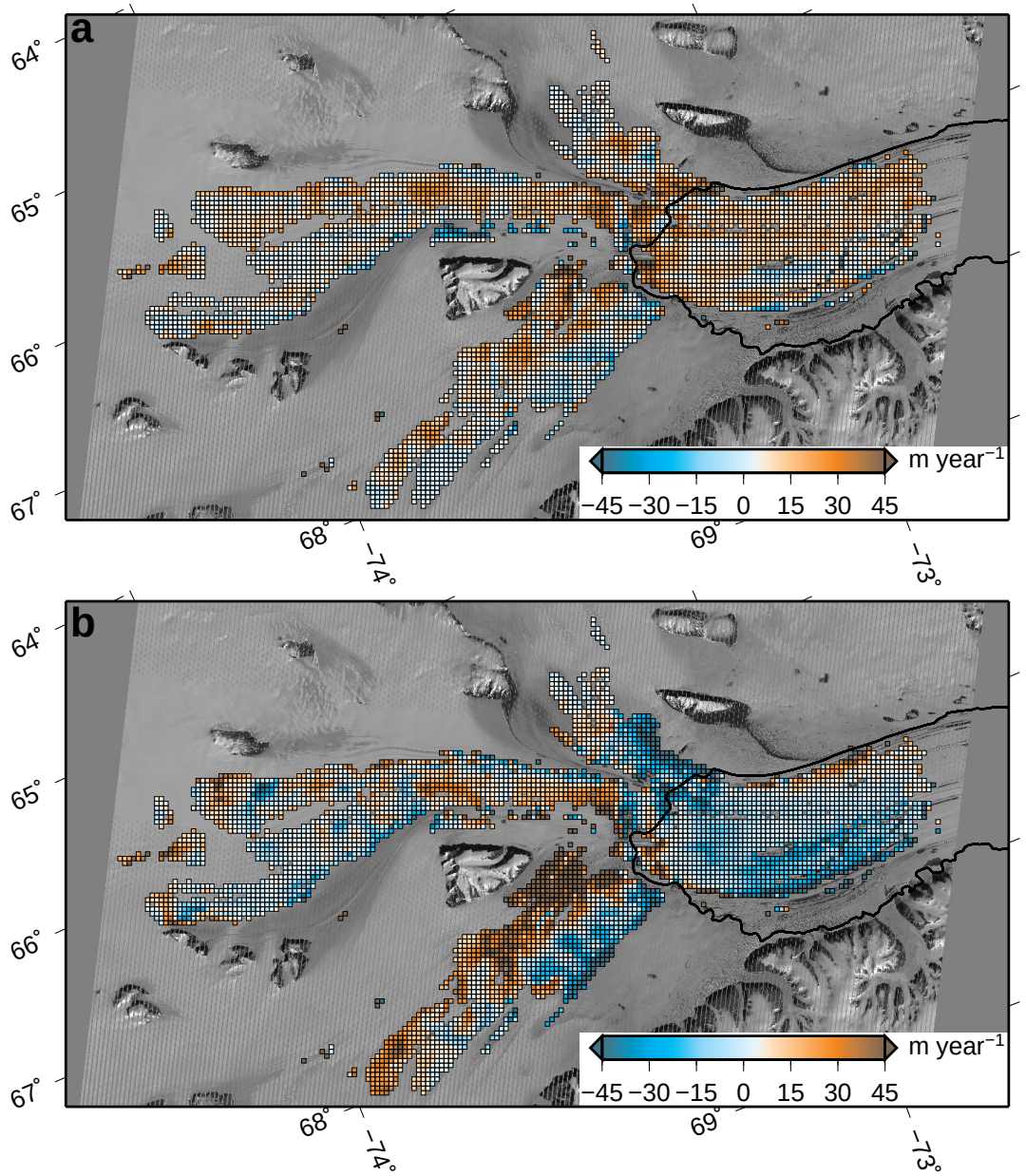

Figure 3.7: a) The difference in speed between VAIS and MEaSUREs. VAIS is largely faster then MEaSUREs with the exception towards the edges. b) The difference in speed between VAIS and RAMP-MAMM. The comparison shows an inconsistent pattern of velocity, particularly on the Lambert Glacier. The velocity on the Amery Ice Shelf is faster in the RAMP-MAMM dataset.

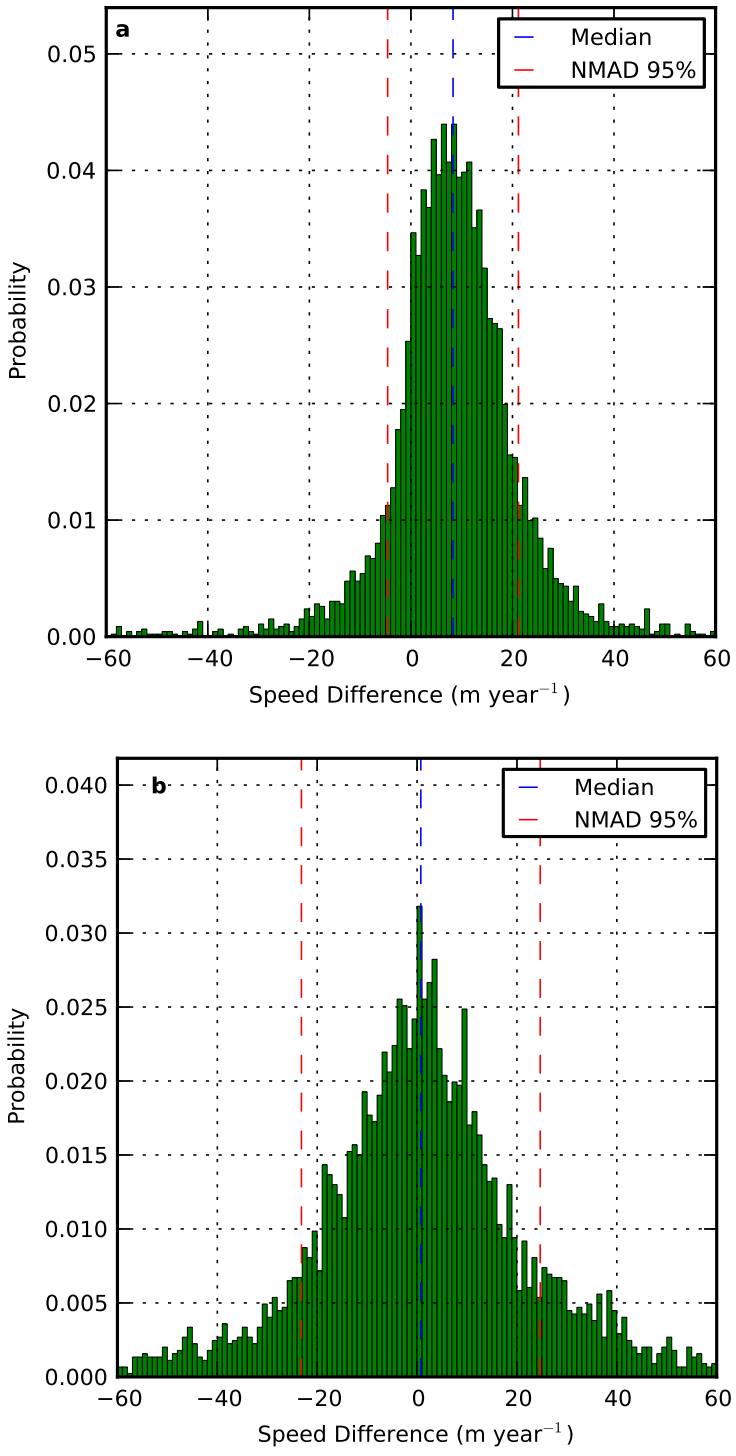

Figure 3.8: a) Histogram of the speed difference between VAIS and MEaSUREs. Error is the highest error (NMAD 95% confidence interval) from the comparison centred on the median. b) Histogram of the speed difference between VAIS and RAMP-MAMM. Error is the highest error (NMAD 95% confidence interval) from the comparison centred on the median.

3.6 Discussion

The velocity derived for the 2004/2005 image pair (Figure 3.4a) shows the expected velocity pattern for the AIS and tributary glaciers, with increasing velocities as the glaciers approach the grounding zone, with faster velocities just downstream on the ice shelf before they begin to slow down as the ice flows northwards. The error field is fairly uniform in distribution across the image at around 10 m year^{-1} (95% confidence interval), but with slightly higher error towards N6 and lower towards N3 indicating that the geolocation error is higher at N6. The coverage of the velocity estimates is spatially incomplete, with variations between each of the image pairs. There are a number of reasons for correlations breaking down in various regions and these may vary from year to year. The feature tracking technique breaks down in regions where the ice is deforming so rapidly that the feature changes shape, or where the ice is moving too slowly to generate detectable surface features, the surface has melted or there is cloud cover. Such phenomena translate to a lack of persistence of any given surface feature between images, hence little or no correlation in the IMCORR process. The large gap across the grounding zone as the Lambert Glacier enters the AIS may be caused by increased flow curvature causing surface features to not be clearly identifiable between two images as they will have deformed and changed orientation. Another possibility is that changing surface features caused by crevassing at the grounding zone deforms the features. In some years there was significant surface melt, which destroyed features across the AIS, as seen in the south-eastern portion of the AIS (Figure 3.3). Some of the images used throughout the study had varying levels of cloud cover which impacted the derived velocity coverage and geo-location corrections (Table S3.1).

There was no significant change in velocities between 2004/2005 and 2011/2012 on the Fisher, Lambert and Mellor glaciers and the southern portion of the AIS (Figure 3.4a). While there is evidence of spatially coherent change, particularly on the Mellor Glacier, given the method of correction for geo-location, we have low confidence in the change unless the magnitude is greater than the derived error (Figure 3.4c). This is highlighted by Figure 3.5a, where greater than 80% of the data is within the error bounds. This is consistent with year-to-year comparisons (Figure 3.5b) that show that while there are variations in median velocity for the individual image pairs, the differences are not significant. The NMAD (95% confidence interval) error ranges from 15 to 26 m year^{-1} across the region, which equates to a range of 2-10% depending on the velocity. Whilst we cannot rule out changes in velocity below this threshold, it suggests that any change that is occurring would be below 2% over a period of 8 years, otherwise it would be observed in our analysis in the fast flowing ice regions (where velocities reach 1000 m year^{-1}). Our results suggest that the ice surface velocity in the grounding zone region of the AIS has been in steady state between 2004 and 2012.

The VAIS velocity dataset agrees within error bounds with both the MEaSUREs and RAMP-MAMM datasets. The VAIS-MEaSUREs comparison shows that the VAIS velocities are higher in a spatially coherent pattern, with a median difference of 8.81 m

year^{-1}. The VAIS is faster in regions of high curvature, which was unexpected as the MEaSUREs dataset should measure the velocity along curves more accurately. This is possibly caused by a relatively large smoothing footprint in the MEaSUREs dataset. The VAIS-RAMP comparison shows an inconsistent spatial pattern. This contrasts with VAIS-MEaSUREs where the offset in speed was spatially consistent. The overall median difference of the VAIS-RAMP comparison is 0.75 m year^{-1}. The VAIS-RAMP comparison displays velocity differences in some regions of high curvature, such as the Fisher Glacier. The velocity difference due to curvature is $\approx 1\%$, indicating that it is only a component of the velocity difference in the VAIS-RAMP comparison. A number of approximations go into the InSAR technique, such as surface slope and firn depth, which may lead to the difference in velocity between the two techniques. Comparing MEaSUREs and RAMP-MAMM dataset shows that RAMP-MAMM is faster on the ice shelf, where errors associated with surface slope should be small. The common slow area on the eastern Lambert Glacier that is seen in both the VAIS-MEaSUREs and VAIS-RAMP comparisons may be an indication of a systematic difference in the techniques, or, be due to the higher error in the corrections due to N6.

Comparison of the three velocity fields with *in situ* GPS showed that GPS velocity estimates were generally faster. Two of the three GPS sites (v5 and TS05, Figure 3.2) agreed most closely with the VAIS dataset, however differences were of comparable magnitude to error within the velocity fields, making meaningful inference problematic. The remote-sensing techniques underestimate the velocity in this region relative to the GPS, but the limited spatial coverage and epochs of the GPS sites make it difficult to determine the cause of this discrepancy. Further GPS deployments on the tributaries and the AIS would be recommended to assist in a more comprehensive validation of the remote sensing techniques in this region. GPS located on the correction nunataks would also aid in the geo-location of the images.

One avenue for future work to reduce the uncertainties of our velocities (and hence the tolerance required to identify significant change), would be to improve the geo-rectification of the images prior to analysis. The residual geo-rectification error accounts for at least 50% of the error. This can be improved in various ways including by GPS receivers to accurately coordinate ground control points, using higher quality digital elevation models (which could then be used to reprocess the raw imagery) and/or using higher resolution imagery. The recent launch of the Landsat 8 satellite (15m resolution) will allow for the continued monitoring of the AIS region and possible extension of velocity changes further inland than covered in this study.

The observed velocities of the AIS region from our study and the previous work by *King et al.* (2009) indicate that the ice velocities have been stable over the respective study periods commencing in 1968 and concluding in 2012. There are limitations to the observations in the AIS region before 1998, with the estimates in change from *King et al.* (2009) limited with respect to spatial coverage in particular. Recent gravimetry studies indicate that the drainage basin of the AIS may be increasing in mass (*King*

et al., 2012), but this phenomena must be inconsequential for changing the driving stress and hence flow, given we do not see a change in surface velocities over the period of time adopted for this study. An unusual characteristic of the AIS, is that amongst major ice shelves, that as it flows towards the sea the width of the ice shelf initially narrows as it progresses, creating a choke point in the ice shelf which likely provides significant buttressing to the glacial flow. Additionally, there is evidence of a re-grounding zone after this choke point indicated by the ice rise known as the Budd Ice Rumples. The southern grounding zone of the AIS is a significant distance from the calving front and it has a long aspect ratio compared to the other major ice shelves. These features combine to provide the tributary glaciers with considerable buttressing which would not necessarily reduce if the front of the ice shelf began to retreat. The AIS also has one of the deepest grounding zones in Antarctica, which, if warmer water was to intrude could cause high melt rates in the grounding zones of the three major tributaries. The Lambert Glacier in particular drains a large marine basin which could be vulnerable to retreat in future climate scenarios. It will be important to continue monitoring this region since changes will not necessarily be as obvious as in other regions where ice shelves have dramatically retreated or collapsed. Ice sheet modelling will undoubtedly help identify the risk in this region due to possible future climate scenarios, and give indications of what may be the precursor indication of change in the region.

3.7 Conclusion

The southern region of the AIS and its primary tributary glaciers, the Fisher, Mellor and Lambert glaciers, show no significant change in velocity between 2004/2005 and 2011/2012 when investigated using feature tracking on optical Landsat 7 imagery. A spatially variable error field has been calculated from the variance of the geo-rectification correction, with the error varying between 14 to 22 m year^{-1}. Change in ice surface velocity may have occurred below this threshold which would have been less than 2% of the flow velocity over an eight year period. The output velocity dataset, termed VAIS, was calculated by averaging the yearly velocities from sequential image pairs between 2004 and 2012. VAIS shows higher velocities on the grounded ice, and slower velocities on floating ice than the older RAMP-MAMM dataset, but shows higher velocities compared to the more recent MEaSUREs dataset. The few GPS velocities were generally faster than all three velocity datasets, and further observations are required to determine if this is a significant systematic difference. There is no evidence of rapid changes in velocity in the AIS and its tributary glaciers, and all recent observations indicate the AIS region has been in approximate equilibrium over recent decades (since 1968). The AIS has a unique configuration which may dictate it responds differently to climate change than other regions, and as a major outlet of the EAIS it is important to continue to monitor and assess the risk of change in this region, and what impact it may have on sea level rise into the future.

3.8 Acknowledgements

This work was supported by the Australian Government's Cooperative Research Centres programme through the Antarctic Climate & Ecosystems Cooperative Research Centre (ACE CRC). Landsat 7 images courtesy of the U.S. Geological Survey. The VAIS dataset and associated velocity and error files for each image pair used within are available on the Australian Antarctic Data Centre (https://data.aad.gov.au/). We thank Allen Pope (NSIDC (University of Colorado)) and an anonymous reviewer for comments and suggestions that greatly improved this paper.

3.9 Supplementary Information

See Appendix A for the supplementary information for this chapter.

3.10 Concluding Remarks

This chapter presented new methodology for calculating the spatial offset between Landsat 7 images, applying an area weighted correction rather than a point source correction as in Chapter 2. This allowed for detailed error analysis to be conducted, allowing for the significance of any changes to be considered. Using a longer temporal period and the improved methods, no significant change in velocity was found for the Amery Ice Shelf and its tributaries between 2004 and 2012. This result allows for an ice sheet model of this region to be initialised through parameter optimisation by minimising the misfit between the numerical solution and observations of grounding line position, surface velocities and ice thickness.

Chapter 4

Organization of ice flow by localized regions of elevated geothermal heat flux

This chapter investigates the importance of high heat flux regions, generated by localised sources of elevated geothermal heat such as radioactive crustal heat production or groundwater flux. The methodology, development and initialisation of the Lambert-Amery glacial system regional domain are first published in this research. The content of this chapter is published as *Pittard et al.* (2016a) and is re-formatted for this thesis but otherwise presented as published in:

Pittard, M. L., B. K. Galton-Fenzi, J. L. Roberts, and C. S. Watson (2016), Organization of ice flow by localized regions of elevated geothermal heat flux, *Geophysical Research Letters*, 43, doi:10.1002/2016GL068436.

4.1 Abstract

The impact of localized regions of elevated geothermal heat flux on ice sheet dynamics is largely unknown. Simulations of ice dynamics are produced using poorly resolved and low resolution estimates of geothermal heat flux. Observations of crustal heat production within the continental crust underneath the Lambert-Amery glacial system in East Antarctica indicate high heat flux regions of at least 120 mWm^{-2} exist. Here we investigate the influence of simulated but plausible, localized regions of elevated geothermal heat flux on ice dynamics using a numerical ice sheet model of the Lambert-Amery glacial system. We find that high heat flux regions have a significant effect across areas of slow moving ice with the influence extending both upstream and downstream of the geothermal anomaly, while fast moving ice is relatively unaffected. Our results suggest that localized regions of elevated geothermal heat flux may play an important

role in the organization of ice sheet flow.

4.2 Introduction

Geothermal Heat Flux (GHF) has an important control on ice dynamics and contributes to the temperature distribution of the ice and influences ice flow by varying ice viscosity and basal lubrication. The magnitude of the GHF depends on spatially varying geological conditions that control heat production and conduction such as the mantle heat flux, crustal thickness, local radiogenic crustal heat production (RCHP) and groundwater flow (*Sandiford and McLaren*, 2002; *Fox Maule et al.*, 2005; *Carson et al.*, 2014; *Gooch et al.*, 2016). GHF is difficult to directly measure under the Antarctica Ice Sheet due to limited access to the bedrock, with only a few point measurements in ice free areas or from borehole sampling (*Fisher et al.*, 2015). The lack of direct measurements led to the development of model based methods that infer GHF from seismic (*Shapiro and Ritzwoller*, 2004) and magnetic field (*Fox Maule et al.*, 2005) models. *Shapiro and Ritzwoller* (2004) created a global seismic model of the crust and upper mantle based on known GHF observations then extrapolated it to regions where observations were rare or absent. The resulting GHF dataset has a coarse resolution (600 km) and does not reflect fine scale spatial variability in GHF caused by RCHP. *Fox Maule et al.* (2005) use satellite magnetic data to calculate GHF by estimating the depth to the Curie temperature (the depth where the magnetic properties of rocks are still dependant on temperature), and then constructing a thermal model assuming various thermal properties including the placements of the Curie isotherm at the lower boundary of the magnetic crust. The resulting GHF dataset is limited in resolution to a few hundred kilometres, yet it is known that GHF can vary by a factor of at least two on scale of tens of kilometres as a result of geological settings such as RCHP (*Carson and Pittard*, 2012; *Carson et al.*, 2014) and groundwater (*Gooch et al.*, 2016). A direct measurement of the GHF at a subglacial lake in west Antarctica found that the GHF was highly elevated at 285 mWm^{-2}, compared to the calculated background field from remote sensing of approximately 115-150 mWm^{-2} (*Fisher et al.*, 2015).

Geochemical analysis of exposed rocks in the Prydz Bay region observed high RCHP which may be present in the inland regions (*Carson et al.*, 2014). During a number of expeditions in this region, rock samples were taken and later analysed for heat producing elements (Th, Ur, K) to determine crustal heat production (*Carson and Pittard*, 2012). The heat producing elements are preferentially found in the upper $10-15$ km of crust, and can contribute over 50% of the total surface heat flow (*Sandiford and McLaren*, 2002). A standard granite with a heat production value of 2.5 $\mu\mathrm{Wm}^{-3}$ is typical of regions with a surface heat flow of approximately 60 mWm^{-2} (*Sandiford and McLaren*, 2002), while outcrops of Cambrian granites measured in the Prydz Bay region had heat production values of 3.75 to 65.85 $\mu\mathrm{Wm}^{-3}$ (*Carson and Pittard*, 2012), which 2D modelling of the region estimated the surface heat flow could be 80-90 mW^{-2}, with peak values of at least 120 mWm^{-2} (*Carson et al.*, 2014). Groundwater flow towards the

base of the ice could also contribute to elevated GHF, with estimates of the contribution within East Antarctica from groundwater flow of up to 24-28.8 mWm^{-2} (*Gooch et al.*, 2016). An updated GHF regional map based on the M7 magnetic model (*Fox Maule et al.*, 2005) agrees well with *Carson et al.* (2014) showing elevated GHF in the Prydz Bay region with values up to 150 mWm^{-2}, albeit primarily offshore. The updated seismic derived GHF from *An et al.* (2015), shows elevated GHF at 70-80 mWm^{-2} in a similar region; however, this method uses a regionally constant RCHP and hence would not reflect any spatial variations in GHF due to RCHP. Both these data sets do not capture the local fine scale variations in GHF from local crustal heat production or possible groundwater flow.

The East Antarctic Ice Sheet likely has heterogeneous sub-glacial heat flow due to the spatial variability of high heat producing granites in the upper crust (*Carson et al.*, 2014), and possibly groundwater flow (*Gooch et al.*, 2016). *Carson et al.* (2014) highlight that further quantifying the sub-glacial heat flow would require the delineation of the location and distribution of these Cambrian aged orogenic terraces under the ice sheet, while *Gooch et al.* (2016) suggest that groundwater volume flux rates will increase local GHF across sedimentary basins and in discrete locations such as fault zones. Given the prohibitive logistical constraints to directly measure the sub-glacial conditions, we investigate how these heat producing regions, if they extended inland underneath the Lambert-Amery glacial system, would influence ice sheet flow within a numerical model of the region. We insert simulated, but likely realistic, high heat flux regions (HHFR) into the background GHF of different regions that characterise different flow regimes and investigate the influence elevated GHF has on modeled ice sheet flow.

4.3 Lambert-Amery glacial system regional model

The Lambert-Amery glacial system is located in East Antarctica (Figure 4.1). It has been shown to be relatively stable under present conditions (*King et al.*, 2007; *Yu et al.*, 2010; *Wen et al.*, 2010; *King et al.*, 2012; *Pittard et al.*, 2015), yet is a region which is often poorly represented in Antarctic Ice Sheet models due to large regions that lack topographic measurements (*Fretwell et al.*, 2013) and difficulties in stabilising the grounding line in its present location (*Martin et al.*, 2011; *Golledge et al.*, 2012).

The model used for this study is the Parallel Ice Sheet Model (PISM) version 0.6.2 (*Bueler et al.*, 2007; *Bueler and Brown*, 2009; *Winkelmann et al.*, 2011). PISM is a three-dimensional thermodynamically coupled model with a shallow ice approximation (SIA) and shallow shelf approximation (SSA) hybrid scheme that utilises a structured finite difference discretisation. The SIA approximates ice flow for grounded ice where vertical shear dominates and the SSA approximates ice flow for floating ice where horizontal shear dominates. In grounded regions where sliding occurs, the sliding portion of the ice flow is calculated from the SSA and the grounded from the SIA. Ice temperature is calculated through an enthalpy scheme for its thermodynamics (*Aschwanden et al.*,

2012) and a non-dynamic basal hydrology where local melt will fill the till until it is saturated (2 m), all further melt will be lost.

A regional model domain has been developed by estimating the drainage basin of the Lamert-Amery glacial system by using the PISM drainage basin delineation tool (https://github.com/pism/regional-tools) and the BEDMAP2 surface elevation data (*Fretwell et al.*, 2013). The drainage basin was manually edited to be slightly larger to allow for slight shifts in the ice divide, and to incorporate sections of the coastline. It is used within a square domain (Figure 4.1) where the region outside the drainage basin is held at a constant thickness by modifying the surface mass balance to nullify the impact from the rest of Antarctica on the regional domain (-force_to_thickness PISM mechanism). The topography of the region is a combination of two datasets, with BEDMAP2 (*Fretwell et al.*, 2013) used beneath the grounded ice sheet, with RTOPO (*Timmermann et al.*, 2010) which incorporates *Galton-Fenzi et al.* (2008) under the floating ice. A 5 km region between the two datasets seaward of the grounding line was filled by linear interpolation. The surface mass balance and surface temperatures are the average fields of 1979-2013 from RACMO2.3 ANT27/2 (*van Wessem et al.*, 2014). The GHF dataset is derived using the *Fox Maule et al.* (2005) methodology on the M7 magnetic field data. The basal melt parametrisation for floating ice varies dependant on the depth of the ice and is derived from *Winkelmann et al.* (2011), with an additional scalar $(\frac{z}{1800})^3$, which changes the distribution of melt to approximately replicate basal melt rates produced from an Amery Ice Shelf ocean cavity model (*Galton-Fenzi et al.*, 2012).

The regional model was optimised to minimise the difference between observed and modelled grounding line location, ice thickness and surface velocity by testing a range of plausible values for the SIA and SSA enhancement factors, strength of the deformable till layer and a variable within the pseudo-plastic flow law (see Appendix C). The optimisation process iteratively modified the set of parameters (See Table S5.4,S5.5), until a final set of parameters were found which best matched the observed system. These final parameters were used to initialise the model by running a non-mass evolving model simulation with 10 km horizontal resolution and 15 m vertical resolution for 200,000 years until thermal equilibrium was reached. Once thermal equilibrium was reached, a simulation with 5 km horizontal resolution and 15 m vertical resolution was run until a steady state solution was achieved (approximately 5,000 years). Our model solution is different to observations in the southern portion of the Amery Ice Shelf and adjacent grounded regions with slower velocities and increased thickness (See Figure S5.1). In addition there is less ice at high elevations towards the ice divides. These differences are attributed to a mixture of model resolution, over-buttressing of the ice shelf, and slightly high velocities at higher elevations shifting ice mass towards the grounding line. The velocities at the front of the ice shelf are lower than observations, with the lack of a pinning point on the north-western front of the ice shelf leading to a wider and slower flow. The regional model solution is considered sufficient for the

purpose of this study as we are investigating the changes geothermal heat flux compared to a control solution.

4.4 Methods

A large portion of the Lambert-Amery glacial system is estimated to have a similar tectonic crustal history to the region in Prydz Bay that has been identified to contain HHFR (*Carson et al.*, 2014). It is therefore plausible that HHFR will exist within the domain. To test the potential sensitivity of ice sheet flow to localized elevated GHF, five regions where chosen to insert an idealised HHFR into the background field of the Lambert-Amery glacial system regional model. However, as we do not have any evidence to suggest specific locations we perform five experiments, each representative of a different ice flow regimes (Figure 4.1):

1. Exp_1: fast ice stream flow region ($\approx$ 250 m year^{-1})

2. Exp_2: slow ice stream flow region ($\approx$ 25 m year^{-1})

3. Exp_3: region at high elevation with no delineated flow pathways

4. Exp_4a: region between two glaciers (Lambert and Mellor Glacier)

5. Exp_5: region drains through an outlet glacier (Charybdis Glacier)

The magnitude and size of the HHFR is representative of *Carson et al.* (2014), which showed GHF of 120 mWm^{-2} with horizontal extents ranging from 10–80 km. We include the HHFR anomalies by removing a 50 km x 50 km square of the background GHF for each of the five experiments, inserting a region of 25 km x 25 km with GHF equal to 120 mWm^{-2} and then use a cubic interpolation to smoothly transition from the idealised HHFR to the background GHF.

In addition, we supplement Exp_4 with two additional experiments to test the importance of the magnitude and extent of the HHFR. Exp_4 was chosen as it provided the opportunity to investigate potential ice piracy between the two drainage basins, and whether the ice is controlled by changes in the HHFR:

1. Exp_4b: elevated magnitude of the HHFR, 240 mWm^{-2}

2. Exp_4c: larger HHFR, removing a 100 km x 100 km square and inserting a 50 km x 50 km region with background GHF of 120 mWm^{-2}

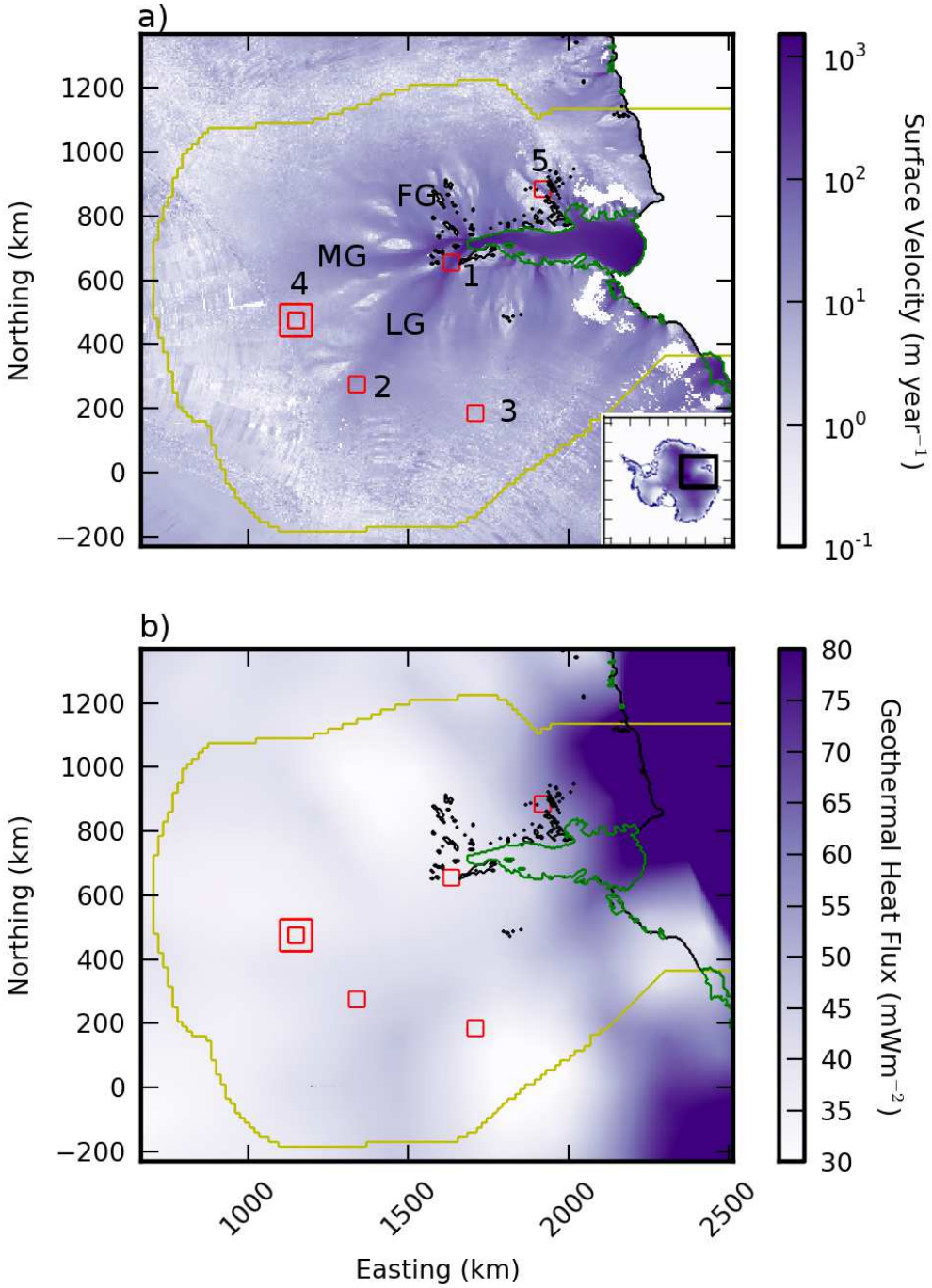

Figure 4.1: a) The surface velocities of Lambert-Amery glacial system (*Rignot et al.*, 2011b). Inset indicates location within Antarctica. LG = Lambert Glacier, MG = Mellor Glacier, FG = Fisher Glacier. b) The background GHF. The bedmap2 grounding line indicated in green, the coastline and ice free regions in black, the HHFR and associated experimental numbers indicated in red (with Exp_4c the larger region at 4) and the force to thickness mask in yellow.

4.5 Sensitivity to localized regions of elevated geothermal heat flux

The ice velocity and thickness showed substantial change in three of the five ice flow regions (Table 4.1). The spatial changes in velocity (Figure 4.2) and thickness (Figure 4.3) show the effects of the HHFR impacting both upstream and downstream of the region.

Table 4.1: HHFR differences for Thickness, Velocity and Basal Temperature.

	Ice Thickness (m)		Surface Velocity (m year^{-1})		Basal Temperature (K)	
Exp	Mean	Difference (%)	Mean	Difference (%)	Mean	Difference (K)
1	1993	0.03	257.7	-0.33	270.7	0.1
2	3100	-0.06	24.6	1.54	269.9	0.9
3	2686	-0.36	3.9	30.74	266.0	6.4
4a	1915	-0.84	2.8	52.84	261.0	8.9
5	965	-1.42	7.7	10.94	264.5	2.7
4b	1904	-1.42	3.7	100.2	265.4	13.3
4c	2200	-1.22	3.7	59.36	263.1	9.1

Exp_1 showed minimal change to velocity, thickness or basal temperature of the Lambert Glacier with the addition of the HHFR in the ice stream region of flow. The ice at the base of the ice sheet was at or close to melting before the HHFR was introduced, as velocities are in excess of 600 m year^{-1} which will generate frictional and internal strain heating, and hence the HHFR has limited effect on the velocities or thickness. The second region on the Lambert Glacier, Exp_2, showed acceleration at the edges of the flow but slower ice flow near the centre of the HHFR and the ice flow, but overall there was limited change in the velocity within the region and consequently there was minimal change in ice thickness. These results are consistent with *Larour et al.* (2012) which found that regions of fast flow are not sensitive to GHF.

Exp_3 showed increased basal temperature, higher velocities in the HHFR with associated drops in the ice thickness. The velocity increase extended both downstream and upstream of the HHFR. What was previously a slow moving region of no delineated flow has a region of flow that is now moving faster than the surrounding ice. The flow adjacent to the stream like flow is slower than the control. The mean basal temperature is still below melting point and no basal melt was produced.

When the HHFR is placed at the edge of the drainage basin (Exp_4a), the ice flow increased in a similar manner to that of Exp_3. There is evidence of the additional heat flowing along two separate pathways. The dominant pathway is towards the Lambert Glacier, but a visible increase can also be seen flowing towards the Mellor Glacier. This suggests that with the addition of the HHFR, more ice is flowing into the Lambert glacier than before. The basal temperatures increased by 8.92 K, but the region is still well below pressure melting point.

The simulation with the HHFR located beneath the outlet glacier (Exp_5), showed

faster velocities in the localized region along with changes in the ice thickness. The change in velocity is carried downstream and as the mass flux through the glacier has increased the ice margin has migrated inland as indicated by the change in velocity adjacent to the increase in flow. The basal temperature increased marginally.

Exp_4b shows increased basal temperature, however, melting point was still not quite reached with such high input. There was a small layer of temperate ice in the region, which suggests that it was nearing basal melting at some point within the HHFR. The velocity increased relative to Exp_4a, with a corresponding change in the local thickness. The enhanced velocity is transferred downstream, with more velocity heading down the west branch of the ice flow.

When the region was doubled in size (Exp_4c), the basal temperature, surface velocity and thickness changes are less pronounced than the Exp_4a, however, the spatial patterns are more pronounced. The local velocity increase is seen downstream, with the slowdown either side more pronounced. The spatial extent of the decrease in thickness is substantially larger relative to the HHFR than in other experiments. There is no evidence of basal melting, indicating that the increased flow is due to changes in the rheology of the ice and not due to basal lubrication.

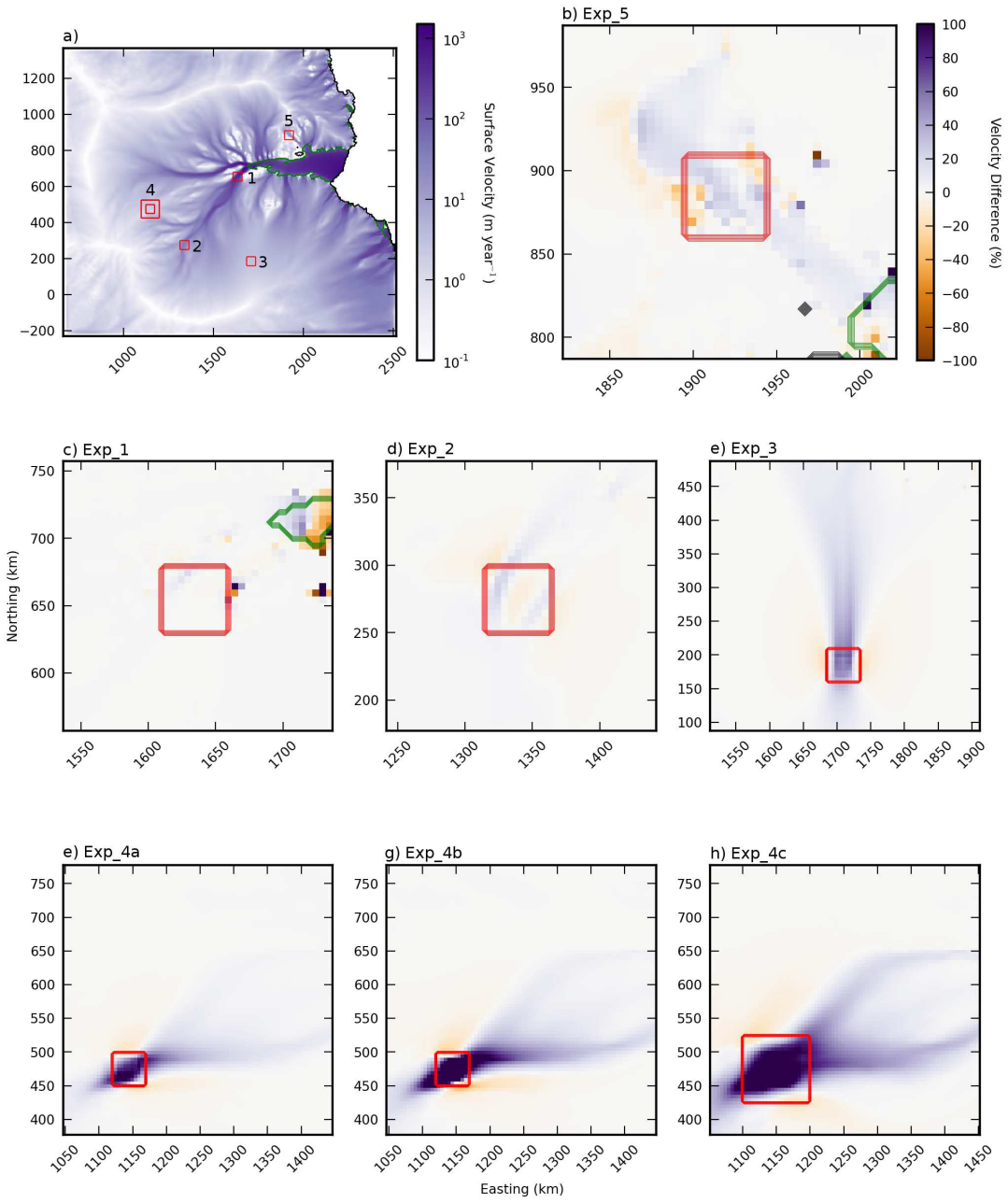

Figure 4.2: a) Control surface velocity. Difference in surface velocity between control and b) Exp_5, c) Exp_1, d) Exp_2, e) Exp_3, f) Exp_4a, g) Exp_4b, h) Exp_4c. HHFR indicated in red, grounding line in green, and coastline in black. Colorbar on top right applies to b)-h).

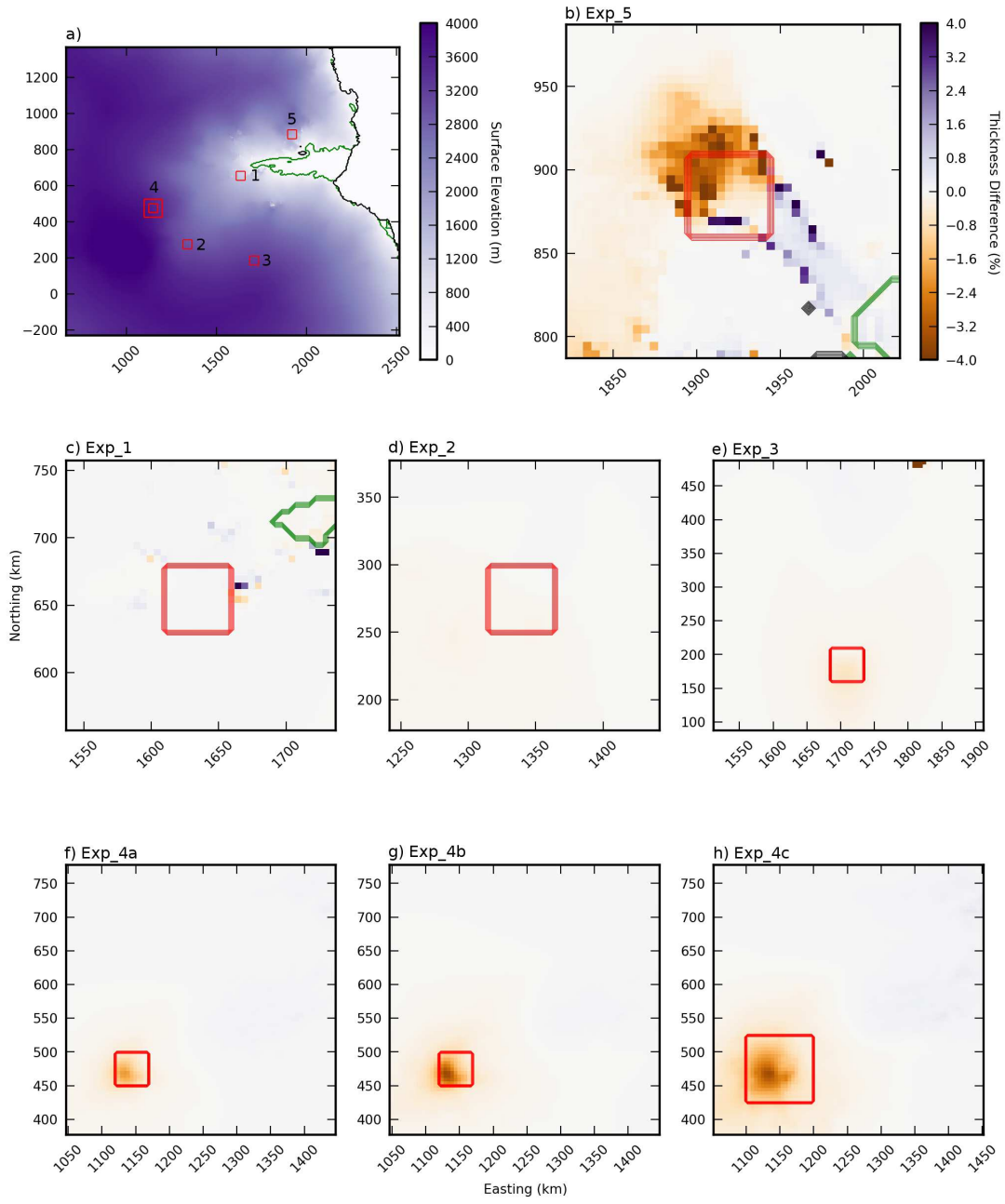

Figure 4.3: a) Control surface elevation. Difference in surface elevation between control and b) Exp_5, c) Exp_1, d) Exp_2, e) Exp_3, f) Exp_4a, g) Exp_4b, h) Exp_4c. HHFR indicated in red, grounding line in green, and coastline in black. Colorbar on top right applies to b)-h).

4.6 Discussion

Comparison of outputs from an ice sheet model perturbed with HHFRs show that localized flow anomalies are important and aid in understanding areas of slow flow. In regions of low ice velocity, the addition of localized high GHF leads to a change in flow behaviour, with the increase in ice velocity delineated from the surrounding ice flow into a stream-like flow. The increased velocity is seen up to hundred km upstream and hundreds of km downstream from the HHFR. The increase in velocity slows downstream to control values as the elevated ice temperature is diffused with distance. In the case of Exp_3, the diffusion continued approximately 300 km downstream of the 50 km wide HHFR. The basal temperatures were enhanced substantially within the HHFR, however, no basal melt was generated in any of the experiments. The upstream effect of the HHFR could indicate the GHF may be an important factor that is likely to influence the location of ice divides. HHFRs can influence ice flow pathways and may help explain current organization of ice flow, particularly where sub-glacial hydrological pathways may play a role. If a region has higher local GHF it may preferentially flow along certain pathways, particularly combined with sub-glacial hydrology that may also enhance this effect. This is unlikely to be important on short time scales, but over millions of years combined with preferential erosion, a small difference in regional heat flow could contribute to the organization of ice flow. The current configuration of the present day ice sheet will have already responded to HHFRs, with subglacial lakes at the onset of East Antarctic ice streams potentially caused by HHFR. This is supported by *Näslund et al.* (2005) who found that introducing variable regional heat flux in a Fennoscandian ice sheet model led to faster ice flow, commensurate with findings from post-glacial studies. We expect as ice sheet models improve, the evidence of fine scale variations in GHF will become more apparent.

The lack of basal melt in the HHFR was surprising, as the 120 $\mathrm{mWm^{-2}}$ and 240 $\mathrm{mWm^{-2}}$ GHF values are substantially more than the GHF calculated above sub-glacial lakes *Siegert* (2000). This could be due to the GHF anomaly still being too low, with the 240 $\mathrm{mWm^{-2}}$ used still less than the 285 $\mathrm{mWm^{-2}}$ measured by *Fisher et al.* (2015) at a sub-glacial lake in West Antarctica. Alternatively, the regions chosen may have had sufficient ice flow to advect heat downstream fast enough to stop basal melting. The sub-glacial lake mapping of this region suggests the existence of a lake somewhere between Exp_1 and Exp_2 (*Smith et al.*, 2009), which would be consistent with basal melt generated from frictional and strain heating as opposed to GHF. Sub-glacial lakes could be a finger-print of regions of HHFR underneath the ice sheet, given that some of these sub-glacial lakes are found at the head of fast-flowing ice streams (*Bell et al.*, 2007). It is possible HHFRs are initiating ice flow through reduced friction as they flow over sub-glacial lakes in addition to the localized effect from enhanced viscosity due to warmer ice. There is dire need for further techniques for estimating the GHF beneath the Antarctic ice sheet. Direct measurements would be ideal but the logistical requirements for an Antarctic wide validation make this an unrealistic aim, with tar-

geted observations aimed to validate remote sensing techniques potentially a realistic goal.

GHF is an important boundary condition for determining the temperature profile throughout an ice sheet, but often the selection of parameters for basal conditions over-rides the difference GHF may have on the solution of an ice sheet model. Surface velocities of ice flow is our primary mechanism of evaluation of ice sheet models. The initiation of ice sheet models is reliant on an a priori surface velocity field derived from observations where the observational error is often similar or higher than the magnitude of the signal in slow flowing regions. Improved resolution and accuracy of surface velocity measurements could identify regions of high heat flow in slow flowing ice regions from their flow characteristics which would improve the initialisation of ice sheet models. Often to obtain numerical solutions of ice sheets which match observed surface velocities, basal parameters which are the least observed components of the system are optimised or inverted for. If the region has faster flow due to higher GHF, it would be possible to erroneously simulate a match to observed surface velocities by using a softer till for example. However, this could lead to other changes in the simulation as the rate heat is advected downstream could be affected, possibly leading to changes in the rheology of the ice and how it may respond to changes in buttressing. In terms of our model and how this may possibly effect our results, we have used a relatively strong till resistance which may restrict the efficiency of possible feedbacks due to basal melting.

An alternative to altering a few parameters to match surface observations is basal inversions which provide a spatial distribution of key model variables (*Pattyn*, 2010). These invert for the conditions at the bed based on surface velocity. Often these inversions include a viscosity term (*Morlighem et al.*, 2013), dependant on a temperature profile through the ice (*Gong et al.*, 2014). These methods often have identified regions of sticky or slippery beds, but given these are influenced by the estimated ice temperatures, they may be in fact identifying local scale variations in the GHF. Regions of strong basal resistance may actually be colder ice, and regions of slippery bed may be regions of warmer ice. This could have ramifications for feedback mechanisms in ice models as regions inaccurately characterised as having slippery or sticky beds, or as being lubricated or frozen, will respond differently to accelerations in ice flow.

4.7 Conclusion

The inclusion of high heat flow regions caused by synthetic but plausible estimates of localized radiogenic crustal heat production caused local variation in ice velocity and consequently ice thickness. The largest influence was in regions of low ice velocity, with the impact seen 100 km upstream and 300 km downstream of the high heat flow region with a change in the flow behaviour of the region. The flow changes from sheet flow to stream flow, with slight decreases in velocity seen adjacent to the region of stream-like flow. The increased local ice velocities will influence the organization of ice flow,

which will affect long period model runs. The direct influence on regions of fast flow is minimal, with heat generated by the fast flow dominating the local high heat flow, with no change in ice flow behaviour. The existence of high heat flow regions may impact basal inversions for the initiation of ice sheet models by influencing the ice temperature and local viscosity of the ice. Further techniques to estimate or measure geothermal heat flux is required to fully assess possible impacts on ice dynamics and mass budget estimates.

4.8 Acknowledgements

This work was supported by the Australian Government's Cooperative Research Centres programme through the Antarctic Climate & Ecosystems Cooperative Research Centre. This research was supported under Australian Research Council's Special Research Initiative for Antarctic Gateway Partnership (Project ID SR140300001). This research was undertaken with the assistance of resources under projects m68 and gh8 from the National Computational Infrastructure (NCI), which is supported by the Australian Government. Development of PISM is supported by NASA grants NNX13AM16G and NNX13AK27G. The Geothermal Heat Flux dataset updated using the MF7 magnetic field based on the (*Fox Maule et al.*, 2005) was provided by Michael E. Purucker, NASA.

4.9 Supplementary Information

See Appendix C for the supplementary information for this chapter.

4.10 Concluding Remarks

This chapter shows that regions of localised elevated geothermal heat flux may affect the organisation of ice flow by changing the behaviour of the ice flow from sheet flow to stream flow. The following chapter uses the regional model outlined here to investigate the thermal regime of the Lambert-Amery glacial system, and how different available geothermal heat flux datasets can influence the dynamics of the region.

Chapter 5

Sensitivity of the Lambert-Amery glacial system to geothermal heat flux

This chapter presents the thermal regime of the Lambert-Amery glacial system. It then assesses the importance of the choice of geothermal heat flux dataset, an important boundary condition for ice sheet models, on the thermal properties of the region.This chapter is published as *Pittard et al.* (2016b):

Pittard, M. L., J. L. Roberts, B. K. Galton-Fenzi, and C. S. Watson (2016), Sensitivity of the Lambert-Amery glacial system to geothermal heat flux, *Annals of Glaciology*, 57, doi: 10.1017/aog.2016.26.

5.1 Abstract

Geothermal heat flux (GHF) is one of the key thermal boundary conditions for ice sheet models. We assess the sensitivity of the Lambert-Amery glacial system in East Antarctica to four different GHF datasets using a regional ice sheet model. A control solution of the regional model is initialised by minimising the misfit to observations through an optimisation process. The Lambert-Amery glacial system simulation contains temperate ice up to 150 m thick and has an average basal melt of 1.3 mm year^{-1}, with maximum basal melting of 504 mm year^{-1}. The simulations which use a relatively high GHF compared to the control solution increase the volume and area of temperate ice, which causes higher surface velocities at higher elevations which leads to the advance of the grounding line. The grounding line advance leads to changes in the local flow configuration which dominates the changes within the glacial system. To investigate the difference in spatial patterns within the geothermal datasets, they were scaled to have the same median value. These scaled GHF simulations showed that the ice flow

was most sensitive to the spatial variation in the underlying GHF near the ice divides and on the edges of the ice streams.

5.2 Introduction

Numerical ice sheet models are an important tool for understanding the contribution of the cryosphere to past, present and future sea level rise. The temperature of the ice sheet is an important control on the flow rate of ice, influencing both the rate of internal deformation, basal melt and subsequent basal sliding. The thermal boundary conditions of the ice sheet are the GHF at the base of the ice sheet, the air surface temperature at the exposed surface of the ice, and the ocean temperature beneath floating ice. An additional control on the thermal boundary conditions is the surface vertical velocity which in pseudo steady state is the same as the accumulation rate. This governs how quickly the surface temperature is advected into the ice sheet. GHF influences the temperature of the ice and in part controls the conditions at the base of the ice sheet. The temperature of the ice is also controlled by the deformational heat generated from strain within the ice, the advection of heat due to ice motion, the conduction of heat through the ice sheet and frictional heating from basal sliding. The temperature of the ice is a control on the rheology of the ice and subsequently the rate of its deformation (*Budd et al.*, 2013), with temperate ice (ice at melting point which may contain a small fraction of liquid water) enhancing the flow significantly (*Lliboutry and Duval*, 1985). In addition, basal melt can lead to the lubrication of the till, lowering the resistance of the bed and leading to basal sliding (*Pattyn*, 2010). The performance of ice sheet models in modelling ice temperature is difficult to evaluate as only spatially limited observations of *in situ* ice temperatures exist, with most being situated either at ice divides or on ice shelves, which represent two extremes of ice flow. Ice divides have near zero flow rates, limiting the contributions of deformational heating and basal frictional heat, while ice shelves are dependent on properties of the underlying ocean, with no contribution from GHF.

The Antarctic GHF is difficult to observe due to the ice sheet itself, which impedes access to the bed to measure the GHF directly with the exception of some isolated coastal ice free regions and deep ice core drilling sites (*Fisher et al.*, 2015). Limited crustal heat production measurements (*Carson and Pittard*, 2012) are also used to estimate the GHF in localised regions (*Carson et al.*, 2014). The magnitude of the GHF depends on spatially varying geological conditions such as the mantle heat flux, crustal thickness, sediment deposits and local radiogenic crustal heat production (RCHP) (*Sandiford and McLaren*, 2002; *Fox Maule et al.*, 2005; *Carson et al.*, 2014).

Early ice sheet models input GHF as a constant (*Hansen and Greve*, 1996; *Kerr and Huybrechts*, 1999) or a regionally varying constant based on the origin of the crust (*Pollard et al.*, 2005). Later developments provided spatially variable fields of GHF using inference based on magnetic fields (*Fox Maule et al.*, 2005) and seismic models (*Shapiro and Ritzwoller*, 2004). Both of these techniques make assumptions about the

local RCHP and acknowledge that they will not capture local small scale variations in the GHF. The two datasets, *Fox Maule et al.* (2005) and *Shapiro and Ritzwoller* (2004) are significantly different (Figure 5.1), and are used in a variety of ice sheet studies, mainly being used for basal inversions and boundary conditions (e.g. *Pattyn*, 2010; *Martin et al.*, 2011; *Larour et al.*, 2012; *Sato and Greve*, 2012; *Morlighem et al.*, 2013; *Golledge et al.*, 2015). The large differences between the two datasets often means studies utilise both datasets, or simply choose one without discussing the implications of using that particular dataset (*Martin et al.*, 2011; *Sato and Greve*, 2012; *Morlighem et al.*, 2013; *Golledge et al.*, 2015). This may be because validation of these datasets is limited and therefore determining which dataset may offer better performance within an ice sheet model is difficult. Understanding the influence that variations in GHF have on ice flow is not fully understood.

A number of studies have investigated the effect of differences in the GHF in Antarctica, and while local ice flow has been shown to be sensitive to variations in GHF (*Pittard et al.*, 2016a), the overall effect on ice volume has been found to be small, at least when compared to errors in other components of the model such as ice thickness (*Larour et al.*, 2012; *Pollard et al.*, 2005). *Larour et al.* (2012) comment that slower flowing ice in the interior of the ice sheet will be more sensitive to the GHF, but that the ice temperature in regions of fast ice flow are dominated by frictional sliding. This suggests that GHF in these regions are unimportant, although this contrasts with northern hemisphere ice sheets, with both the Greenland Ice Sheet (*Rogozhina et al.*, 2012) and the Ferroscandian Ice Sheet (*Näslund et al.*, 2005) found to be sensitive to the chosen GHF in numerical studies. *Näslund et al.* (2005) found that the sensitivity in GHF was due to localised basal melt leading to a feedback mechanism where ice flow was faster with an elevated GHF which lead to faster ice flow and an increase in frictional heating, leading to increased basal melt. The average basal melt expected under Antarctica ranges from 1 mm year^{-1} to 5.3 mm year^{-1} (*Llubes et al.*, 2006; *Bell et al.*, 2007; *Bell*, 2008; *Pattyn*, 2010). While this basal melt rate is relatively low, under ice streams such as Pine Island Glacier, the basal rates could be as high as 600 mm year^{-1} (*Bell*, 2008). An investigation by *Hansen and Greve* (1996) shows that as the GHF increases, it changes the basal properties of the ice sheet significantly, with higher GHF leading to greater areas of the base of the ice sheet reaching melting point, and the formation of temperate ice layers. The GHF required to reach the melting point of ice is a function of ice thickness and surface temperature (*Cuffey and Paterson*, 2010), with GHF as low as 40 mWm^{-2} at the base of the ice allowing for basal melting in low accumulation regions(*Pattyn*, 2010).

Part of the difficulty determining the importance of GHF is that the conditions at the base of the ice sheet are mostly unknown. Ice sheet models may take different approaches to estimating basal properties and utilise the GHF differently. The GHF may be used as a thermal boundary condition to many ice sheet models, with basal properties such as the strength of the till parametrised or estimated to allow for an

evolving base of the ice sheet (*Bueler et al.*, 2007; *Bueler and Brown*, 2009; *Winkelmann et al.*, 2011). Another method of estimating the properties at the base of the ice is inverting for basal friction coefficients and/or viscosity of the ice (*Morlighem et al.*, 2013; *Gong et al.*, 2014) with GHF being used to generate a temperature profile through the ice to be used in the inversion.

The Lambert-Amery glacial system in East Antarctica (Figure 5.2) has been observed to be relatively stable since 1968 (*King et al.*, 2007; *Yu et al.*, 2010; *Wen et al.*, 2010; *King et al.*, 2012; *Pittard et al.*, 2015). The Lambert basin drains into the Amery Ice Shelf, which is long, relatively narrow and its grounding line is one of the deepest in Antarctica with an ice depth up to 2500 metres (*Fricker et al.*, 2002). The stability of this region allows models to be evaluated against a steady state benchmark, which is difficult in many regions of Antarctica due to the localised rapid changes in ice dynamics. (*Rignot et al.*, 2008; *Shepherd et al.*, 2012; *Pritchard et al.*, 2012). The Lambert-Amery glacial system has been difficult to model, with the location of the modelled grounding line advancing relative to observations which leads to the over-estimation of the ice volume in the region (*Martin et al.*, 2011; *Golledge et al.*, 2012).

This study utilises a regional ice sheet model of the Lambert-Amery glacial system used to investigate the influence of both the magnitude and variability of GHF on the ice sheet. We first outline the regional domain and then detail the optimisation of a number of ice sheet model parameters until a steady state solution which approximately estimates the current configuration of the region is found. We then test the sensitivity of the optimisation to different GHF datasets. Finally, we scale each dataset to the control GHF to assess the impact of spatial differences between the various datasets on the thermal regime of the region.

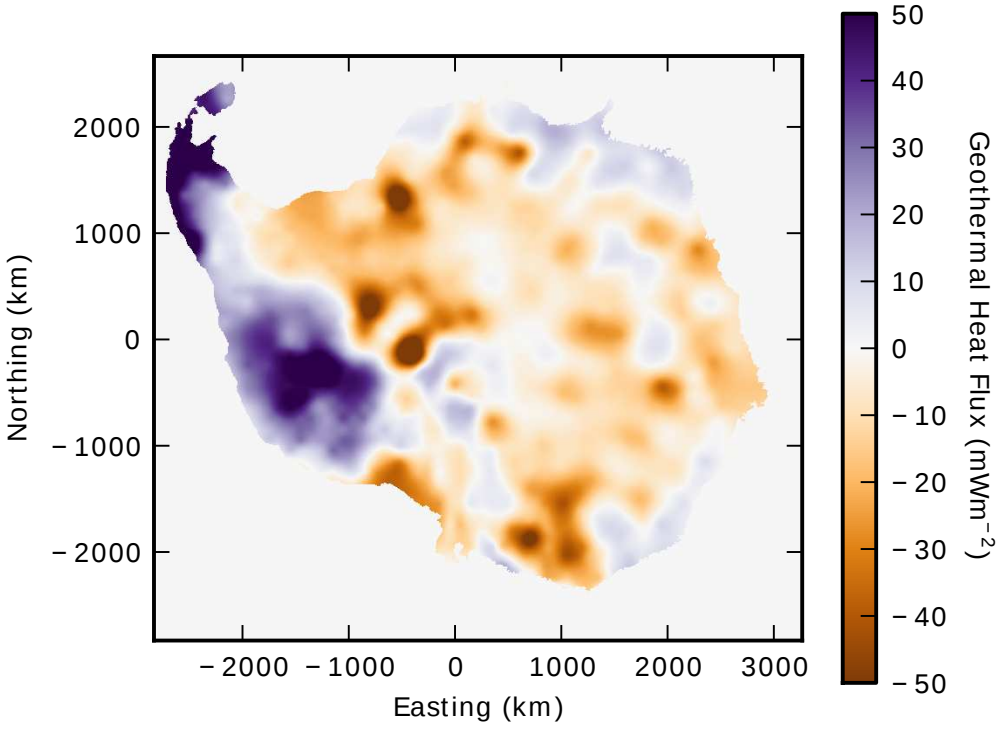

Figure 5.1: The difference between seismic sourced GHF dataset (*Shapiro and Ritzwoller*, 2004) and a magnetic sourced GHF dataset (*Fox Maule et al.*, 2005).

5.3 Model Description

5.3.1 Ice Sheet Model

The ice sheet model utilised by this study is the Parallel Ice Sheet Model (PISM) version 0.6.2 (*Bueler et al.*, 2007; *Bueler and Brown*, 2009; *Winkelmann et al.*, 2011). PISM is a three-dimensional thermodynamically coupled model with a shallow ice approximation (SIA)/shallow shelf approximation (SSA) hybrid scheme that utilises a structured finite difference discretization. The SIA approximates ice flow for grounded ice where vertical shear dominates and the SSA approximates ice flow for floating ice where horizontal shear dominates. In grounded regions that are sliding, part of the ice flow is calculated from the SSA and part from the SIA (*Bueler and Brown*, 2009). PISM utilises an enthalpy scheme for its thermal model component and is both mass and energy conserving (*Aschwanden et al.*, 2012). The calving law options utilised by this study is an eigen calving law (*Levermann et al.*, 2012) combined with a minimum thickness calving law. When the principal strain rate of a region of ice shelf exceeds a threshold set (eigen_calving_k), or the region drops below a set ice thickness (thickness_calving_threshold), the region will calve. The regional model used herein is described by *Pittard et al.* (2016a).

5.3.2 Regional Domain

The Lambert-Amery glacial system is identified through the PISM drainage basin delineation tool (included in the PISM regional-tools), which determines the drainage basin by using the gradient of the surface elevation to determine the maximum source point of ice from a terminus specified by the user. The calculated basin was enlarged slightly to capture the ice divides more accurately. The drainage basin outline is shown in Figure 5.2, and within this basin the full PISM model applies. The region outside the basin has an adaptive surface mass balance mechanism (using PISMO executable and the force to thickness mechanism) which forces the ice thickness within this region, denoted by the force to thickness mask (ftt_mask), to match the initial ice thickness. This ensures that the boundary conditions at the edge of the domain, and the region outside the drainage basin of interest will minimally impact the solution within the domain itself (See Supplementary Information for full details).

5.3.3 Input Datasets

The regional model requires a set of boundary, initial and forcing conditions. The boundary conditions of the ice sheet are the bed topography and GHF. The initial condition is the ice thickness. The bedrock topography and initial ice thickness for the regional model is given by a modified bedmap2 dataset (*Pittard et al.*, 2016a). The GHF dataset used was created by using the *Fox Maule et al.* (2005) methodology on an updated magnetic field model 7 (http://websrv. cs.umt.edu/isis/ index.php/ Antarctica_Basal_Heat_Flux).

The forcing conditions used by the regional model are surface mass balance, ice surface temperature, oceanic forced basal melt rate and ocean temperature. The surface mass balance and ice surface temperature are from the 1979-2013 ANT27\2 RACMO2.3 (*van Wessem et al.*, 2014) dataset, with minor modifications over nunataks to reduce ice growth on these regions (See Supplementary Information for full details). The ice shelf basal mass balance is controlled by a parametrisation for oceanic basal melt rates with ocean temperature held at a constant 271.45 K. The oceanic basal melt rate parametrisation is calculated following the modifications outlined in *Pittard et al.* (2016a). The initial oceanic melt rate is approximately the same as that in *Galton-Fenzi et al.* (2012) with an average melt of 0.8 m year^{-1} from our parametrisation compared to 0.78 m year^{-1} from the ocean cavity model (See Supplementary Information for full details).

5.3.4 Model Parameters

The PISM ice sheet model is controlled by a range of input parameters (See PISM User's Manual, date accessed June 17, 2014). The regional model used within this study uses a horizontal resolution of 5 km, with the exception of thermal only simulations, which are simulated at 10 km horizontal resolution. The vertical resolution is 15 m for all simulations. The domain edge boundary conditions are derived from a low resolution full Antarctic domain model (see supplementary information). The PISM model variables bmelt, tillwat, enthalpy and velocity for the dirichlet velocity boundary, u_ssa_bc,v_ssa_bc, are applied in a 10 km strip outside the domain (See Supplementary Information for full details). Six of the model input parameters were chosen to vary through an optimisation process to create a realistic simulation of the Lambert-Amery glacial system. All other input parameters were held at the defaults (See PISM User's Manual)(See Supplementary Information for full details).

The four variables which the model was firstly optimised for were the shallow ice approximation enhancement factor (sia_e), the shallow shelf approximation enhancement factor (ssa_e), the quotient in the pseudo plastic sliding law (pseudo_plastic_q, See PISM User's Manual), and the parametrisation of till strength (topg_to_phi). These variables were chosen guided by the previous experiments of *Martin et al.* (2011); *Golledge et al.* (2015) and initial experiments testing the relative importance of each variable. The final two variables which are optimised vary the calving front location and calving rate within the model, with the threshold of the principal strain rate for eigen calving (eigen_calving_k)(*Levermann et al.*, 2012) and threshold where the ice shelf is considered too thin to be realistic and is automatically calved (thickness_calving_threshold). The primary criterion for a stable solution was the grounding line being situated on the same topographic sill as observations, with secondary criteria being how accurately the simulated ice thickness and velocities matched observations. These secondary criteria were assessed by comparing the misfit between the observed and simulated ice sheet for ice thickness and surface velocity, calculating the mean and standard deviation of

both the simulated and observed ice sheet, and finally computing the root-mean-square error between the two values. Each of the variables were iteratively varied and assessed using the two criteria, until a final set of variables which most accurately matched observations were found.

The final parameters from this optimisation process were sia_e = 1.8, ssa_e = 1.6, pseudo_plastic_q = 0.5 and topg_to_phi = 10,30,-1500,-500, eigen_calving_k = 1.9e15 and thickness_calving_threshold = 225. The sia_e is lower than expected from laboratory experiments which indicate that the enhancement due to anisotropy should be at least 3 on average across the domain (*Budd and Jacka*, 1989; *Budd et al.*, 2013). This indicates that there is another factor which is being convolved into the sia_e optimisation, such as basal resistance. PISM utilises a parametrisation, which aims to reflect the reduction in flow due to the roughness of the bed topography (See PISM User's Manual). This parametrisation is limited by the interpolation and smoothing of the bed topography datasets, which causes the reduction in flow as the bed is relatively rough in regions with high-resolution data and relatively smooth where the topography is under-sampled. The final regional model solution was simulated for a 200,000 year thermal simulation (-no_mass turned on which holds the ice thickness constant and evolves only the thermal ice sheet), followed by a 45,000 year simulation (henceforth the control solution).

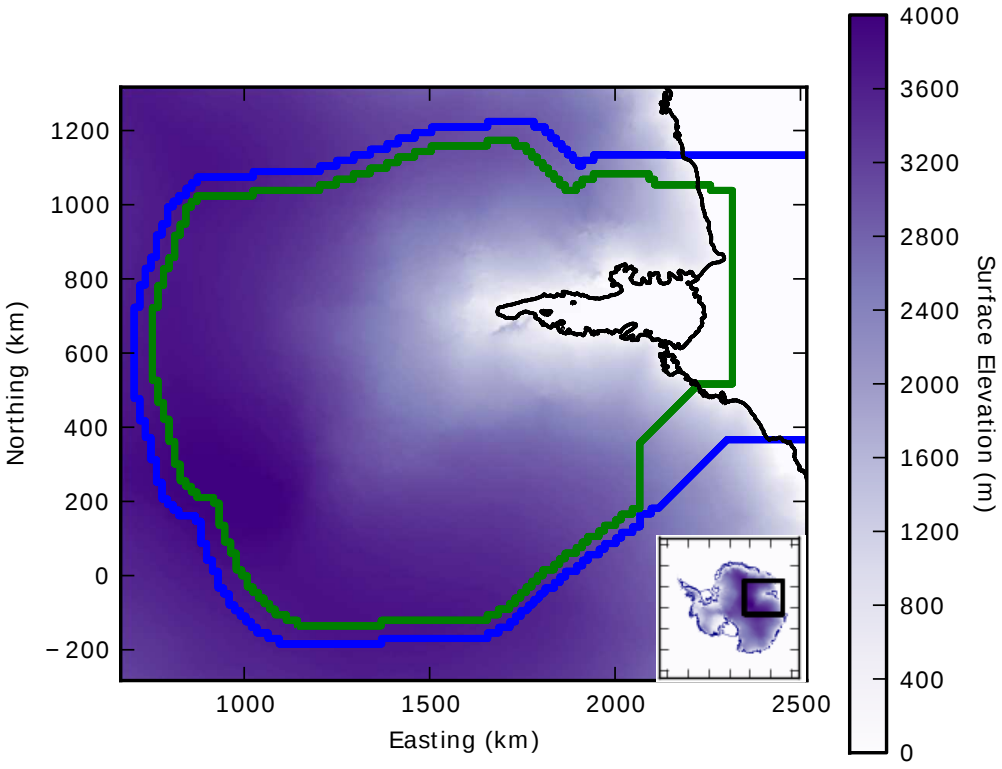

Figure 5.2: The regional domain with the initial ftt_mask (green) and the final ftt_mask (blue) indicated. The ice shelf extent from bedmap2 is indicated in black. Inset: Location of the Lambert-Amery glacial system within Antarctica, showing the square region (black) that encompasses the regional model.

5.4 Methods

5.4.1 Geothermal Flux Datasets

Three geothermal flux databases were chosen to investigate their influence on the ice configuration of the regional domain compared to the GHF chosen in our regional domain (Figure 5.3). The GHF used in the control solution utilises the *Fox Maule et al.* (2005) methodology, but using an updated magnetic field model, FM7 (http://geomag .org/models/ MF7.html)(henceforth fm_2012). The three databases which we will compare our control solution to are *Fox Maule et al.* (2005) (fm_2005), *Shapiro and Ritzwoller* (2004)(sr_2004) and *An et al.* (2015)(an_2015), as shown in Figure 5.3. The fm_2005 and sr_2004 datasets were accessed through the ALBMAP compilation (*Le Brocq et al.*, 2010). The sr_2004 and an_2015 datasets utilise a seismic model, while fm_2005 and fm_2012 are based on magnetic models.

The fm_2005 dataset shows spatial similarities to the fm_2012 dataset, with similar features including a relatively higher GHF beneath the Lambert Glacier, the elevated region north west of the ice shelf and the relatively cold region beneath the Fisher Glacier. Overall, fm_2005 has a much higher GHF, with a median GHF of 59.1 mWm^{-2} compared to just 40.8 mWm^{-2} for the fm_2012 dataset. The sr_2004 dataset has significantly less spatial details than the other datasets, with a very small gradient in GHF from south-east to north-west. The median GHF in sr_2004 is 52.6 mWm^{-2}. The an_2015 dataset shares similar features to the magnetic field datasets, with a higher GHF in the north west, but in contrast to the magnetic datasets the region beneath the Lambert Glacier is relatively cooler than the background field. The median GHF in an_2015 is 53.9 mWm^{-2}.

To test the differences of the spatial variability of the GHF datasets without being influenced by the elevated GHF, four additional GHF datasets are constructed. The first dataset constructed was created by using the median of the fm_2012 dataset, 40.8 mWm^{-2}, as a constant region wide value (labelled as fm_median, Figure 5.3e). The three other datasets are created by scaling the fm_2005, sr_2004 and an_2015 datasets by the median of fm_2012 datasets. The fm_scaled, sr_scaled and an_2015 datasets were scaled by multiplying the GHF dataset by the median of fm_2012 divided by the median of each respective dataset (40.8/59.1, 40.8/52.1, 40.8/53.9), forcing the median of each dataset to match that of the fm_2012 dataset. These datasets are labelled fm_scaled, sr_scaled and an_scaled respectively (Figure 5.3f,g,h). The median was chosen over the mean as there is a region of high GHF in the north eastern corner of the fm_2012 dataset which skewed the mean to a much higher value of 49.1 mWm^{-2}, which would have caused the constructed datasets to have an elevated GHF relative to fm_2012 in the regions beneath the major active glaciers.

5.4.2 Experimental Design

Each of the eight different GHF datasets are used in experimental model simulations (summarised in Table 5.1) with 10 km horizontal resolution, a constant ice thickness (-no_mass), simulated until the enthalpy is close to thermal equilibrium for the given ice thickness of the control solution. This step was conducted on the control solution GHF (fm_2012) as well, to measure any lingering transient thermal effects from the control solution. Following the thermal equilibrium runs, each GHF dataset is run at 5 km horizontal resolution for another 2,000 years yielding a pseudo-steady state solution for ice thickness. However, any significant grounding line migration or changes in surface velocities should be evident over this time period.

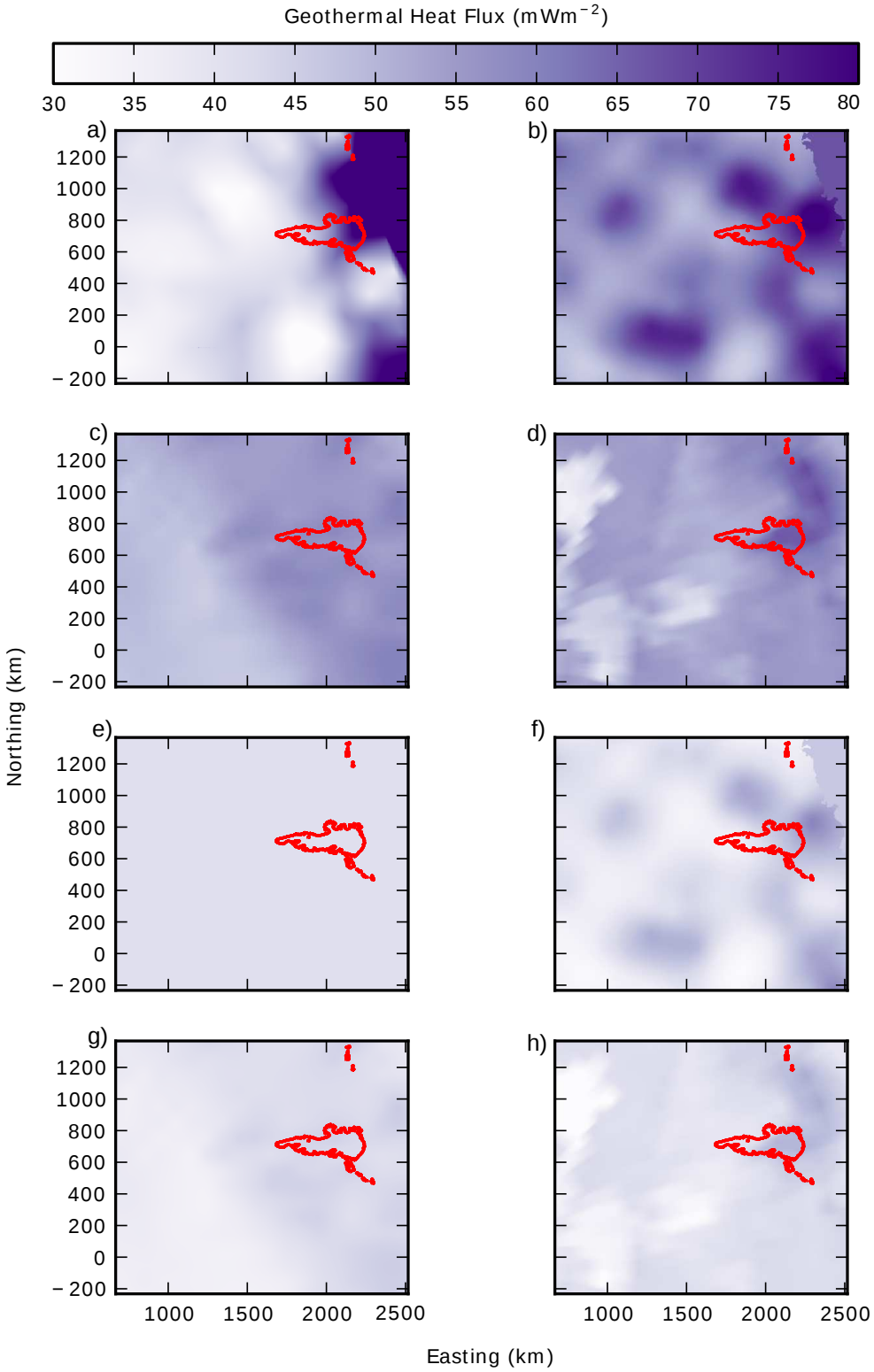

Figure 5.3: GHF over the domain from a) fm_2012 b) fm_2005 c) sr_2004 d) an_2015 e) fm_median f) fm_scaled g) sr_scaled h) an_scaled. Ice shelf mask from bedmap2 shown in red.

Table 5.1: List of Experimental Runs.

Experiment	GHF dataset	Resolution	Constant Ice Thickness	Time (year)
thermal_control	fm_2012	10km	Yes	200,000
thermal_fm_2005	fm_2005	10km	Yes	400,000
thermal_sr_2004	sr_2004	10km	Yes	400,000
thermal_an_2015	an_2015	10km	Yes	400,000
thermal_fm_scaled	fm_scaled	10km	Yes	200,000
thermal_sr_scaled	sr_scaled	10km	Yes	200,000
thermal_an_scaled	an_scaled	10km	Yes	200,000
thermal_fm_median	fm_median	10km	Yes	200,000
exp_control	fm_2012	5km	No	2,000
exp_fm_2005	fm_2005	5km	No	2,000
exp_sr_2004	sr_2004	5km	No	2,000
exp_an_2015	an_2015	5km	No	2,000
exp_fm_scaled	fm_scaled	5km	No	2,000
exp_sr_scaled	sr_scaled	5km	No	2,000
exp_an_scaled	an_scaled	5km	No	2,000
exp_fm_median	fm_2012_mean	5km	No	2,000

5.5 Control Solution

5.5.1 Comparison to Observations

The control solution (Figure 5.4) meets our primary goal of a stable grounding line position along the same topographic sill as the observed grounding line. The velocities of the control solution are characterised by faster ice flow through the main trunks of the glaciers compared to observation and slower velocities adjacent to the main glaciers. This characteristic could be caused by the satellite footprints which are lower-resolution than the numerical model. The ice thickness of the control solution is thicker in the drainage basin of the Fisher and Charybdis Glaciers than observations. These glaciers flow through narrow channels between nunataks, which will likely require higher horizontal resolution to better resolve. Conversely, the Lambert Glacier, and to a lesser extent the Mellor Glacier, have an ice thickness thinner than observations. This is likely due to the deep topographic troughs that exist within these basins, which will lead to the topg_to_phi parametrisation enforcing a very weak till in these regions and allowing faster flow and easier sliding. The control solution's grounding line has advanced slightly compared to the observations, however, given the uncertainty in the bedrock elevation and the modified bedmap2 dataset used it is considered an accurate representation. The calving front of the control solution is further north along the western edge of the embayment and further south to the eastern edge. The northward position of the western ice front could be due the lack of a pinning point in the topography which restricts and shifts the flow to the eastern edge in observations. The surface velocities are slower towards the deep grounding line of the AIS, but slightly faster towards the middle of the AIS before slowing towards the calving front. The slower velocities at the deep grounding line could be due to horizontal resolution of the model, or potentially over-buttressing from the side wall drag. The model reaches close to observed ice thickness and velocities through the centre of the ice shelf, which is due to the thickness based ice shelf parametrisation we apply. As the ice flow is restricted, the ice gets thicker at the deep grounding line leading to the basal melt rate increasing. The ice thickness at the calving front is very similar to the observed ice thickness, however, with the lower velocities relatively less ice mass is being calved within the model. Overall, this means that while the combination of calving and basal melt from the ice shelf preserves a similar ice thickness within our control solution, we are preferentially losing more ice loss from basal melting than what would be expected by combining the MEaSUREs velocities (*Rignot et al.*, 2011b) and the bedmap2 (*Fretwell et al.*, 2013) ice thickness at the calving front.

5.5.2 Thermal Regime of the Lambert-Amery Glacial System

The thermal regime of the Lambert-Amery glacial system is displayed in figure 5.5. The average ice hardness (describes viscosity) varies from 5×10^8 Pa $s^{\frac{1}{3}}$ towards the ice divides, softening to 2×10^8 Pa $s^{\frac{1}{3}}$ towards the grounding line with the exception

of the three major ice streams. The Mellor and Lambert Glaciers are harder than the surrounding ice, with the faster velocities from basal temperate ice and basal sliding allowing for the transport of harder ice towards the grounding line. The regions that are at the basal melting point temperature are primarily the major ice streams and the region with significantly elevated GHF north of the Charybdis Glacier. The spatial distribution of the temperate ice matches the distribution of the regions at the basal melting point temperature. The temperate ice thickness varies from up to 150 m in the Lambert Glacier, 100m in the Mellor Glacier and as thin as 30m in the Fisher Glacier. These layers are likely formed due to the relatively small width of the ice streams compared to the drainage region, with compression leading to higher internal heating and thicker layers of temperate ice. The saturated till shows the regions which will slide relatively easily, with an average basal melt rate within the area of the saturated till of 17.4 mm year^{-1}. This converts to an entire glacial system basal melt rate of 1.3 mm year^{-1}. The maximum basal melt rate is 504 mm year^{-1}. The basal melt rates fall within the expected range for ice sheets, with the range of basal melt rates calculated by previous models ranging from 1-5.3 mm year^{-1}. The maximum basal melt rate is relatively high, but is lower than the expected 600 mm year^{-1} estimated for the faster flowing Pine Island Glacier. The thermal regime described falls with the bounds for our limited knowledge of the thermal properties of the ice sheet base.

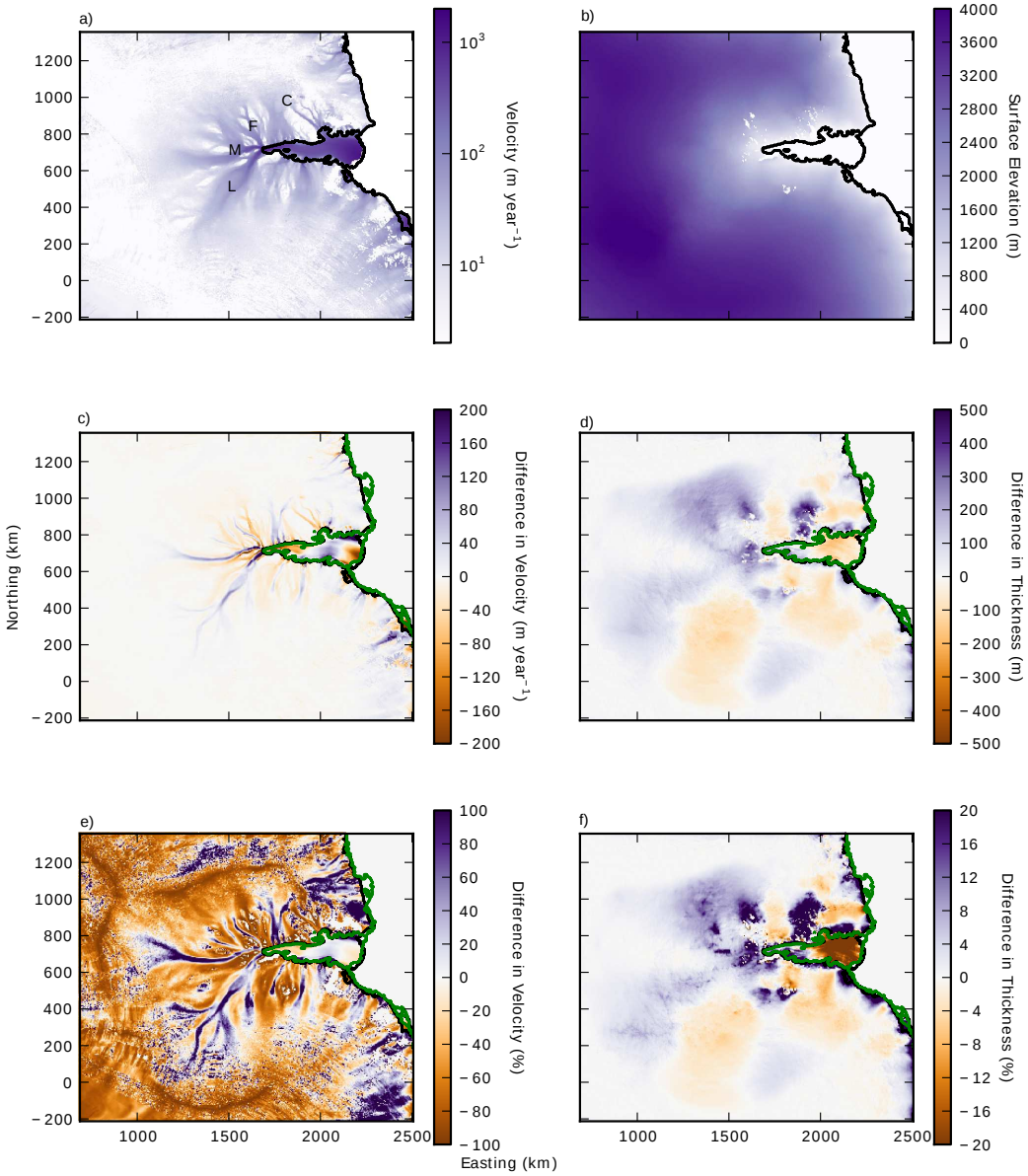

Figure 5.4: a) The MEaSUREs surface velocities (*Rignot et al.*, 2011b). L=Lambert Glacier, M= Mellor Glacier, F=Fisher Glacier, C=Charybdis Glacier. b) The bedmap2 ice thickness (*Fretwell et al.*, 2013) c) The difference between the control solution and the MEaSUREs velocities d) The difference between the control solution and the bedmap2 ice thickness e) The percentage difference between the control solution and the MEaSUREs velocities (*Rignot et al.*, 2011b) f) The percentage difference between the control solution and the bedmap2 ice thickness. The bedmap2 ice shelf and coastline is outlined in black, the control solution's ice shelf and coastline is shown in green.

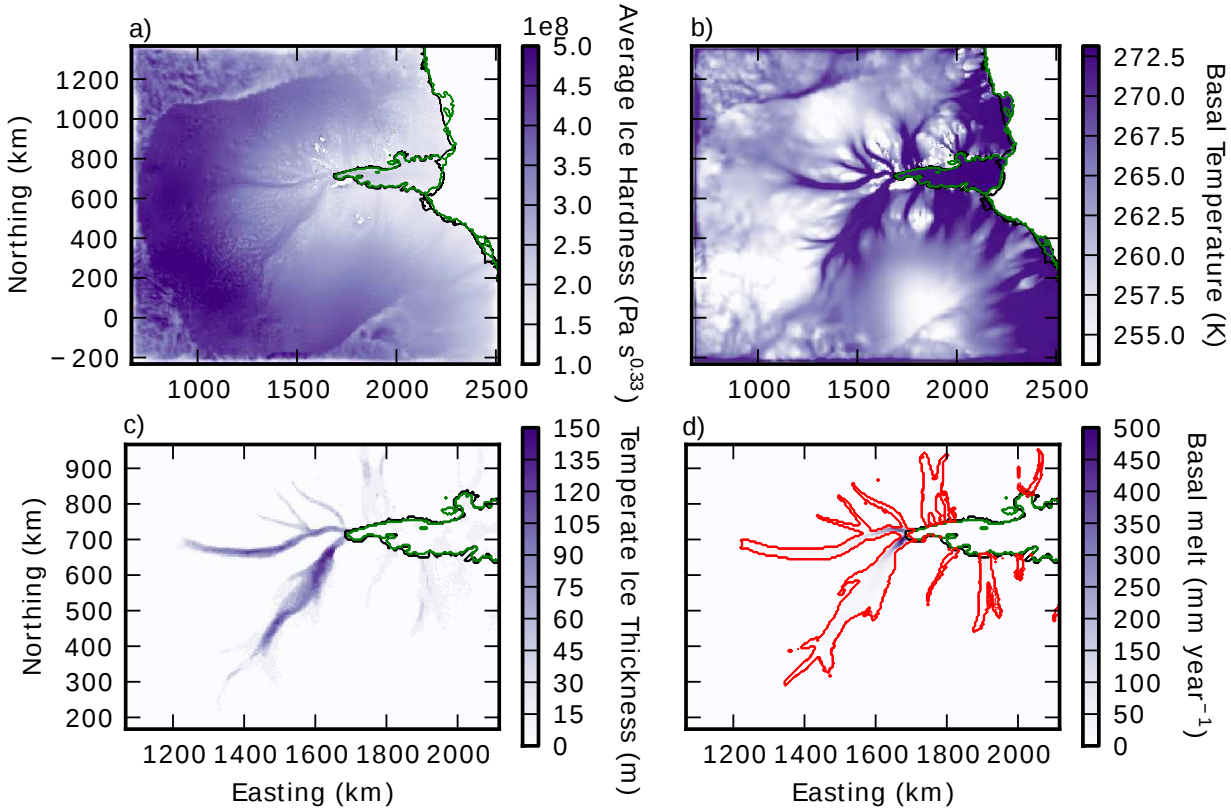

Figure 5.5: Thermal properties of the control solution: a) The average ice hardness. b) The temperature of the ice at the base of the ice sheet. c) The thickness of the temperate ice layer at the base of the ice sheet. d) The basal melt rate of the grounded ice sheet with the region within the red contour indicating the extent of the saturated till. The green line indicates the control solution's grounding line and the black the observed grounding line.

5.6 Ice Sheet response to Geothermal Heat Flux

5.6.1 Thermal Equilibrium Experiments

Each GHF dataset was run until thermal equilibrium was reached. The three GHF datasets with a higher average GHF required 400,000 years to reach equilibrium. The overall change in enthalpy was less than 1% for all simulations, with the enthalpy of each simulation approximately 2×10^{23} Joules. Even though this change is small, it is important as the spatial distribution varies. The volume and area of temperate ice increases in thermal_fm_2005, thermal_sr_2004 and thermal_an_2015 simulations (Table 5.2). The fm_2005 GHF dataset has the highest average heat flux, which leads to the simulation having twice as much temperate ice as the thermal_control in addition to an increase in over 50% in area. The thermal_sr_2004 and thermal_an_2015 simulations demonstrate that the datasets lead to different spatial distributions, with thermal_an_2015 showing more temperate ice in a smaller region relative to thermal_sr_2004. The area of temperate ice also represents the area within the ice streams at basal melting point. The scaled datasets show relatively small amount of change, with the control solution having 10-20% more temperate ice. The basal melt rates (bmelt) of the hotter GHF datasets is higher than the control and scaled datasets, however, most are lower than the control solution which demonstrates the influence of the horizontal resolution change. Analysis of changes in the main ice streams is limited by the lower horizontal resolution, which does not resolve the Mellor or Fisher Glaciers sufficiently to create a smooth surface velocity. This impacts the formation of temperate ice within the ice streams, with an uneven layer forming based on the variable surface velocities.

5.6.2 Comparing the Geothermal Heat Flux Datasets

The three simulations using the original GHF datasets (exp_fm_2005, exp_sr_2004 and exp_an_2015) had higher volumes of temperate ice compared to the control experiment, which indicates the velocities in the experimental run will be higher. The initially higher velocities leads to the transfer of mass from interior of the ice sheet towards the coast, consequently causing the grounding line to advance (Figure 5.6). Once the grounding line advances, the flow configuration of the region changes. The observed flow configuration, which is simulated in the control solution, shows three tributary glaciers flowing into the Amery Ice Shelf, each with its own grounding line. As the grounding line advances, the three glaciers now converge into a single outlet glacier, which has a smaller area of outflow, but is significantly deeper. The upstream velocities reduce as the thickness around the former grounding line increases. These changes make it difficult to assess the impact of the three geothermal datasets as the primary changes in the thermal regime are linked to the changes in flow configuration rather than the change in GHF. While this confirms that the ice sheet is sensitive to elevated GHF, the model was optimised for a GHF with a lower overall magnitude. Further optimisation would stabilise the grounding line with any GHF, however, this is computationally

expensive and hence the scaled datasets will be used to assess the importance of the spatial variability of the GHF.

5.6.3 Comparing the Scaled Geothermal Heat Flux Datasets

The thermal properties of the scaled dataset experiments are relatively similar, with the control maintaining the slightly elevated volume and area of temperate ice seen in the thermal experiments (Table 5.3). The average melt rates vary only slightly, although the exp_control has slightly lower average melt rate within the regions where the till is saturated. More importantly, the average melt rates have increased to be similar to the control solution, and now fall within the expected range for the Antarctic Ice Sheet.

The scaled datasets maintain a grounding line on the same topographic slope as the control (Figure 5.7), which enables the comparison of the relative changes in GHF. There are some clear differences in the surface elevation and surface velocities between the four datasets. The exp_fm_median simulation compared to the control solution has faster velocities through the Mellor and Fisher Glaciers than the Lambert Glacier, which corresponds with the thickness change in these regions. The simulation using the older magnetic derived dataset, exp_fm_scaled, shows significant differences to the control solution using updated magnetic derived dataset. All three major ice streams are slower relative to the control solution, with the main increases in velocity and thickness being outside these main ice streams. The two simulated using the GHF derived from seismic methods (exp_sr_scaled and exp_an_scaled) have similarities, with both showing increases in velocities within the Fisher and one arm of the Mellor Glacier, while the Lambert Glacier is considerably slower. This leads to changes in the ice thickness. One characteristic which holds across all scaled datasets is that the region north of the Charybdis Glacier is affected by the relatively high GHF in the fm_2012 dataset.

To assess the importance of these changes, and where the changes are directly related to the geothermal change, the ratio of change in surface velocities (Figure 5.7e,f,g,h) to the underlying GHF change (Figure 5.8a,b,c,d) is derived (Figure 5.8e,f,g,h). A positive ratio indicates that a higher relative GHF leads to an increase in velocity or a lower GHF leads to a decrease in velocity. We assume that a negative ratio indicates that there is no link between the underlying change in GHF and the surface velocity.

Three main patterns can be discerned from observing the ratios. The first is that the ice divides are sensitive to changes in local GHF, with strong ratios linked across all four scaled simulations. The second is that the ice streams are insensitive to change in the underlying GHF. The final pattern is that the edges of the ice streams are sensitive to changes, with their widths and upstream extent both being modified by the underlying GHF. This could be important to correctly modelling climate feedbacks, as regions which are cold relative to warmer adjacent ice streams may resist the acceleration driven by changes in bordering ice shelves. Conversely, if the regions adjacent to the ice streams are already close to pressure melting point and therefore sliding due to enhanced lubrication at the base from melt water, the system could respond far more

rapidly. There also appears to be evidence of ice piracy in exp_an_scaled, with the change in velocities between the two arms of the inland extent of the Mellor Glacier linked to an increase in the GHF in one arm which causes the decrease in velocity within the other arm, regardless of the underlying GHF in that region.

Assessing the GHF in terms of which dataset is most realistic is difficult based on this study, as the optimisation process creates a bias towards the fm_2012 dataset. It is evident that higher GHF leads to faster velocities, however, under an optimisation process the solutions could end relatively close to the same in all cases. The relative differences could be important, for example, our control solution had a relatively thick Fisher Glacier and a relatively thin Lambert Glacier compared to observations. The exp_an_scaled dataset would alleviate this discrepancy as it preferentially leads to a thicker Lambert Glacier and a thinner Fisher Glacier, but would probably lead to the Mellor Glacier also becoming too thick. The regional variations between each dataset likely will lead to each dataset excelling in different regions, and these relative differences could be used to choose an ideal GHF dataset for each region.

Table 5.2: The thermal properties of the ice sheet across all thermal simulations.

	Volume of temperate ice (m^3)	Area of temperate ice (m^2)	Max basal melt rate (mm $year^{-1}$)	Average basal melt rate (mm $year^{-1}$)	Glacial system basal melt rate (mm $year^{-1}$)
thermal_control	6.8×10^{12}	2.6×10^{11}	466.7	12.3	0.7
thermal_fm_2005	1.2×10^{13}	4.2×10^{11}	468.9	11.9	1.4
thermal_sr_2004	8.7×10^{12}	3.4×10^{11}	468.3	12.1	1.0
thermal_an_2015	9.2×10^{12}	3.1×10^{11}	468.0	10.1	0.8
thermal_fm_median	5.7×10^{12}	2.0×10^{11}	466.5	17.0	0.6
thermal_fm_scaled	6.0×10^{12}	2.1×10^{11}	466.8	13.6	0.6
thermal_sr_scaled	5.6×10^{12}	2.1×10^{11}	466.9	17.4	0.7
thermal_an_scaled	5.4×10^{12}	2.0×10^{11}	467.0	17.6	0.7

Table 5.3: The thermal properties of the ice sheet across all scaled exp simulations.

	Volume of temperate ice (m^3)	Area of temperate ice (m^2)	Max basal melt rate (mm $year^{-1}$)	Average basal melt rate (mm $year^{-1}$)	Glacial system basal melt rate (mm $year^{-1}$)
exp_control	7.2×10^{12}	2.7×10^{11}	503.09	18.25	1.3
exp_fm_median	6.3×10^{12}	2.0×10^{11}	489.69	24.72	1.4
exp_fm_scaled	6.4×10^{12}	2.1×10^{11}	504.65	23.07	1.4
exp_sr_scaled	6.3×10^{12}	2.1×10^{11}	455.13	23.88	1.3
exp_an_scaled	6.0×10^{12}	1.9×10^{11}	472.85	24.81	1.3

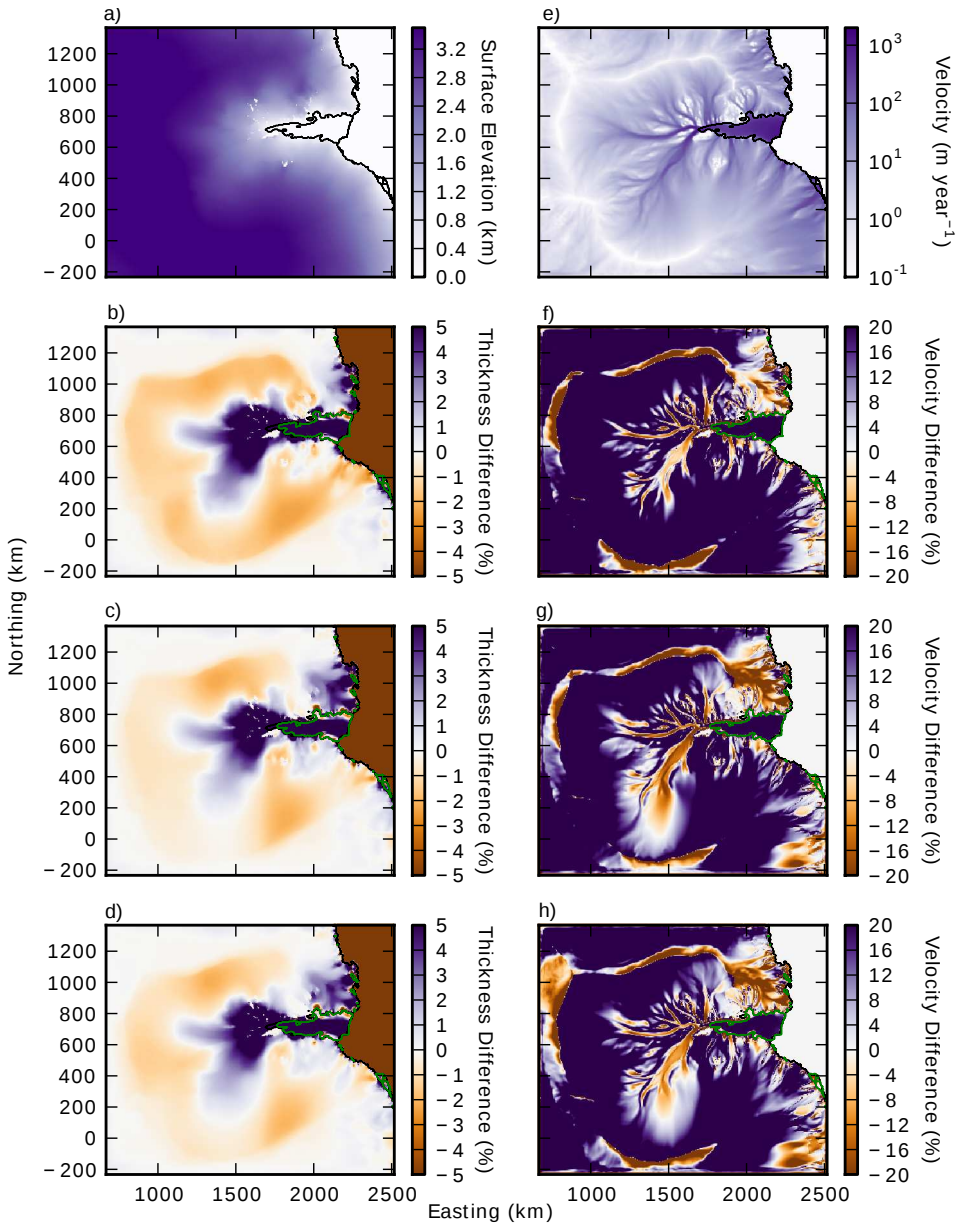

Figure 5.6: a) The surface elevation of the thermal_control simulation. The difference in ice thickness between the exp_control and b) exp_fm_2005, c) exp_sr_2004 and d) exp_an_2015. e) The surface velocity of the exp_control simulation. The difference in surface velocity between the exp_control and f) exp_fm_2005, g) exp_sr_2004 and h) exp_an_2015.

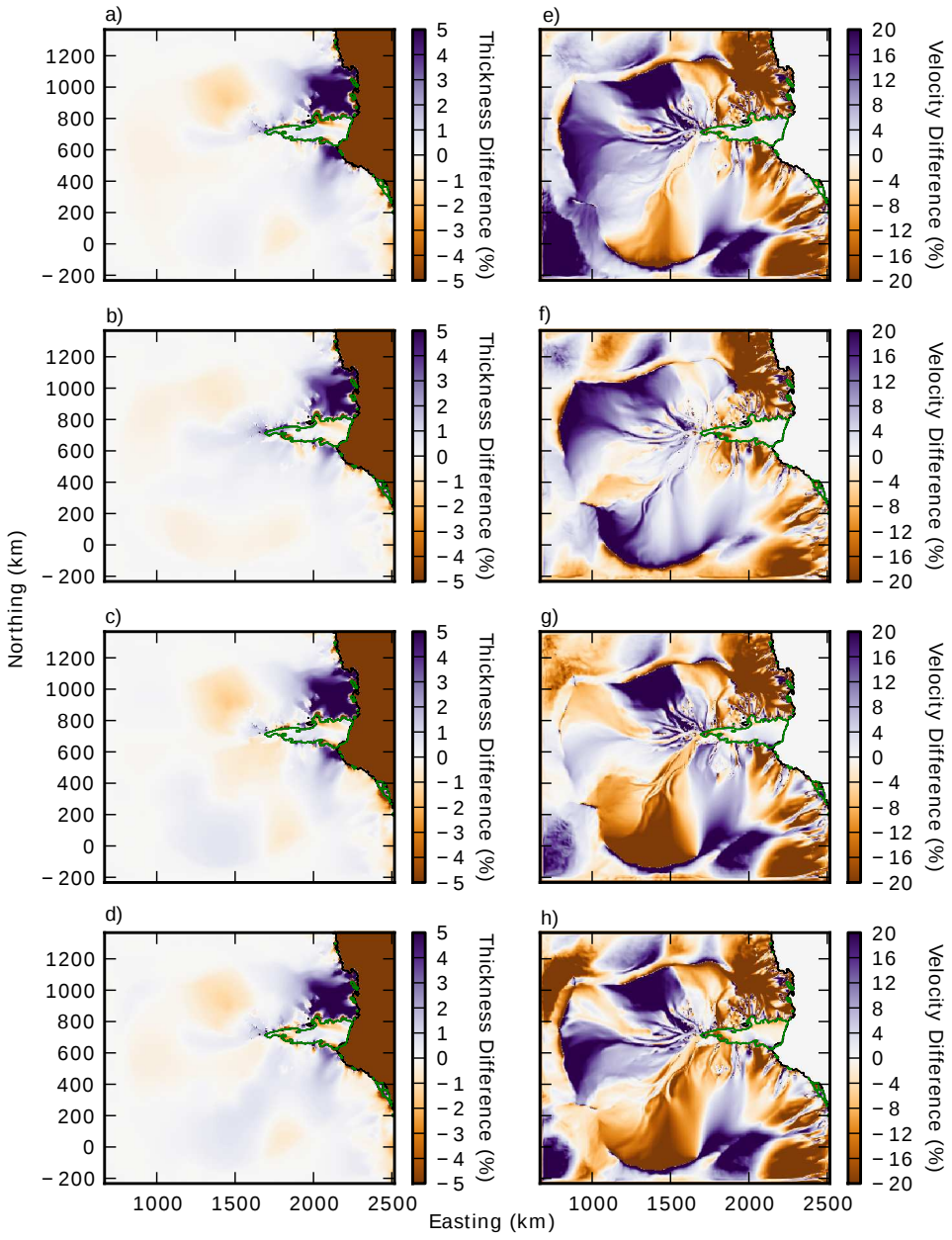

Figure 5.7: The difference in ice thickness between the exp_control and a) exp_fm_median, b) exp_fm_scaled, c) exp_sr_scaled and d) exp_an_scaled. The difference in surface velocity between the exp_control and e) exp_fm_median, f) exp_fm_scaled, g) exp_sr_scaled and h) exp_an_scaled. The control solution grounding line is shown in black and the scaled datasets in green.

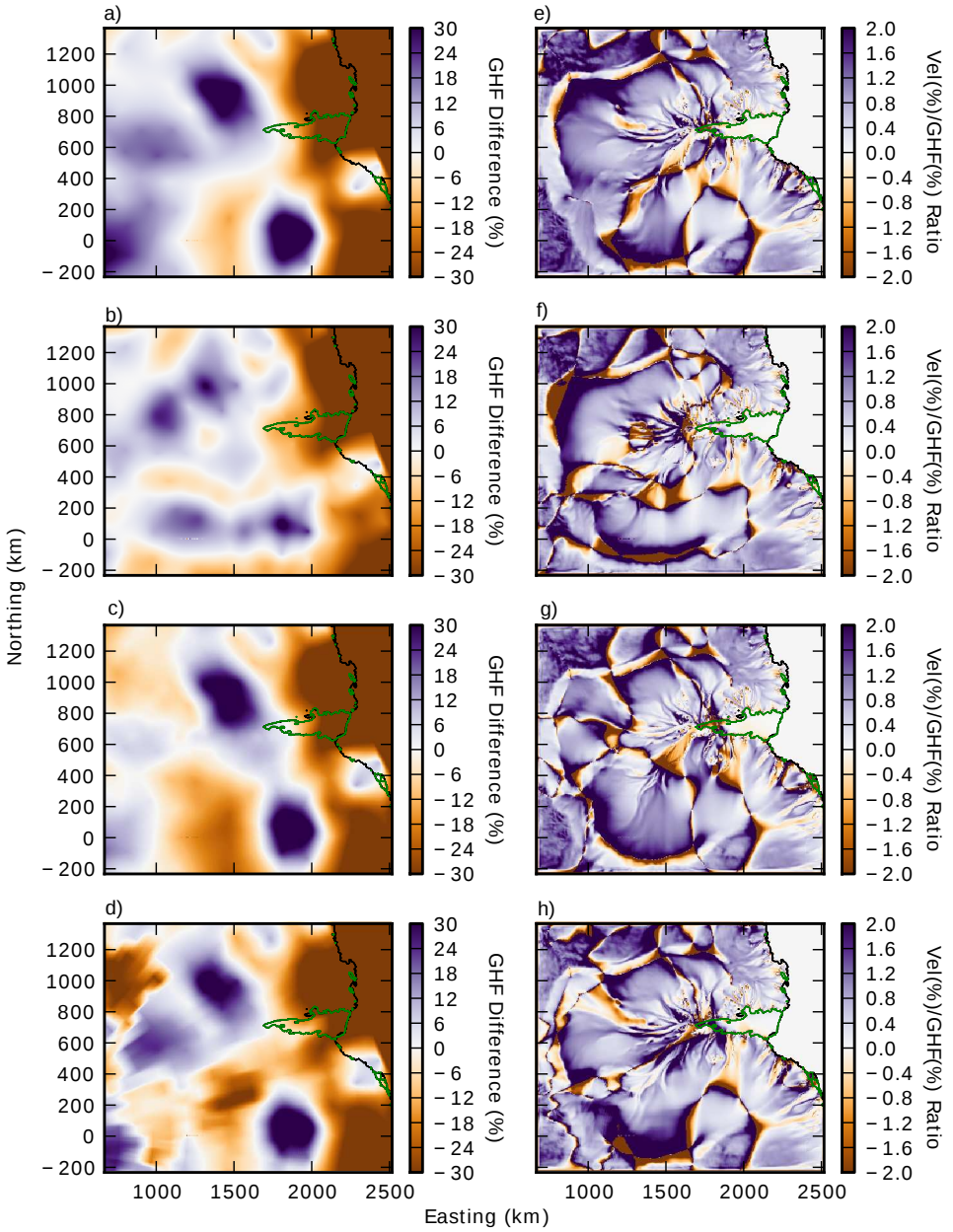

Figure 5.8: The relative difference in GHF between fm_2012 and a) fm_median, b) fm_scaled, c) sr_scaled and d) an_scaled. The ratio between the change in velocity (Figure 5.7e,f,g,h) and the relative change in GHF between exp_control and e) exp_fm_median, f) exp_fm_scaled, g) exp_sr_scaled and h) exp_an_scaled. The control solution grounding line is shown in black and the scaled datasets in green.

5.7 Conclusions

We present a realistic simulation of the Lambert-Amery glacial system, with the grounding line and calving front accurate with observations. The thermal regime of the control solution shows temperate ice layers up to 150 m thick in the Lambert Glacier and up to 100 m thick in the Mellor. The control solution's glacial system wide average melt rate is 1.3 mm year^{-1}, with a maximum basal melt rate of 504 mm year^{-1}. These numbers are consistent with previous modelling estimates from Antarctica. Three different geothermal heat flux datasets are compared to the control dataset, with higher geothermal heat flux leading to the formation of significantly more temperate ice. The increase in temperate ice leads to faster surface velocities which causes an advance in the grounding line, changing the flow configuration of the region. To compare the spatial differences a set of scaled geothermal heat geothermal heat flux datasets were created. The regions which were most sensitive to changes in the underlying geothermal heat flux were near ice divides and adjacent to the ice streams. The ice streams themselves were relatively insensitive to changes. Future studies should consider a robust evaluation of the effects of choosing one geothermal heat flux dataset over another on the solution. Further direct observation of geothermal heat flux are needed to evaluate the remote sensing derived products available to modellers, and additional techniques are needed to quantify geothermal heat flux and impact on the ice sheet flow.

5.8 Acknowledgements

This work was supported by the Australian Government's Cooperative Research Centres programme through the Antarctic Climate & Ecosystems Cooperative Research Centre. This research was supported under Australian Research Council's Special Research Initiative for Antarctic Gateway Partnership (Project ID SR140300001). This research was undertaken with the assistance of resources under projects m68 and gh8 from the National Computational Infrastructure (NCI), which is supported by the Australian Government. Development of PISM is supported by NASA grants NNX13AM16G and NNX13AK27G. The Geothermal Heat Flux dataset updated using the MF7 magnetic field based on the (*Fox Maule et al.*, 2005) was provided by Michael E. Purucker, NASA. We would like to acknowledge the anonymous reviewers for their suggestions which greatly improved this manuscript.

5.9 Supplementary Information

See Appendix B for the supplementary information for this chapter.

5.10 Concluding Remarks

This chapter details the thermal regime of the Lambert-Amery glacial system. It found that the choice geothermal heat flux can influence the locations of both the ice divides and the extent of basal lubrication in ice sheet simulations. Choice of geothermal heat flux could influence the final outcomes of ice sheet simulations and should be carefully considered. Further observations and evaluation of geothermal heat flux products is required.

Chapter 6

Response of the Lambert-Amery glacial system to climate variations

This chapter examines the response of the Lambert-Amery glacial system to climate variability. The mechanisms which leads to the advance and retreat of the grounding line over glacial-interglacial cycles will be investigated. A positive and negative anomaly is applied to variables for surface temperature, surface mass balance, oceanic driven basal mass balance and sea level change. Simulations on realistic time-scales investigate the mechanisms which allow for the grounding line to advance to the continental shelf, and subsequently retreat to its present location. This work is not presently under preparation for publication.

6.1 Abstract

The Lambert-Amery glacial system in East Antarctica has been observed to be highly variable over glacial cycles (*White et al.*, 2011). The grounding line has been interpreted to have advanced to the continental shelf break during the last glacial maximum (*Mackintosh et al.*, 2014). Understanding the mechanisms which leads to the advance and retreat of the grounding line will help improve our ability to assess the risks of future change from this region. The response of the Lambert-Amery glacial system to positive and negative anomalies in four primary climate forcing variables, surface temperature, surface mass balance, oceanic driven basal mass balance and sea level change, is investigated. The climate forcing variables are varied to represent a global atmospheric temperature change of $\pm 3^{\circ}$C. This sensitivity study shows that the ice sheet responded most rapidly to changes in surface mass balance and oceanic driven basal mass balance, whilst changes in surface temperature led to the largest change in mass, but over time scales longer than the most recent glacial-interglacial cycles.

The glacial system is more sensitive to mass gain than mass loss. When the glacial

system gains mass, the grounding line advances, leading to the flow regime of the system changing and consequently leading to further mass gain. This contrasts with the mass loss scenarios, as the grounding line is unable to retreat up the positive sloping bed where it is presently grounded to the negative sloping bed beyond, reducing the consequent mass loss. We were unable to simulate the expected surface ice profile during last glacial maximum as the ice sheet did not generate the theorised fast flowing ice stream, which led to the growth of a substantial ice sheet on the continental shelf as the grounding line advanced. Our results suggest that there is a possibility that ice sheet growth within Prydz bay could lead to an enclosed ocean cavity as the northern grounding line advances faster than the southern grounding line, which would have a significant effect on the ice flow. Furthermore, we were unable to retreat the thicker last glacial maximum ice sheet in our simulation to the present day grounding line, suggesting that this amount of mass growth is unrealistic.

6.2 Introduction

Ice sheets grow and retreat over glacial-interglacial cycles, contributing to the rise and fall of sea level through time. These cycles can be seen in ice core records such as the Vostok ice core (*Petit et al.*, 1999), with periodicities of 100 kyear, 40 kyear and 20 kyear cycles associated with climate variations. The timing of the climate cycles, and the growth and retreat of the ice sheets are linked to the Milankovitch cycles, although complex feedbacks make this less clear (e.g *Huybers and Curry*, 2006). The global temperature was colder than the present at LGM, with estimates ranging from 3-6°C (e.g *Annan and Hargreaves*, 2013). A re-analysis with additional proxy data estimates the cooling at 4-4.5°C, with a range of 3-6°C across the error of all models (*Annan and Hargreaves*, 2013).

At the last glacial maximum (LGM) the Antarctic Ice Sheet was grounded at or close to the continental shelf break. There is some debate surrounding the level of mass gain, with estimates ranging between ≈ -5.9 m to -19.2 sea level rise equivalent (e.g. *Wright et al.*, 2008; *Whitehouse et al.*, 2012; *Golledge et al.*, 2014; *Mackintosh et al.*, 2014). One of the primary interests in understanding the growth and subsequent retreat of the Antarctic Ice Sheet over the LGM is to better understand the viscous response of the solid earth to the mass changes (e.g. *King et al.*, 2012; *Whitehouse et al.*, 2012). The solid earth response is important for both interpreting the present mass changes from gravimetry (e.g. *King et al.*, 2012; *Shepherd et al.*, 2012), and for understanding regional sea level variations (*Carson et al.*, 2016).

Numerical modelling of ice sheets are used to investigate the mechanisms which leads to the advance and retreat of the ice sheet through glacial-interglacial cycles. The ice sheet mass change is driven through variations in surface temperature (e.g. *Huybrechts*, 2002), sea level change (e.g. *Gomez et al.*, 2013), ocean temperature (e.g. *Golledge et al.*, 2012, 2014)) and changes in surface accumulation. Surface temperature changes affect the temperature of the ice, which will change the rate of deformation

and subsequently its flow rate. As sea level rises and falls, it modifies the relative depth of topography, which can trigger retreat or advance of the grounding line as the thickness of ice required for flotation changes. Ocean temperature changes the rate of basal melting on the underside of ice shelves, leading to thickening or thinning of the ice shelf, which has a dynamic effect on the upstream ice flow. Surface accumulation is the primary mass input into the glacial system, and changes in its rate or distribution will lead to changes in the ice sheet. It has been interpreted that ice streams which are only just below the flotation point existed in regions which are currently ice shelves (*White et al.*, 2011; *Mackintosh et al.*, 2014). These regions of shallowly grounded ice are difficult to model when the basal friction is determined by a parametrisation (*Golledge et al.*, 2012), however, empirical data can be used to force the surface elevation to match the interpreted glacial history, in addition to setting low basal friction beneath the ice streams (*Whitehouse et al.*, 2012).

A region which underwent significant change is the Lambert-Amery glacial system (Figure 6.1a), with the grounding line estimated to have advanced over 700 km to near the continental shelf break at the LGM (*White et al.*, 2011; *Mackintosh et al.*, 2014). The Lambert-Amery glacial system discharges through the Amery Ice Shelf into Prydz Bay (Figure 6.1b). The current grounding line is situated $\approx$ 650 km from the calving front, in a narrow embayment within the Prince Charles Mountains (PCM) which protrude through the ice sheet and constrict ice flow within this region. Three major glaciers, the Lambert, Mellor and Fisher Glaciers discharge into the Amery Ice Shelf within this narrow embayment, converging into a single ice flow on the ice shelf. The Lambert-Amery glacial system is estimated to be more sensitive to changes in surface temperature than the global average, with both reconstructed surface temperatures at the LGM and future climate modelling showing regional amplification (*Annan and Hargreaves*, 2013; *Pachauri et al.*, 2014).

The reconstructed surface temperatures show an decrease of -4°C to -8 °C over the high elevated regions of the ice sheet, with a -8°C to - 12°C over the present day ice shelf (*Annan and Hargreaves*, 2013), while the predicted increases in temperature under the RCP8.5 scenario between 2081-2100 (3.7°C global temperature increase), shows a 5°C temperature increase (*Pachauri et al.*, 2014). The colder temperatures led to the advance of ice sheet to the continental shelf break, with marine observations of the bed in Prydz Bay indicating that grounded ice was present during the last glacial maximum (*O'Brien and Harris*, 1996; *Domack et al.*, 1998). The minimum extent of the advance was estimated to be the current calving front position, and the maximum position the continental shelf break (*Mackintosh et al.*, 2014).

While there is strong evidence of grounded ice in Prydz Bay at the LGM, the observed elevation profile from weathering of exposed rock within the Lambert-Amery glacial system indicates that an ice plain existed from the edge of the PCM to the shelf break, with the thickening of the ice sheet behind this region (*White et al.*, 2011). The authors hypothesise that this was due to a fast flowing ice stream which limited

the ice growth in the region, with a total net growth of the ice sheet in the Lambert-Amery glacial system leading to change in sea level by -0.4 ± 0.3 m sea level equivalent compared to present. The retreat of the ice within the Lambert-Amery glacial system commenced as early 18 kyears and finished by 8 kyears (*White et al.*, 2011). The initial advance is less understood, as ice flow erodes evidence below the maximum height of the ice. It is estimated that the maximum time period the advance took was ≈ 10 kyears (*Domack et al.*, 1998, Personal Communication, Duanne White 2016). The mechanisms which leads to the advance and retreat of the ice sheet within the Lambert-Amery glacial system throughout the glacial-interglacial cycles are still unclear.

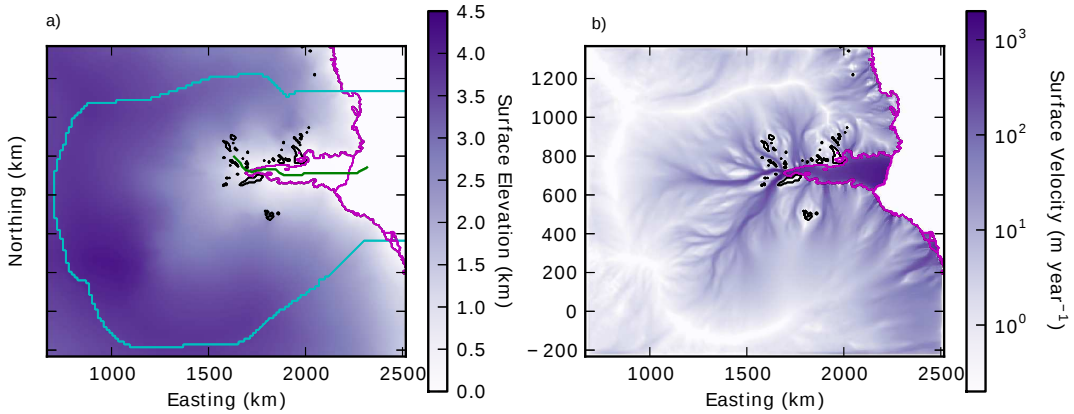

Figure 6.1: a) Surface elevation and b) Surface velocity of a model simulation of Lambert-Amery glacial system (*Pittard et al.*, 2016a). Ice Shelf and ocean boundaries indicated in magenta. The three main tributary glaciers are indicated. Ice free regions outlined in black. Solid green line in a) indicates transect in Figure 6.3.

This study is split into two parts: the first study will investigate the response of the Lambert-Amery glacial system to oceanic driven basal mass balance, surface mass balance, sea level rise and surface temperature changes. Following and guided by these experiments, the second study will investigate the mechanisms which could lead to the advance and subsequent retreat of the ice sheet over time periods representative of interglacial-glacial cycles by conducting a series of iterative experiments.

6.3 Part 1: Sensitivity to positive and negative climatic variations

6.3.1 Experimental design of climatic variables

To test the response time to both a warming and cooling climate, an average global atmospheric temperature change of +3°C (_pos) and -3°C (_neg) was chosen. These values fall within the range of both the upper end of temperature increases during the interglacial, as well as the temperature decreases during the last glacial maximum. The last glacial maximum was probably colder, with global atmospheric temperatures between -4°C and -6°C (with regional temperatures in Antarctica up to -12°C), compared

to present estimated for its coolest period (*Annan and Hargreaves*, 2013). Future climate model runs also find local amplification near the Lambert-Amery glacial system relative to the zonal average (*Pachauri et al.*, 2014).

The four climate forcing parameters that will be investigated are surface temperature (stemp), surface mass balance (smb), ocean driven basal mass balance (bmb) and changes in sea level (slr), with each being run individually for both positive and negative changes on the regional model. Each climatic variable change was implemented by:

- stemp: The regional change in atmospheric temperature is approximately double the global average (*Annan and Hargreaves*, 2013), therefore we apply a ± 6°C across the entire domain (stemp_pos, stemp_neg).

- smb: The Clausius–Clapeyron relation suggests approximately a 7.5% change increase in precipitation per °C of atmospheric temperature increase. We multiply this value by three to represent a ±3°C global change (This is an oversimplification of the Clausius–Clapeyron relation, but sufficient for this sensitivity study), for a ± 22.5% change in SMB (smb_pos, smb_neg). We assume that changes in precipitation will correspond to an identical change in SMB.

- bmb: There is little information on how variations in oceanic circulation and temperatures will effect the Amery Ice Shelf. *Galton-Fenzi* (2009) produced a quadratic relationship for changes in atmospheric temperature for the Amery Ice Shelf (Equation 6.1) where x is the change in atmospheric temperature and B_{mf} is the scalar change in overall basal melt.

$$B_{mf} = 0.1012x^2 + 0.0406x + 0.9939 \tag{6.1}$$

  Equation 6.1 generates a B_{mf} of 2.02× increase for a 3°C increase in atmospheric temperature. This relationship is implemented in our model by adding an additional scalar of 1.5× to the oceanic melt relationship and applying an additional 0.38 m $year^{-1}$ melt across the entire ice shelf (50% of the average control basal melt). For -3°C, we mirror the change from the positive scenario, which is reversed to a scalar of 0.5× and an additional ice shelf wide melt rate of -0.38 m $year^{-1}$. This is representative of an ice shelf system of close to 0 net mass loss, as refreezing will be approximately the same as melting (bmb_pos, bmb_neg).

- slr: Changes in sea level are considered to be a trigger for ice sheet advance/retreat. Paleo studies indicate sea level has risen and fallen by over 100 m in the past (*Lambeck and Chappell*, 2001). A step change of 100 m is applied instantaneously at the start of the numerical simulations (slr_pos, slr_neg). This step change causes an unrealistically high sea level rise in the slr_pos scenario, but any mechanisms triggered by such a change are of interest.

A regional model of Lambert-Amery glacial system has been created and simulated within PISM (Figure 6.1). The regional outline and model parameters are outlined in *Pittard et al.* (2015) and Appendices B and C. Each climatic forcing will be simulated for 45,000 years at 5 km horizontal resolution and 15 m vertical resolution. Each climatic forcing has been applied as a step change at the start of the simulation. It would have been possible to apply a time varying smb (paleo_precip option) and slr, but the bmb was limited to step changes, as time varying bmb would not have adapted to the changes in the grounding line position which are essential to this research. In addition, scenarios combining all four climatic variations will be simulated for both positive and negative global temperature change (all_pos, all_neg).

6.3.2 Response to climatic variations

The Lambert-Amery glacial system lost mass under slr_pos, bmb_pos, stemp_pos and smb_neg and gained mass under slr_neg, bmb_neg, stemp_neg and smb_pos (Figure 6.2). The all_pos simulation initially gained mass through increased smb, but over time the rate of mass loss increased, and overall it lost mass relative to the control simulation. The all_neg simulation gained mass the quickest of all the simulations, with the final mass gain the largest of all simulations. The influence of decreased smb had little effect on slowing the ice sheet growth in the all_neg simulation.

The Lambert-Amery glacial system was most sensitive to surface temperature changes over long time periods, with both the negative and positive variations in surface temperature not reaching a steady state over the 45,000 year simulation, indicating that the response time to surface temperature changes is relatively slow compared to the other climate variations. The simulations were not continued past 45,000 years as it is longer than the recent glacial-interglacial cycles, but it also suggests that changes in surface temperatures can lag behind changes in other climate variables. For example, the ice sheet may still be relatively warm during the initial drop in global surface temperatures, which could allow the ice sheet to respond faster to the changes as it has higher initial flow rates.

The ice sheet was sensitive to changes in smb, with an increase in precipitation leading to substantial growth of the ice sheet while smb_neg leads to the ice sheet losing mass. There are step changes in the rate of mass growth in the smb_pos simulation, while the mass loss in the smb_neg simulation slowly decreases through time to a new steady state.

The bmb_pos simulation has very little effect on the mass of the ice sheet, while the bmb_neg simulation leads to the growth of the ice sheet, with the step change in mass growth seen in this simulation.

The slr_pos and slr_neg simulations show an instantaneous change in the volume of ice grounded above sea level. This results in the initial change in mass grounded above sea level in the slr simulations. The raising of the sea level leads to no significant dynamical changes after the initial change in volume, with only minor changes in ice

volume throughout the length of the simulation. The raising of the sea level would lead to minor retreat of the grounding line, but unless the grounding line shifted from a positive to a negative sloping bed (relative to the continental shelf) then no major change would occur as the grounding line is still on a stable slope. The initial fall in sea level leads to further dynamical changes, with the ice sheet gaining mass and leading to further decreases in sea level. This is likely due to a feedback where the grounding line advances until it finds another stable position, which may have different mass flux. This change in flow configuration can lead to further changes as the system adjusts to the lower sea level.

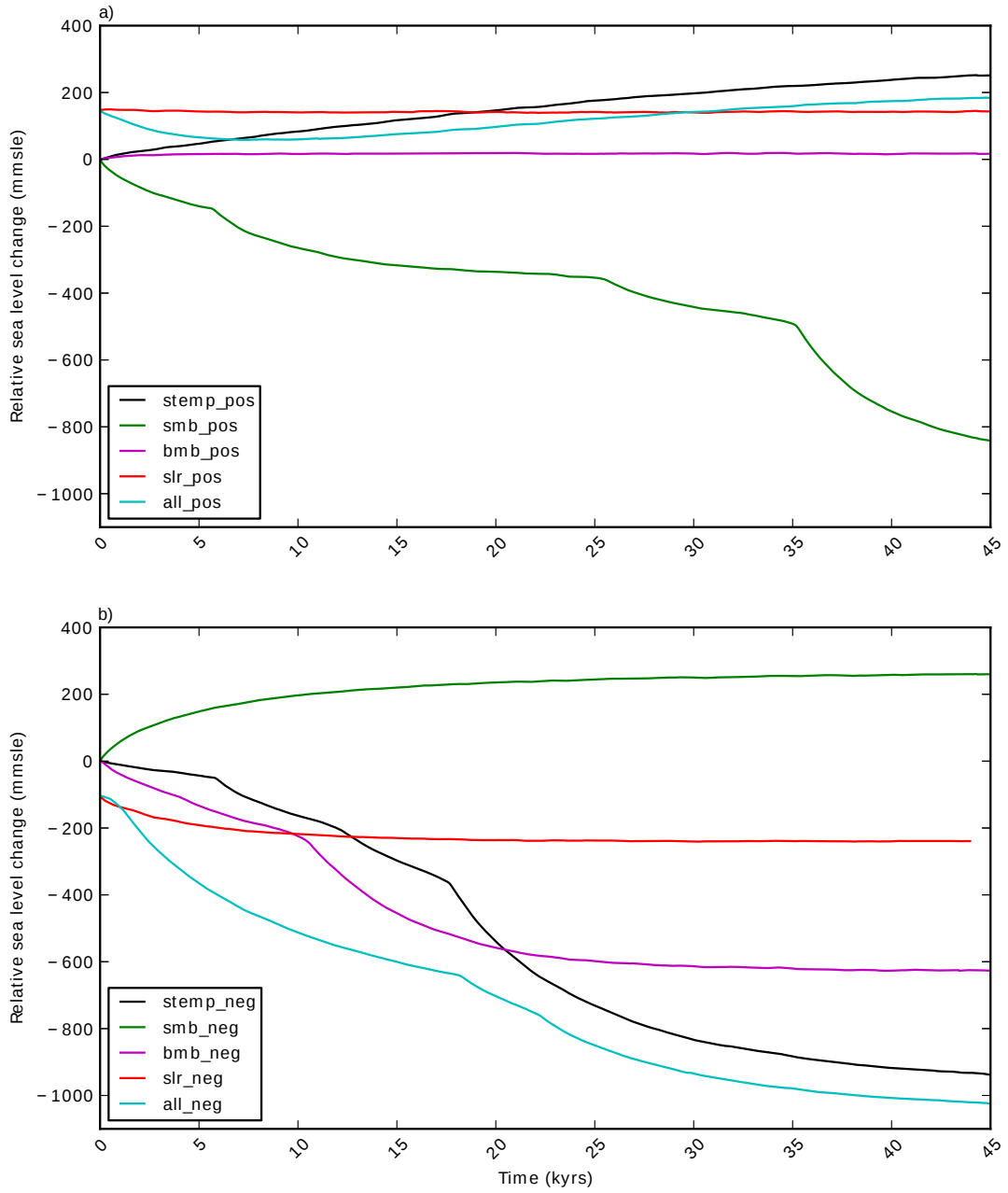

Figure 6.2: Sea level change relative to the control simulation (See Appendix B and C) for a) positive climatic variations. b) negative climatic variations.

The advance of the grounding line occurred in all simulations when the ice sheet gained mass (Figure 6.3a,b). Each simulation advanced to a different location, but in all cases the grounding line was located on bed topography which slopes down towards the continental shelf break (Figure 6.3c). The experiments which gained mass each show step changes in the rate of mass gain where the growth rapidly increases before gradually slowing. These rapid events in growth represent the periods where the grounding line is advancing to a new stable position. Once the grounding line stabilises, the ice sheet slowly builds until the driving stress causes the flow to increase such that the grounding line shifts off the stable position and rapidly advance.

The ice sheet profiles that are generated from the simulations are unable to reproduce the observed paleo ice sheet profile (*White et al.*, 2011), with the grounding line advancing and then the ice sheet thickening at the grounding line, rather than forming an ice stream. This could suggest that the basal traction is still too high in this region, but the parametrisation is domain wide, and further reducing the already low basal traction would lead to faster flow in the deep marine basins. In the all_neg simulations, the grounding line advanced 350 km, still 300 km away from the hypothesised grounding line at the last glacial maximum, however, the ice sheet profile at the grounding line has advanced further than the estimated paleo extent, with no shallow grounded ice stream forming within our simulations.

The loss of mass of the ice sheet is restricted by the topography where the grounding line is currently situated (Figure 6.3a). The grounding line has to thin by over 1500 m to be able to migrate over the shallow sill until it can retreat into deeper regions again. The climate variations tested are unable to generate such a change, with the ice shelf continuing to buttress the ice sheet, restricting the acceleration of the grounded ice and limiting the retreat of the ice sheet.

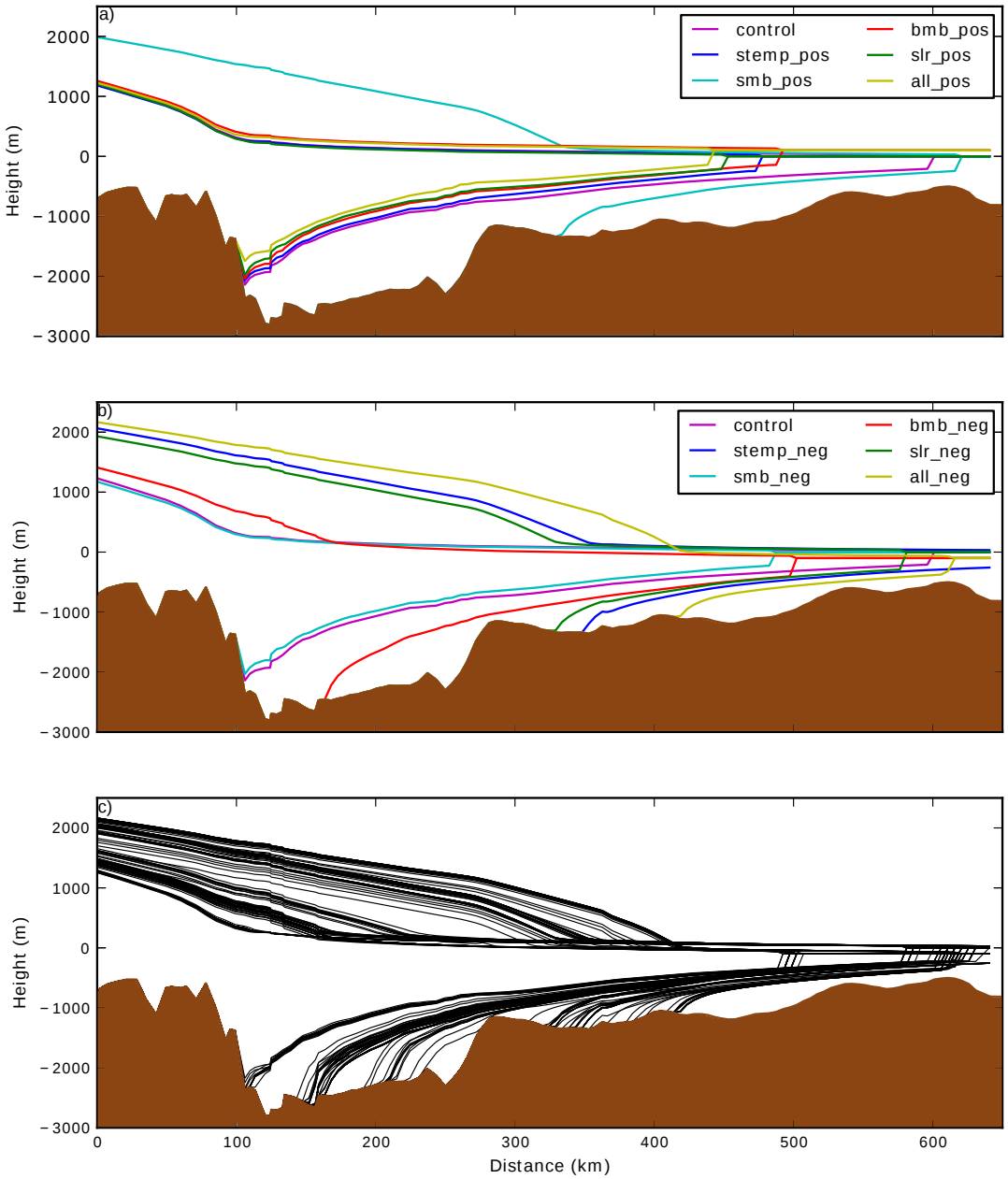

Figure 6.3: Transect from Figure 6.1 showing the ice sheet profile after 45,000 years for a) positive climatic variations and b) negative climatic variations. c) 1,000 year snapshots from smb_pos, stemp_neg, slr_neg, bmb_neg and all_neg showing the tendency of the grounding line to stabilise on beds that slope negatively towards the continental shelf break.

6.4 Part 2: Mechanisms of advance and retreat over glacial cycles

6.4.1 Experimental design

Observations of the paleo extent of the ice sheet from weathering marks on exposed rocks within the glacial system suggest the ice sheet was grounded to the continental shelf break, with a lightly grounded ice plain/stream present throughout most of the current ice shelf region (*White et al.*, 2011). The simulations where the grounding line advanced could not recreate this configuration, with the grounded ice sheet growing in thickness, and not forming a lightly grounded ice plain/stream. The advance and subsequent retreat of the grounding line likely occurred over a temporal period of at most 10,000 years (Personal Communication, Duanne White 2016).

We design a set of experiments that investigate the advance and subsequent retreat of the grounding line in the Lambert-Amery glacial system over a 20,000 year period. We hypothesise that prior to the advance of the ice sheet, increased precipitation paired with increased oceanic driven basal melt, leads to the build-up of ice at higher elevations, which leads to a steeper surface profile, with a greater volume of ice in the system and increased flow. As the decrease in global temperatures leads to the decrease in mass loss from the oceanic driven basal melt this allows the system to advance faster than otherwise as the higher driving stresses combined with lower melt rates shift the grounding lines onto beds which become shallower towards the continental shelf leading to rapid advance as seen in Part 1 of this chapter.

To achieve this, we initialise the advance experiments with the all_pos simulation after 10,000 years, as the increased smb has led to an increase in the surface elevation at the ice plateaus and the ice divides, while higher melt rates have led to mass loss at the coast (Figure 6.4), creating a steeper surface profile. The climate forcing utilised in the simulation was initially the all_neg conditions (ADV_1), however, iterative variations on these conditions were attempted to improve the simulation and are discussed in detail within the next section.

Following the advance simulations, a range of simulations aimed at returning the grounding line to the control state were conducted. The initial retreat experiment applied the control climate forcing. These had a temporal period of 10,000 years and were iteratively varied as discussed in detail within the next section.

6.4.2 Advance of the grounding line

The initial advance simulation (ADV_1) was run with the negative climatic parameters, however, the ice sheet responded similarly to the all_neg experiment and the grounding line did not advance to the continental shelf (Figure 6.5a). The initialisation using 10,000 year all_pos experiment did not advance faster than the initial 10,000 years of the all_neg simulation.

To enhance the rate at which the ice shelf advances and grounds on pinning points in

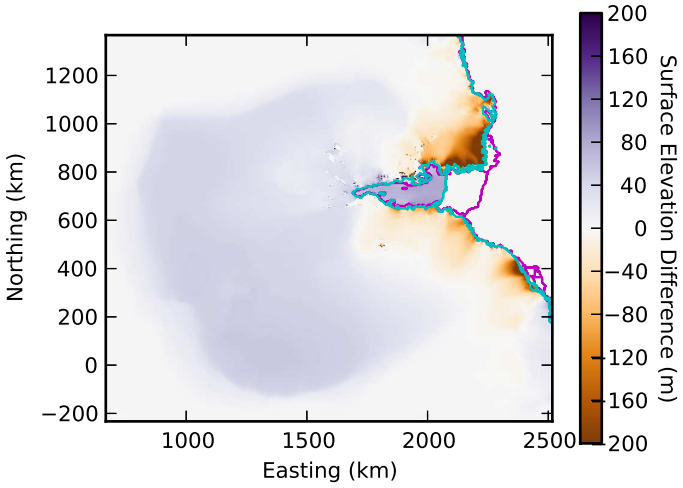

Figure 6.4: Surface elevation change for the all_pos simulation at 10,000 years relative to the control simulation (Figure 6.1). Cyan line indicates grounding line of all_pos simulation and red line indicates the grounding line of control solution.

Prydz Bay, a parameter controlling the thickness at the calving front (thickness_calving_threshold) was reduced to 112.5 m from 225 m (ADV_2). This is to represent an hypothesis that under a colder climate, the calving front will be more stable (possibly due to increased and thicker multi-year fast ice). The fall of sea level leads to regions of Prydz Bay rising above sea level. This change allows for the calving front to grow into Prydz Bay over time, where it grounds at numerous shallow points and locally can grow from precipitation on regions which previously were ocean (Figure 6.6). The additional buttressing leads to the rapid advance of the grounding line, but also to the rapid advance of the ice sheet, with the surface elevation well over 1500 m in regions where the LGM surface is interpreted to be under 300 m. The total mass gain throughout the ADV_2 simulation leads to a change of -1400 mm sea level equivalent, which is significantly more than the estimated amount of -400 $\pm$ 300 mm sea level equivalent (*White et al.*, 2011). The flow of ice in the newly grounded region is less than 100 m year^{-1}, which is representative of broad scale ice sheet flow rather than a fast flowing ice stream. During the advance of the ice sheet, the ice shelf became closed off from the ocean as the front of the embayment grounded faster than the rear of the ice shelf, creating an enclosed ocean cavity. The response of the ice shelf and ice sheet to such a configuration is unknown, but the possibility of an enclosed ocean cavity suggests an alternative theory to generate the interpreted LGM surface profile within this region.

To investigate the possibility of the ice sheet grounding within Prydz Bay from local ice sources and forming an enclosed ocean cavity, rather than from the advance of the present grounding line, a simulation with enhanced basal melt (scalar of 2 $\times$ to the oceanic melt relationship) is combined with the lowered thickness_calving_threshold is tested (ADV_3). This allows for the grounding line to be maintained it its current position while local ice grows within Prydz Bay, leading to the formation of an enclosed

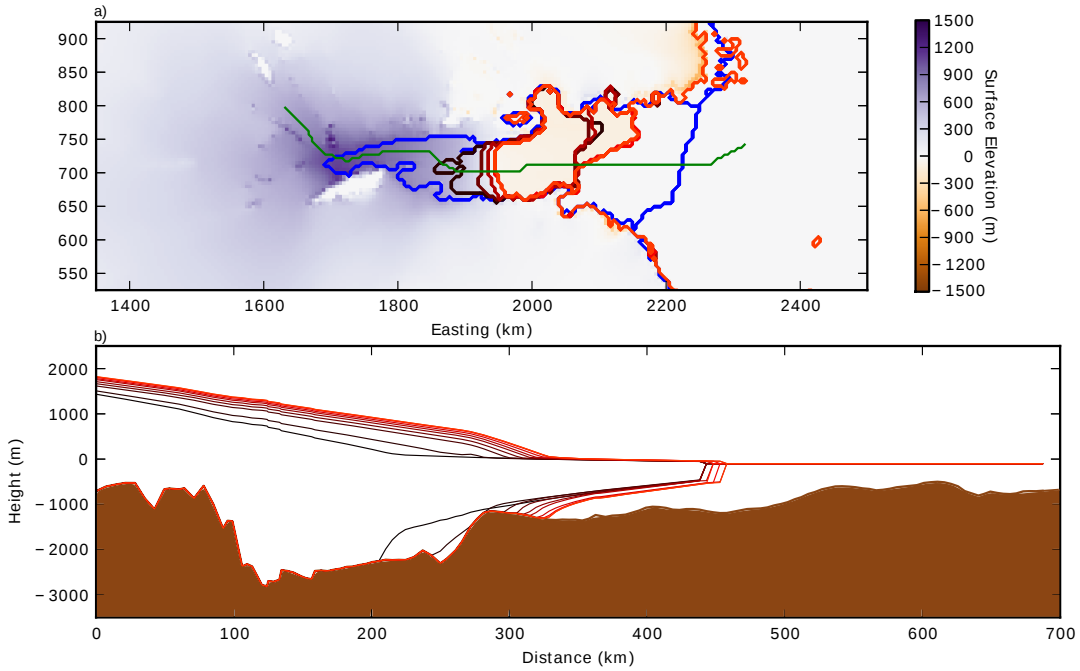

Figure 6.5: a) Surface elevation change for the ADV_1 simulation at 10,000 years relative to the control simulation (Figure 6.1). Grounding lines every 2,000 years are plotted for the ADV_1 simulation. Dark to light colours indicates incremental time slices. Green line indicates transect used in b) cross section of the grounding line position every 1,000 years. Dark to light colours indicates incremental time slices.

ocean cavity (Figure 6.7a). After the formation of the enclosed ocean cavity, the basal melt rates are returned to the forcing conditions within the bmb_neg simulation. This results in the enclosed ocean cavity rapidly filling with ice. Under this scenario, there are snapshots in time within the simulation which have an ice plain like profile, however, for the observable features to exist, the ice sheet retreat would have had to already have begun.

6.4.3 Retreat of the grounding line

The three LGM experiments were used as the initial point for simulations to investigate the mechanism of how the grounding line may have retreated during the LGM. The initial experiments simply reset the climatic conditions to the control conditions, but under these conditions the ice sheet continued to grow with increased precipitation over a larger surface area dominating any increase in basal mass loss. A limitation of the basal melt parametrisation we utilise is that it is thickness dependent, and it is optimised for the depth of the current grounding line (See Appendix B), which is far deeper than the grounding line in the advanced positions. To remedy this the basal melt scalar was changed to $\frac{z}{400}$, which results in a flatter melt profile with relatively elevated melt rates of 20 m year^{-1} at 1000 m ice thickness, increasing up to 60 m year^{-1} at 2000 m ice thickness, and up to 120 m year^{-1} at 3000 m ice thickness. With this enhanced melt rate, the scenario initialised with ADV_1 (ADV_1_retreat), retreated to

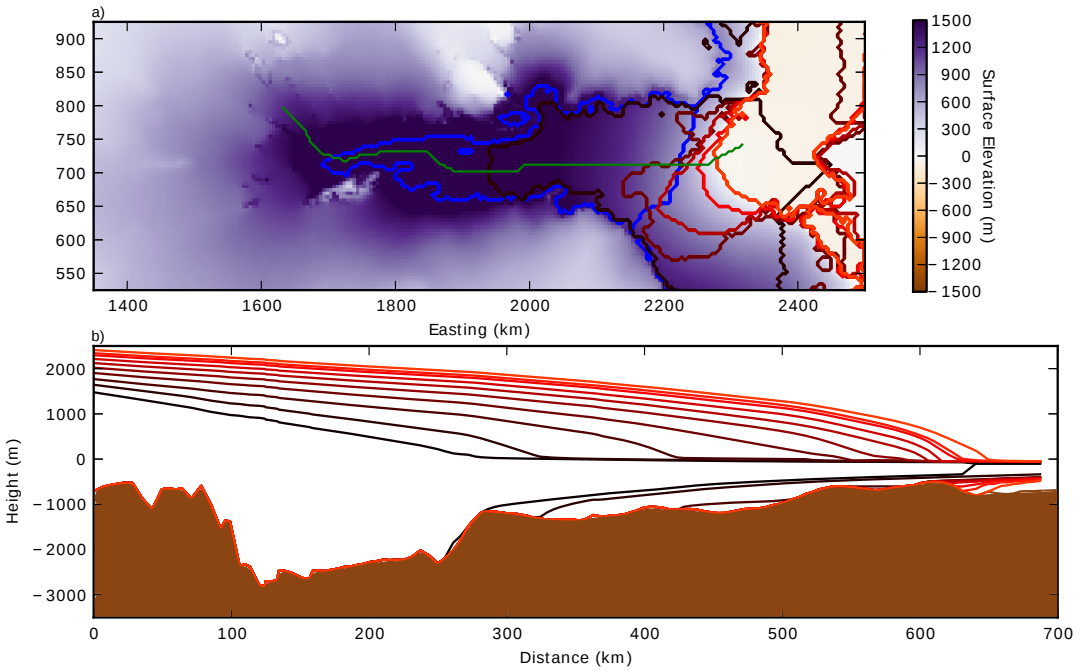

Figure 6.6: a) Surface elevation change for the ADV_2 simulation at 10,000 years relative to the control simulation (Figure 6.1). Grounding lines every 2,000 years are plotted for the ADV_2 simulation. Dark to light colours indicates incremental time slices. Green line indicates transect used in b) cross section of the grounding line position every 1,000 years. Dark to light colours indicates incremental time slices.

the present day grounding position (Figure 6.8a), although the ice shelf area was also severely reduced. The entire retreat took 600 years once the grounding line shifted onto a negative slope, with the quickest retreat rate being 150 km in 200 years. Scenarios initialised with the ADV_2 simulation were unable to retreat, even when forced with an extreme 100 m year^{-1} basal melt scenario. Simulations initialised with the ADV_3 simulation (ADV_3_retreat), retreated to the grounding line position of ADV_1 (Figure 6.9a) with the enhanced melt rate. However, at the last time step in the ADV_3_retreat simulation it had almost retreated off the sill where it was grounded, indicating that it was very close to retreating to the present day grounding line.

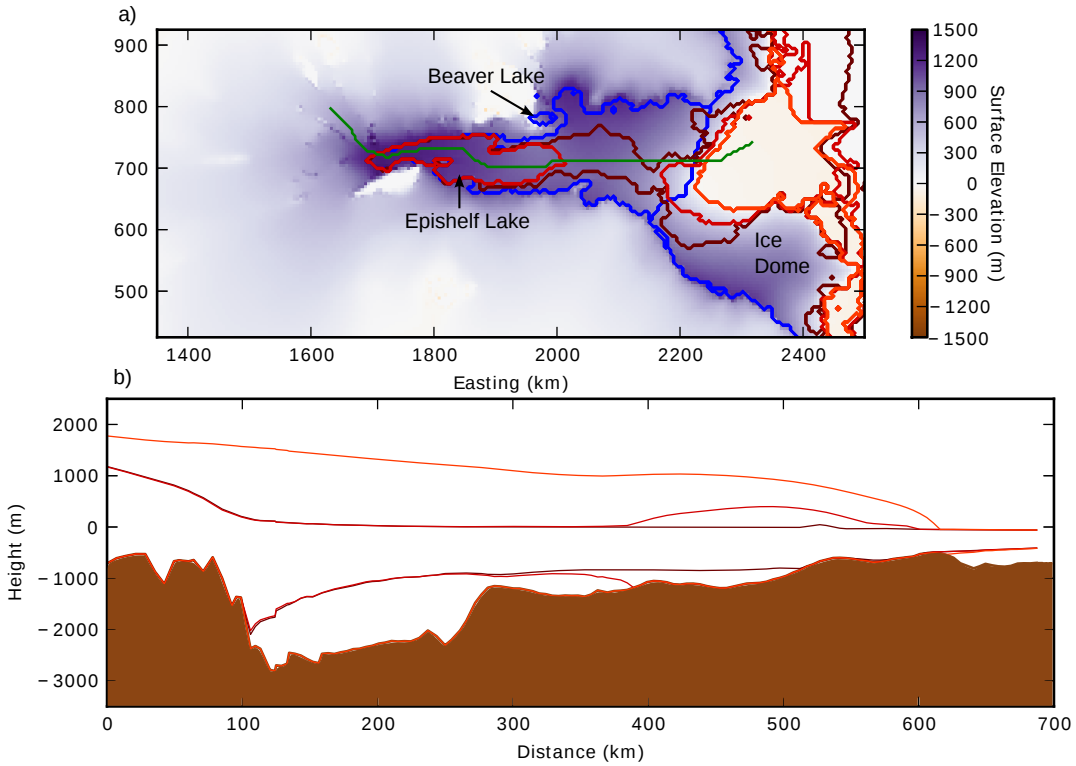

Figure 6.7: a) Surface elevation change for the ADV_3 simulation at 10,000 years relative to the control simulation (Figure 6.1). Grounding lines at 3,000, 6,000 and 10,000 years are plotted for the ADV_3 simulation. Dark to light colours indicates incremental time slices. Green line indicates transect used in b) cross section of the grounding line position every 1,000 years. Dark to light colours indicates incremental time slices. The enclosed ocean cavity and new ice dome are indicated.

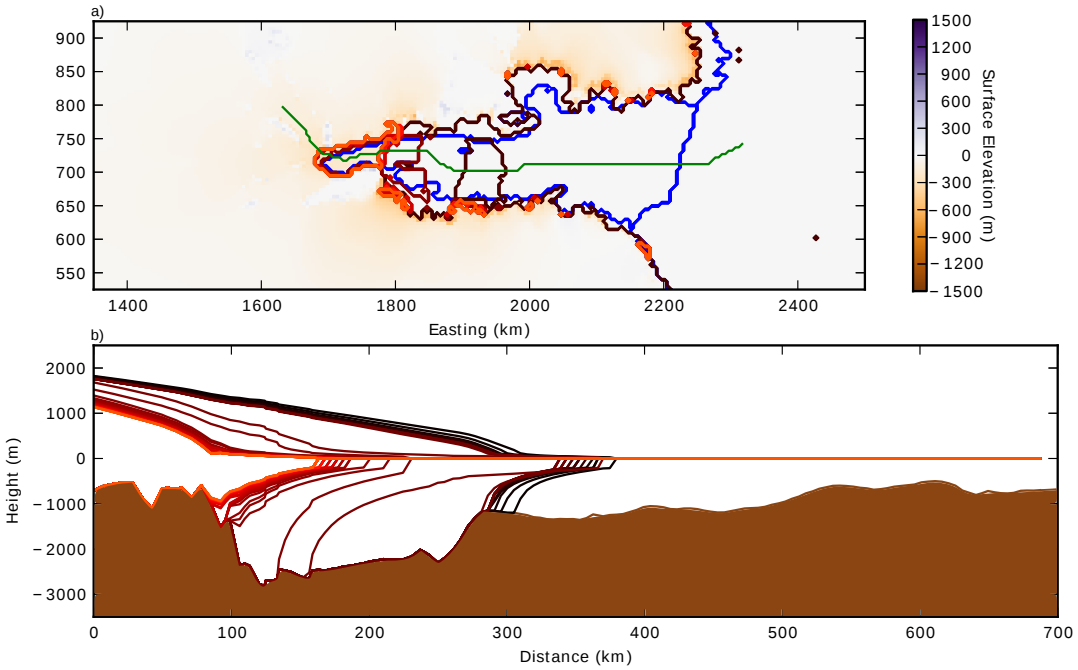

Figure 6.8: a) Surface elevation change for the ADV_1_retreat simulation at 10,000 years relative to the control simulation (Figure 6.1). Grounding lines every 2,000 years are plotted for the ADV_1_retreat simulation. Dark to light colours indicates incremental time slices. Green line indicates transect used in b) cross section of the grounding line position every 200 years. Dark to light colours indicates incremental time slices.

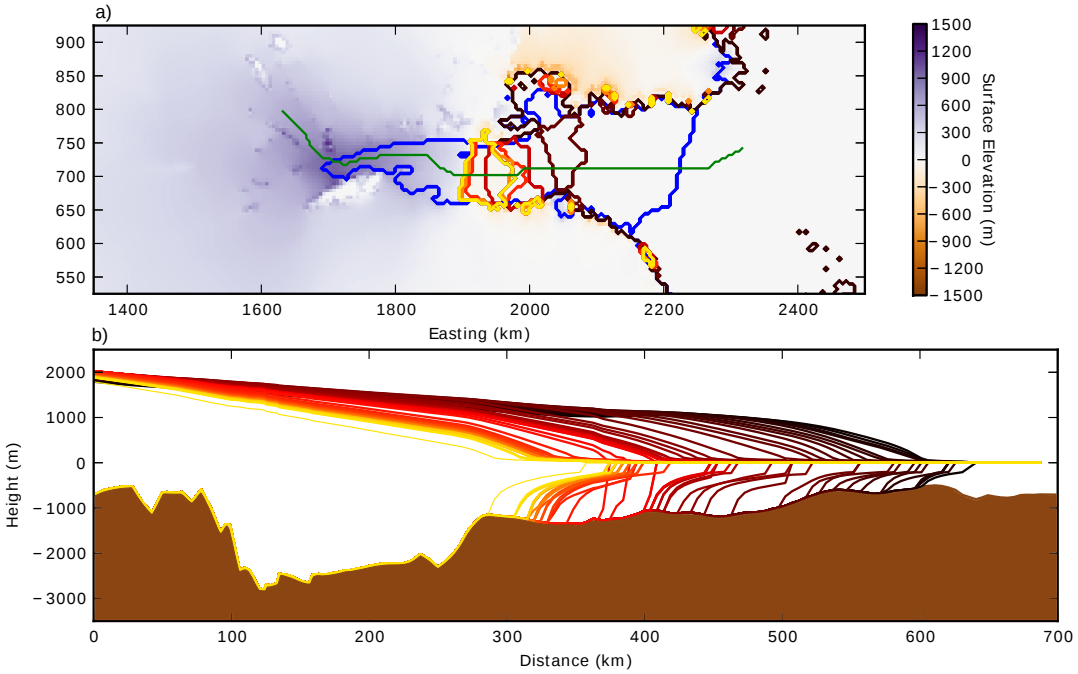

Figure 6.9: a) Surface elevation change for the ADV_3_retreat simulation at 10,000 years relative to the control simulation (Figure 6.1). Grounding lines every 2,000 years are plotted for the ADV_3_retreat simulation. Dark to light colours indicates incremental time slices. Green line indicates transect used in b) cross section of the grounding line position every 200 years. Dark to light colours indicates incremental time slices.

6.5 Discussion

As inferred from the modelling undertaken, the Lambert-Amery glacial system is able to gain mass within a colder climate faster than it loses mass in a warmer climate, as the grounding line was able to advance and lead to ice sheet growth. The warmer climate variations were unable to simulate the retreat of the grounding line, which stabilises the system and minimises the mass loss. The ice sheet responded the quickest to changes in surface mass balance and oceanic driven basal mass balance, while surface temperature changes influenced the flow of the ice sheet the most. These changes in flow occurred over longer time scales than recent interglacial-glacial cycles (*Petit et al.*, 1999).

Changes in sea level led to an instantaneous changes in mass, with the lowering of sea level triggering a partial ice sheet advance. Our sensitivity to sea level change was less than previous models (*Huybrechts*, 2002). The response of the ice sheet to changes in oceanic driven basal melt over short periods has been observed from changes in the bordering ice sheets (*Rott et al.*, 2002; *Scambos et al.*, 2004; *Rignot et al.*, 2008; *Warner and Roberts*, 2013) which supports our findings that the ice sheet has a relatively short response time to oceanic driven basal mass balance compared to surface temperature, sea level change and surface mass balance. This result is also supported by coarse resolution Antarctic modelling studies (*Golledge et al.*, 2012, 2014). Without the presence of warmer oceans, models are unable to generate pulses of meltwater such as meltwater pulse1a(*Golledge et al.*, 2014). The long response time to changes in the surface temperature indicate that it could lead to a lag in the response after climate reversals. A warmer ice sheet would allow for faster flowing ice during the early stages of ice advance during a glacial period, which combined with a decrease in oceanic driven basal melt rates could allow for a faster advance of the grounding line. Conversely, a cold ice sheet would be less sensitive to a retreating grounding line, as the less deformable ice sheet would respond slower to the downstream changes, which would in turn reduce the basal melt which is important in the feedback mechanism which leads to rapid collapse.

A warmer ice sheet would allow for faster flowing ice during the early stages of ice advance during a glacial period, which combined with a decrease in oceanic driven basal melt rates could allow for a faster advance of the grounding line. Conversely, a cold ice sheet would reduce the acceleration of the ice sheet to a retreating grounding line from increase in the oceanic driven melt rate.

The range of forcing conditions investigated were unable to recreate the estimated paleo extent of the Lambert-Amery glacial system at the LGM (*White et al.*, 2011). As the grounding line advances, the velocities of the grounded ice are less than the velocities of the previous ice shelf in the same location. The ice slowly builds up behind the new grounding line, which leads to the slow advance of the grounding line at the stable position, before the bed reverses in slope and it can advance to the next stable location. This is contrary to the indication of a lightly grounded fast flowing ice stream from paleo observations.

The realistic temporal period experiments were able to advance the grounding line

to the continental shelf only by decreasing the calving sensitivity, allowing for the ice shelf to spread into Prydz Bay and become grounded on islands exposed by the falling sea level, which form a new ice dome within Prdyz Bay (Figure 6.9a). As the ice builds up in the new ice dome, and the ice shelf grows in thickness as the surface mass balance exceeds the mass loss from calving and basal melt, the relatively shallow entrance to the Prydz Bay embayment can become completely grounded. This can occur faster than the advance of the grounding line within the Amery Ice Shelf which leads to the formation of an enclosed ocean cavity. This idea will require more research to determine if it is plausible in nature, as it is possible it is an artefact of the choice of modelling parametrisations.

The ADV_3 experiment was unable to accurately match the observed paleo extent of the ice sheet, however, if the grounding line partially advanced in addition to the formation of a smaller enclosed ocean cavity, this would have a very similar profile. The observed surface elevation on the exposed surfaces represents the highest extent of the ice sheet, with other possible configurations erased from the rock surface by ice flow. The advance and subsequent retreat of the ice shelf likely impacted the topography through erosion and the deposition of sediments, so potentially the mechanisms which led to the advance can no longer be reproduced without making assumptions of paleo topography. This is supported by work suggesting that previous levels of glaciation is no longer possible due to the over-deepening of the bed (*Taylor et al.*, 2004).

Another possibility that we could not investigate within these simulations is the formation of large sub-glacial lakes. The transect of the topography shows basins between sills where sub-glacial lakes could theoretically form. This could allow for a fast ice stream to form. There is a great deal of uncertainty over the mechanism which would allow for a lightly grounded fast flowing ice stream. This suggests that the mechanisms which will lead to realistic LGM ice extent within the Lambert-Amery glacial system are either unknown, or unable to be represented within our ice sheet model, with possible implications for other regions.

The simulations had difficulty in forcing the grounding line to retreat from the continental shelf over 10,000 years in the highly glaciated cases to the present day grounding line. It is likely that over longer time periods, the increase in surface temperature would have led to a gradual increase of the surface velocities and subsequent retreat of the ice front, but this process will take many thousands of years longer than the 10,000 years used in the simulation. This suggests that the volume of glaciation we achieved within the simulations is unlike the LGM as compared to the interpreted conditions at the LGM. The other factor which may be reducing the retreat is that the precipitation field is based on current day topography where precipitation is high over the current coastal ocean. As these regions become glaciated, the relatively high surface mass balance is now being deposited onto the ice sheet, helping to sustain them in retreat scenarios. If this surface mass balance was reduced, it is likely that retreat would occur more rapidly. This process should be investigated with a coupled ice sheet

- atmosphere model.

The partial grounding line retreat was shown to occur relatively rapidly when with the entire process occurring over $\approx$ 600 hundred years, however, the fastest period of retreat was 150 km over 200 years. There is support for retreat over these time periods, with the time between the initiation of the retreat from Prydz Bay and it stabilising near Mt. Stinear only being approximately 1000 years (*White et al.*, 2011). The basal melt parametrisation which is dependent on depth potentially enhances this process, but the dynamical effect of enhanced thickness and velocity will also contribute to the rapid retreat. The stabilisation on positive sloping bed topography was also seen during the retreat of the ice sheet. The steep and shallow positive bed slope at the current grounding line position impedes any further retreat of the grounding line.

6.6 Conclusion

The Lambert-Amery glacial system was more sensitive to climate variations which led to the growth of the ice sheet in our simulations, as the grounding line was able to advance rapidly leading to the growth of a thick ice sheet over the continental shelf. This large change contrasts with the climate variations which we would expect to reduce the volume of the ice sheet, which only led to marginal change as the grounding line was unable to retreat over topographic sill it is currently grounded on to the retrograde bed south of the grounding line. The ice sheet responded quickly to changes in oceanic driven basal mass balance and surface mass balance, while changes in surface temperature slowly but continuously modified the ice sheet. As the ice sheet gains mass, it slowly advances along beds which slope negatively towards the continental shelf. Once the grounding line advances off the negatively sloped bed to a positively sloped bed, it rapidly advances until it reaches the next negatively sloping bed where it stabilises.

Our advance experiments did not reproduce the inferred extent of the Lambert-Amery glacial system at the last glacial maximum, with the grounding line either not advancing to the continental shelf, or the ice sheet grew with the advance and we could not simulate a lightly grounded fast flowing ice stream. The entrance to Prydz Bay was shown to be able to grow and become grounded from local ice growth rather than from the advance of the grounding line from the rear of the Amery Ice Shelf, creating an enclosed ocean cavity. Further investigation on the effect that an enclosed ocean cavity would have on the ocean and ice flow could determine if it is a plausible idea.

The retreat of the advanced grounding line is in agreement with the marine instability theory (*Weertman*, 1974; *Schoof*, 2007), with rapid collapse into the deep sections of the embayment. It then stabilised on the bed positively sloping towards ice sheet. This positive sloping sill is what restricts further retreat and hence is likely a significant control on future retreat.

6.7 Concluding Remarks

We show that the Lambert-Amery glacial system is more sensitive to advancing from its current grounding position than retreating, which suggests that as precipitation increases into the future, this region may gain mass. This will be investigated for a 500 year period in the next chapter.

Chapter 7

Future sea level change from Antarctica's Lambert-Amery glacial system

This chapter investigates the possible contribution of the Antarctica's Lambert-Amery glacial system to sea level rise over the next 500 years. This work is in preparation for Geophysical Research Letters.

7.1 Abstract

Future sea level rise (SLR) is highly dependent on the complex response of the Antarctic Ice Sheet to ongoing changes and feedbacks from climate, with accelerating mass losses from ice dynamic changes (*Scambos et al.*, 2004; *Pritchard et al.*, 2012) competing against increasing precipitation (*Krinner et al.*, 2007; *Boening et al.*, 2012; *Frieler et al.*, 2015). The Lambert-Amery glacial system drains a volume of ice greater than that of the West Antarctic Ice Sheet and discharges through the Amery Ice Shelf. Two of the three primary outlet glaciers of the Lambert-Amery glacial system have regions grounded below sea level (*Fretwell et al.*, 2013), which if destabilised, could lead to substantial global SLR (*Schoof*, 2007). The unique geometry of the Amery Ice Shelf may allow the system to maintain its current stability (*King et al.*, 2007; *Shepherd et al.*, 2012; *Pittard et al.*, 2015) and potentially act as a global sea-level sink under likely future climate scenarios. Here we model a suite of future climate scenarios using a regional numerical ice model of the Lambert-Amery glacial system. We show that under a range of temperature increase and extreme scenarios, the grounding line within our simulations was unable to become unstable and retreat into the deep marine basins. Mass gain from increased accumulation exceeded mass loss in our simulations, as even a modest sized ice shelf provided substantial buttressing. This suggests that the Lambert-Amery glacial system region may gain mass and mitigate a portion of the Antarctic contribution to SLR over the next 500 years.

7.2 Introduction

The projected global increase in temperature over the next 500 years varies between 0°C and 10°C, pending CO_2 emissions from anthropogenic sources (*Pachauri et al.*, 2014). The mean global temperature increases from the RCP scenarios in the AR5 for 100 and 500 years (in brackets) are RCP2.6 (1.0° C, 0.5° C), RCP4.5 (1.8° C, 2.5° C), RCP6.0 (2.2° C, 3.5° C) and RCP8.5 (3.7° C, 7.5° C) (*Pachauri et al.*, 2014). The expected response to the Antarctic Ice Sheet under these warming scenarios is uncertain, with the range of maximum sea level contribution estimates varying between 3 m (*Golledge et al.*, 2015) to 10 m (*DeConto and Pollard*, 2016) until 2300, and over 15 m SLR-equivalent by 2500 (*DeConto and Pollard*, 2016).

Whole Antarctic Ice Sheet simulations have the disadvantage of using coarser horizontal resolution than regional models, in addition to Antarctic wide parametrisations not necessarily being appropriate for all regions. Simulations of the present extent of the Antarctic Ice Sheet have poorly represented the Lambert-Amery glacial system with an unrealistically advanced grounding line (*Martin et al.*, 2011; *Golledge et al.*, 2012; *Winkelmann et al.*, 2012). Recent studies using a revised parametrisation of ice flow yielded a realistic grounding line (*Golledge et al.*, 2015; *Pittard et al.*, 2016a), however, the region has a number of ice streams which flow through narrow constriction points which will remain unresolved in low resolution whole Antarctic Ice Sheet simulations.

The Lambert-Amery glacial system's three major tributaries, the Lambert, Mellor and Fisher Glaciers, all flow between nunataks with widths as narrow as 30 km, before converging into the rear of the Amery Ice Shelf. The Amery Ice Shelf occupies a long and relatively thin embayment, which after the initial flotation narrows over the first $\approx$ 60 km to a width of $\approx$ 35 km, leading to a minimum in surface velocity on the ice shelf (Minimum Ice Shelf Width (MISW), Figure 7.1a). In addition to the MISW, there are a number of major pinning points and regions of re-grounding within the Amery Ice Shelf, such as Clemence Massif and the Budd Rumples (Figure 7.1b). These features are likely important to the flow of the Amery Ice Shelf (*Favier et al.*, 2012) and are not properly resolved in models with horizontal resolution coarser than 10 km.

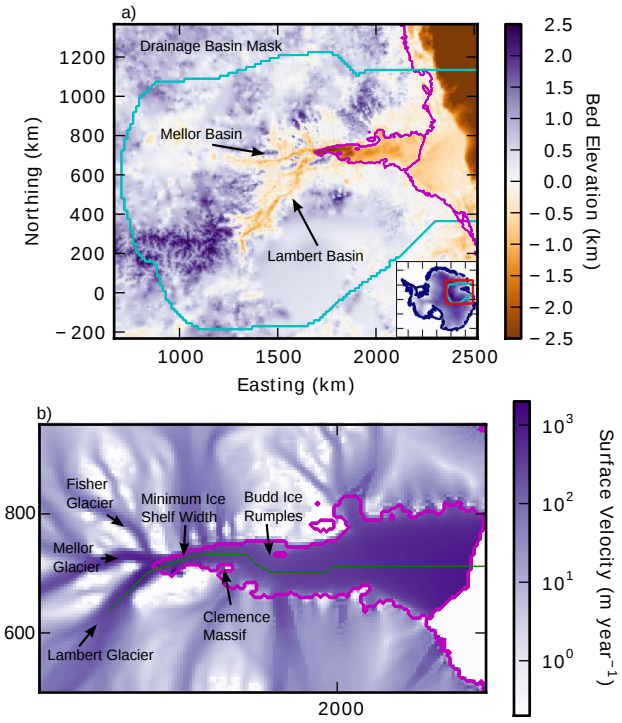

Figure 7.1: Locality map showing the topography used (See Appendix D) in the regional model of the Lambert-Amery glacial system. The full model domain is shown with red outline in the inset, the cyan line shows the drainage basin mask. b) Control surface velocities (*Pittard et al.*, 2016a) and main contributory glaciers and relevant features. Magenta line indicates the ocean and ice shelf boundaries, green line is the location of transect featured in Figure 7.2b.

7.3 Regional Model

Using the Parallel Ice Sheet Model (PISM)(*Bueler and Brown*, 2009; *Winkelmann et al.*, 2011; *Aschwanden et al.*, 2012), a regional domain of the Lambert-Amery glacial system is simulated (*Pittard et al.*, 2016a). PISM utilises a hybrid shallow shelf and shallow ice approximation physical model. The model domain and drainage basin mask is shown in Figure 7.1. Outside of the drainage basin mask, the surface thickness is held constant by adjusting the surface mass balance to maintain the thickness at the initial condition. The topography is given by a modified bedmap2 dataset (see *Pittard et al.* (2016a)). The modifications were required as a portion of the ice shelf adjacent to the southernmost grounding line had an ocean depth beneath the ice shelf of less than 2 m. This was caused by seismic data points being included in bedmap2 dataset, which were recorded during the period where this section of the Amery Ice Shelf was believed to be grounded. It is suspected that the ice draft was recorded as the first return was expected to be bedrock. The initial thickness was given by bedmap2 (*Fretwell et al.*, 2013), the geothermal heat flux by a dataset generated by using the *Fox Maule et al.* (2005) methodology on the M7 magnetic data field and the surface mass balance and surface temperatures are the average fields of 1979-2013 from RACMO2.3 ANT27/2 (*van Wessem et al.*, 2014). The ocean parametrisation adds a scalar to the PISM-PIK melt (*Winkelmann et al.*, 2011) which leads to a steeper melt profile with higher melt at the grounding line and lower melt towards the calving front than the original parametrisation. This scalar was guided by a modelling study of the Amery Ice Shelf cavity (*Galton-Fenzi et al.*, 2012) (see Appendix D). The horizontal resolution is 5 km and the vertical resolution 15 m in the control model and all simulations.

The model was initialised by optimising the model solution for four physical parameters (ssa_e, sia_e, topg_to_phi, pseudo_plastic_q) and two calving parameters (eigen _calving _k, minimum _calving _threshold) by iteratively varying each parameter, and minimising the misfit (by manually comparing mean and RMS error for a range of surface elevation bands) to observations (*Pittard et al.*, 2016a) (see Appendix D for full table of parameters).

7.4 Experimental design

We use a range of temperature increases (incorporating high latitude intensification compared to the global mean, see below) that spans the possible future scenarios from the RCP experiments (*Pachauri et al.*, 2014) (+2°C, +4°C, +8°C), to test the sensitivity of the Lambert-Amery glacial system to future climate change. We apply the expected regional changes reflective of the global temperature variations to surface temperature (stemp), surface mass balance (smb) and melting at the underside of ice shelves (bmelt). We design a scenario for each temperature increase with a lower chance of substantial SLR, by implementing high smb and low bmelt (lower), a scenario with a balanced chance of substantial SLR (middle) with average smb and average bmelt,

and a scenario with a high chance of substantial SLR (upper) with a low smb and high bmelt. All changes are applied as a step change at the beginning of the simulation, as the variations in bmelt were restricted to step changes, as time varying bmelt fields would not track the grounding line position. The consequence of the step change is our scenarios will likely over-estimate sea level change, as the higher rates are applied for longer. In this context, this means our results will likely be inaccurate over the first 100 years of our simulation, but provide useful bounds over 500 years.

The increase in stemp applied to the control solution is twice the global temperature change in each scenario. This was chosen as the regional temperature increase in *Pachauri et al.* (2014) is approximately twice the global average within the Lambert-Amery glacial system (see figure 2.2a in *Pachauri et al.* (2014)). The surface temperature increase is held constant between the lower, middle and upper scenario for each experiment.

The increase in smb which are applied are 10%, 7.5% and 5% for the lower, middle and upper scenarios respectively. The upper scenario is guided by modelling which suggests the Lambert-Amery glacial system experiences 30-50% increase in precipitation until 2100 under the RCP8.5 scenario (see figure 2.2b in *Pachauri et al.* (2014)), which corresponds with a mean temperature increase of 3.7°C. The lower scenario is given by the Antarctic zonal average of 5% (*Pachauri et al.*, 2014; *Golledge et al.*, 2015), with the middle scenario of 7.5% approximating the Clausius-–Clapeyron relation (*O'Gorman and Muller*, 2010) and falls between the other two scenarios.

The ocean melt parametrisation is varied for the middle scenario guided by a sensitivity study of an ice shelf cavity model oceanic model of the AIS *Galton-Fenzi* (2009) and is given by equation 7.1.

$$bmelt = 0.1012x^2 + 0.0406x + 0.9939 \tag{7.1}$$

Where x = increase global surface temperatures.

In the lower scenario the bmelt is varied by 66.7% and the upper scenario by 133.4% of the calculated change in bmelt from equation 7.1. With no information to guide this change, we match the proportional change in surface mass balance. This equation was used to calculate the overall change in melt, however, due to the nature of the thickness dependence, and expected melt regimes the increase in basal melt was applied in two different ways. Half of the calculated increase was applied as an additional scalar to the melt equations, and the other half was applied as an ice shelf wide increase in melting. The first represents an increase in melt near the grounding line, while the second represents an overall increase in the energy within the cavity causing ice shelf wide increases in melt.

We additionally test two extreme scenarios using the +4°C case by applying an enhanced melt at the grounding line (extreme_1) and melt rate of 100 m year^{-1} to the entire ice shelf (extreme_2). We simulate each scenario for 500 years with 5 km

horizontal resolution and 15 m vertical resolution as a perturbation to the control. The full scenarios are outlined in Table 7.1.

Table 7.1: List of experiments and their climate forcing parameters.

Scenario	stemp increase	smb increase	bmelt increase
+2°C middle	+4°C	115%	148%
+2°C upper	+4°C	110%	164%
+2°C lower	+4°C	120%	132%
+4°C middle	+8°C	130%	276%
+4°C upper	+8°C	120%	335%
+4°C lower	+8°C	140%	217%
+8°C middle	+16°C	160%	772%
+8°C upper	+16°C	140%	996%
+8°C lower	+16°C	180%	548%
extreme_1	+8°C	130%	Enhanced GL melt
extreme_2	+8°C	130%	+100 m year^{-1}

7.5 Results

The simulated climate scenarios all yielded a decrease in sea level over the 500 year period (Figure 7.2a), with a change of -15.1 (+2°C), -24.5 (+4°C) and -38.3 (+8°C) mm SLR-equivalent. The upper scenario simulations estimated near zero change, with a -6.7 (+2°C), -8.3 (+4°C) and -3.8 (+8°C) mm SLR-equivalent change over the 500 years, although the +8°C upper scenario had risen from -7.2 mm SLR-equivalent at 200 years, indicating it was losing mass at the end of the simulation. The lower scenario simulated estimated mass gain of -24.4 (+2°C), -43.7 (+4°C) and -74.7 (+8°C) mm SLR-equivalent, indicating that increased snowfall drives the changes in relative SLR. The extreme scenarios led to sea level change of 18.50 (extreme_1) and 45.30 (extreme_2) mm SLR-equivalent. The majority of the change occurred within the first 200 years, with 64% and 70% of the change respectively, with the rate of mass loss slowing with time.

The mass gain occurs near the ice divides and mass loss near the grounding line (Figure 7.3), creating a steeper surface gradient. The extreme_2 scenario has lost substantially more ice, particularly in the Lambert Glacier basin. There is also retreat of the grounding line along the edges of the Amery Ice Shelf. These changes are also seen in the 8°C and extreme_1 scenario (not shown).

The thinning, retreat and removal of the ice shelf causes acceleration in the glacial flow of the primary tributary glaciers, with grounded surface velocities 80 km upstream of the initial grounding line increasing. The maximum velocity increases in the simulations were 106%, 46% and 49% for the extreme_2 scenario within the Fisher, Lambert and Mellor Glaciers respectively after 50 years of simulation, with the increase slowing over the simulation to 69%, 25% and 29% respectively for each glacier. The increases in surface velocity with a remaining ice shelf in the +8°C middle estimate scenario

were 34%, 15% and 10% for the Fisher, Lambert and Mellor glaciers after 50 years, increasing in velocity to 35%, 23% and 17% over the full simulation.

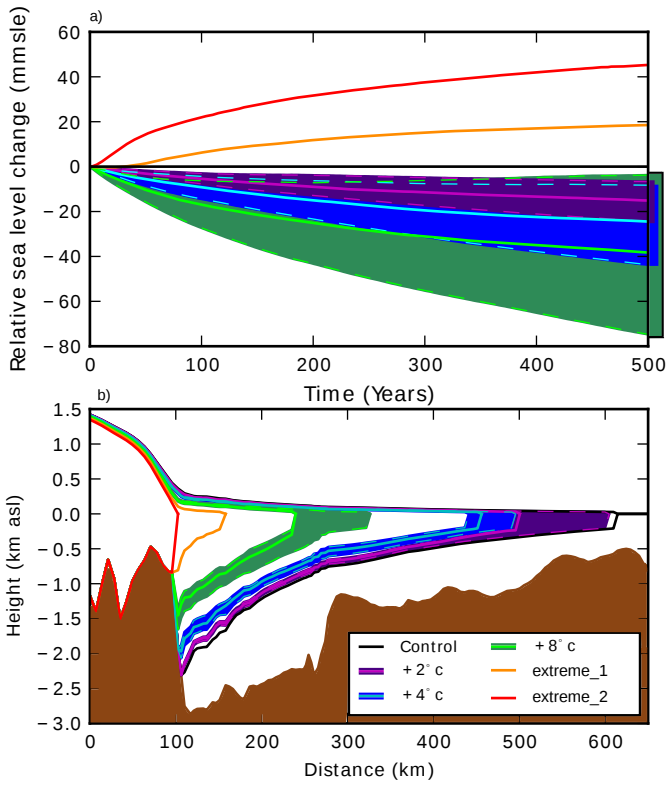

Figure 7.2: a) Relative global mean sea level change with respect to the control solution out to 500 years. Darker shaded regions shows extent of the lower and upper scenario, with full extent shown in box on right hand side of the figure. b) Cross section along the Lambert Glacier and AmIS following the transect shown in green, Figure 7.1b.

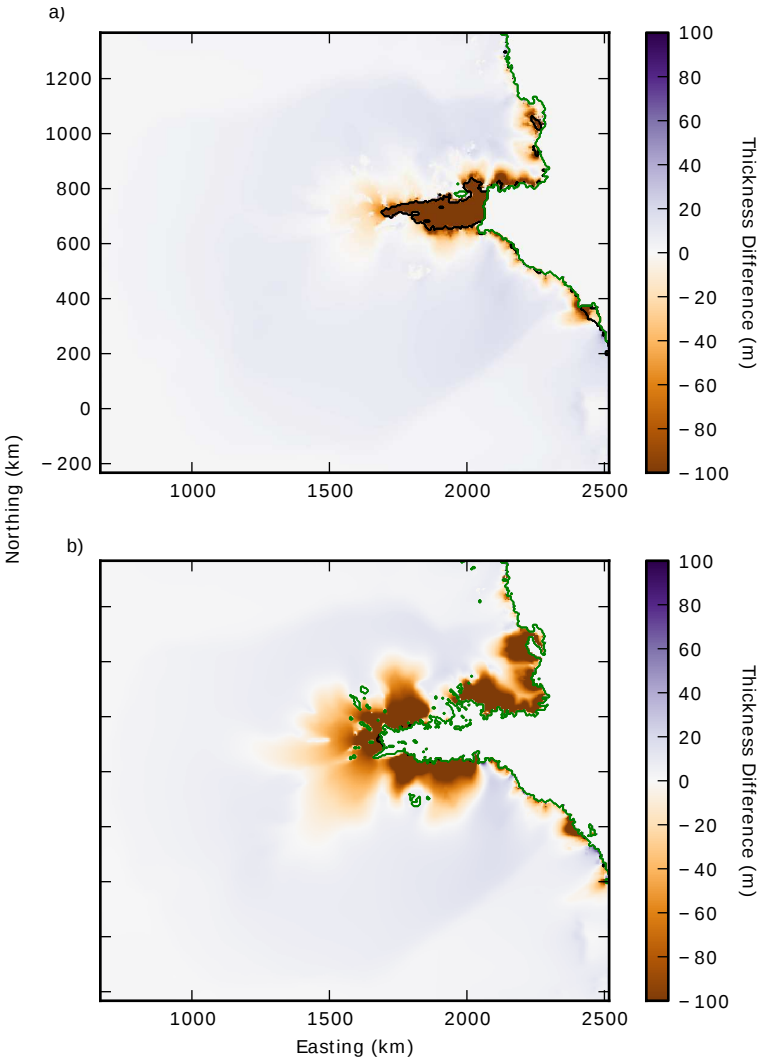

Figure 7.3: a) Surface elevation change compared to the control solution for a) middle °C scenario and b) extreme_2. Grounding line is shown and black and the coastal line in green.

7.6 Discussion

These results show greater variability than a previous regional study (*Gong et al.*, 2014), which found a range of -15 and 11 mm SLR-equivalent over a simulation spanning 1980-2200, which compares to our 200 year range of -43 and +32 mm SLR-equivalent. It is difficult to directly compare the loss from our regional model to that of whole Antarctic models as they do not provide a basin by basin report of the increases. In both *Golledge et al.* (2015) and *DeConto and Pollard* (2016) the grounding line appears to be further retreated than in both *Gong et al.* (2014) and our simulations. Our results contrast with *Winkelmann et al.* (2012) who found increased velocities reduced the mass gain from increased precipitation, however, the study used a shallow ice enhancement factor (sia_e) of 4.5 compared to the lower values of 1.5 (*Golledge et al.*, 2015) and 1.8 (*Pittard et al.*, 2016a) found when the model is initialised through optimisation. This will affect the flow rates at high elevations, which may suggest the through-flow is sensitive to the rate of deformation within the shallow ice approximation portion of the flow.

The topography changes we apply to the bedmap2 dataset may change the response of the ice sheet significantly in this region which must also be considered. The regional study of *Gong et al.* (2014) uses ALBMAP (*Le Brocq et al.*, 2010), which uses similar topography beneath the Amery Ice Shelf but will not have the significant marine basins identified in bedmap2. Both *Golledge et al.* (2015) and *DeConto and Pollard* (2016) use bedmap2, which include the unrealistically shallow topography immediately adjacent to the grounding line. This will have a significant impact on their ability to realistically model the Lambert-Amery glacial system.

The simulation of *Gong et al.* (2014) utilises an adaptive mesh, which maintains a fine resolution ($<$ 500m) at the grounding line. The finer the resolution at the grounding line, the more accurately the model responds to grounding line migration (*Schoof*, 2007; *Pattyn et al.*, 2012). The differences between the high resolution regional models and the low resolution whole Antarctic models could be a cause for concern. Both regional models agreed in that the grounding line of the Amery Ice Shelf was unable to retreat into the retrograde beds, which contrasted with the whole Antarctic models. This could be directly linked to smoothing of the topography in the coarser resolution models, which could reduce the maximum height of the sill, and therefore maintain a higher mass flux across a deeper grounding line.

The projected mitigation of SLR in the scenarios is caused as the increase in mass gain at high elevations is greater than the mass loss near the grounding line. A significant factor in the mass loss not being greater is that the grounding line was unable to retreat over the shallow sill into regions grounded below sea level (Figure 7.2b). The increase in oceanic melt, even under the extreme scenarios, causes the retreat of the calving front, but leads to very little change in the southernmost grounding line location (Figure 7.2b).

The ice shelf thins significantly and the calving front location retreats with increasing temperature, with the +8°C middle estimate and upper scenario showing the

calving front of the Amery Ice Shelf significantly retreated by ≈ 400 km into the embayment, however, it is still situated north of the MISW and Clemence Massif (Figure 7.1b). These features maintain the present day velocity profile, specifically that the ice shelf flow decreases as it approaches the MISW, with the flow at the rear of the ice shelf in our control simulation over 1000 m year^{-1}, which slows to 750 m year^{-1} before increasing again to 1100 m year^{-1} at the calving front. The observed minimum velocity on the ice shelf could be as low as 300 m year^{-1}, with our model simulations underestimating this effect (*Pittard et al.*, 2013).

This horizontal compression occurring in the region between the grounding line and the MISW can been seen in the profile of the ice shelf (Figure 7.2b), with a slight depression that is present in the draft of the ice shelf just before 300 km along the transect. The ice shelf likely remains thicker between this feature and the grounding line relative to other ice shelves due to a reduction in velocity from the buttressing at the MISW. This result is supported by a previous study which found that significant buttressing exists within the Amery Ice Shelf until the calving front retreats past Clemence Massif (*Gong et al.*, 2014).

The extreme scenarios led to the increase in sea level, with the ice shelf retreating past the MISW and Clemence Massif in both cases, with the complete collapse of the ice shelf in the extreme_2 scenario. The average melt rate in the +8°C upper scenario was 5.4 m year^{-1}, the extreme_1 was 10.4 m year^{-1} and extreme_2 was 100.2 m year^{-1}. While the average melt rates within the temperature scenarios are lower than some of the coastal ice shelves in the Amundsen Sea sector (*Rignot et al.*, 2014), it is higher than the modelled increases in oceanic basal melt on the Filcher-Ronne Ice shelf (*Hellmer et al.*, 2012), with the Filchner Ice Shelf the most similar to the Amery Ice Shelf of the large ice shelves in that it is bounded on one side by the Berkner Island and on the other by the coastline. However, given the partial and complete collapse in the two extreme scenarios, increasing the melt rate further will not yield different results. The difference in sea level change between the middle +4°C and the Extreme_2 (which used the +4°C surface temperature and surface mass balance) highlights the importance the last ≈ 100 km of ice shelf to buttressing the upstream ice flow.

For substantial mass loss to occur within our simulations, the grounding line would have to retreat over the sill where it is presently grounded. This would require the velocity at the grounding line to have increased sufficiently to ensure the net mass lost over the grounding line does not decrease as the ice shelf thins as it moves up the positive bed slope. The depth and shape of this sill is therefore fundamentally important to the stability of the region. The modifications to bedmap2 (*Pittard et al.*, 2016b) includes a 5 km region of interpolation between the two datasets, which will be just north of the observed grounding line. Further observations of the topography, and in particular the height of the sill and the current depth of the ice at the grounding line are important to improved modelling studies of this region.

The PISM ice sheet model does not include the ice cliff failure and hydrofracture

mechanisms (*Pollard et al.*, 2015) which have been modelled to lead to further retreat (*DeConto and Pollard*, 2016). There is evidence to suggest tidewater glaciers may have existed within this region in the past (*McKelvey et al.*, 2001), with marine sediments found at Fisher Massif, near the Budd Ice Rumples (Figure 7.1). However, these ice cliffs were also likely located at a grounding line located further north than the MISW position, with the current grounding line a consequence of substantial erosion through the glacial-interglacial cycles (*Taylor et al.*, 2004).

The hydrofracture mechanism depends on the divergence of the ice shelf to grow crevasses and surface melting to occur (*Pollard et al.*, 2015). The Amery Ice Shelf should be resistant to hydrofracture, as the region between the grounding line and the MISW region is compressed, which would act to close, rather than continue to open any crevasses. This is supported by velocity measurements which track surface features (*Pittard et al.*, 2013), as the algorithm breaks down following this point, suggesting the crevasses which were previously being tracked are changing sufficiently to not be visually identified across two images a year apart. Additionally, the hydrofracture mechanism has been observed on relatively thin ice shelves ($\approx$ 200 m ice thickness (*Scambos et al.*, 2000)), while the Amery Ice Shelf maintains a thickness of over 600 m even under the +8°C scenario for the region approaching the MISW. Even if the ice shelf does disintegrate, the region may resist the ice cliff failure mechanism as the bed topography is shallower than the 800 m depth expected to stabilise the position of the grounding line undergoing ice cliff failure, although this is dependent on the ice thickness at the grounding line (*Pollard et al.*, 2015).

The parametrisation of the hydrofracture and ice cliff failure mechanisms which led to over 15 m SLR-equivalent over the next 500 years from the Antarctic Ice Sheet (*DeConto and Pollard*, 2016) does not account for the effect of ice mélanges (*Pollard et al.*, 2015). It has been found that the ice melange in front of the Jakobshavn glacier, one of the fastest flowing glaciers in the world, slows down considerably in winter when the ice mélange is at its strongest (*Amundson et al.*, 2010). This mechanism is important to understanding the response of the ice sheet to the ice cliff failure mechanism, particularly within narrow embayments with shallow bedrock as ice bergs may ground along the coastline or on shallow regions, leading to the possibility of a strong ice melange forming and filling the embayment.

The long narrow embayment of the Amery Ice Shelf will likely aid the development of an ice melange, particularly as any significant collapse of the ice shelf will likely generate icebergs that will have an ice draft deeper than the bed topography at the entrance of the embayment. The entrapment of icebergs within the embayment will lead to the physical blockage of the ocean circulation and melt water input which will have a large effect on the local circulation (e.g. *Mayet et al.*, 2013). Additionally, the change from an ice-atmosphere to ocean-atmosphere interface could lead to significant changes in the atmospheric circulation. The effect these changes would have on the system is uncertain, but likely to be different from the current configuration (e.g. *Mayet et al.*,

2013). Further research is needed to investigate the response of large ice shelves to rapid collapse via hydrofracture and potential ice cliff failure.

7.7 Conclusion

The grounding line was unable to retreat from the topographic sill it is presently grounded upon in our simulations, which limits the possible mass loss from the Lambert-Amery glacial system into the future. The ice flow was unable to accelerate sufficiently for a net increase in mass flux to cause the grounding line to retreat. Even the complete, but unlikely removal of the ice shelf was unable to force the grounding line to retreat over the sill the grounding line is presently grounded on. The extreme scenarios yielded 45.3 mm SLR-equivalent from the Lambert-Amery glacial system over 500 years. Under all temperature increase scenarios, a modest sized ice shelf remained, contributing significant buttressing to the three main tributary glaciers. The stability of the grounding line combined with the buttressing of the ice shelf limited the dynamic response of the Lambert-Amery glacial system, leading to a net mass gain due to elevated surface mass balance. We found that the Lambert-Amery glacial system region will be a sink with a likely range between approximately 0 - 75 mm of sea level over the next 500 years. It is important to improve our knowledge of the bed topography near, and behind the grounding line, as any significant differences in the height of the sill could influence the stability of the Lambert-Amery glacial system, and its possible future contribution to sea level change.

7.8 Acknowledgements

This work was supported by the Australian Government's Cooperative Research Centres programme through the Antarctic Climate & Ecosystems Cooperative Research Centre (ACE CRC). This research was supported under Australian Research Council's Special Research Initiative for Antarctic Gateway Partnership (Project ID SR140300001). This research was undertaken with the assistance of resources under projects m68 and gh8 from the National Computational Infrastructure (NCI), which is supported by the Australian Government. Development of PISM is supported by NASA grants NNX13AM16G and NNX13AK27G.

7.9 Supplementary Information

See Appendix D for the supplementary information for this chapter.

7.10 Concluding Remarks

The buttressing from even a small ice shelf allows for mass gain to be greater than ice lost in our simulations. If this is true in nature then the Lambert-Amery glacial system

may gain mass into the future and partially mitigate the predicted overall positive contribution from Antarctica.

Chapter 8

Conclusions and future directions

8.1 Main Findings

Observations utilising surface feature tracking on visible spectrum imagery show that the surface velocity of the Lambert-Amery glacial system has remained unchanged between 2004 and 2012. This is supported by studies using gravimetry and radar altimetry which suggest only a slight mass gain in the interior of the glacial system. Assuming the glacial system is at, or near to steady state, allows for a regional model of the Lambert-Amery glacial system to be initialised by minimising the misfit between observations and the simulation within the numerical ice sheet model, PISM. As part of the creation of the regional domain, the importance of a primary boundary condition, geothermal heat flux, is investigated. The choice of geothermal dataset is important for the creation of an ice sheet domain, as it affects the surface velocities at high elevations and leads to relative differences in final surface elevation. Estimates of geothermal heat flux based on observations within Prydz Bay show localised high heat flux regions generated from elevated radiogenic crustal heat production. Guided by these realistic estimates, high heat flux regions are inserted into the background field to test the effect on a set of different flow regimes. It is shown that regions of slow sheet flow would change into regions of stream-like flow with the presence of a high heat flux region, which suggests local variations of geothermal heat flux may play a key role in the organisation of the ice sheet over long periods of time.

Using the regional domain, the sensitivity of the Lambert-Amery glacial system to climatic variations over glacial cycles is investigated. The system responds fastest to changes in surface mass balance and oceanic driven basal melt rates, while surface temperature has the slowest, but long term largest response. The system is more sensitive to a growing ice sheet than a shrinking ice sheet, as the increase in mass leads to the grounding line advancing. As the grounding line advances, it stabilises on beds which become deeper the further it advances, and advances rapidly along beds which become shallower as it advances. The ice sheet then thickens behind the new grounding line, building up slowly before rapidly advancing again. Conversely, when the ice sheet loses mass, the grounding line is unable to retreat up the bed slope where it is presently

grounded, which limits the overall mass loss. Simulations were unable to recreate the advance mechanisms which generate a similar ice sheet to the interpreted advance at the last glacial maximum. This suggests mechanisms which are not fully understood may play a role in the advance of the ice sheet.

The retreat of the grounding line was restricted by the shallow sill where it is presently situated. During both the longer glacial cycle length simulations and the short extreme future scenario simulations, the grounding line did not retreat into the deep marine basins. This led to the Lambert-Amery glacial system gaining mass under a range of future climate scenarios over a 500 year period. If this stability is true in nature, than the Lambert-Amery glacial system will likely be a sink for sea level rise over the next 500 years.

Each of the thesis objectives outlined in Chapter 1 have been achieved, as summarised:

Objective 1

- The current surface velocity, strain rates and vorticity have been calculated for the Amery Ice shelf and its tributary glaciers. The three main glaciers converge at the rear of the Amery Ice Shelf, with the floating ice experiencing compression upon floating. This is likely to be caused by the width of the embayment narrowing before widening, leading to the compression of the ice and buttressing of the glaciers.

- The surface velocities at the rear of the Amery Ice Shelf and its three main tributary glaciers, the Lambert, Mellor and Fisher glaciers have been stable for the period 2004-2012.

Objective 2

- Using the Parallel Ice Sheet Model, a regional model of the Lambert-Amery glacial system was designed.

- The stability of the Lambert-Amery glacial system allows for a numerical ice sheet model to be initialised by minimising the misfit between the simulation and observations of surface velocity and ice thickness.

- The presence of a high heat flow region can change the flow behaviour in regions of slow sheet flow to stream-like flow, while making no significant difference to regions of fast flow. This mechanism may contribute to the long term organisation of ice flow.

- Differences in both magnitude and spatial distribution of geothermal heat flux cause changes in regions of slow surface velocities which led to relative surface elevation differences between simulations.

Objective 3

- The Lambert-Amery glacial system was more responsive to climate variability that lead to the growth of the ice sheet, as the grounding line was able to advance allowing for the ice sheet to gain significant amount of mass. This contrasts with the inability of the grounding line to retreat, which subsequently restricted the amount of mass loss possible.

- The mechanisms which led to the Lambert-Amery glacial system advancing differed from the expected mechanisms at the last glacial maximum. As the grounding line advanced, a thick ice sheet grew rather than a shallowly grounded ice stream. This could possibly be due to the lightly grounded ice stream having either sub-glacial lakes or an enclosed ice shelf cavity beneath. Lack of knowledge of paleo ice density and bed topography limits our ability to say with certainty if this region was grounded or not. The retreat of the ice sheet was not possible from the simulations where the grounding line and the ice sheet had advanced all the way to the continental shelf, supporting the idea that mechanisms that were not incorporated into the model were important in the advance of the ice sheet at the last glacial maximum. The retreat of the partially advanced grounding line to the present day position occurred over a period of 600 years, showing the susceptibility of regions to rapid collapse when the grounding line is retreating over a negatively sloping bed.

- The grounding line of the Lambert-Amery glacial system is unable to retreat over the bed topography where its currently grounded, limiting mass loss from this region.

- Under a range of plausible future scenarios covering the range of temperatures estimated from RCP2.6 through to RCP8.5, the Lambert-Amery glacial system grew in mass, with a range of to -3.8 to -74.7 mm sea level rise equivalent over the next 500 years.

8.2 Future directions

Objective 1

The feature tracking software was performed on Landsat 7 images which were processed Level 1Gt using the Ramp v2 DEM. The results may be improved if the raw data is re-processed with an improved digital elevation model and new ground control points corresponding with Global Positioning System deployments. In addition, Landsat 8 has been operating since late 2013 and ongoing monitoring of the region could be conducted using the same strategy as developed for Landsat 7.

The relative differences we found between MEaSUREs, RAMP-MAMM, GPS and VAIS velocity fields suggest there are discrepancies between the datasets. The surface velocity fields are an important tool in both initialising and evaluating ice sheet models, and a concerted effort to evaluate and compare velocity datasets across the Antarctica and Greenland Ice Sheets is important for the accuracy of ice sheet modelling. An example is the VAIS dataset had relatively faster flow through the centre of the glaciers and slower flow towards the edges than MEaSUREs.

Objective 2

The ice sheet model, PISM, and the regional domain used within this model have a number of limitations which are primarily driven by a lack of observations that drive boundary and forcing conditions. The bed topography still has vast regions of unobserved areas within the Lambert-Amery glacial system and when combined with uncertainty in the current dataset, reality could differ greatly from the current estimates. Further observations of bed topography, particularly in regions where there are no data points, significant uncertainty, or important to the flow dynamics will improve the ability of the model to simulate the Lambert-Amery glacial system.

Another source of uncertainty in most shallow ice sheet models is the implementation of enhancement factors. The shallow ice enhancement factor used throughout our simulations is below what is understood to be realistic for the enhancement due to anisotropy in the Antarctic Ice Sheet (*Treverrow et al.*, 2012; *Budd et al.*, 2013), with physical values expected to range between 3 and 8. Our value of 1.8 through the optimisation to observations suggests that PISM ice flow was unrealistically fast, with a possible explanation that the parametrisation of bed roughness was limited by the quality of the data input. This could be due to the smoothness of the bed created from interpolation between data observations. This suggests that our optimised value of 1.8 is also accounting for increased basal drag from bed roughness. Increasing the bed roughness will lead to more realistic enhancement factors, however, this should not be done arbitrarily. An increase could be implemented by taking the average bed roughness from the regions with highest resolution topography, and applying this to regions with low resolution topography. An alternative method could be to vary the topography by a small factor to introduce bed roughness to the domain. Additionally, enhancement factors vary both horizontally and vertically in the ice sheet, and implementing an enhancement factor which varies across the domain could improve the ability to match observations.

There was evidence that smaller glaciers may be more sensitive to localised elevated geothermal heat flux, however, given that glacier's width it is possible it was influenced by our horizontal resolution. Further research on relatively small outlet glaciers with

higher horizontal resolution should be conducted, with a focus on identifying if there is a connection between the thickness of the ice and/or the width of the glacier to the importance of basal heat flux on the flow.

There is the potential for using the modelling of ice flow to identify regions of both relatively low and high geothermal heat flux. An inverse model which is constrained by surface velocities, combined with a thermodynamic model could potentially identify regions of "sticky" or "slippery" bed which may represent anomalous geothermal heat flux rather than actual difference in the frictional properties at the bed. The difficulty with this method is ensuring that all other possible causes for the discrepancies are accounted for. For example, errors in bed depths, strength of the underlying till, and the presence of liquid water at the base of the ice could all lead to similar expression within an inverse ice sheet model.

Objective 3

The numerical simulations investigating change over glacial cycles is limited by our present day initialisation, with the boundary and initial conditions of the regional model controlled by a present day Antarctic simulation. As the ice sheet advances to the continental shelf, the boundary conditions near the coast in particular, would be incorrect. This will likely lead to flow of ice out of the main domain as it thickened more than the prescribed ice thickness at the boundaries. This could contribute to the inability of our simulations to recreate the profile at the last glacial maximum. In addition, the spatial pattern of precipitation used is the present day distribution. As the ice sheet advances, it is likely that the regions of currently high precipitation at the coastlines would shift north, which could potentially change the response of the ice shelf. Improved simulations of the ice sheet at the last glacial maximum should use updated boundary conditions and a coupled atmospheric and ocean model. It is also likely that erosion during the advance and retreat of the ice sheet has led to changes in the bed topography which may play an important role in understanding the mechanisms which lead to the advance of the ice sheet over glacial cycles. Estimates of erosion rates should be used to estimate the bed topography at the LGM, and the importance of error in both topography and the calculated erosion rates to modelling the extent of the ice sheet at LGM should be considered through a sensitivity analysis.

The topography at, and adjacent to, the current grounding line of the Amery Ice Shelf is still relatively unknown. Due to bedmap2 using two data-points at the rear of the Amery Ice Shelf which have bed topography shallower than the estimated ice draft, the topography beneath the ice shelf was replaced by RTOPO using *Galton-Fenzi et al.* (2008) by merging the two datasets. If the topography is significantly different to our current estimates, then this could affect the simulations of the Lambert-Amery glacial

system contribution to sea level rise. A range of experiments testing the sensitivity of the system to different topography should be conducted, and, if found to be important, further constraints on the topography will be required.

The numerical model of the Lambert-Amery glacial system utilises an average surface mass balance and surface temperature field from RACMO2.3 which was not varied throughout model runs. The precipitation patterns are likely to vary through time, particularly in a warming climate. However, without a fully coupled high resolution global climate model that includes ice sheets, any attempt to implement a variable precipitation scheme is unlikely to yield results that significantly improve the results of our simulations. This is also due to a large range of uncertainties in the response to polynyas, sea ice production and the local effects of icebergs if mass calving events occur. The ocean temperatures within the embayment may change, particularly if ocean and atmospheric circulation patterns vary significantly. The ice is thicker at the rear of the ice shelf than the depth of the ocean at the entrance to the embayment, which could lead to the entrapment and re-grounding of icebergs which would impact ocean and atmospheric circulation, and possibly re-stabilise the ice shelf. A coupled ocean-atmosphere-sea ice model should investigate the response of local circulation to the collapse of the Amery Ice Shelf to help guide future scenarios.

8.3 Final Conclusions and Implications

The Lambert-Amery glacial system is currently showing no signs of acceleration in ice flow upstream of the grounding line, indicating that the ice shelf is stable and not experiencing rapid melting seen throughout other regions of Antarctica. The region of ice shelf between the grounding line and the narrowest point of the embayment provides a significant proportion of the buttressing, allowing for large portions of the ice shelf to disappear without substantial change in in the grounded flow. With increased precipitation present in the region from increased global temperatures, the Lambert-Amery glacial system was found within our simulations to gain mass and mitigate a proportion of the predicted overall positive contribution to sea level rise from Antarctica.

Appendices

Appendix A: Supplementary Information Chapter 3

The following information provides a list of the dates and images used in the study (Table S3.1)) and the velocity and error fields calculated for each set of image pairs (Figures S3.1-S3.7). All image backdrops are based on the 2004 Landsat 7 Image.

Table S3.1: Landsat 7 images names and acquisition time used in the study.

Date	File Name	Time (days)	Cloud %
02/01/2004	LE71271122004032ASN01	N/A	2%
02/19/2005	LE71271122005050PFS00	384	4%
02/22/2006	LE71271122006053PFS00	368	0%
02/09/2007	LE71271122007040SGS00	352	4%
02/12/2008	LE71271122008043SGS01	368	3%
02/14/2009	LE71271122009045SGS00	368	28%
02/01/2010	LE71271122010032SGS00	352	45%
02/20/2011	LE71271122011051PFS00	384	3%
02/23/2012	LE71271122012054PFS00	368	19%

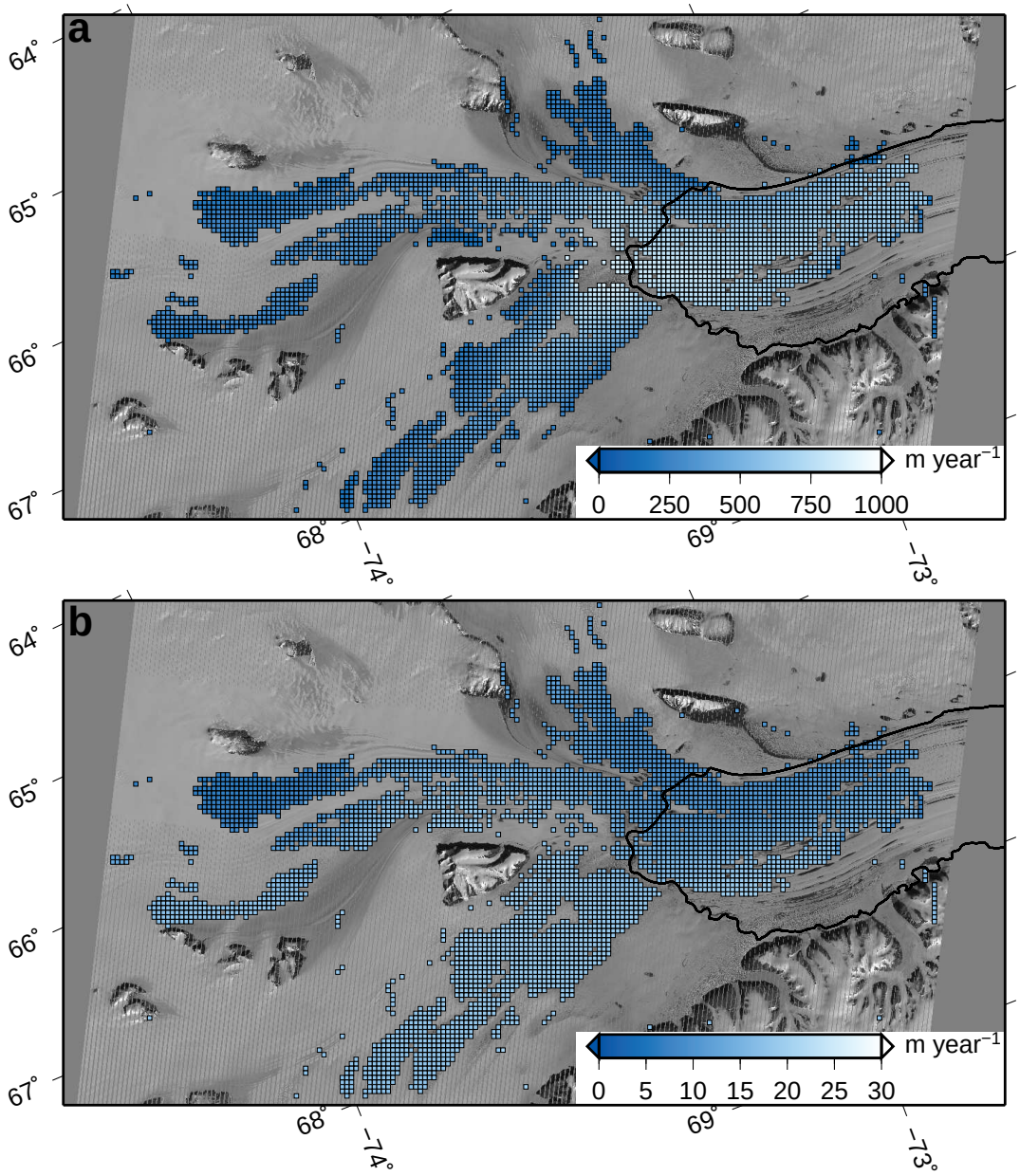

Figure S3.1: a) The coverage of velocities for the 2004/2005 image pairs. b) The coverage of errors for the 2004/2005 image pairs.

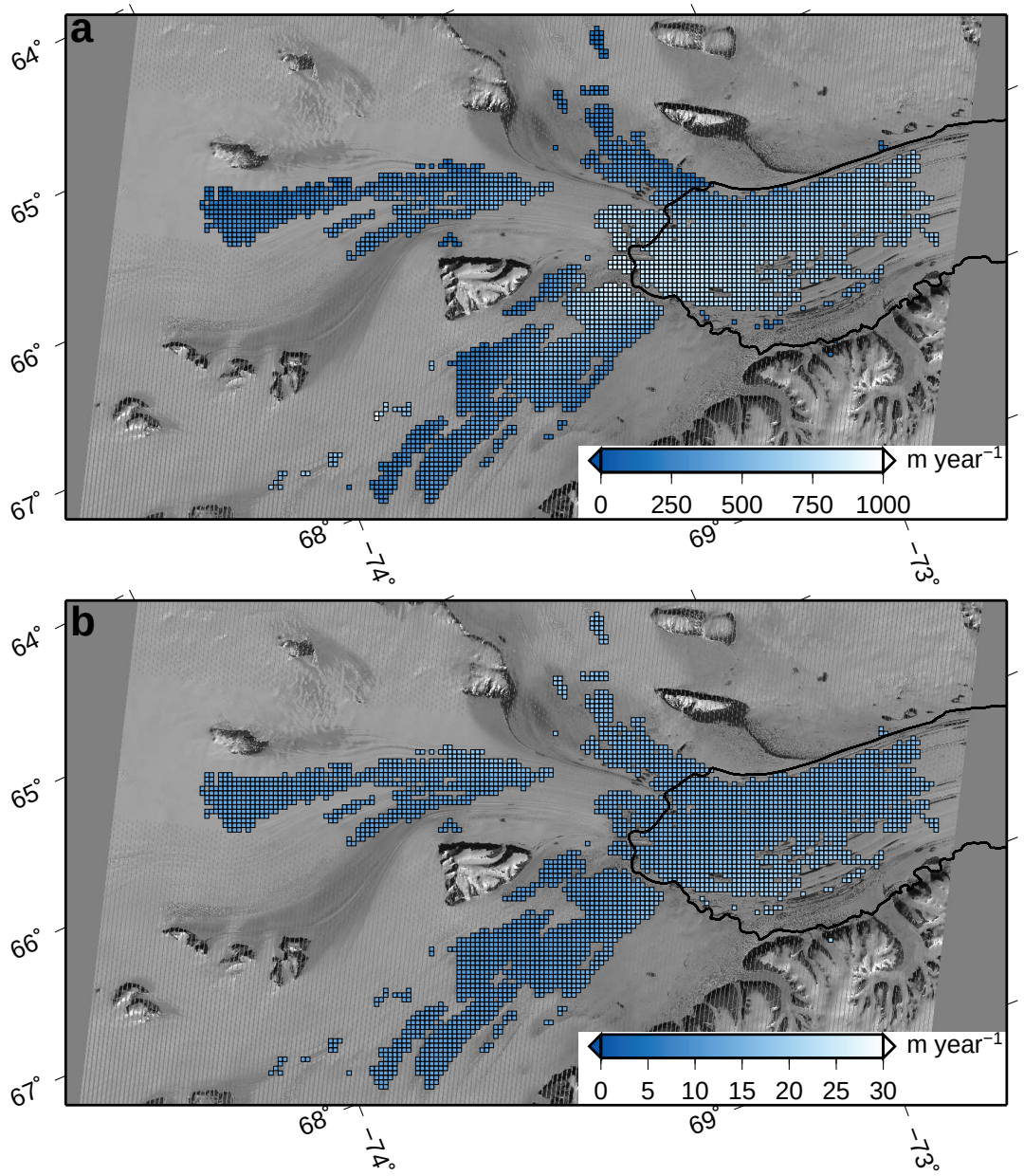

Figure S3.2: a) The coverage of velocities for the 2005/2006 image pairs. b) The coverage of errors for the 2005/2006 image pairs.

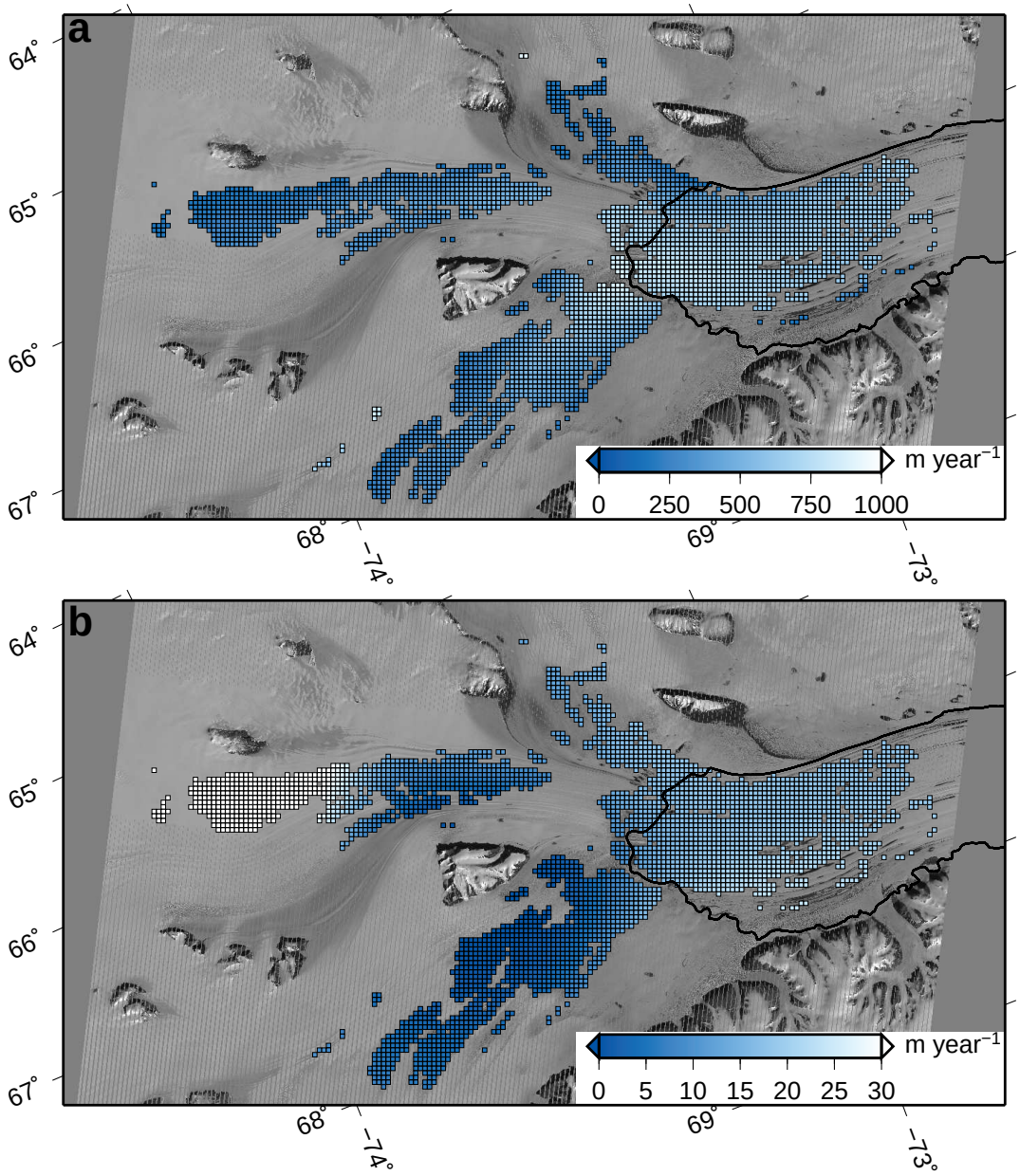

Figure S3.3: a) The coverage of velocities for the 2006/2007 image pairs. b) The coverage of errors for the 2006/2007 image pairs.

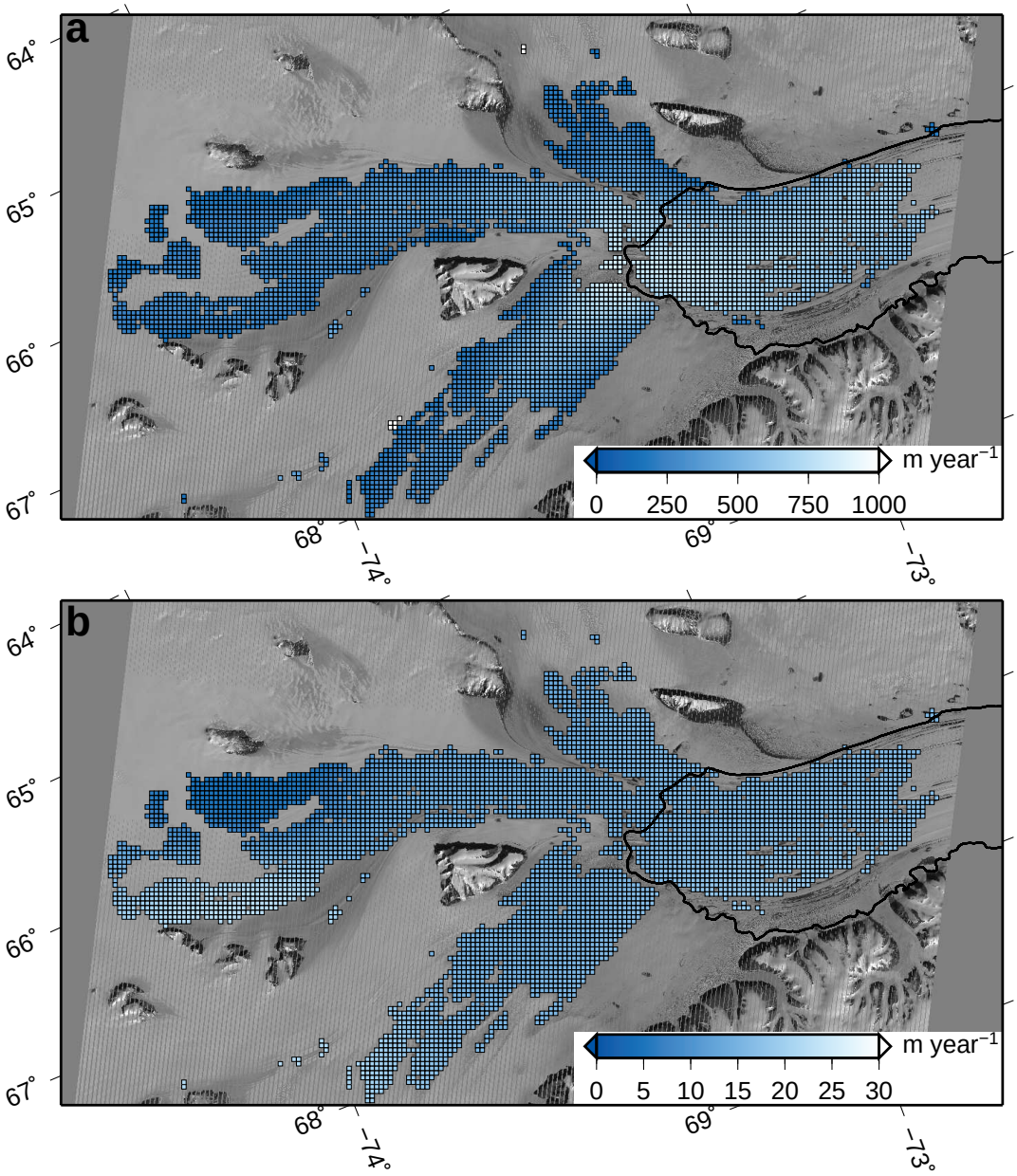

Figure S3.4: a) The coverage of velocities for the 2007/2008 image pairs. b) The coverage of errors for the 2007/2008 image pairs.

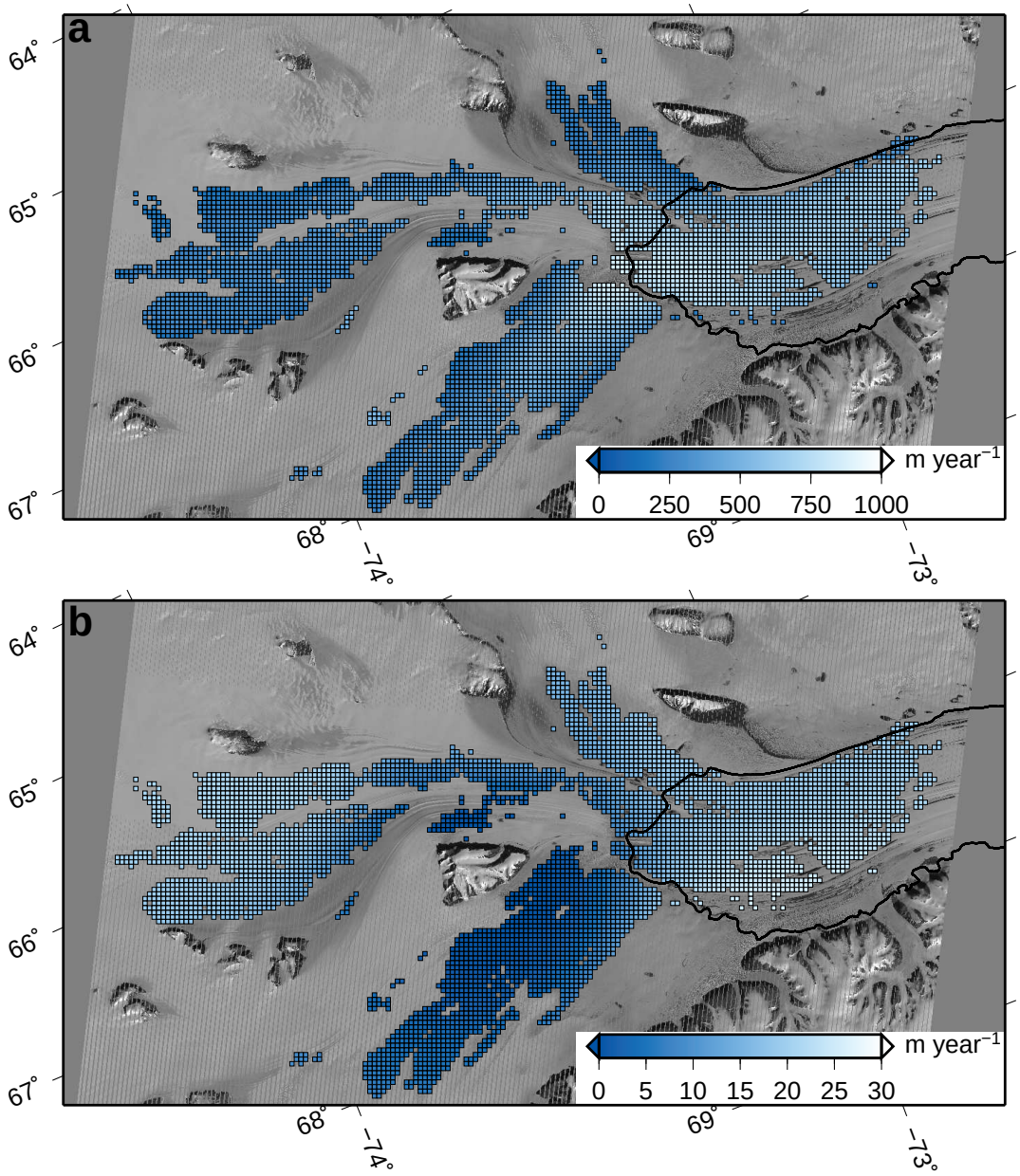

Figure S3.5: a) The coverage of velocities for the 2008/2009 image pairs. b) The coverage of errors for the 2008/2009 image pairs.

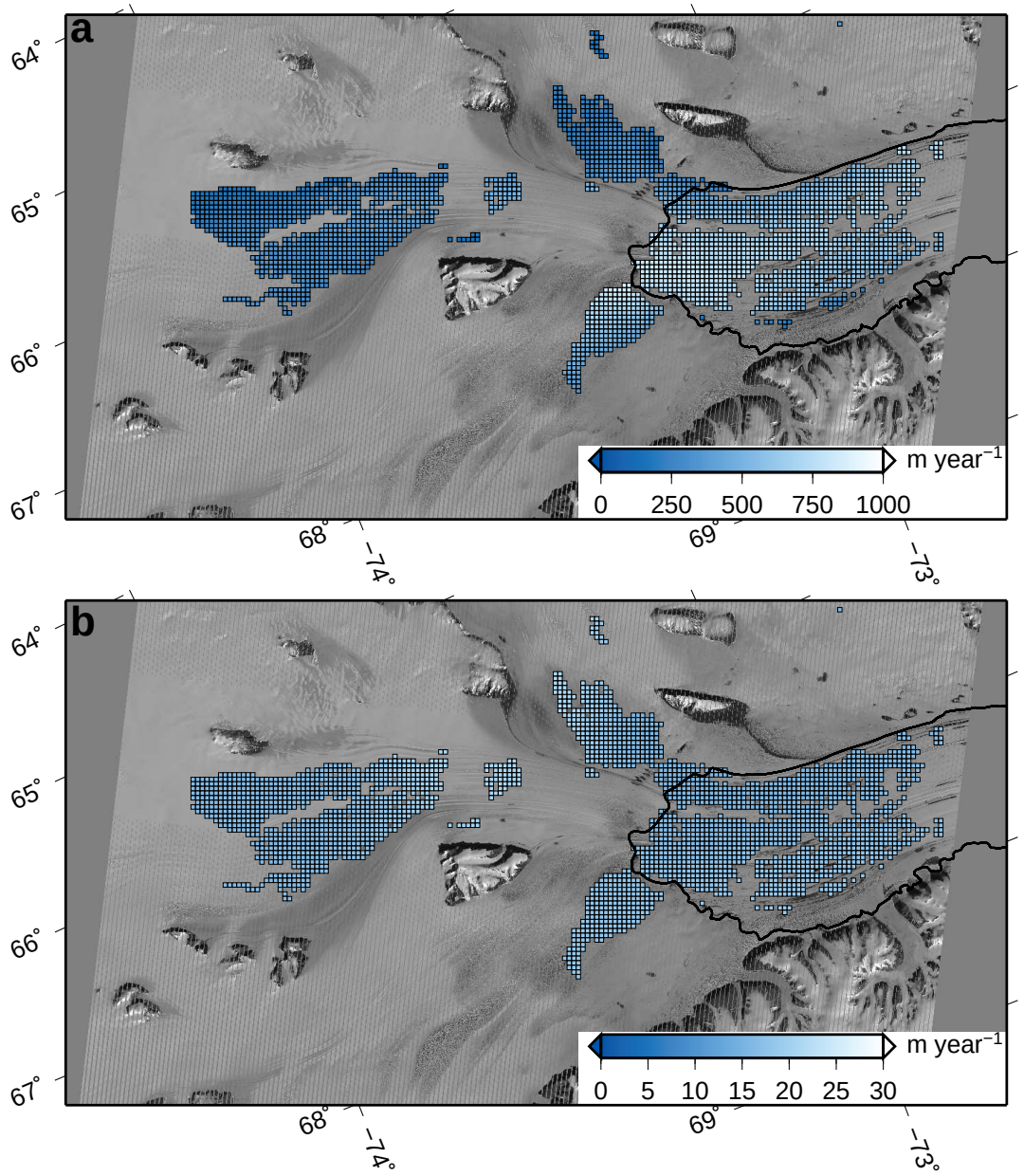

Figure S3.6: a) The coverage of velocities for the 2010/2011 image pairs. b) The coverage of errors for the 2010/2011 image pairs.

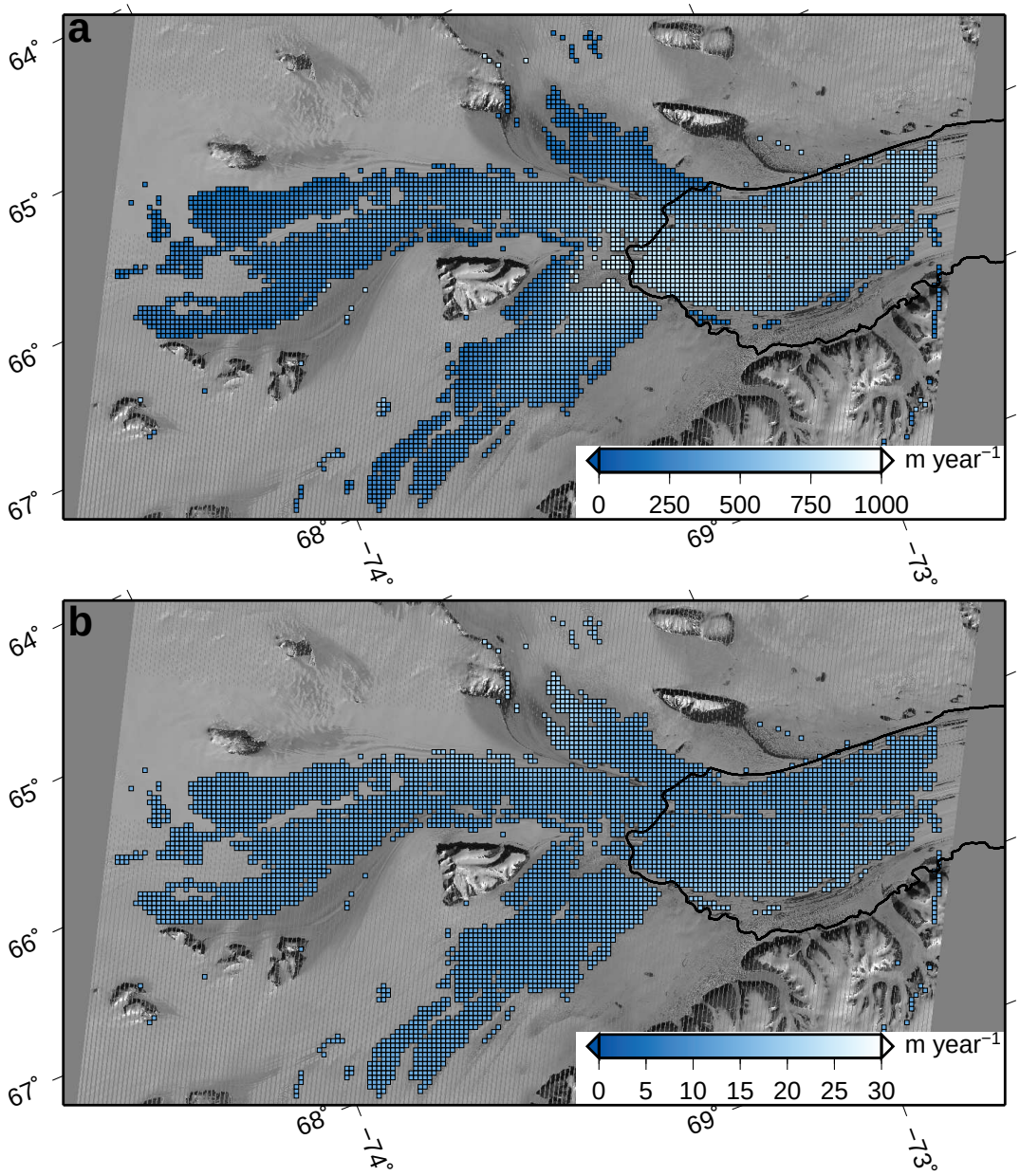

Figure S3.7: a) The coverage of velocities for the 2011/2012 image pairs. b) The coverage of errors for the 2011/2012 image pairs.

Appendix B: Supplementary Information Chapter 4

Introduction

The model simulations used the parameters in Table S4.1, S4.2, S4.3 as inputs to PISM. The parameters in Table S4.4 and S4.5 show the initial optimisation parameters, the tested parameters and their final values. The surface velocity and surface elevations of the regional input model compared to observations are shown in Figure S4.1.

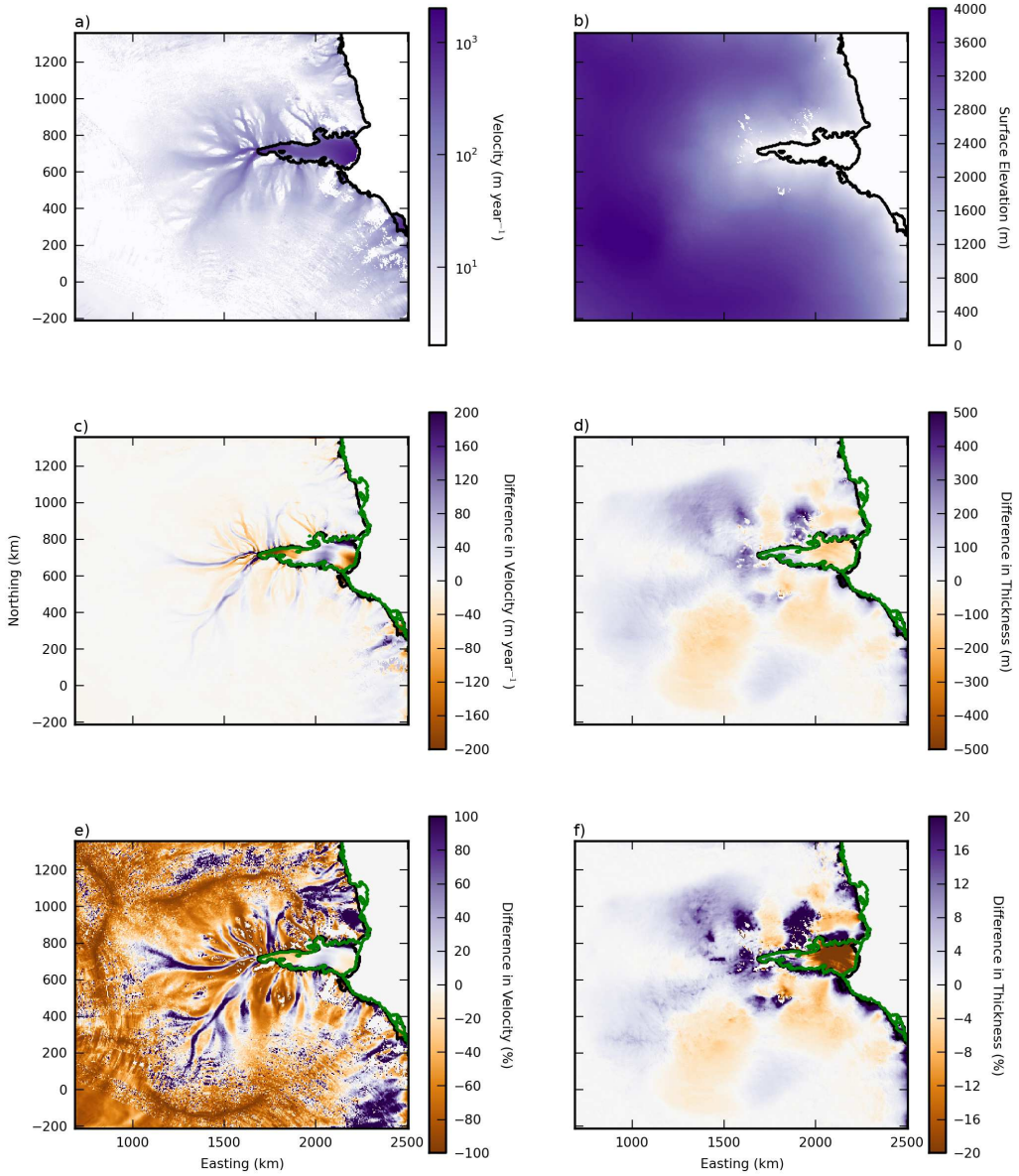

Figure S4.1: a) The MEaSUREs surface velocities (*Rignot et al.*, 2011b). b) The BEDMAP2 ice thickness (*Fretwell et al.*, 2013) c) The difference between the control solution and the MEaSUReS velocities d) The difference between the control solution and the BEDMAP2 ice thickness e) The percentage difference between the control solution and the MEaSUREs velocities (*Rignot et al.*, 2011b) f) The percentage difference between the control solution and the BEDMAP2 ice thickness. The BEDMAP2 ice shelf and coastline is outlined in black, the control solution's ice shelf and coastline is shown in green.

Table S4.1: List of domain parameters used in PISM input file for regional model (other parameters not listed here are left at default values from user manual from http://www.pism-docs.org/wiki/doku.php, date accessed 20/02/2015)

Paramater	**Value**	**Description**
Mx	371	With domain width of 1850 this creates a 5km resolution.
My	321	With domain height of 1600 this creates a 5km resolution.
Myz	300	300 vertical layers.
Mbz	11	Number of vertical layers in the lithosphere.
Lz	4,500	Height of vertical domain, creating 15 m resolution vertical resolution.
Lbz	2,000	Height of Lithospheric domain, creating a 200 m vertical resolution.
no_model_strip	10	Sets a 10 km strip around the domain where the model is kept constant.

Table S4.2: List of stress parameters used in PISM input file for regional model (other parameters not listed here are left at default values from user manual from http://www.pism-docs.org/wiki/doku.php, date accessed 20/02/2015)

Paramater	**Value**	**Description**
stress_balance	ssa+sia	Sets the flow physics model to use the hybrid physics scheme.
sia_flow_law	gpbld	Sets the shallow ice approximation flow law to Glen-Paterson-Budd-Lliboutry-Duval (*Lliboutry and Duval*, 1985).
ssa_flow_law	gpbld	Sets the shallow shelf approximation flow law to Glen-Paterson-Budd-Lliboutry-Duval (*Lliboutry and Duval*, 1985).
pseudo_plastic		Sets the sliding law to be follow a pseudo plastic law (See PISM User's Manual, Equation 4.)

Table S4.3: List of physical parameters used in PISM input file for regional model (other parameters not listed here are left at default values from user manual from http://www.pism-docs.org/wiki/doku.php, date accessed 20/02/2015)

Paramater	**Value**	**Description**
hydrology	null	Simple hydrological model where a 2 m till can be filled my local meltwater, but if it reaches 2 m and further melting is simply lost.
surface	given,forcing	Given directs the model to use the data from an input file. Forcing sets the ftt mask which then holds thickness close to constant by modifying the surface mass balance.
calving	thickness_calving, eigen_calving	thickness_calving sets a thickness limit where ice below this thickness is calved. Eigen_calving sets a calving rate based on principal strain rates (*Levermann et al.*, 2012).
pik		Sets options -cfbc -kill_icebergs -part_grid -part_redist -subgl developed by *Martin et al.* (2011); *Winkelmann et al.* (2011); *Feldmann et al.* (2014).
ocean	pik	Ocean melt parametrisation.
tauc_slippery-_grounding_lines		Reduces basal yield stress at grounded below sea level grid points one cell away from floating ice or ocean.

Table S4.4: List of initial optimisation values, tested values, and final values and description used in PISM input file for regional model

Parameter	Initial	Optimisation values	Final Value	Description
sia_e	3	3.3, 2.7, 2.4, 2.1, 1.8	1.8	The value of the shallow ice enhancement factor for anisotropy.
ssa_e	1	0.7, 1.3, 1.6	1.6	The value of the shallow shelf enhancement factor for anisotropy.
pseudo_plastic_q	0.25	0, 0.375, 0.5, 0.75	0.5	Value for the pseudo plastic flow law (See PISM User's Manual, Equation 4.)
topg_to_phi	5,20,-1000,0	See Table S4.5	10,30,-1500,-500	Sets a piecewise linear function for till angle based on depth of the topography. At -1500 bedrock depth (topg_min), till angle is 10 (phi_min), which changes linear to -500 depth (topg_max) where the till angle is 30 (phi_max).
eigen_calving_k	1.00e+15	1.90e+15	1.90e+15, 1e+16	Threshold for eigen calving.
thickness_calving-_threshold	200	175, 225, 250	225	Threshold for thickness calving.

Table S4.5: List of Optimisation values for the topg_to_phi paramater.

topg_min	topg_max	phi_min	phi_max
-1000.0	0	5	20
-1000.0	0	5	30
-1000.0	0	15	30
-1500.0	-500	5	20
-500.0	500	5	20
-1500.0	500	5	30
-1000.0	0	5	40
-1500.0	-500	5	30
-1250.0	-250	10	30

Appendix C: Model Initialisation

Model Initialisation

An optimisation process is required to identify the ideal value for a range of model parameters. The summary within the manuscript is described here in detail. The optimisation process is aimed to reduce the error between the regional models grounding line location, surface velocity and ice thickness and observations. The performance of each optimisation was assessed and iteratively modified to minimise the misfit between the simulation and observations. The four initial parameters that the model was optimised for are sia_e, ssa_e, psuedo_plastic_q, topg_to_phi. The sia_e and ssa_e directly influence the rate of ice flow in both the SIA and SSA equations and represent the enhancement of flow due to ice anisotropy. The psuedo_plastic_q changes the exponent in the sliding power law (See PISM User's Manual, Equation 4). The topg_to_phi parameters varies the strength of the basal resistance in the till. The topg_to_phi parameter is a piecewise linear function that is dependant on topography. The input is in the form of (minimum till angle (degrees), maximum till angle (degrees), minimum depth (m), maximum depth (m)). After a stable grounding line, surface velocity and ice thickness is found, the calving front was optimised by varying the eigen_calving_K parameter and calving_thickness_threshold (m).

Methods

The optimisation process is broken down into a series of iterative steps:

- Step 1: Identify the initial values for the optimisation parameters
- Step 2: Individual parameter optimisation for a) sia_e b) ssa_e c) psuedo_plastic_q d) topg_to_phi
- Step 3: Combined optimisation with the ideal parameters from Step 2
- Step 4: Optimisation process including a thermal equilibrium run using the ideal parameters from Step 3
- Step 5: Calving Optimisation
- Step 6: Steady state solution

Step 1: Identify the initial values for the optimisation parameters

The parameters held constant throughout the experiments are summarised in table C.1. The initial values for the experimental parameters are outlined in table C.2. The choice of initial sia_e and ssa_e were guided by literature. There is a wide range of numbers that have been used in previous experiments with PISM for Antarctica, with values of sia_e of 1.2 or 1.47 and ssa_e of 0.5 or 0.57(*Golledge et al.*, 2015), sia_e 4.5 and ssa_e

0.512 (*Winkelmann et al.*, 2011), sia_e 3 (*Bindschadler et al.*, 2013) (See PISM Manual) and sia_e 3 (*Golledge et al.*, 2012). With this large range of values, we chose sia_e 3 for our initial experiments as they were consistent with two of the previous studies. For ssa_e, we chose 1 as our initial value, as experiments with values below 1 performed poorly. The psuedo_plastic_q default value is 0.25 and our initial value. The initial value of the topg_to_phi parameter is (5,20,-1000,0), from *Winkelmann et al.* (2011). The initial parameter was 5,20,-1000,0 meaning that below -1000 topographic depth, the till angle is 5, and above 0 topographic depth, the till angle is 20, with a linear function varying the till angle between 5 and 20 in-between the minimum depth of -1000 and the maximum depth of 0. The idea behind this parametrisation is that bedrock with a marine history is likely to have had sedimentation and therefore a weaker till than bedrock that is elevated and undergone continuous erosion. The optimisation experiments have an initial run time of 2,000 years at 5 km horizontal resolution and 15 m vertical resolution.

Table C.1: List of resolution parameters used in PISM input file for regional model (Other parameters not listed here are left at default values from user manual from http://www.pism-docs.org/wiki/doku.php, date accessed 20/02/2015).

Paramater	**Value**	**Description**
Mx	371	With domain width of 1850 this creates a 5km resolution.
My	321	With domain height of 1600 this creates a 5km resolution.
Myz	300	300 vertical layers.
Mbz	11	Number of vertical layers in the lithosphere.
Lz	4,500	Height of vertical domain, creating 15 m resolution vertical resolution.
Lbz	2,000	Height of Lithospheric domain, creating a 200 m vertical resolution.
no_model_strip	10	Sets a 10 km strip around the domain where the model is kept constant.

Step 2a: Individual sia_e optimisation

To optimise the solution for the choice of sia_e, two initial experiments were performed along with the initial model run (1_1). The two initial factors chosen were 2.7 and 3.3, 10% either side of the initial model run. After these initial runs, 2.7 yielded results that were closer to observations, particularly within the high thickness regions of the ice sheet (Table C.5). Additional experiments using sia_e 2.4 and 2.1 were run. The volume changes over the 2000 years (Figure C.1) indicate that a high values of sia_e leads to ice volume loss while a low value leads to ice volume gain. The ice shelf did not advance off the topographical slope that the grounding position is presently located on throughout

Table C.2: List of parameters used in PISM input file for regional model (Other parameters not listed here are left at default values from user manual from http://www.pism-docs.org/wiki/doku.php, date accessed 20/02/2015)

Paramater	**Value**	**Description**
sia_flow_law	gpbld	Sets the shallow ice approximation flow law to Glen-Paterson-Budd-Lliboutry-Duval (*Lliboutry and Duval*, 1985).
ssa_flow_law	gpbld	Sets the shallow shelf approximation flow law to Glen-Paterson-Budd-Lliboutry-Duval (*Lliboutry and Duval*, 1985).
pseudo_plastic		Sets the sliding law to be follow a pseudo plastic law(See PISM User's Manual, Equation 4.)
hydrology	null	Simple hydrological model where a 2 m till can be filled my local meltwater, but if it reaches 2 m and further melting is simply lost.
surface	given,forcing	Given directs the model to use the data from an input file. Forcing sets the ftt mask which then holds thickness close to constant by modifying the surface mass balance (Figure S5.1).
stress_balance	ssa+sia	Sets the flow physics model to use the hybrid physics scheme.
calving	thickness_calving, eigen_calving	thickness_calving sets a thickness limit where ice below this thickness is calved. See step 5 for full details.
eigen_calving_k	1e15	Threshold for eigen calving.
thickness_calving-_threshold	200	Threshold for thickness calving.
pik		Sets options -cfbc -kill_icebergs -part_grid -part_redist -subgl developed by *Martin et al.* (2011); *Winkelmann et al.* (2011); *Feldmann et al.* (2014).
ocean	pik	See Oceanic Basal Melt section.
tauc_slippery-_grounding_lines		Reduces basal yield stress at grounded below sea level grid points one cell away from floating ice or ocean.

Table C.3: List of initial parameters used in PISM input file for regional model optimisation experiments

Paramater	**Value**	**Description**
sia_e	3	The value of the shallow ice enhancement factor for anisotropy.
ssa_e	1	The value of the shallow shelf enhancement factor anisotropy.
pseudo_plastic_q	0.25	Default value for the pseudo plastic flow law.
topg_to_phi	5,20,-1000,0	Sets a piecewise linear function for till angle based on depth of the topography. At -1000 bedrock depth, till angle is 5, which changes linearly to 0 depth where the till angle is 20.

the model, although in all cases it advanced slightly (Table C.4). Decreasing the sia_e improved the rms error but caused significant ice growth at higher elevations (Table C.4). Due to this, the ideal parameter was decided to be 2.7.

Table C.4: List of Experiments of the sia_e optimisation and the ice shelf extent change compared to the BEDMAP2 ice shelf south of 2067 km Easting.

Experiment	sia_e	Change (%)
1_1	3	82.8
1_2	2.7	85.3
1_3	3.3	81.3
1_4	2.4	85.6
1_5	2.1	88.7

Step 2b: Individual ssa_e optimisation

To optimise the solution for the choice of ssa_e, two initial experiments were performed along with the initial model run (1_1). The two initial factors were 0.7 and 1.3. While this is a larger percent change than in the sia_e it is the same total change. The 1.3 experiment yielded results that were closer to observations than 0.7 experiment (Table C.7). An additional experiment was added using ssa_e 1.6. The ice volume change for 1.3 was stable (Figure C.2), with a similar floating velocity mean and standard deviation (std) to observations, and the lowest root mean-square-error (rms). 1.6 had a marginally better rms error for the thickness of floating ice (Table C.7). The ice shelf extent was stable for all values, with 1.6 providing the best solution marginally (Table C.6). We chose 1.3 as our ideal solution as the floating velocities were closer to observations, however, 1.6 would also be a viable choice.

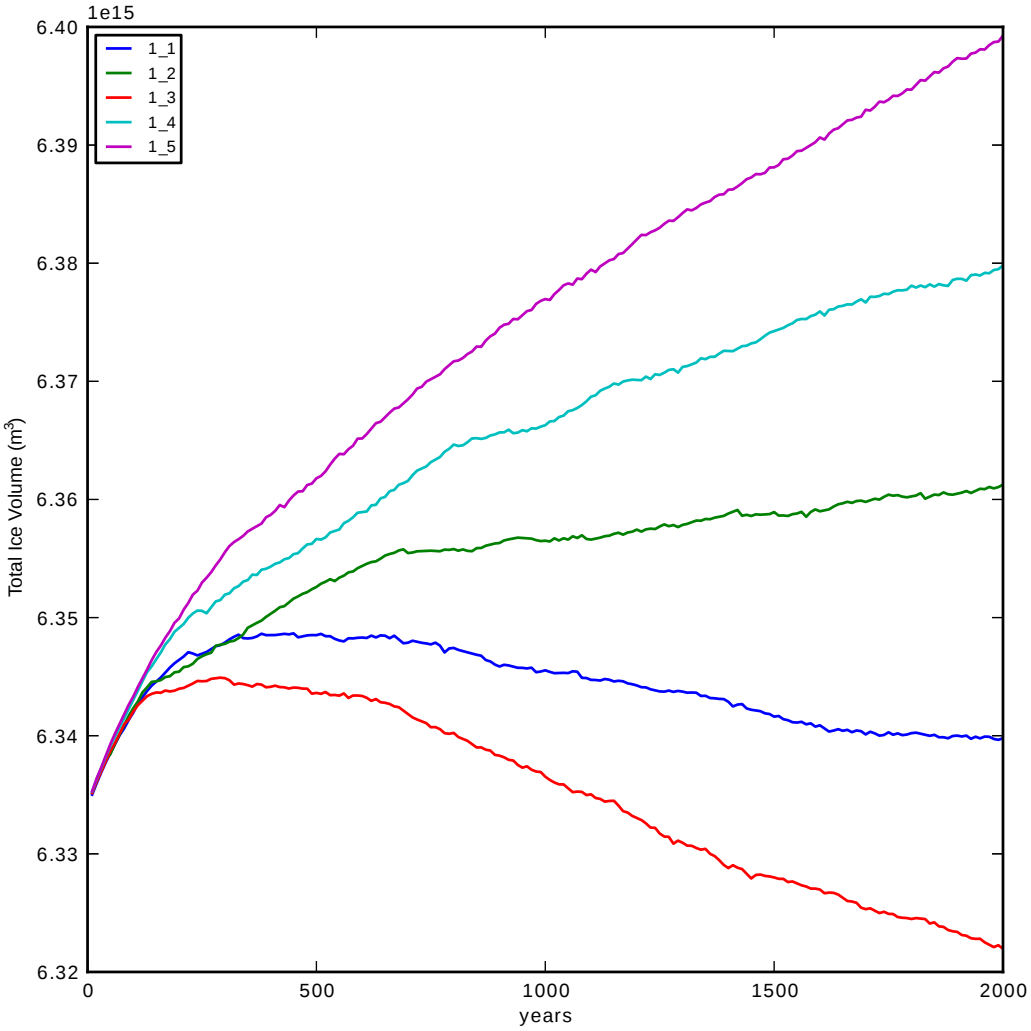

Figure C.1: Change of total ice volume through model simulation for the sia_e optimisation.

Table C.5: The mean, standard deviation (std) and root-mean-square error (rms) for the sia_e optimisation. Velocity is in m year $^{-1}$ and thickness in m.

	Ice Shelf Velocity			Ice Shelf Thk			Ice Sheet Velocity			Ice Sheet Thk		
Exp	mean	std	rms	mean	std	rms	mean	std	rms	mean	std	rms
obs	435.3	313.1	0	583.6	328.8	0	12.1	26.6	0	2420.2	778.8	0
1_1	385.4	257.2	179.9	634.7	416	165.2	20.4	89.1	82.1	2397.4	808.7	77.5
1_2	376.8	257.7	184.5	624.2	398.4	157	18.5	86.1	79.6	2404.8	806.9	74.3
1_3	397	257.2	170.1	647	427.8	174.1	23.4	114.6	108.2	2389.1	810.3	81
1_4	369.4	255	203.4	612.3	379.9	149.5	16.3	75.1	69.3	2412.1	806.6	72.4
1_5	369.7	305.7	270.3	584.7	354.5	138.7	14.2	72.2	67.2	2421.3	803.4	71.6
	Velocity 0-1000			Thk 0-1000			Velocity 1000-2000			Thk 1000-2000		
Exp	mean	std	rms	mean	std	rms	mean	std	rms	mean	std	rms
obs	29.2	45.6	0	637.6	255.7	0	26.1	42.2	0	1584.3	282	0
1_1	90.6	234.9	245.2	617.7	285.4	165.4	39.3	114.9	100.1	1561.1	303.3	104.8
1_2	84.8	222.8	232.4	626.1	290	165.8	35.6	115.7	102.1	1574	299.8	97.2
1_3	100.8	300.9	310.1	614.6	282.5	165.1	46.5	156.4	144.6	1550.9	302.9	109.7
1_4	82.5	209	220.3	626.3	293.7	167.3	29.6	89.3	74.3	1584.1	299.4	92.2
1_5	75.1	211	219.8	635.7	297	167.3	25.7	81.8	68.3	1597	297.2	88.9
	Velocity 2000-3000			Thk 2000-3000			Velocity 3000+			Thk 3000+		
Exp	mean	std	rms	mean	std	rms	mean	std	rms	mean	std	rms
obs	8.4	16.3	0	2563.9	281.9	0	3.8	5.2	0	3278.5	209.8	0
1_1	10.2	37.5	27.8	2560.9	292.7	56	3.6	17	12.9	3286.7	208.2	36.2
1_2	9	34.5	25	2568.7	290.5	52.5	3.1	15.2	11.3	3291.7	208.2	35.5
1_3	11.6	41	30.9	2553.1	294.9	61.2	4.1	19	14.8	3281.4	208.3	38.3
1_4	7.6	29.3	19.9	2577	288.1	50	2.7	13.3	9.5	3296.8	208.2	35.7
1_5	6.3	24.7	16.3	2585.1	285.8	50.1	2.2	11	7.6	3301.7	208.4	37

Table C.6: List of Experiments of the ssa_e optimisation and the ice shelf extent change compared to the BEDMAP2 ice shelf south of 2067 km Easting

Exp	ssa_e	Change (%)
1_1	1	82.8
2_1	1.3	85.7
2_2	0.7	79.1
2_3	1.6	87.6

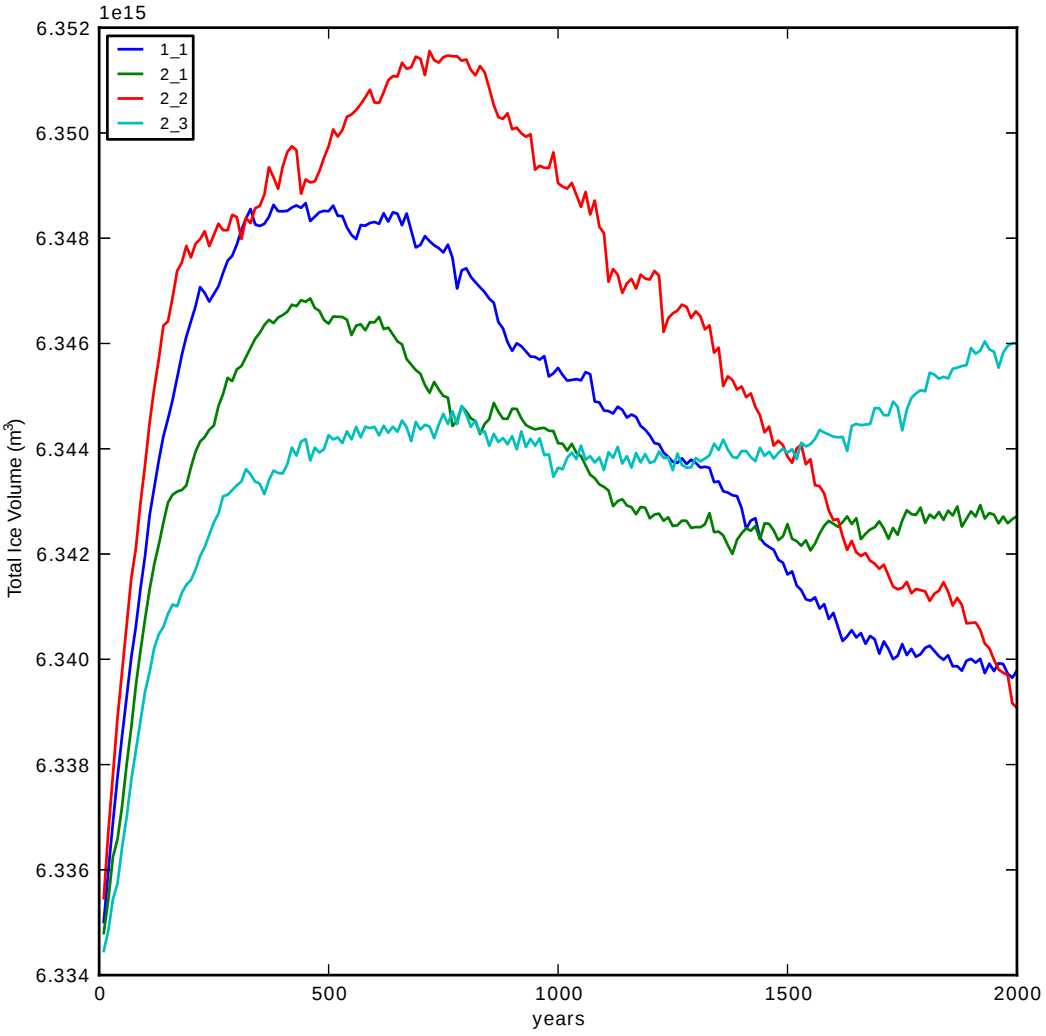

Figure C.2: Change of total ice volume through model simulation for the ssa_e optimisation.

Table C.7: The mean, standard deviation (std) and root-mean-square error (rms) for the ssa_e optimisation. Velocity is in m year $^{-1}$ and thickness in m.

	Ice Shelf Velocity			Ice Shelf Thk			Ice Sheet Velocity			Ice Sheet Thk		
Exp	mean	std	rms	mean	std	rms	mean	std	rms	mean	std	rms
obs	435.3	313.1	0	583.6	328.8	0	12.1	26.6	0	2420.2	778.8	0
1_1	385.4	257.2	179.9	634.7	416	165.2	20.4	89.1	82.1	2397.4	808.7	77.5
2_1	439.3	284.6	165.2	614.7	405.3	158.3	18.9	89.2	81.8	2404.6	802.7	74.6
2_2	323.5	215.5	213	670	426.1	180.6	27.6	116.1	111.8	2377.6	826.9	83
2_3	511.6	327.9	198.5	590	394.6	156	17.6	85.7	78.3	2408.1	801.4	71.4
	Velocity 0-1000			Thk 0-1000			Velocity 1000-2000			Thk 1000-2000		
Exp	mean	std	rms	mean	std	rms	mean	std	rms	mean	std	rms
obs	29.2	45.6	0	637.6	255.7	0	26.1	42.2	0	1584.3	282	0
1_1	90.6	234.9	245.2	617.7	285.4	165.4	39.3	114.9	100.1	1561.1	303.3	104.8
2_1	78.1	231.3	236	628.6	286.3	158.6	38.4	123.3	109.4	1565.3	302.5	101.8
2_2	162.2	318.5	351.9	586	292	179	42.9	121.8	108	1555.2	302.5	107.7
2_3	73.1	229.4	233.2	626.6	285.9	153	35.9	116	101.3	1569.3	302.7	97.9
	Velocity 2000-3000			Thk 2000-3000			Velocity 3000+			Thk 3000+		
Exp	mean	std	rms	mean	std	rms	mean	std	rms	mean	std	rms
obs	8.4	16.3	0	2563.9	281.9	0	3.8	5.2	0	3278.5	209.8	0
1_1	10.2	37.5	27.8	2560.9	292.7	56	3.6	17	12.9	3286.7	208.2	36.2
2_1	9.7	36.5	26.5	2563.5	291.5	54	3.4	16.4	12.4	3287.8	208.1	35.3
2_2	10.9	38.6	28.6	2556.8	294.5	59.3	3.9	18.3	14.1	3284.8	208.4	38.1
2_3	9	33.6	23.3	2566.4	294.5	51	3.3	15.6	11.7	3288.9	208	33.9

Step 2c: Individual pseudo_plastic_q optimisation

To optimise the solution for the choice of pseudo_plastic_q, two initial experiments were performed along with initial model run (1_1). The two initial factors chosen were 0 and 0.5. The 0 case represents a Coulomb sliding law. The Coulomb sliding law behaved substantially different to the other simulations, with a decreasing ice volume (Figure C.3), and was immediately discarded. After the initial runs, 0.5 yielded results closer to observations than 0.25 (Table C.9). Additional experiments using 0.75 and 0.375 were also tested. The ice volume change for the experiments varied slightly, but they were all stable. The results indicate that the 0.5 and the 0.75 experiments were the closest to observations (Table C.9), however, there was not much to separate the two parameters, with minor differences in mean and rms error. The ice shelf extent is 4% better for 0.5 (Table C.8), and with the overall rms error being better for both the floating ice and grounded ice, we chose 0.5 as the ideal parameter.

Table C.8: The ice shelf extent change compared to the BEDMAP2 ice shelf south of 2067 km Easting for the pseudo_plastic_q optimisation.

Exp	Pseudo_plastic_1	Change (%)
1_1	0.25	82.8
3_1	0.5	86.6
3_2	0	81.3
3_3	0.75	82.8
3_4	0.375	82.5

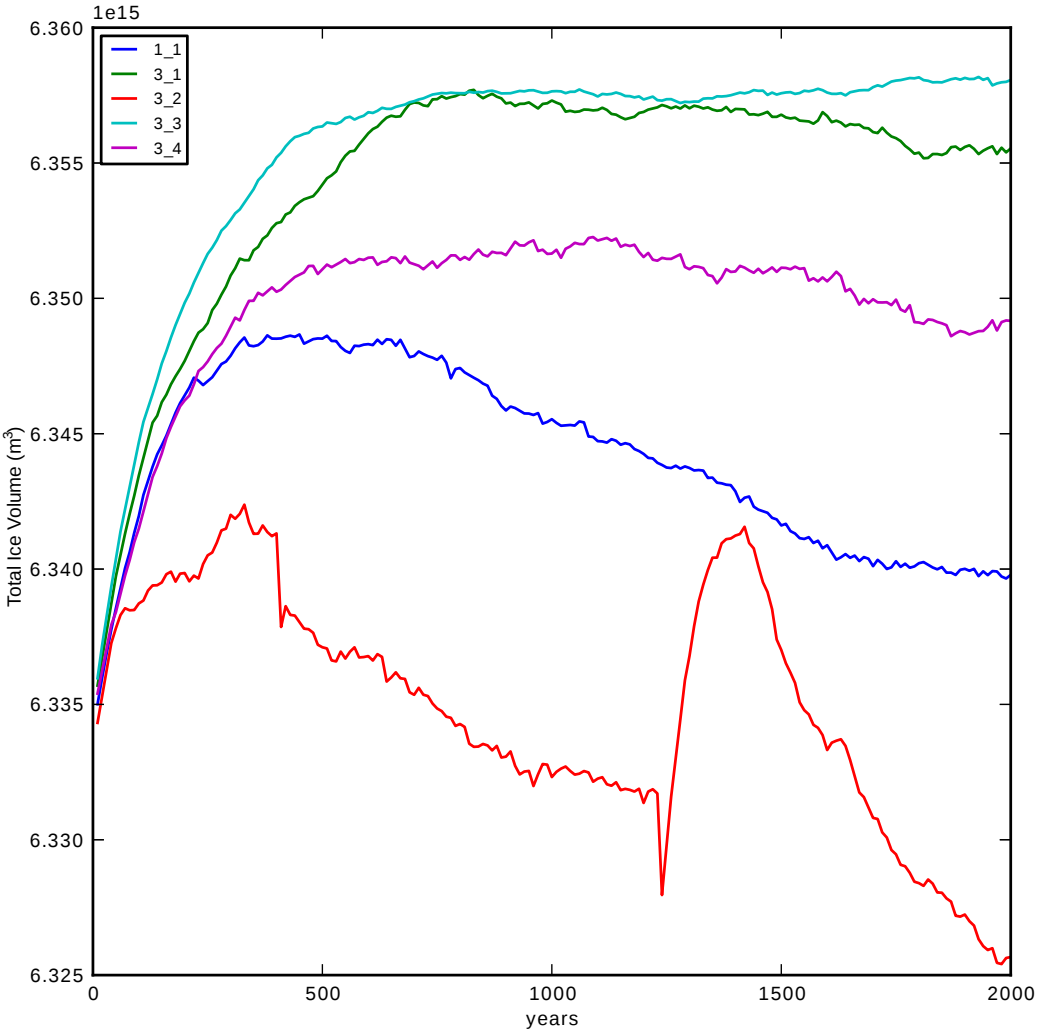

Figure C.3: Change of total ice volume through model simulation for the psuedo_plastic_q optimisation.

Table C.9: The mean, standard deviation (std) and root-mean-square error (rms) for the pseudo_plastic_q optimisation.

	Ice Shelf Velocity			Ice Shelf Thk			Ice Sheet Velocity			Ice Sheet Thk		
Exp	mean	std	rms	mean	std	rms	mean	std	rms	mean	std	rms
obs	435.3	313.1	0	583.6	328.8	0	12.1	26.6	0	2420.2	778.8	0
1_1	385.4	257.2	179.9	634.7	416	165.2	20.4	89.1	82.1	2397.4	808.7	77.5
3_1	439.5	302.3	199.8	604.9	398.7	160.9	15.9	64.3	56.6	2408	800.6	74.5
3_2	405.5	256.3	173.2	636.9	422.1	163.4	24.1	141.7	136.8	2391.4	810.8	85.4
3_3	345.3	242.5	191.1	640.4	413.7	186.2	16.8	64.5	58.1	2400.1	807.3	77.8
3_4	363.7	240.3	173.4	638.6	411.6	169.8	19.2	80.3	73.7	2399	807.7	74.9
	Velocity 0-1000			Thk 0-1000			Velocity 1000-2000			Thk 1000-2000		
Exp	mean	std	rms	mean	std	rms	mean	std	rms	mean	std	rms
obs	29.2	45.6	0	637.6	255.7	0	26.1	42.2	0	1584.3	282	0
1_1	90.6	234.9	245.2	617.7	285.4	165.4	39.3	114.9	100.1	1561.1	303.3	104.8
3_1	65.8	180.9	186	635.9	292.9	182.6	30.6	72.4	53.5	1576.6	301.2	94.6
3_2	92	253.6	262.5	620.7	283.2	167.9	48.9	244.6	238.4	1550.5	302.4	113.9
3_3	75.5	185.6	196	621.8	300.9	195	30	63.9	44.4	1577.2	302.2	97.7
3_4	91	227.4	239	621.6	287.8	167.9	35	89.2	72.2	1568.3	301.1	98.6
	Velocity 2000-3000			Thk 2000-3000			Velocity 3000+			Thk 3000+		
Exp	mean	std	rms	mean	std	rms	mean	std	rms	mean	std	rms
obs	8.4	16.3	0	2563.9	281.9	0	3.8	5.2	0	3278.5	209.8	0
1_1	10.2	37.5	27.8	2560.9	292.7	56	3.6	17	12.9	3286.7	208.2	36.2
3_1	8.7	30.3	19.8	2567.2	288.3	48.7	3.3	15.7	11.7	3288.7	208	33.1
3_2	13.5	69.5	63	2554.3	298.7	68.5	3.8	18	13.9	3285.1	208.6	39.8
3_3	8.9	29.6	19	2565.1	288.1	48.3	3.4	16	12	3287	208	32.5
3_4	9.5	33	22.4	2563.2	290.7	52.3	3.5	16.6	12.6	3287.3	208.1	34.8

Step 2d: Individual topg_to_phi optimisation

To optimise the solution for the choice of topg_to_phi, a large number of different parameters needed to be tested due to the large degree of freedom in the four changeable inputs of (minimum till angle (degrees), maximum till angle (degrees), minimum depth (m), maximum depth (m)). To minimise the different options for optimisation, we identified four different likely scenarios for the initial experiments. The first investigated a stronger till angle maximum of 30 (4_1) and the second investigated shifting both the minimum till angle and maximum till angle by 10 to 15 and 30 respectively (4_2). The next set of initial experiments investigated changes in the depths, with the third experiment lowering both the topographic maximum and minimum by 500 m (4_3), with the fourth experiment rising the topographic maximum and minimum by 500 m (4_4). The results from the initial experiments found that stiffening the till angle maximum from 20 to 30 and dropping the topographic minimum and maximum by 500 m both improved the solution relative to observations (Table C.11). We added additional experiments to test whether the the distance between minimum depth and the maximum depth was important by decreasing the minimum depth by 500 m and increasing the maximum depth by 500 m, creating a distance between them of 2000 m (4_5), using the improved till angle maximum from 4_1 and an additional increase in the strength of the till angle maximum by an additional 10, to a till angle maximum of 40 (4_6). We also tested the best combination from the initial experiments, stiffening

the till angle maximum to 30 and lowering the minimum and maximum depth by 500 m (4_7). The results indicated that 4_7 was the best solution, however, the 500 m changes to the bed elevation were quite high, so as a final test we raised the till angle minimum with a slight increase in the topographic depth (4_8). The full list of experiments are listed in table C.10. The ice volume change for experiments 4_7 and 4_8 are stable and slightly thicker than the other experiments (Figure C.4). The results do not provide a definitive answer on the ideal solution (Table C.11), with some solutions comparing better to observations at some elevation bands, but worse at others. We decided that the ice thickness grounded at elevations above 1000 meters were more important as they control the rate of ice towards the grounding line. This in turn controls the stability of the grounding line, which was most important to have close to observations. Experiment 4_7 and 4_8 perform similarly, with 4_7 slightly better throughout the 1000-3000 range bands, but with little different at 3000+ ice thickness. The ice shelf extent for 4_8 is slightly closer to observations than 4_7, but still along the same topographic slope (Table C.10). We decided to choose 4_7 as our ideal parameter, but they both performed adequately.

Table C.10: List of experiments for the topg_to_phi optimisation and the ice shelf extent change compared to the BEDMAP2 ice shelf south of 2067 km Easting

Exp	topographic depth min	topographic depth max	till angle min	till angle max	Change (%)
1_1	-1000.0	0	5	20	82.8
4_1	-1000.0	0	5	30	81.3
4_2	-1000.0	0	15	30	78
4_3	-1500.0	-500	5	20	83.0
4_4	-500.0	500	5	20	83.4
4_5	-1500.0	500	5	30	84.3
4_6	-1000.0	0	5	40	80.3
4_7	-1500.0	-500	5	30	79.7
4_8	-1250.0	-250	10	30	80.2

Step 3: Combined optimisation with the ideal parameters from Step 2

The initial experiment for the ideal optimisation used the set of ideal parameters from step 2 (5_1). The initial set of ideal parameters led to an increase in the ice volume of the region, that showed no signs of slowing down over our initial 2,000 year run time (Figure C.5). This was likely caused as both the sia_e and the topg_to_phi changed in the individual optimisation and acted to restrain the flow of the ice sheet, hence combining them restricted the ice flow further, leading to growth in the ice sheet. This can be seen by the discrepancy between observations and the 5_1 in the increased ice thickness at the 2000-3000, 3000+ and floating ice bands (Table C.13). Additionally, the ice shelf ice flow was also below observations. Two experiments were designed based on the individual parameter studies to resolve the discrepancies at high elevation ice thickness and ice shelf velocities. The first experiment increased the sia_e and the ssa_e

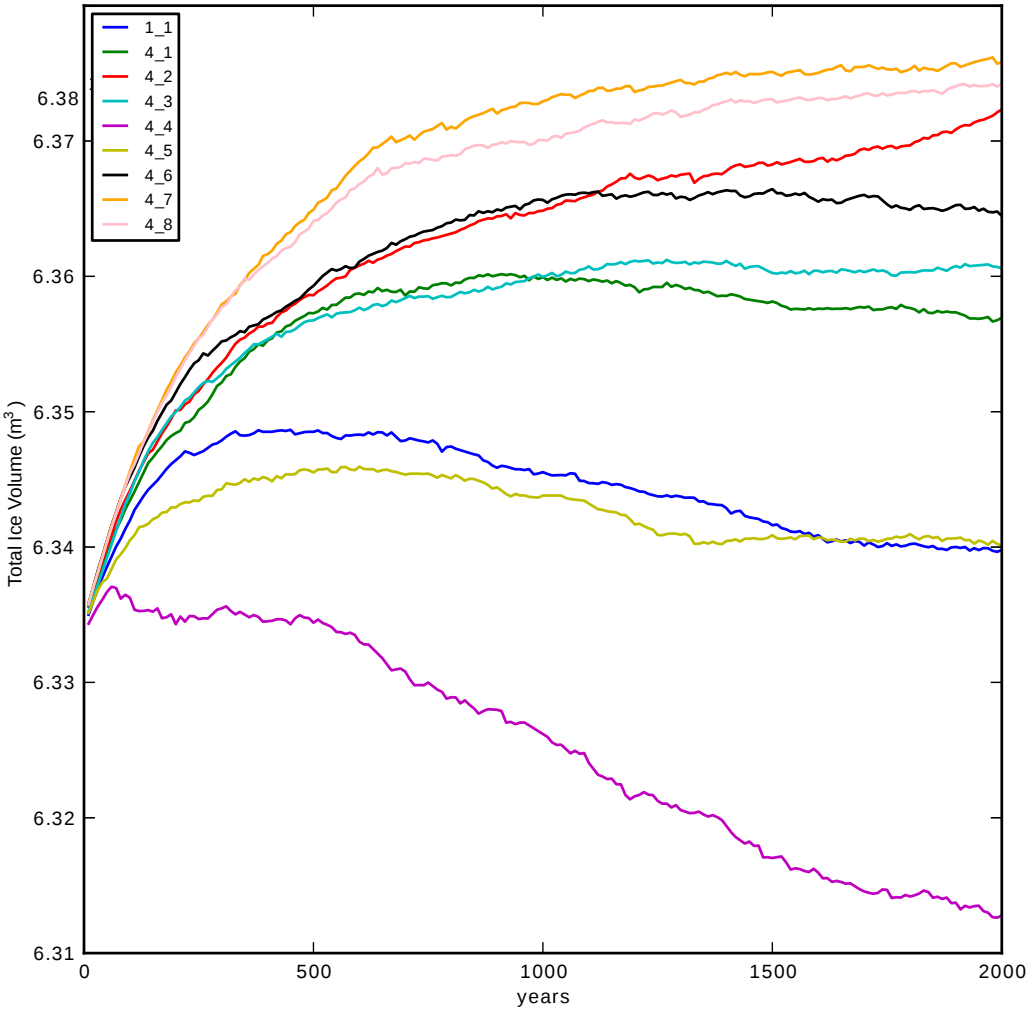

Figure C.4: Change of total ice volume through model simulation for the topg_to_phi optimisation.

Table C.11: The mean, standard deviation (std) and root-mean-square error (rms) for the topg_to_phi optimisation. Velocity is in m year $^{-1}$ and thickness in m.

	Ice Shelf Velocity			Ice Shelf Thk			Ice Sheet Velocity			Ice Sheet Thk		
Exp	mean	std	rms	mean	std	rms	mean	std	rms	mean	std	rms
obs	435.3	313.1	0	583.6	328.8	0	12.1	26.6	0	2420.2	778.8	0
1_1	385.4	257.2	179.9	634.7	416	165.2	20.4	89.1	82.1	2397.4	808.7	77.5
4_1	349.4	232.3	172.7	644.8	413.2	172.1	18.7	76	69	2401.5	804.6	75.7
4_2	322.8	220.7	192.5	648.8	458	206.9	17.4	69.4	65	2410.6	799.8	70.3
4_3	333.4	225.7	188.8	626.7	408.2	162.7	18.6	78.5	72.6	2403.2	805.6	74.8
4_4	457.1	381.1	314.5	629.8	417.3	163.6	28	162.4	156.5	2389.5	812	88.8
4_5	376.7	250.6	177	627.8	412.7	158.9	20.7	98.2	91.9	2400.1	808	75.9
4_6	322.6	225.1	195.1	651.1	413	180.2	19	79.8	74.2	2403.1	804	72.7
4_7	306.6	216.4	207.6	642.9	415.5	182.2	17	65.1	59.4	2408.3	800.5	74.3
4_8	310.4	220.3	204.4	637.8	417	179.6	16.7	63.1	57.1	2409.4	799.4	73.6
	Velocity 0-1000			Thk 0-1000			Velocity 1000-2000			Thk 1000-2000		
Exp	mean	std	rms	mean	std	rms	mean	std	rms	mean	std	rms
obs	29.2	45.6	0	637.6	255.7	0	26.1	42.2	0	1584.3	282	0
1_1	90.6	234.9	245.2	617.7	285.4	165.4	39.3	114.9	100.1	1561.1	303.3	104.8
4_1	85	211	221.5	635.7	286.7	183.3	34.9	86.6	69.4	1572.6	297.8	94.1
4_2	89.8	213.3	226.3	639.3	292.7	165	30.6	61.1	48.6	1586.1	298.7	93.5
4_3	91.6	230.3	241.8	630.7	288.2	182.9	33.5	81.4	65.9	1575.2	300.5	95.3
4_4	112.3	360.4	369.1	609.2	284.9	158.6	56.8	251.1	241.8	1545.3	306.7	120.3
4_5	96	274	283.3	614.5	285.7	159.6	40.2	122.7	109.6	1561.4	305.9	106.1
4_6	97.8	238.9	253.2	636.3	290.3	174.8	32.9	75.8	58	1579	296.8	91.4
4_7	82.7	192.3	205.1	647.9	293.1	191.5	30.1	60.7	42.2	1586.9	296.5	90.6
4_8	77.6	184.3	194.9	649.5	291	188	30.5	61.7	44	1586.3	296.7	90.7
	Velocity 2000-3000			Thk 2000-3000			Velocity 3000+			Thk 3000+		
Exp	mean	std	rms	mean	std	rms	mean	std	rms	mean	std	rms
obs	8.4	16.3	0	2563.9	281.9	0	3.8	5.2	0	3278.5	209.8	0
1_1	10.2	37.5	27.8	2560.9	292.7	56	3.6	17	12.9	3286.7	208.2	36.2
4_1	9.4	32.3	21.6	2564.6	290	50.9	3.4	16.2	12.1	3287.7	208.1	34
4_2	8.3	25.5	16.4	2570.9	286.3	46	3.1	13.7	9.7	3290.2	207.8	30.1
4_3	8.9	29.4	18.9	2567.4	288.4	48	3.3	15	11	3289.1	207.9	31.7
4_4	15.4	80.7	74.7	2550.1	301.1	75.4	3.9	19.6	15.5	3284.3	208.9	41.6
4_5	10	35.5	25.8	2562.7	291.8	53.8	3.4	16.1	12.1	3287.8	208.1	34
4_6	9	30.4	19.5	2566.5	288.6	48.6	3.4	15.6	11.6	3288.3	208	32.9
4_7	8.5	27.3	16.9	2570.3	286.5	45.6	3.2	14.4	10.4	3289.9	207.8	30.5
4_8	8.5	27.3	17	2570.3	286.5	45.8	3.2	14.3	10.3	3289.9	207.8	30.5

by 0.3 each (5_2), which will act to increase the ice velocity globally within the model. The second experiment increased the sia_e by 0.3, but rather than increase the ssa_e the maximum depth in topg_to_phi was raised to attempt to decrease the basal resistance at the grounding line and hence increase ice velocities within the ice shelf (5_3). Both experiments yielded results that improved the ice velocities at high elevations relative to observations, but both cases still led to an increase in ice volume (Figure C.5). The 5_2 solution yielded floating ice velocities that were closer to observations and 5_3 (Table C.13). Another experiment was designed to stabilise the volume change, with an additional increase in the sia_e of 0.3 designed to increase the flow from high elevations to the ice shelf and limit ice growth (5_4). Experiment 5_4 stabilised the ice volume growth and yielded the best results relative to observations. The summary of the experimental runs is in Table C.12. The ice shelf extent was insensitive to changes in this optimisation experiment C.12. With a steady ice sheet profile, the next stage in the optimisation process is to test the thermal equilibrium state of the regional model.

Table C.12: List of iterative experiments for the ideal optimisation process and the ice shelf extent change compared to the BEDMAP2 ice shelf south of 2067 km Easting.

Exp	sia_e	ssa_e	pseudo_plastic_q	topg_to_phi	Change (%)
5_1	2.7	1.3	0.5	5,30,-1500,-500	86.2
5_2	3	1.6	0.5	5,30,-1500,-500	87.4
5_3	3	1.3	0.5	5,30,-1500,500	87.0
5_4	3.3	1.6	0.5	5,30,-1500,-500	85.2

Step 4: Optimisation process including a thermal equilibrium run using the ideal parameters from Step 3

The thermal regime of the ice sheet responds to changes in ice volume on time scales of over hundreds of thousands of years, which is longer than is practical to run the regional model at 5 km resolution. To test how close the thermal regime is to steady state, the horizontal resolution is decreased to 10 km and the mass-continuity equations are turned off (-no_mass in PISM options). A 200,000 year simulation showed an increase in enthalpy by 8% over the 200,000 years (Figure C.6). Using the new thermal equilibrium as an input using the parameters from 5_4 an experiment was run for 2,000 years and at 5 km resolution. The increase in enthalpy had a far larger influence on the ice flow than expected, causing the advance of the grounding line (Table C.14). This lead to another iterative set of optimisation experiments, which included a new thermal equilibrium run before each new experiment.

The advance of the grounding line in 6_1 indicates that the flux of ice into the ice shelf is too high, so the the sia_e was reduced iteratively by 0.3 until the grounding

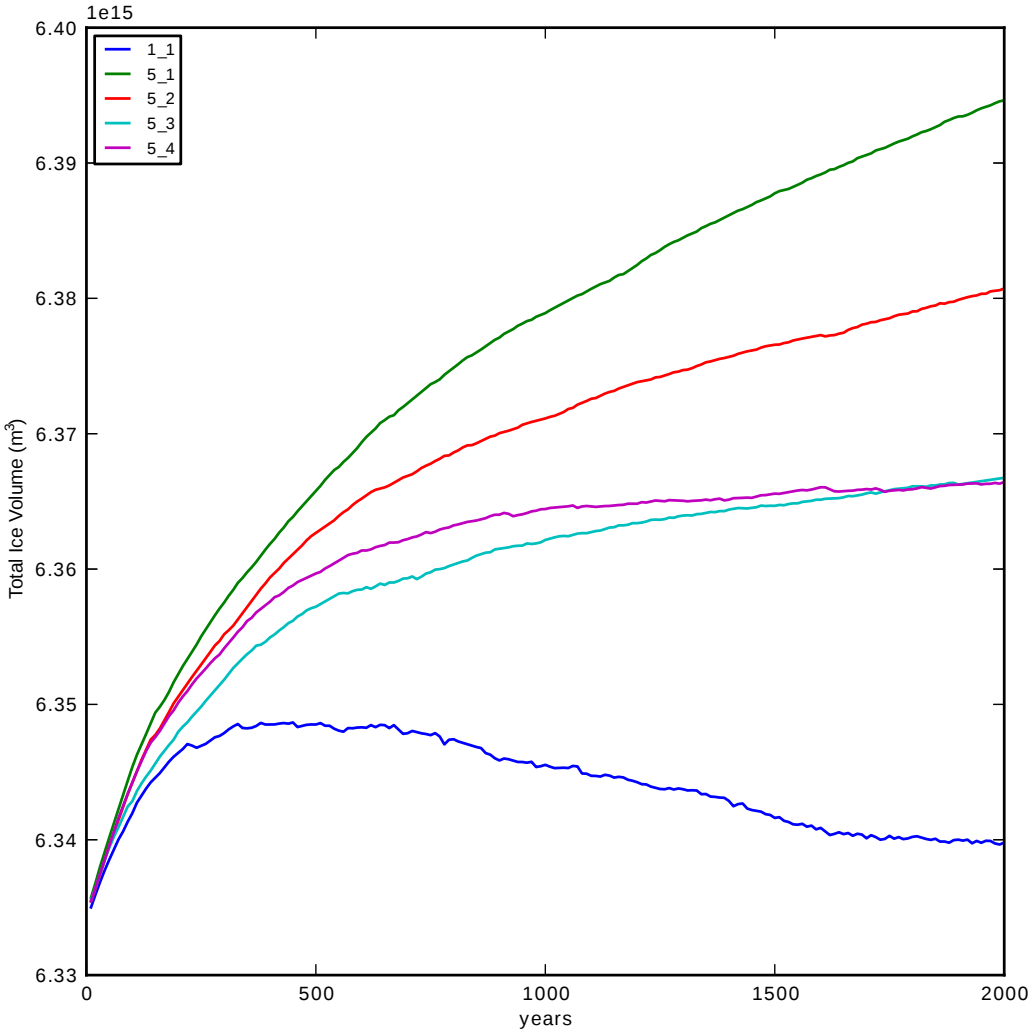

Figure C.5: Change of total ice volume through model simulation for the ideal optimisation.

Table C.13: The mean, standard deviation (std) and root-mean-square error (rms) for the ideal optimisation. Velocity is in m year $^{-1}$ and thickness in m.

	Ice Shelf Velocity			Ice Shelf Thk			Ice Sheet Velocity			Ice Sheet Thk		
Exp	mean	std	rms	mean	std	rms	mean	std	rms	mean	std	rms
obs	435.3	313.1	0	583.6	328.8	0	12.1	26.6	0	2420.2	778.8	0
5_1	343	246.8	193.5	597.6	386.4	170.2	13.3	51.1	45.4	2422.8	793	70.6
5_2	397.7	279.4	174.2	594.1	390.4	174.7	13.8	51.3	44.5	2419.2	792.5	70.1
5_3	396.1	313.6	243.9	605.3	395.6	167.1	15.3	59.4	52.6	2412	798.5	71.5
5_4	416.3	299.8	178.4	609	406.8	187.8	14.9	53.4	45.6	2412.9	793.3	72.5
	Velocity 0-1000			Thk 0-1000			Velocity 1000-2000			Thk 1000-2000		
Exp	mean	std	rms	mean	std	rms	mean	std	rms	mean	std	rms
obs	29.2	45.6	0	637.6	255.7	0	26.1	42.2	0	1584.3	282	0
5_1	59.7	150.5	158	661.2	296.1	183	24.7	50.5	33.9	1602.4	294.1	86.2
5_2	56.7	146.4	152	658.1	292.3	180.5	26.5	54.4	36	1595.7	296.4	88
5_3	66.9	172.9	180.1	641.3	290	175.3	28.7	61	42.2	1583.8	300.8	93
5_4	57.1	147	152.5	656.8	290.5	185.7	29	59.1	39.3	1587.5	298.1	92
	Velocity 2000-3000			Thk 2000-3000			Velocity 3000+			Thk 3000+		
Exp	mean	std	rms	mean	std	rms	mean	std	rms	mean	std	rms
obs	8.4	16.3	0	2563.9	281.9	0	3.8	5.2	0	3278.5	209.8	0
5_1	7	23.2	13.6	2579.8	283.5	43.8	2.6	11.9	8.2	3295.5	208	30.7
5_2	7.7	25.1	15	2575	284.1	43.1	2.9	13	9.2	3291.9	207.8	29.1
5_3	8.2	27.3	17	2570.9	286.3	45.5	3.1	14.4	10.4	3290.2	207.9	30.7
5_4	8.6	27.8	17.1	2568.7	285.5	44.5	3.3	14.7	10.7	3287.4	207.7	29

line no longer advanced. This took three iterations and the grounding line first became stable at a value of 2.4 (6_4). This solution still had a negative gradient in the change of ice volume (Figure C.7), and a further reduction in the sia_e by 0.3 was conducted to try to stabilise the ice volume growth. This solution yielded results closer to observations than the previous experiments, however, the thickness at the grounding line was higher than observations (not shown) so a final experiment with a higher minimum till angle was run (6_6). The 6_6 experiment performed marginally better than 6_5 for the grounded ice, but marginally worse for the floating ice. The final solution was decided on 6_6, however, 6_5 would have also provided a reasonable solution. The difference between the initial estimated enthalpy and the final enthalpy on the solution was higher than expected, and for future optimisations a thermal equilibrium step would be placed between Step 1 and Step 2 assuming the Step 1 initial run produced a correct grounding line position.

Table C.14: List of iterative experiments for the thermal optimisation process and ice shelf change.

Exp	sia_e	ssa_e	pseudo_plastic_q	topg_to_phi	Change (%)
6_1	3.3	1.6	0.5	5,30,-1500,-500	70.9
6_2	3	1.6	0.5	5,30,-1500,-500	72.6
6_3	2.7	1.6	0.5	5,30,-1500,500	75.4
6_4	2.4	1.6	0.5	5,30,-1500,-500	85.1
6_5	2.1	1.6	0.5	5,30,-1500,500	86.2
6_6	2.1	1.6	0.5	10,30,-1500,-500	85.5

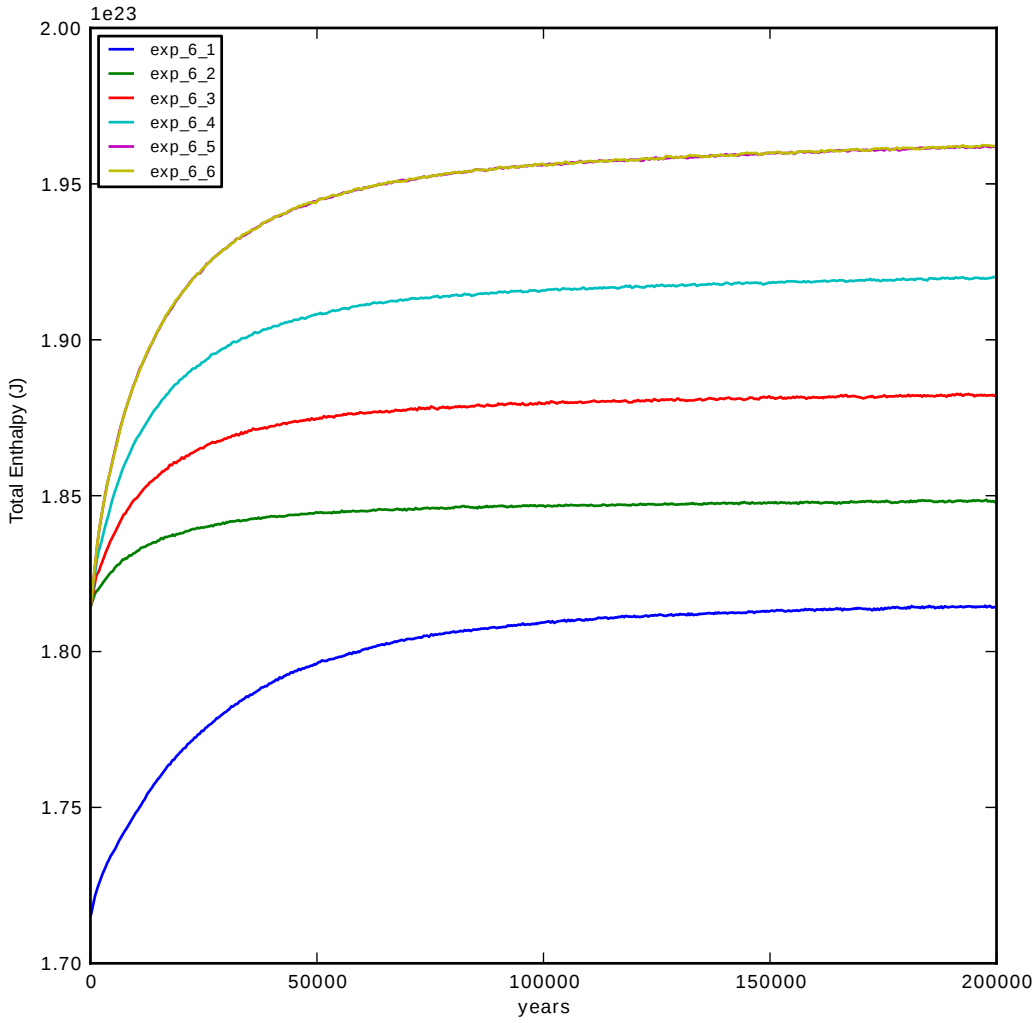

Figure C.6: Change of total enthalpy through model simulation for the thermal optimisation.

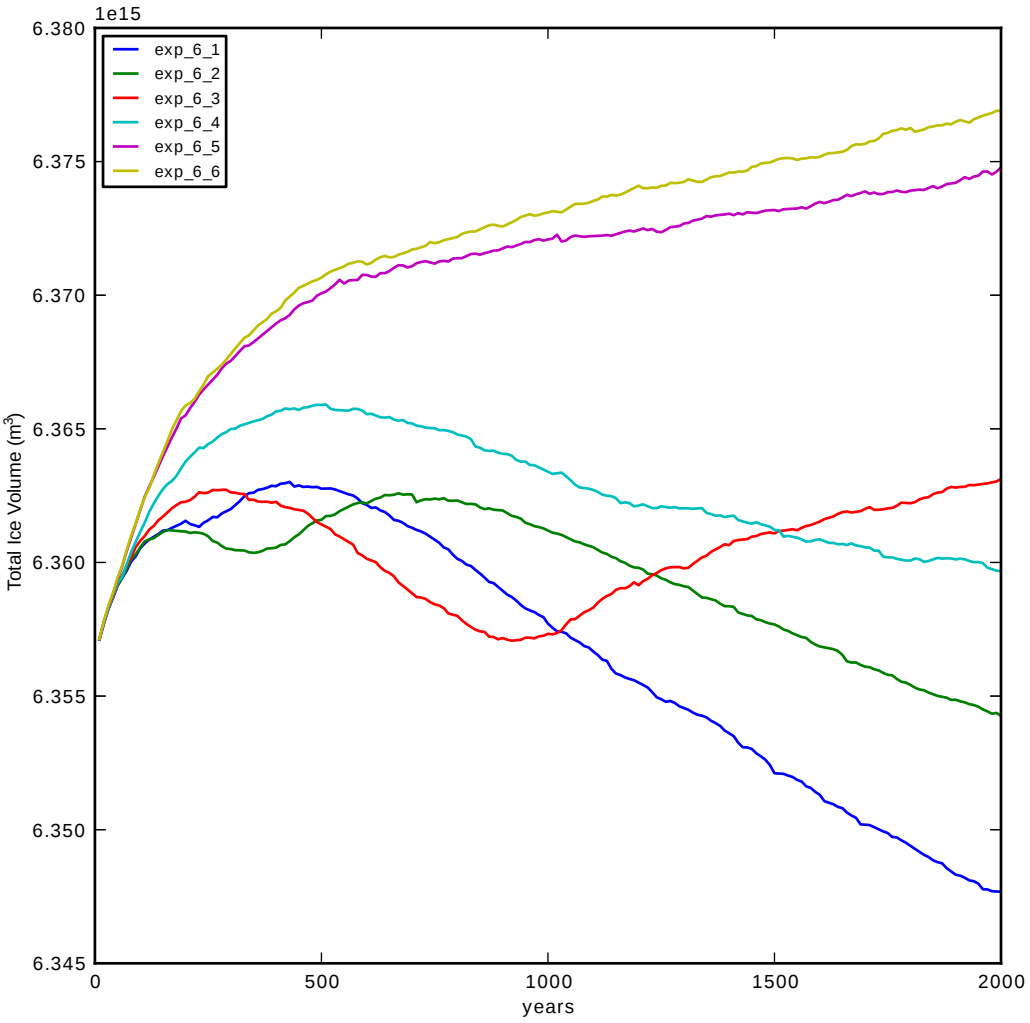

Figure C.7: Change of total ice volume through model simulation for the thermal optimisation.

Table C.15: The mean, standard deviation (std) and root-mean-square error (rms) for the thermal optimisation. Velocity is in m year $^{-1}$ and thickness in m.

	Ice Shelf Velocity			Ice Shelf Thk			Ice Sheet Velocity			Ice Sheet Thk		
Exp	mean	std	rms	mean	std	rms	mean	std	rms	mean	std	rms
obs	435.3	313.1	0	583.6	328.8	0	12.1	26.6	0	2420.2	778.8	0
6_1	529.3	371.7	227.2	728.3	573.7	332.3	17.4	60.3	53.7	2398.5	792.3	89.4
6_2	504.3	349.4	201.5	712.1	555.8	309.1	16.5	57.3	50.7	2402.4	790.7	86.6
6_3	495.2	337.1	188.8	696.1	544.8	293.2	15.7	56.4	50.3	2394.3	788.2	87.8
6_4	411.5	288.5	167.1	616.5	425.4	192	15.1	52.9	44.8	2393.4	789.3	83.9
6_5	409.3	275.3	163.3	600.5	405.7	179	13.9	50.7	43.3	2400.6	788.5	81
6_6	395.7	274.1	172.6	599.2	412.2	182.5	13.6	47.1	39.7	2402.7	787.1	80.9
	Velocity 0-1000			Thk 0-1000			Velocity 1000-2000			Thk 1000-2000		
Exp	mean	std	rms	mean	std	rms	mean	std	rms	mean	std	rms
Obs	29.2	45.6	0	637.6	255.7	0	26.1	42.2	0	1584.3	282	0
6_1	69.7	181.3	189.1	662.7	293.9	200.9	32.1	56.2	35.6	1578.8	303.2	110.9
6_2	65.6	171.9	179	666.4	293.3	199.1	30.5	54.4	33.7	1582.9	301	105.8
6_3	64.7	171.4	178.7	665.4	293	199.3	28.3	51.7	31.9	1577.5	298.7	104.1
6_4	55.8	149	154.5	662.7	290.5	193.9	28	57.9	34.6	1571.4	294.3	91.6
6_5	54.8	146	151.8	666.8	292.9	193.6	25.6	53.9	31.4	1580.4	292.5	86.6
6_6	50.9	132.6	137.6	670.5	292.9	194.1	25.4	51.9	30.6	1583.5	292.2	87.4
	Velocity 2000-3000			Thk 2000-3000			Velocity 3000+			Thk 3000+		
Exp	mean	std	rms	mean	std	rms	mean	std	rms	mean	std	rms
obs	8.4	16.3	0	2563.9	281.9	0	3.8	5.2	0	3278.5	209.8	0
6_1	10	25.9	14.2	2556	286.9	67.1	4.2	13.2	8.8	3271.6	209.3	44.4
6_2	9.6	24.8	13	2559.2	285.9	64.6	4	12.6	8.3	3273.8	209	42.2
6_3	9	23.6	12	2551.6	286.4	65.6	3.9	12.3	8	3262.1	206.2	50.9
6_4	9.1	25.5	12.9	2550.7	287.9	65.2	4	13.2	8.8	3263.1	206.5	52.7
6_5	8.1	23.2	11	2558	286.2	62	3.6	11.9	7.6	3268.9	206.5	48.4
6_6	8	22.5	10.6	2559.3	285.6	61.8	3.5	11.6	7.3	3269.5	206.4	47.5

Step 5: Calving Optimisation

The two parameters which control calving within our regional model domain are the thickness_calving and eigen_calving mechanisms. The thickness_calving mechanism simply calves the ice off when it is below the threshold thickness chosen. The basis of this calving criterion is observations that there is a limit to how thin an ice shelf can be, for example, the Amery Ice Shelf's calving front has no observed ice thinner than 200 m, and little below 300 m (Figure C.8). The eigen_calving mechanism was developed by *Levermann et al.* (2012), and sets the the calving rate proportional to the product of a constant eigen_calving_K and the principal components of the horizontal strain rate. *Levermann et al.* (2012) suggest a range of values for the eigen_calving_K for different ice shelves, with large wide ice shelves having a higher eigen_calving_K, 5e16 ms, compared to narrow ice shelves which can be as low as eigen_calving_K, 1.5e15 ms. The derived value for the Amery Ice shelf was eigen_calving_K, 1.9e15 ms. The initial value of eigen_calving_K of 1e15 ms that we have been using is less than the suggested value, so the calving rates was reduced in our current optimisation experiments. To optimise the model for the calving parameters a series of short 100 year runs were conducted to test the changes they made to the calving front. These experiments used the final solution of 6_6 as the input. The first value tried was eigen_calving_K of 1.9e15 ms (7_1). This provides a similar initial calving front, with the north western front advanced compared to observations, most likely due to the ice along the coastline advancing on the north-western side of the Amery Ice Shelf. The final experiment we increased the thickness_calving_threshold from the 200 m initial value to 225 m (7_2). This provides a calving front that approximately resembles observations (Figure C.8) and these parameters was used for the final steady state solution of the Lambert-Amery glacial system regional model.

Step 6: Steady State Solution

To find the final steady state solution, experiment 6_6 was run for an additional 3,000 years using the new calving parameters from 7_2. The rate of change for the last 1,000 years for total ice volume is 0.007% and for the total enthalpy is 0.085%. This is a stable solution and was used as the initial conditions for the experiments in the manuscript.

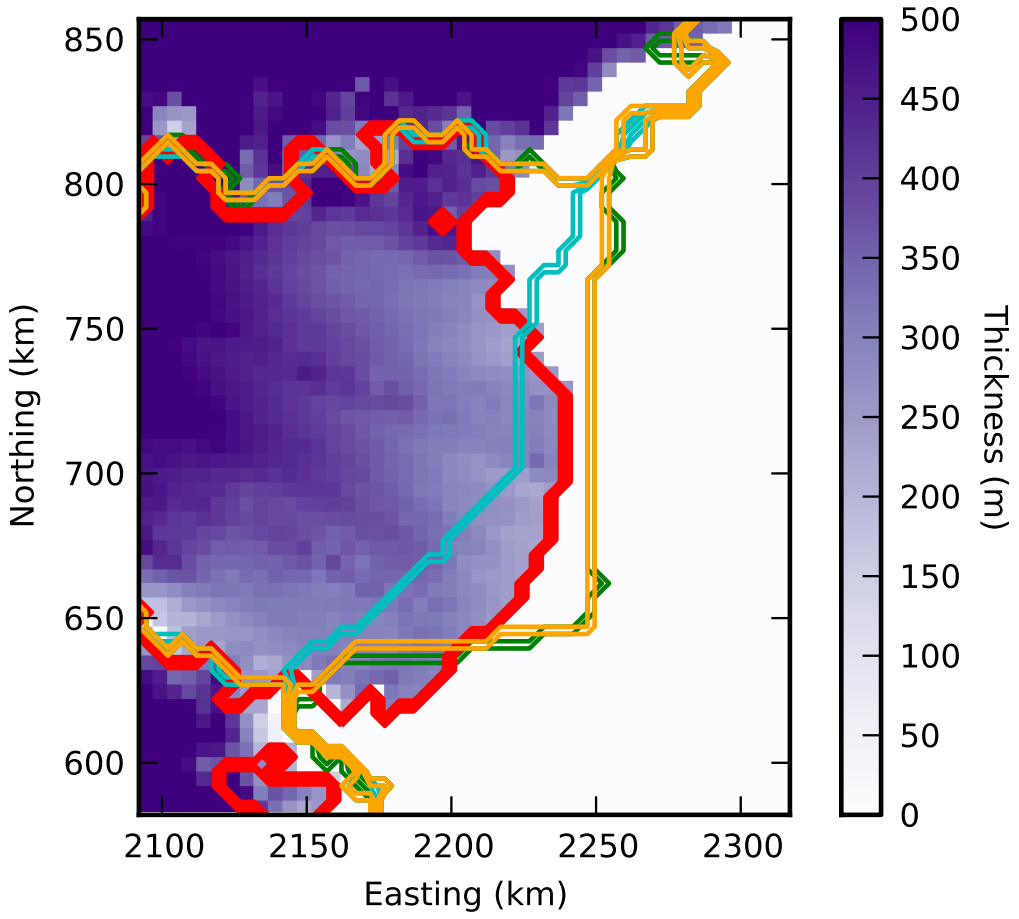

Figure C.8: The BEDMAP2 ice thickness at the calving front, the ice shelf mask of BEDMAP2 and the grounding lines of the 6_4 (green), 7_1 (orange) and 7_2 (cyan).

Appendix D: Supplementary Information Chapter 5

Creating the Regional Model

Regional Domain Mask

To identify and create the domain for a regional model of the Lambert-Amery glacial system the following steps were taken:

1. An Antarctic Ice Sheet domain was created for a low resolution run. The data source for this domain was the PISM searise experiment (*Bindschadler et al.*, 2013)(http://www.pism-docs.org/wiki/doku.php, date accessed 20/02/2015). It was run with 30 km horizontal resolution and 50 m vertical resolution.

2. PISM was run for 100 years in SIA only mode to smooth out roughness in surface elevation created by the initial thickness of the ice and artifacts from the re–gridding to low resolution.

3. The PISM drainage basin tool (http://www.pism-docs.orgwiki/doku.php, date accessed 20/02/2015) was used to calculate the drainage basin of the Amery Ice Shelf by running a simple gradient flow model. The output is a mask, ftt_mask (force to thickness mask), which PISM uses in its pismo executable. The ftt_mask designates the region outside the drainage basin. This is used by the surface model to modify the surface mass balance to ensure that ice thickness stays at a constant value within this mask.

4. A square region which encompasses the drainage basin is cropped to make the regional domain which is used to crop high–resolution datasets (Figure S5.1). This allows for outlet glaciers to be numerically solved without the outside basins overtly influencing the numerical solution. The coordinates for this region are -233000 m to 1367000 m Easting and 667000 m to 2517000 m Northing, in Polar Stereographic projection (EPSG:3031).

5. The ftt_mask was manually edited to encompass regions of the coastline and to allow for movement of the ice divides inland as the regional model may be used for glacial cycle experiments. The ftt_mask was expanded 50 km's outwards and the region along the coastline was manually increased to encompass regions along the Prydz Bay coastline (Figure S5.1).

Regional Domain Data

PISM requires five main data inputs. These are bed elevation (topg), initial ice thickness (thk), ice surface temperature (surf_temp), surface mass balance (smb) and geothermal heat flux (ghf). The source of each data is summarised in Table S5.1.

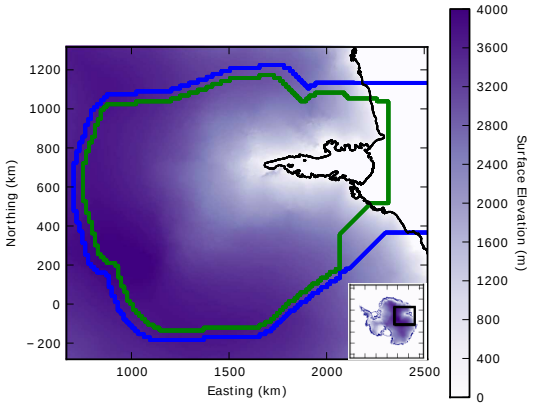

Figure S5.1: The regional domain with the initial ftt_mask (green) and the final ftt_mask (blue) indicated. The ice shelf extent from bedmap2 is indicated in black. Inset: Location of the Lambert-Amery glacial system within Antarctica, showing the square region (blue) that encompasses the regional model.

Table S5.1: Table of input data types and sources

Variable	Data Name	Reference
topg	BEDMAP2+RTOPO	(*Fretwell et al.*, 2013)+(*Timmermann et al.*, 2010)
thk	BEDMAP2+RTOPO	(*Fretwell et al.*, 2013)+(*Timmermann et al.*, 2010)
smb	RACMO2.3	(*van Wessem et al.*, 2014)
surf_temp	RACMO2.3	(*van Wessem et al.*, 2014)
ghf	fm_2012	(*Fox Maule et al.*, 2005) and magnetic Field Model 7

Topography and Thickness

The BEDMAP2 complimation is an update to the grounded portions of the Antarctic Ice Sheet from BEDMAP1 with the topography under ice shelves coming from a number of different sources (*Fretwell et al.*, 2013). The topography under the Amery Ice Shelf was sourced from the RTOPO dataset with modification. However, when the BEDMAP2 dataset is compared with RTOPO dataset, the topography is approximately 1000 metres too shallow under a significant portion of the ice shelf. This causes the water column under the ice shelf at the southern grounding line to be less than 2 metres deep (Figure S5.2a) which leads to the grounding line immediately advancing in preliminary numerical model runs. To remedy this, the topography of BEDMAP2 was replaced by the RTOPO topography under the ice shelf.

To create the new topography, the ice shelf mask was used to remove the BEDMAP2 topography. A second mask was created by shrinking the extent of the ice shelf mask in by approximately 5 km. This second mask was used to crop and insert the RTOPO dataset into the original topography, with linear interpolation joining the two datasets (Figure S5.2b). The resulting changes in the bed topography are shown in Figure S5.2c. The final topography is shown in Figure S5.3.

The ice thickness used was as per original BEDMAP2, as any impact changing the topography may have on the surface elevation would be minor as the ice thickness will evolve during the model runs and smooth out any changes.

Surface Mass Balance and Surface Temperature

The surface mass balance (Figure S5.4a) and surface temperature fields (Figure S5.4b) are sourced from the RACMO 2.3 ANT27\2 dataset. An average over the model run of 1979–2013 is used. Minor modifications are made to the surface mass balance field, with many of the rock outcrop zones sub–grid scale for the RACMO2.3 resolution. There is no wind ablation included in the PISM surface model so precipitation on rock outcrops can lead to ice growth in regions which are known to be ice free. To ensure that ice free regions remain ice free during model runs, the surface mass balance over these locations was set to be -50 kg m^{-2} $year^{-1}$.

Geothermal Heat Flux

The geothermal heat flux (Figure S5.5) for the regional domain was created by using *Fox Maule et al.* (2005) with an updated magnetic field model (MF7). It was chosen as the most recent release, however, we found no information to guide this choice, which lead to the study of the effect of GHF.

Initial Boundary Conditions

Initial values for the enthalpy, water content of the till (tillwat) and shallow shelf approximation velocities (ssa_u, ssa_v) are needed to initialise the regional model. A

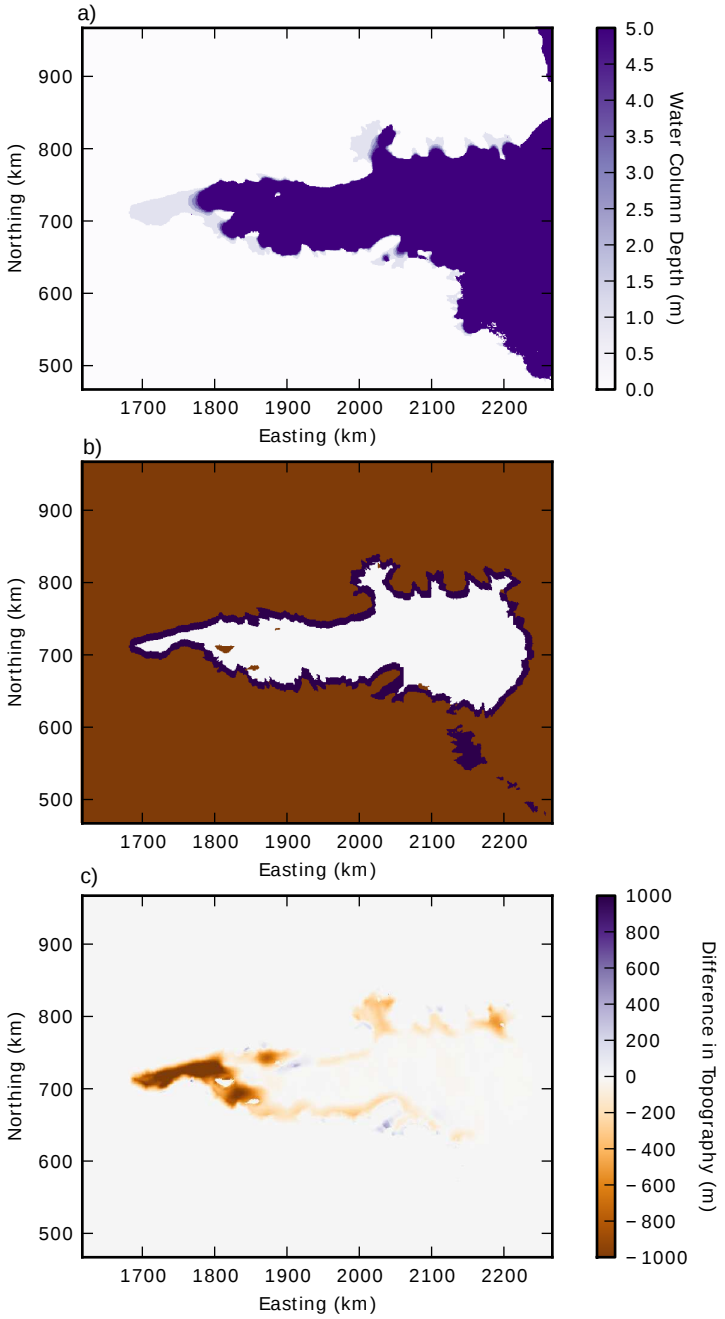

Figure S5.2: a) The difference between ice draft and the bedrock topography of the BEDMAP2 dataset (*Fretwell et al.*, 2013). b) White is the region where RTOPO was inserted, brown is the region where BEDMAP2 was retained, with blue the region of interpolation. c) The difference between the new topography and the BEDMAP2 topography.

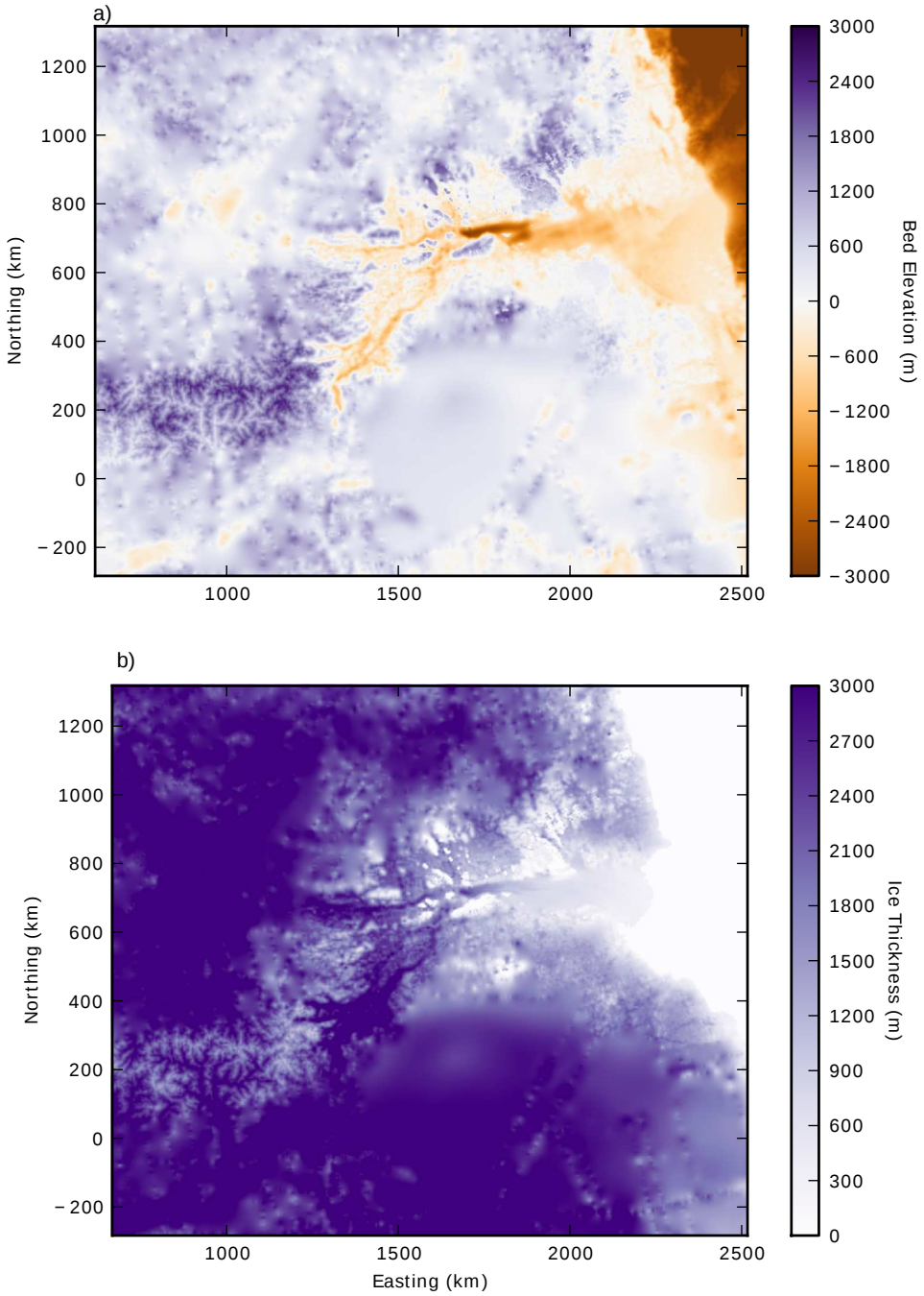

Figure S5.3: a) Final topography used in the regional model. b) The final ice thickness used in the regional model.

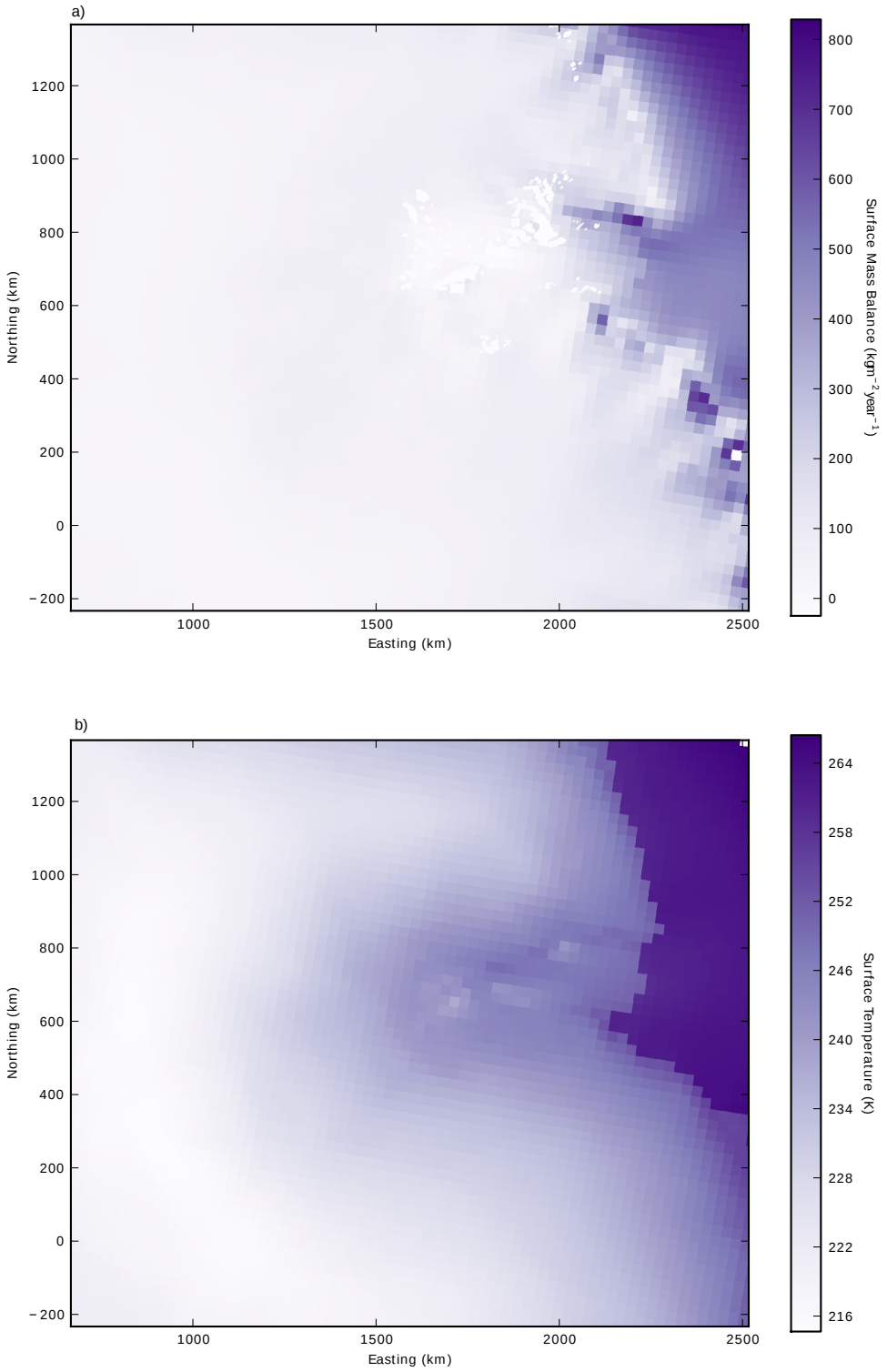

Figure S5.4: a) Surface mass balance field final input. b) Surface temperature final input.

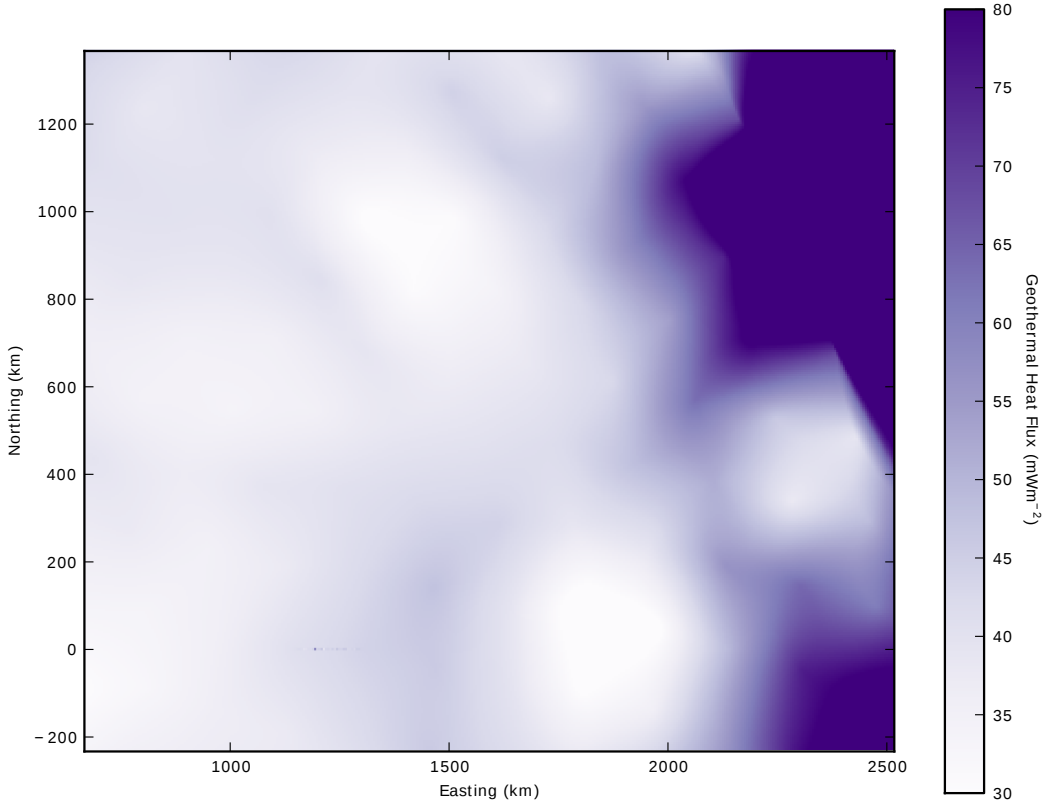

Figure S5.5: Geothermal Heat Flux field final input.

low resolution (20 km) whole Antarctic domain model run was initialised for 200 years using BEDMAP2 and RACMO2.3 unmodified datasets in addition to the modified basal melt rates. From the 200 year output file, an initial condition file was created with the enthalpy, tillwat, and new variables ssa_u_bc and ssa_v_bc, to be used to initialise these variables in the high resolution regional model.

Vertical Resolution Testing

PISM has three options which control the vertical resolution: max vertical extent (-Lz), number of layers (-Mz) and layer spacing (Equal or Quadratic). An optimisation experiment was conducted to determine the ideal balance between computational efficiency and quality of solution. The max vertical extent was set to 4500m, as ice should not be thicker than this within our domain. The four different layer counts (150, 300, 600 and 1200) combined with both types of layer spacing are tested. The model was run for 50,000 years with the parameters in table S5.2-S5.4. The data sources were the same as for the SEARISE experiments with the exception that the topopgraphy and ice thickness were updated to BEDMAP2. The ftt_mask used was the initial ftt_mask and the domain is slightly smaller. Four locations in Lambert-Amery glacial system were chosen to view the vertical temperature profile representative of different locations (Figure S5.6).

For each vertical profile the temperature converged with increasing resolution inde-

Table S5.2: List of resolution parameters used in PISM input file for regional model used in vertical resolution testing (other parameters not listed here are left at default values from user manual from http://www.pism-docs.org/wiki/doku.php, date accessed 20/02/2015).

Paramater	**Value**	**Description**
Mx	115	Number of cells in Easting direction.
My	107	Number of cells in the Northing direction.
Mbz	11	Number of Vertical Layers in the lithosphere.
Lz	4,500	Height of vertical domain.
Lbz	2,000	Height of Lithosphere, creating a 200 m vertical resolution.
no_model_strip	30	Sets a 10 km strip around the domain where the model is kept constant.

Table S5.3: List of initial parameters used in PISM input file for regional model optimisation experiments.

Paramater	**Value**	**Description**
sia_e	3	The value of the shallow ice enhancement factor for anisotropy.
ssa_e	0.6	The value of the shallow shelf enhancement factor anisotropy.
pseudo_plastic_q	0.25	Default value for the pseudo plastic flow law.
topg_to_phi	15.0,40.0,-2000.0,4500.0	Sets a piecewise linear function for till angle based on depth of the topography. At -2000 bedrock depth, till angle is 15, which changes linearly to 4500 depth where the till angle is 40.

Table S5.4: List of parameters used in PISM input file for regional model (other parameters not listed here are left at default values from user manual from http://www.pism-docs.org/wiki/doku.php, date accessed 20/02/2015).

Paramater	**Value**	**Description**
sia_flow_law	gpbld	Sets the shallow ice approximation flow law to Glen-Paterson-Budd-Lliboutry-Duval (*Lliboutry and Duval*, 1985).
ssa_flow_law	gpbld	Sets the shallow shelf approximation flow law to Glen-Paterson-Budd-Lliboutry-Duval (*Lliboutry and Duval*, 1985).
pseudo_plastic		Sets the sliding law to be pseudo plastic (See PISM User's Manual, Equation 4.)
hydrology	null	The simple hydrology model was used.
surface	simple,forcing	Calculates a SMB based on input precipitation as well as forcing it to stay constant in the region within the ftt mask (Figure S5.1).
stress_balance	ssa+sia	Sets the model to use the hybrid physics scheme.
calving	thickness_calving, ocean_kill	Sets calving to automatically occur when thickness set by thickness_calving_threshold or it extends out past the ice shelf floating mask from observations.
thickness_calving-_threshold	50	
pik		Sets options -cfbc -kill_icebergs -part_grid -part_redist -subgl developed by *Martin et al.* (2011); *Winkelmann et al.* (2011); *Feldmann et al.* (2014).
ocean	pik	Sets default melting in PISM ocean melt parametrisation given by '-meltfactor_pik 0.005'.
tauc_slippery-_grounding_lines		Sets the model to treat the cell just upstream of the grounding line as having maximum amount of till-stored water for a slippery bed.

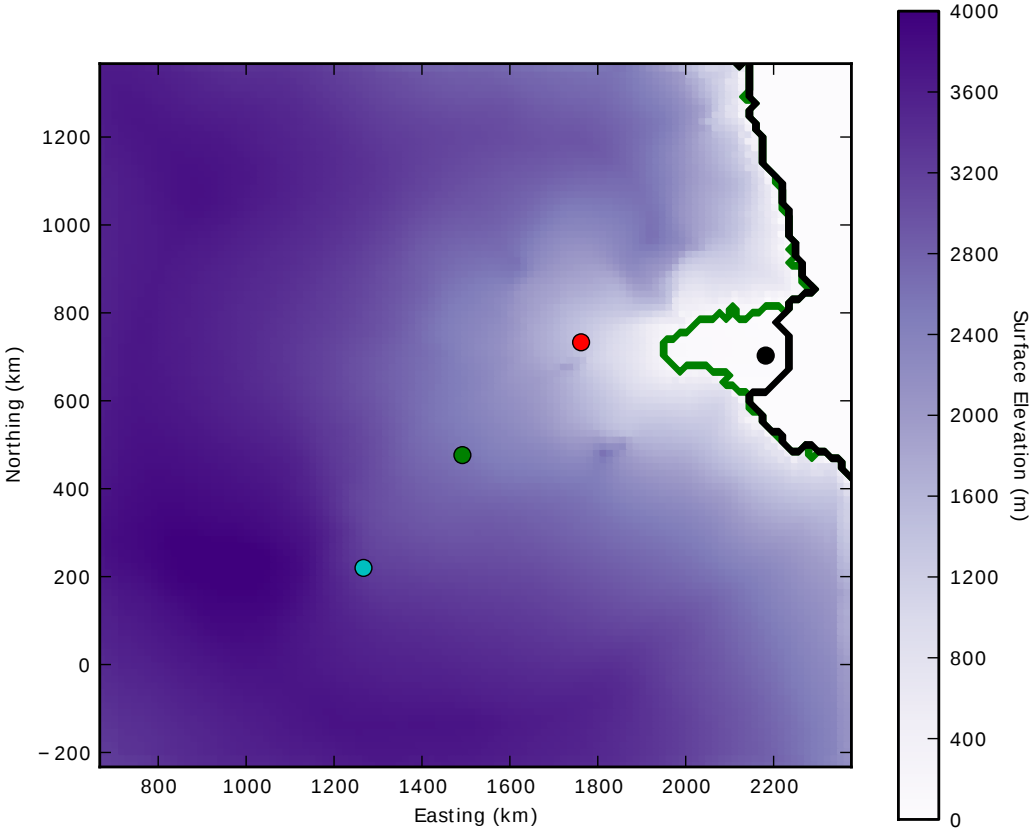

Figure S5.6: The location of the vertical temperature profiles comparing the different types and resolution in the vertical coordinates.

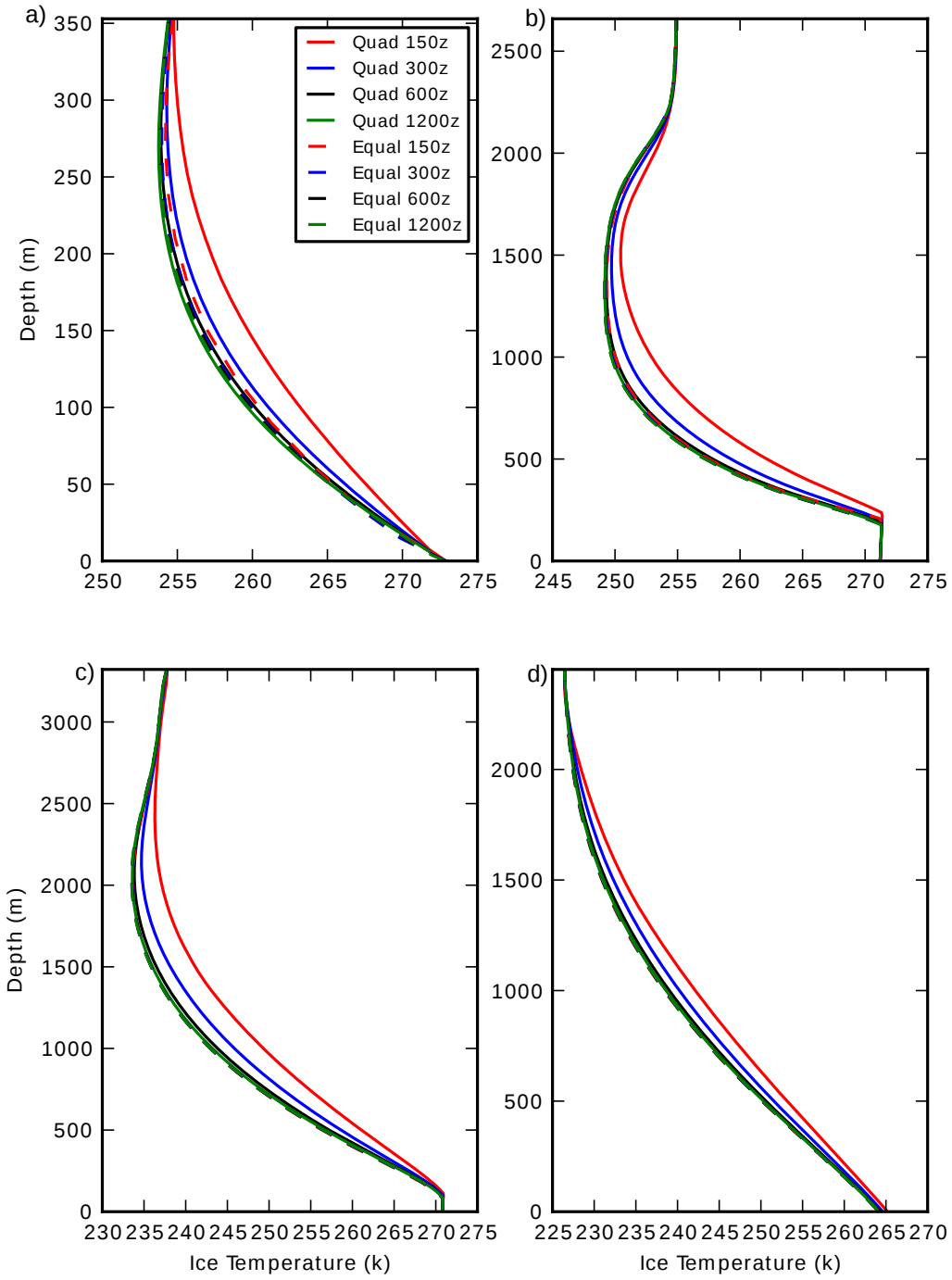

Figure S5.7: Temperature with Depth at 50,000 years. a) Black dot on Figure S5.6. b) Red dot on S5.6. c) Green dot on figure S5.6. d) Blue dot on figure S5.6.

pendent of the layer spacing (Figure S5.7), however, the equal layered case converged quicker, with the 300 layered equal case showing better agreement with the 1200 layered cases than the 600 quadratic case. This indicates that using the 300 equal layers provides a temperature curve that is representative of the 1200 equal layers experiment, but at substantially lower computational cost and therefore is the most efficient choice for the Lambert-Amery glacial system regional domain.

Oceanic Basal Melt

Oceanic sub-ice shelf basal melt within PISM can be via either an input field or inbuilt parametrisations. Using an input field with an evolving ice shelf is not ideal, because if the grounding line advances, the initial high melt rates at the grounding line do not track with the advancement as their distribution is spatially fixed leading to rapid advancement as the melt rates decrease. The default PISM parametrisation is presented in *Martin et al.* (2011). It has a linear profile which results in a small difference between melt rates at the front of the ice shelf compared to the grounding line (Figure S5.8, line for gradient demonstration). An ocean model of the cavity below the Amery Ice Shelf predicts oceanic basal melt rates in excess 20 m year^{-1} at the grounding line, with very small basal melt, and even marine ice growth, near the ice front. To scale the inbuilt parametrisation to match the high melt rates at the grounding line and low melt rates at the front, a scaling factor was designed. The scaling factor chosen was $(\frac{thk}{1800})^3$, and some iterative optimising was done (not shown), however, the final solution was chosen based on its average melt rate compared to the ocean model, and the the approximate fit to the data of the oceanic model (Figure S5.8). The oceanic models average melt rate was 0.78 m year^{-1} and the new scaled parametrisation with initial BEDMAP2 ice thickness is 0.80 m year^{-1}. The scaled parametrisation has higher melt rates near the grounding line, however, this is not seen as unrealistic as melt rates over 30 m year^{-1} have been modelled and it's possible that they could be higher than that at the grounding line (*Galton-Fenzi et al.*, 2012). Figure S5.9 shows a comparison between the oceanic model and the parametrisation. The scalar melt rate does not capture the asymmetrical melt patterns in the oceanic model that form due to the warm inflow along the east leading to higher melt rates, and the colder outflow leading to lower melt rates along the western boundary, however, it does capture similar basal melts rates near the grounding line.

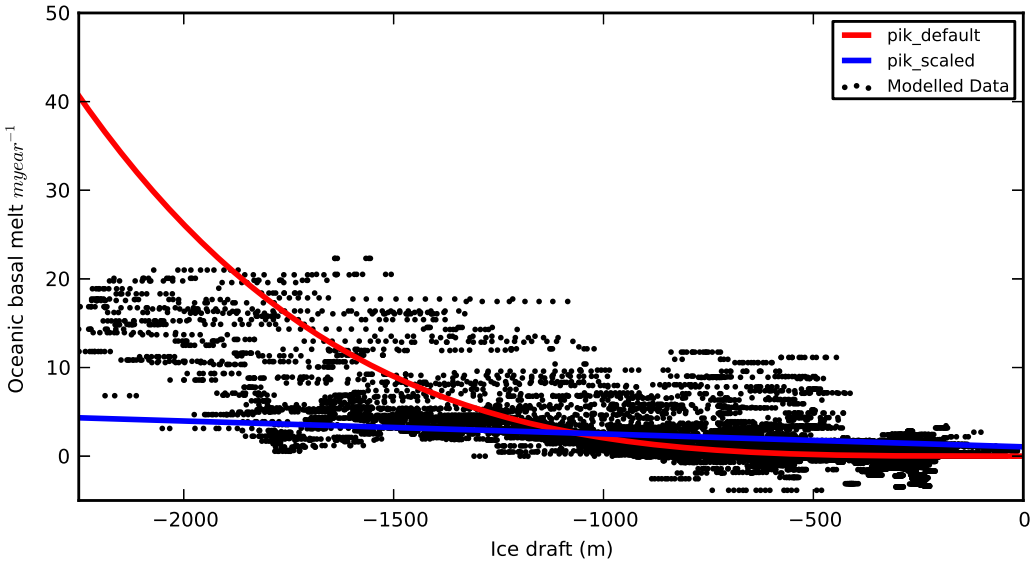

Figure S5.8: Oceanic basal melt rates of the oceanic model and the two parametrisations.

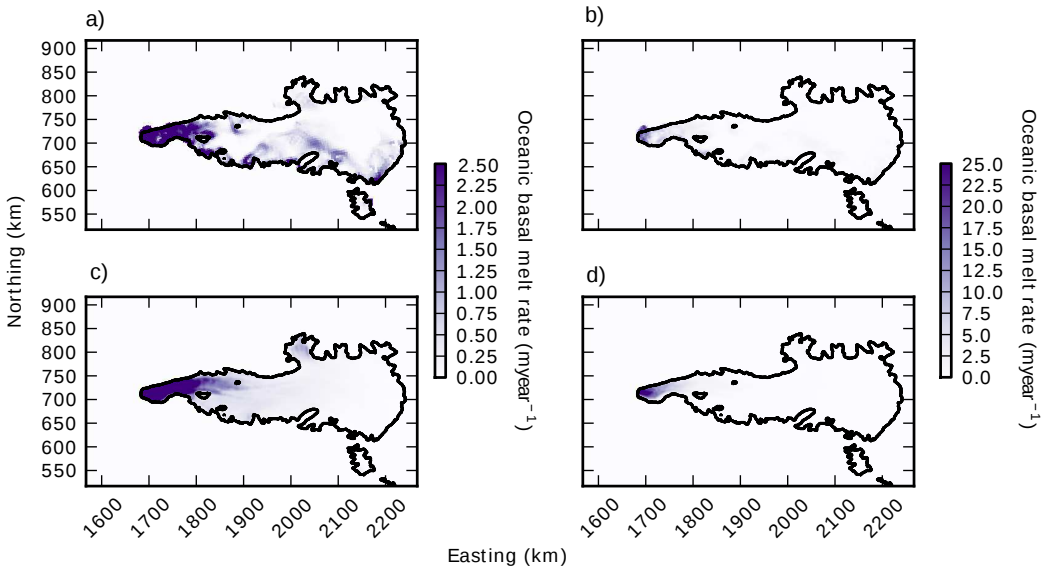

Figure S5.9: Oceanic basal melt rates from the *Galton-Fenzi et al.* (2012) ocean model for a) Low melt focus and b) High melt focus. Oceanic basal melt rates from the Scalar parametrisation for c) Low melt focus and d) High melt focus.

Appendix E: Supplementary Information Chapter 7

Regional Model

Drainage Basin

The regional domain was identified using PISM drainage basin delineation tool See PISM User's Manual (Figure 1). The region outside the drainage basin, but within the domain is held at a constant elevation by modifying the surface mass balance.

Bed Topography

The bed topography used by the regional model of the Lambert-Amery glacial system is a combination of Bedmap2 for grounded ice, and RTOPO (*Timmermann et al.*, 2010) beneath the floating ice, with a 5km region of interpolation seaward of the grounding line to join the two datasets. This was performed as two seismic data points which were excluded from RTOPO on the rear of the Amery Ice Shelf were included in bedmap2. They were calculated to have an ice draft deeper than the bed topography data points measured, and hence were not included in the RTOPO dataset which included the improved ocean cavity data from (*Galton-Fenzi et al.*, 2008). These were included in the Bedmap2 dataset, which led to the initial thickness of the water column beneath the rear of ice shelf to be less the 2 m thick. This led to the grounding line rapidly advancing in initial model simulations, making it untenable to use in our simulations.

Ocean Melt parametrisation

Oceanic sub-ice shelf basal melt within PISM can be via either an input field or inbuilt parametrisations. Using an input field with an evolving ice shelf is not ideal, because if the grounding line advances, the initial high melt rates at the grounding line do not track with the advancement as their distribution is spatially fixed leading to rapid advancement as the melt rates decrease. The default PISM parametrisation is presented in *Martin et al.* (2011). It has a linear profile which results in a small difference between melt rates at the front of the ice shelf compared to the grounding line (Figure S7.1, line for gradient demonstration). An ocean model of the cavity below the Amery Ice Shelf predicts oceanic basal melt rates in excess 20 m year^{-1} at the grounding line, with very small basal melt, and even marine ice growth, near the ice front. To scale the inbuilt parametrisation to match the high melt rates at the grounding line and low melt rates at the front, a scaling factor was designed. The scaling factor chosen was $(\frac{thk}{1800})^3$, and some iterative optimising was done (not shown), however, the final solution was chosen based on its average melt rate compared to the ocean model, and the the approximate fit to the data of the oceanic model (Figure S7.1). The oceanic models average melt rate was 0.78 m year^{-1} and the new scaled parametrisation with initial BEDMAP2 ice thickness is 0.80 m year^{-1}. The scaled parametrisation has higher melt rates near the grounding line, however, this is not

seen as unrealistic as melt rates over 30 m year^{-1} have been modelled and it's possible that they could be higher than that at the grounding line (*Galton-Fenzi et al.*, 2012). Figure S7.2 shows a comparison between the oceanic model and the parametrisation. The scalar melt rate does not capture the asymmetrical melt patterns in the oceanic model that form due to the warm inflow along the east leading to higher melt rates, and the colder outflow leading to lower melt rates along the western boundary, however, it does capture similar basal melts rates near the grounding line.

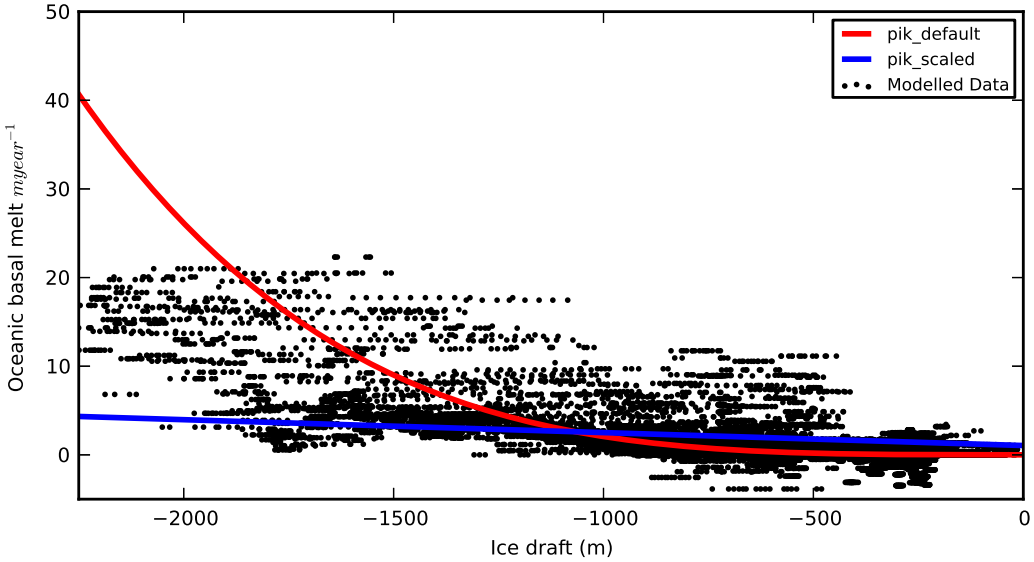

Figure S7.1: Oceanic basal melt rates of the oceanic model and the two parametrisations.

Surface mass balance and ice surface temperatures

The surface mass balance and ice surface temperatures are from RACMO 2.3 (*van Wessem et al.*, 2014), 1979-2013 average. Minor modifications were made over ice free regions to ensure they stayed ice free by introducing a negative mass balance on the Bedmap2 rock mask.

Geothermal Flux

The geothermal heat flux used is an update to the magnetic field sourced dataset (*Fox Maule et al.*, 2005), using the Field Model 7.

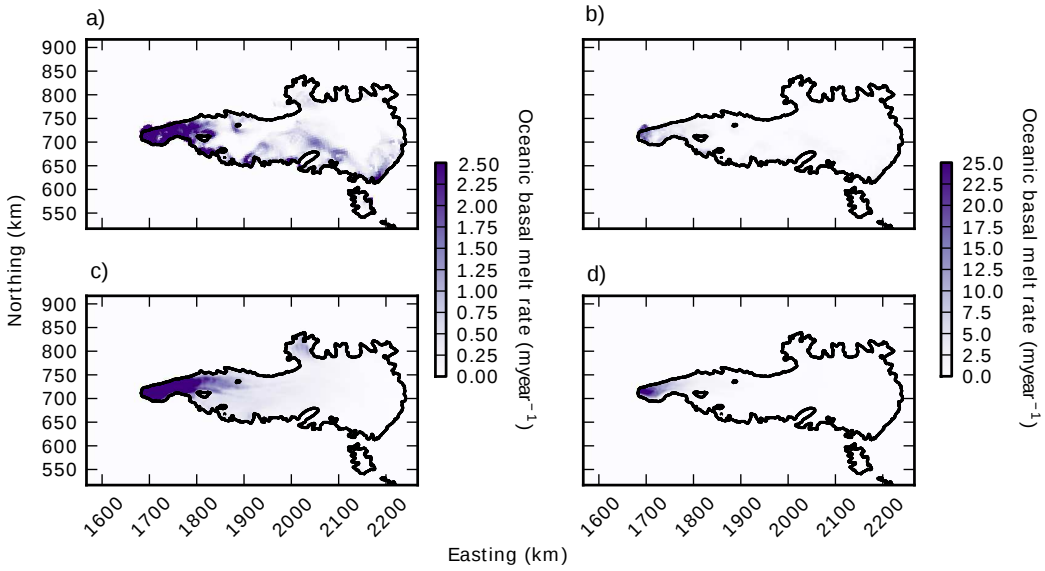

Figure S7.2: Oceanic basal melt rates from the *Galton-Fenzi et al.* (2012) ocean model for a) Low melt focus and b) High melt focus. Oceanic basal melt rates from the Scalar parametrisation for c) Low melt focus and d) High melt focus.

Initialisation of Regional domain

The domain was optimised by varying four variables (listed in table 1) consecutively and then in conjunction with each other guided by the initial experiments to optimise the simulated domain to match grounding line location, ice thickness (Bedmap2) and surface velocity (MEaSUREs (*Rignot et al.*, 2011a)) for the shallow shelf enhancement factor, shallow ice enhancement factor, quotient in the sliding power law (Table S7.1 and parametrisation of till strength (Table S7.2)).

Final Parameters

The final set of parameters used to control the evolution of the ice sheet model, PISM are shown in Tables 3-5. Figure 1 shows the comparison between the control model and observations.

Table S7.1: List of initial optimisation values, tested values, and final values and description used in PISM input file for regional model.

Parameter	Initial	Optimisation values	Final Value	Description
sia_e	3	3.3, 2.7, 2.4, 2.1, 1.8	1.8	The value of the shallow ice enhancement factor for anisotropy.
ssa_e	1	0.7, 1.3, 1.6	1.6	The value of the shallow shelf enhancement factor for anisotropy.
pseudo_plastic_q	0.25	0, 0.375, 0.5, 0.75	0.5	Value for the pseudo plastic flow law (Equation 4, See PISM User's Manual.)
topg_to_phi	5,20,-1000,0	See Table 2	10,30,-1500,-500	Sets a piecewise linear function for till angle based on depth of the topography. At -1500 bedrock depth (topg_min), till angle is 10 (phi_min), which changes linear to -500 depth (topg_max) where the till angle is 30 (phi_max).
eigen_calving_k	1.00e+15	1.90e+15	1.90e+15, 1e+16	Threshold for eigen calving.
thickness_calving-_threshold	200	175, 225, 250	225	Threshold for thickness calving.

Table S7.2: List of Optimisation values for the topg_to_phi paramater.

topg_min	topg_max	phi_min	phi_max
-1000.0	0	5	20
-1000.0	0	5	30
-1000.0	0	15	30
-1500.0	-500	5	20
-500.0	500	5	20
-1500.0	500	5	30
-1000.0	0	5	40
-1500.0	-500	5	30
-1250.0	-250	10	30

Table S7.3: List of domain parameters used in PISM input file for regional model (other parameters not listed here are left at default values from user manual from http://www.pism-docs.org/wiki/doku.php, date accessed 20/02/2015).

Paramater	**Value**	**Description**
Mx	371	With domain width of 1850 km this creates a 5km resolution.
My	321	With domain height of 1600 km this creates a 5km resolution.
Myz	300	300 vertical layers.
Mbz	11	Number of vertical layers in the lithosphere.
Lz	4,500	Height of vertical domain, creating 15 m resolution vertical resolution.
Lbz	2,000	Height of Lithospheric domain, creating a 200 m vertical resolution.
no_model_strip	10	Sets a 10 km strip around the domain where the model is kept constant.

Table S7.4: List of stress parameters used in PISM input file for regional model (other parameters not listed here are left at default values from user manual from http://www.pism-docs.org/wiki/doku.php, date accessed 20/02/2015).

Paramater	**Value**	**Description**
stress_balance	ssa+sia	Sets the flow physics model to use the hybrid physics scheme
sia_flow_law	gpbld	Sets the shallow ice approximation flow law to Glen-Paterson-Budd-Lliboutry-Duval (*Lliboutry and Duval*, 1985).
ssa_flow_law	gpbld	Sets the shallow shelf approximation flow law to Glen-Paterson-Budd-Lliboutry-Duval (*Lliboutry and Duval*, 1985).
pseudo_plastic		Sets the sliding law to be follow a pseudo plastic law (Equation 4, See PISM User's Manual.)

Table S7.5: List of physical parameters used in PISM input file for regional model (other parameters not listed here are left at default values from user manual from http://www.pism-docs.org/wiki/doku.php, date accessed 20/02/2015).

Paramater	**Value**	**Description**
hydrology	null	Simple hydrological model where a 2 m till can be filled my local meltwater, but if it reaches 2 m and further melting is simply lost.
surface	given,forcing	Given directs the model to use the data from an input file. Forcing sets the ftt mask which then holds thickness close to constant by modifying the surface mass balance.
calving	thickness_calving, eigen_calving	thickness_calving sets a thickness limit where ice below this thickness is calved. Eigen_calving sets a calving rate based on principal strain rates (*Levermann et al.*, 2012).
pik		Sets options -cfbc -kill_icebergs -part_grid -part_redist -subgl developed by (*Martin et al.*, 2011; *Winkelmann et al.*, 2011; *Feldmann et al.*, 2014)
ocean	pik	Ocean melt parametrisation.
tauc_slippery-_grounding_lines		Reduces basal yield stress at grounded below sea level grid points one cell away from floating ice or ocean.

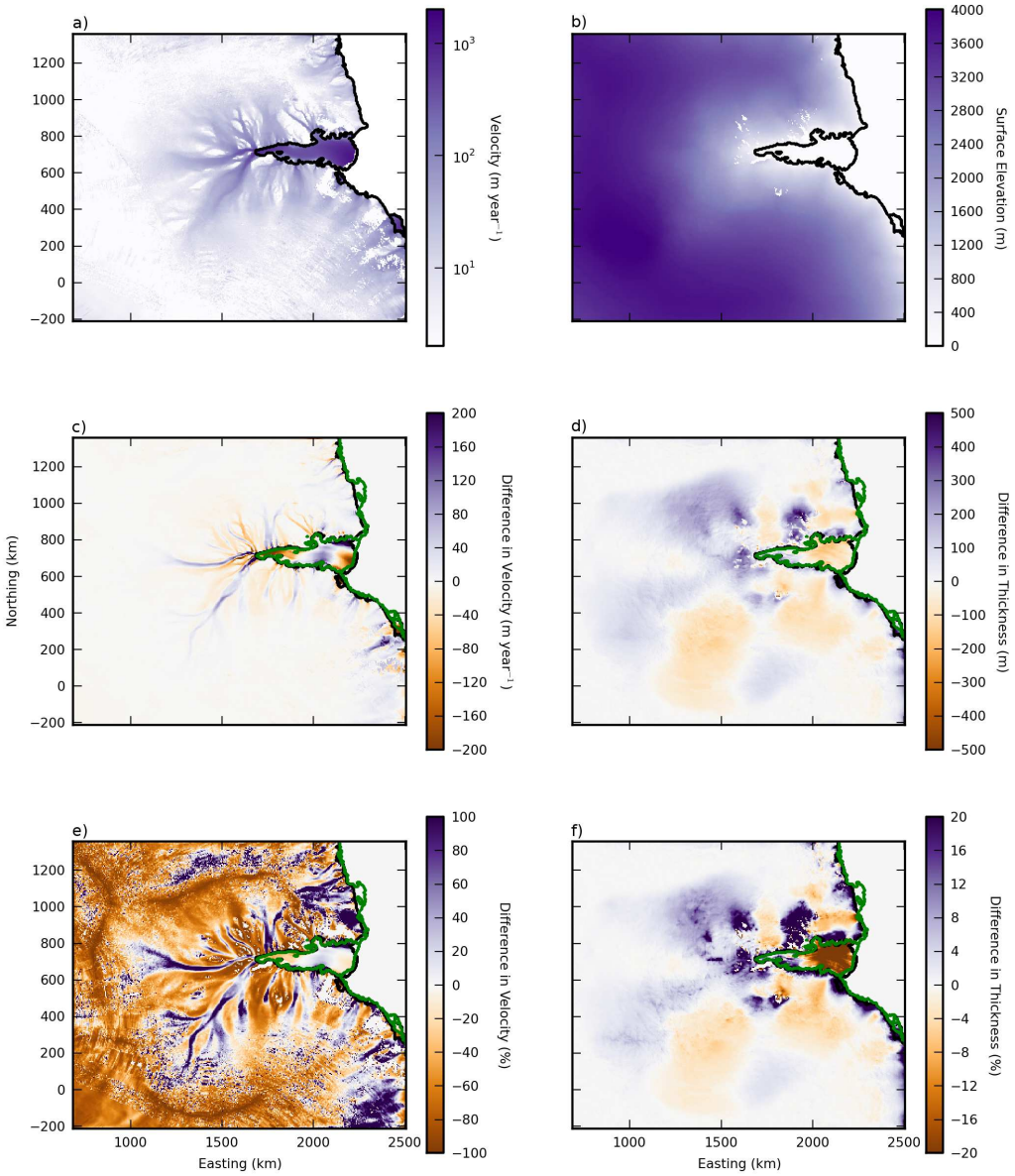

Figure S7.3: a) The MEaSUREs surface velocities (*Rignot et al.*, 2011b). b)The Bedmap2 ice thickness (*Fretwell et al.*, 2013). c) The difference between the control solution and the MEaSUREs velocities. d) The difference between the control solution and the Bedmap2 ice thickness. e) The percentage difference between the control solution and the MEaSUREs velocities (*Rignot et al.*, 2011b). f) The percentage difference between the control solution and the Bedmap2 ice thickness. The Bedmap2 ice shelf and coastline is outlined in black, the control solution's ice shelf and coastline is shown in green.

References

Allison, I. (1979), The mass budget of the Lambert Glacier drainage basin, Antarctica, *Journal of Glaciology*, *22*, 223–235.

Amundson, J. M., M. Fahnestock, M. Truffer, J. Brown, M. P. Lüthi, and R. J. Motyka (2010), Ice mélange dynamics and implications for terminus stability, Jakobshavn Isbræ, Greenland, *Journal of Geophysical Research: Earth Surface*, *115*, F01005, doi: 10.1029/2009JF001405.

An, M., D. A. Wiens, Y. Zhao, M. Feng, A. Nyblade, M. Kanao, Y. Li, A. Maggi, and J.-J. Lévêque (2015), Temperature, lithosphere-asthenosphere boundary, and heat flux beneath the Antarctic Plate inferred from seismic velocities, *Journal of Geophysical Research: Solid Earth*, *120*(12), 8720–8742, doi: 10.1002/2015JB011917.

Annan, J. D., and J. C. Hargreaves (2013), A new global reconstruction of temperature changes at the Last Glacial Maximum, *Climate of the Past*, *9*(1), 367–376, doi: 10.5194/cp-9-367-2013.

Asay-Davis, X. S., S. L. Cornford, G. Durand, B. K. Galton-Fenzi, R. M. Gladstone, G. H. Gudmundsson, T. Hattermann, D. M. Holland, D. Holland, P. R. Holland, D. F. Martin, P. Mathiot, F. Pattyn, and H. Seroussi (2015), Experimental design for three interrelated Marine Ice-Sheet and Ocean Model Intercomparison Projects, *Geoscientific Model Development Discussions*, *8*, 9859–9924, doi: 10.5194/gmdd-8-9859-2015.

Aschwanden, A., E. Bueler, C. Khroulev, and H. Blatter (2012), An enthalpy formulation for glaciers and ice sheets, *Journal of Glaciology*, *58*(209), 441–457, doi: 10.3189/2012JoG11J088.

Bamber, J. L., R. E. M. Riva, B. L. A. Vermeersen, and A. M. LeBrocq (2009), Reassessment of the Potential Sea-Level Rise from a Collapse of the West Antarctic Ice Sheet, *Science*, *324*, 901, doi: 10.1126/science.1169335.

Bell, R. E. (2008), The role of subglacial water in ice-sheet mass balance, *Nature Geoscience*, *1*, 297–304, doi: 10.1038/ngeo186.

Bell, R. E., M. Studinger, C. A. Shuman, M. A. Fahnestock, and I. Joughin (2007),

Large subglacial lakes in East Antarctica at the onset of fast-flowing ice streams, *Nature*, *445*, 904–907, doi: 10.1038/nature05554.

Bindschadler, R., H. Choi, A. Wichlacz, R. Bingham, J. Bohlander, K. Brunt, H. Corr, R. Drews, H. Fricker, M. Hall, R. Hindmarsh, J. Kohler, L. Padman, W. Rack, G. Rotschky, S. Urbini, P. Vornberger, and N. Young (2011), Getting around Antarctica: new high-resolution mappings of the grounded and freely-floating boundaries of the Antarctic ice sheet created for the International Polar Year, *The Cryosphere*, *5*(3), 569–588, doi: 10.5194/tc-5-569-2011.

Bindschadler, R. A., S. Nowicki, A. Abe-Ouchi, A. Aschwanden, H. Choi, J. Fastook, G. Granzow, R. Greve, G. Gutowski, U. Herzfeld, C. Jackson, J. Johnson, C. Khroulev, A. Levermann, W. H. Lipscomb, M. A. Martin, M. Morlighem, B. R. Parizek, D. Pollard, S. F. Price, D. Ren, F. Saito, T. Sato, H. Seddik, H. Seroussi, K. Takahashi, R. Walker, and W. L. Wang (2013), Ice-sheet model sensitivities to environmental forcing and their use in projecting future sea level (the SeaRISE project), *Journal of Glaciology*, *59*, 195–224, doi: 10.3189/2013JoG12J125.

Boening, C., M. Lebsock, F. Landerer, and G. Stephens (2012), Snowfall-driven mass change on the East Antarctic Ice Sheet, *Geophysical Research Letters*, *39*(21), L21501, doi: 10.1029/2012GL053316.

Budd, W., and T. Jacka (1989), A review of ice rheology for ice sheet modelling, *Cold Regions Science and Technology*, *16*(2), 107 – 144, doi: 10.1016/0165-232X(89)90014-1.

Budd, W., M. Corry, and T. Jacka (1982), Results from the Amery Ice Shelf Project, *Annals of Glaciology*, *3*, 36–41.

Budd, W. F., R. C. Warner, T. H. Jacka, J. Li, and A. Treverrow (2013), Ice flow relations for stress and strain-rate components from combined shear and compression laboratory experiments, *Journal of Glaciology*, *59*, 374–392, doi: 10.3189/2013JoG12J106.

Bueler, E., and J. Brown (2009), Shallow shelf approximation as a sliding law in a thermomechanically coupled ice sheet model, *Journal of Geophysical Research (Earth Surface)*, *114*, 3008, doi: 10.1029/2008JF001179.

Bueler, E., J. Brown, and C. Lingle (2007), Exact solutions to the thermomechanically coupled shallow-ice approximation: effective tools for verification, *Journal of Glaciology*, *53*, 499–516, doi: 10.3189/002214307783258396.

Carson, C. J., and M. L. Pittard (2012), *A Reconaissance Crustal Heat Production Assessment of the Australian Antarctic Territory (AAT)*, Geoscience Australia.

Carson, C. J., S. McLaren, J. L. Roberts, S. D. Boger, and D. D. Blankenship (2014), Hot rocks in a cold place: high sub-glacial heat flow in East Antarctica, *Journal of the Geological Society*, *171*(1), 9–12, doi: 10.1144/jgs2013-030.

Carson, M., A. Köhl, D. Stammer, A. B. A. Slangen, C. A. Katsman, R. S. W. van de Wal, J. Church, and N. White (2016), Coastal sea level changes, observed and projected during the 20th and 21st century, *Climatic Change*, *134*(1), 269–281, doi: 10.1007/s10584-015-1520-1.

Cazenave, A., and W. Llovel (2010), Contemporary Sea Level Rise, *Annual Review of Marine Science*, *2*, 145–173, doi: 10.1146/annurev-marine-120308-081105.

Church, J., and N. White (2011), Sea-Level Rise from the Late 19th to the Early 21st Century, *Surveys in Geophysics*, *32*, 585–602, doi: 10.1007/s10712-011-9119-1.

Church, J. A., P. U. Clark, A. Cazenave, J. M. Gregory, S. Jevrejeva, A. Levermann, M. A. Merrifield, G. A. Milne, R. S. Nerem, P. D. Nunn, et al. (2013), Sea level change, *Tech. rep.*, PM Cambridge University Press.

Clark, P. U., J. A. Church, J. M. Gregory, and A. J. Payne (2015), Recent progress in understanding and projecting regional and global mean sea level change, *Current Climate Change Reports*, *1*(4), 224–246, doi: 10.1007/s40641-015-0024-4.

Cornford, S. L., D. F. Martin, D. T. Graves, D. F. Ranken, A. M. Le Brocq, R. M. Gladstone, A. J. Payne, E. G. Ng, and W. H. Lipscomb (2013), Adaptive mesh, finite volume modeling of marine ice sheets, *Journal of Computational Physics*, *232*, 529–549, doi: 10.1016/j.jcp.2012.08.037.

Craven, M., I. Allison, R. Brand, A. Elcheikh, J. Hunter, M. Hemer, and S. Donoghue (2004), Initial borehole results from the Amery Ice Shelf hot-water drilling project, *Annals of Glaciology*, *39*, 531–539, doi: 10.3189/172756404781814311.

Cuffey, K. M., and W. S. B. Paterson (2010), *The physics of glaciers*, Academic Press.

Davis, C. H., Y. Li, J. R. McConnell, M. M. Frey, and E. Hanna (2005), Snowfall-Driven Growth in East Antarctic Ice Sheet Mitigates Recent Sea-Level Rise, *Science*, *308*, 1898–1901, doi: 10.1126/science.1110662.

DeConto, R. M., and D. Pollard (2016), Contribution of Antarctica to past and future sea-level rise, *Nature*, *531*(7596), 591–597, doi: 10.1038/nature17145.

Domack, E., P. O'Brien, P. Harris, F. Taylor, P. G. Quilty, L. D. Santis, and B. Raker (1998), Late Quaternary sediment facies in Prydz Bay, East Antarctica and their relationship to glacial advance onto the continental shelf, *Antarctic Science*, *10*, 236–246, doi: 10.1017/S0954102098000339.

Dupont, T., and R. Alley (2005), Assessment of the importance of ice-shelf buttressing to ice-sheet flow, *Geophysical Research Letters*, *32*(4), L04,503.

Favier, L., O. Gagliardini, G. Durand, and T. Zwinger (2012), A three-dimensional full Stokes model of the grounding line dynamics: effect of a pinning point beneath the ice shelf, *The Cryosphere*, *6*, 101–112, doi: 10.5194/tc-6-101-2012.

Feldmann, J., T. Albrecht, C. Khroulev, F. Pattyn, and A. Levermann (2014), Resolution-dependent performance of grounding line motion in a shallow model compared with a full-Stokes model according to the MISMIP3d intercomparison, *Journal of Glaciology*, *60*, 353–360, doi: 10.3189/2014JoG13J093.

Fisher, A. T., K. D. Mankoff, S. M. Tulaczyk, S. W. Tyler, N. Foley, and the WISSARD Science Team (2015), High geothermal heat flux measured below the West Antarctic Ice Sheet, *Science Advances*, *1*(6), doi: 10.1126/sciadv.1500093.

Fox Maule, C., M. E. Purucker, N. Olsen, and K. Mosegaard (2005), Heat Flux Anomalies in Antarctica Revealed by Satellite Magnetic Data, *Science*, *309*(5733), 464–467, doi: 10.1126/science.1106888.

Fretwell, P., H. D. Pritchard, D. G. Vaughan, J. L. Bamber, N. E. Barrand, R. Bell, C. Bianchi, R. G. Bingham, D. D. Blankenship, G. Casassa, G. Catania, D. Callens, H. Conway, A. J. Cook, H. F. J. Corr, D. Damaske, V. Damm, F. Ferraccioli, R. Forsberg, S. Fujita, Y. Gim, P. Gogineni, J. A. Griggs, R. C. A. Hindmarsh, P. Holmlund, J. W. Holt, R. W. Jacobel, A. Jenkins, W. Jokat, T. Jordan, E. C. King, J. Kohler, W. Krabill, M. Riger-Kusk, K. A. Langley, G. Leitchenkov, C. Leuschen, B. P. Luyendyk, K. Matsuoka, J. Mouginot, F. O. Nitsche, Y. Nogi, O. A. Nost, S. V. Popov, E. Rignot, D. M. Rippin, A. Rivera, J. Roberts, N. Ross, M. J. Siegert, A. M. Smith, D. Steinhage, M. Studinger, B. Sun, B. K. Tinto, B. C. Welch, D. Wilson, D. A. Young, C. Xiangbin, and A. Zirizzotti (2013), Bedmap2: improved ice bed, surface and thickness datasets for Antarctica, *The Cryosphere*, *7*, 375–393, doi: 10.5194/tc-7-375-2013.

Frezzotti, M., A. Capra, and L. Vittuari (1998), Comparison between glacier ice velocities inferred from GPS and sequential satellite images, *Annals of Glaciology*, *27*, 54–60.

Fricker, H. A., I. Allison, M. Craven, G. Hyland, A. Ruddell, N. Young, R. Coleman, M. King, K. Krebs, and S. Popov (2002), Redefinition of the Amery Ice Shelf, East Antarctica, grounding zone, *Journal of Geophysical Research (Solid Earth)*, *107*, 2092, doi: 10.1029/2001JB000383.

Frieler, K., P. U. Clark, F. He, C. Buizert, R. Reese, S. R. M. Ligtenberg, M. R. van den Broeke, R. Winkelmann, and A. Levermann (2015), Consistent evidence of increasing Antarctic accumulation with warming, *Nature Climate Change*, *5*, 348–352, doi: 10.1038/nclimate2574.

Galton-Fenzi, B. (2009), Modelling ice-shelf/ocean interaction, Ph.D. thesis, University of Tasmania.

Galton-Fenzi, B., C. Maraldi, R. Coleman, and J. Hunter (2008), The cavity under the Amery Ice Shelf, East Antarctica, *Journal of Glaciology*, *54*(188), 881–887, doi: 10.3189/002214308787779898.

Galton-Fenzi, B. K., J. R. Hunter, R. Coleman, S. J. Marsland, and R. C. Warner (2012), Modeling the basal melting and marine ice accretion of the Amery Ice Shelf, *Journal of Geophysical Research (Oceans)*, *117*, C09031, doi: 10.1029/2012JC008214.

Glasser, N. F., and T. A. Scambos (2008), A structural glaciological analysis of the 2002 Larsen B ice-shelf collapse, *Journal of Glaciology*, *54*, 3–16, doi: 10.3189/002214308784409017.

Glen, J. (1958), The flow law of ice: A discussion of the assumptions made in glacier theory, their experimental foundations and consequences, *IASH Publ*, *47*, 171–183.

Goldberg, D., D. M. Holland, and C. Schoof (2009), Grounding line movement and ice shelf buttressing in marine ice sheets, *Journal of Geophysical Research (Earth Surface)*, *114*, F04026, doi: 10.1029/2008JF001227.

Goldstein, R. M., H. Engelhardt, B. Kamb, and R. M. Frolich (1993), Satellite Radar Interferometry for Monitoring Ice Sheet Motion: Application to an Antarctic Ice Stream, *Science*, *262*, 1525–1530, doi: 10.1126/science.262.5139.1525.

Golledge, N. R., C. J. Fogwill, A. N. Mackintosh, and K. M. Buckley (2012), Dynamics of the last glacial maximum Antarctic ice-sheet and its response to ocean forcing, *Proceedings of the National Academy of Science*, *109*, 16,052–16,056, doi: 10.1073/pnas.1205385109.

Golledge, N. R., L. Menviel, L. Carter, C. J. Fogwill, M. H. England, G. Cortese, and R. H. Levy (2014), Antarctic contribution to meltwater pulse 1A from reduced Southern Ocean overturning, *Nature Communications*, *5*, 5107, doi: 10.1038/ncomms6107.

Golledge, N. R., D. E. Kowalewski, T. R. Naish, R. H. Levy, C. J. Fogwill, and E. G. W. Gasson (2015), The multi-millennial Antarctic commitment to future sea-level rise, *Nature*, *526*, 421–425, doi: 10.1038/nature15706.

Gomez, N., D. Pollard, and J. X. Mitrovica (2013), A 3-D coupled ice sheet - sea level model applied to Antarctica through the last 40 ky, *Earth and Planetary Science Letters*, *384*, 88–99, doi: 10.1016/j.epsl.2013.09.042.

Gong, Y., S. L. Cornford, and A. J. Payne (2014), Modelling the response of the Lambert Glacier-Amery Ice Shelf system, East Antarctica, to uncertain climate forcing over the 21st and 22nd centuries, *The Cryosphere*, *8*(3), 1057–1068, doi: 10.5194/tc-8-1057-2014.

Gooch, B. T., D. A. Young, and D. D. Blankenship (2016), Potential groundwater and heterogeneous heat source contributions to ice sheet dynamics in critical submarine

basins of East Antarctica, *Geochemistry, Geophysics, Geosystems*, *17*(2), 395–409, doi: 10.1002/2015GC006117.

Gray, A. L., N. Short, K. E. Mattar, and K. C. Jezek (2001), Velocities and Flux of the Filchner Ice Shelf and its Tributaries Determined from Speckle Tracking Interferometry, *Canadian Journal of Remote Sensing*, *27*, 193–206, doi: 10.1080/07038992.2001.10854936.

Hansen, I., and R. Greve (1996), Polythermal modelling of steady states of the Antarctic ice sheet in comparison with the real world, *Annals of Glaciology*, *23*, 382–387, doi: 10.3198/1996AoG23-382-387.

Hellmer, H. H., F. Kauker, R. Timmermann, J. Determann, and J. Rae (2012), Twenty-first-century warming of a large Antarctic ice-shelf cavity by a redirected coastal current, *Nature*, *485*, 225–228, doi: 10.1038/nature11064.

Hindmarsh, R. C. A. (2004), A numerical comparison of approximations to the Stokes equations used in ice sheet and glacier modeling, *Journal of Geophysical Research (Earth Surface)*, *109*, F01012, doi: 10.1029/2003JF000065.

Höhle, J., and M. Höhle (2009), Accuracy assessment of digital elevation models by means of robust statistical methods, *International Journal of Photogrammetry and Remote Sensing*, *64*, 398–406, doi: 10.1016/j.isprsjprs.2009.02.003.

Holland, P. R., A. Jenkins, and D. M. Holland (2008), The Response of Ice Shelf Basal Melting to Variations in Ocean Temperature, *Journal of Climate*, *21*, 2558, doi: 10.1175/2007JCLI1909.1.

Hutter, K. (1983), *Theoretical Glaciology*, 510 pp., D. Reidel, Hingham, Mass.

Huybers, P., and W. Curry (2006), Links between annual, Milankovitch and continuum temperature variability, *Nature*, *441*, 329–332, doi: 10.1038/nature04745.

Huybrechts, P. (2002), Sea-level changes at the LGM from ice-dynamic reconstructions of the Greenland and Antarctic ice sheets during the glacial cycles, *Quaternary Science Reviews*, *21*, 203–231, doi: 10.1016/S0277-3791(01)00082-8.

Jezek, K. C. (2003), Observing the Antarctic Ice Sheet Using the RADARSAT-1 Synthetic Aperture Radar, *Polar Geography*, *27*(3), 197–209, doi: 10.1080/789610167.

Jezek, K. C. (2008), The RADARSAT-1 Antarctic Mapping Project, *Tech. rep.*, Byrd Polar Research Center, The Ohio State University, Columbus, Ohio, USA.

Joughin, I. (2002), Ice-sheet velocity mapping: a combined interferometric and speckle-tracking approach, *Annals of Glaciology*, *34*, 195–201, doi: 10.3189/172756402781817978.

Kerr, A., and P. Huybrechts (1999), The response of the East Antarctic ice-sheet to the evolving tectonic configuration of the Transantarctic Mountains, *Global and Planetary Change*, *23*(1–4), 213 – 229, doi: 10.1016/S0921-8181(99)00058-2.

King, M. (2002), The dynamics of the Amery Ice Shelf from a combination of terrestrial and space geodetic data, Ph.D. thesis, University of Tasmania.

King, M. A., R. Coleman, P. J. Morgan, and R. S. Hurd (2007), Velocity change of the Amery Ice Shelf, East Antarctica, during the period 1968-1999, *Journal of Geophysical Research (Earth Surface)*, *112*, F01013, doi: 10.1029/2006JF000609.

King, M. A., R. Coleman, A.-J. Freemantle, H. A. Fricker, R. S. Hurd, B. Legrésy, L. Padman, and R. Warner (2009), A 4-decade record of elevation change of the amery ice shelf, east antarctica, *Journal of Geophysical Research (Earth Surface)*, *114*, F01010, doi: 10.1029/2008JF001094.

King, M. A., R. J. Bingham, P. Moore, P. L. Whitehouse, M. J. Bentley, and G. A. Milne (2012), Lower satellite-gravimetry estimates of Antarctic sea-level contribution, *Nature*, *491*, 586–589, doi: 10.1038/nature11621.

König, M., J.-G. Winther, and E. Isaksson (2001), Measuring snow and glacier ice properties from satellite, *Reviews of Geophysics*, *39*, 1–27, doi: 10.1029/1999RG000076.

Krinner, G., O. Magand, I. Simmonds, C. Genthon, and J.-L. Dufresne (2007), Simulated Antarctic precipitation and surface mass balance at the end of the twentieth and twenty-first centuries, *Climate Dynamics*, *28*, 215–230, doi: 10.1007/s00382-006-0177-x.

Lambeck, K., and J. Chappell (2001), Sea Level Change Through the Last Glacial Cycle, *Science*, *292*, 679–686, doi: 10.1126/science.1059549.

Larour, E., M. Morlighem, H. Seroussi, J. Schiermeier, and E. Rignot (2012), Ice flow sensitivity to geothermal heat flux of Pine Island Glacier, Antarctica, *Journal of Geophysical Research (Earth Surface)*, *117*, F04023, doi: 10.1029/2012JF002371.

Le Brocq, A. M., A. J. Payne, and A. Vieli (2010), An improved Antarctic dataset for high resolution numerical ice sheet models (ALBMAP v1), *Earth System Science Data*, *2*, 247–260, doi: 10.5194/eed-2-247-2010.

Levermann, A., T. Albrecht, R. Winkelmann, M. A. Martin, M. Haseloff, and I. Joughin (2012), Kinematic first-order calving law implies potential for abrupt ice-shelf retreat, *The Cryosphere*, *6*(2), 273–286, doi: 10.5194/tc-6-273-2012.

Lliboutry, L., and P. Duval (1985), Various isotropic and anisotropic ices found in glaciers and polar ice caps and their corresponding rheologies, *Annales geophysicae*, *3*(2), 207–224.

Llubes, M., C. Lanseau, and F. Rémy (2006), Relations between basal condition, subglacial hydrological networks and geothermal flux in Antarctica, *Earth and Planetary Science Letters*, *241*, 655–662, doi: 10.1016/j.epsl.2005.10.040.

Lucchitta, B., K. Mullins, A. Allison, and J. Ferrigno (1993), Antarctic glacier-tongue velocities from Landsat images: first results, *Annals of Glaciology*, *17*, 356–356.

MacAyeal, D. R. (1989), Large-scale ice flow over a viscous basal sediment: Theory and application to ice stream B, Antarctica, *Journal of Geophysical Research: Solid Earth*, *94*(B4), 4071–4087, doi: 10.1029/JB094iB04p04071.

Mackintosh, A. N., E. Verleyen, P. E. O'Brien, D. A. White, R. S. Jones, R. McKay, R. Dunbar, D. B. Gore, D. Fink, A. L. Post, H. Miura, A. Leventer, I. Goodwin, D. A. Hodgson, K. Lilly, X. Crosta, N. R. Golledge, B. Wagner, S. Berg, T. van Ommen, D. Zwartz, S. J. Roberts, W. Vyverman, and G. Masse (2014), Retreat history of the East Antarctic Ice Sheet since the Last Glacial Maximum, *Quaternary Science Reviews*, *100*, 10–30, doi: 10.1016/j.quascirev.2013.07.024.

Martin, M. A., R. Winkelmann, M. Haseloff, T. Albrecht, E. Bueler, C. Khroulev, and A. Levermann (2011), The Potsdam Parallel Ice Sheet Model (PISM-PIK) - Part 2: Dynamic equilibrium simulation of the Antarctic ice sheet, *The Cryosphere*, *5*, 727–740, doi: 10.5194/tc-5-727-2011.

Mayet, C., L. Testut, B. Legresy, L. Lescarmontier, and F. Lyard (2013), High-resolution barotropic modeling and the calving of the Mertz Glacier, East Antarctica, *Journal of Geophysical Research (Oceans)*, *118*, 5267–5279, doi: 10.1002/jgrc.20339.

McGranahan, G., D. Balk, and B. Anderson (2007), The rising tide: assessing the risks of climate change and human settlements in low elevation coastal zones, *Environment and Urbanization*, *19*(1), 17–37, doi: 10.1177/0956247807076960.

McKelvey, B. C., M. J. Hambrey, D. M. Harwood, M. C. G. Mabin, P.-N. Webb, and J. M. Whitehead (2001), The Pagodroma Group–a Cenozoic record of the East Antarctic ice sheet in the northern Prince Charles Mountains, *Antarctic Science*, *13*(04), 455–468, doi: 10.1017/S095410200100061X.

Monaghan, A. J., D. H. Bromwich, R. L. Fogt, S.-H. Wang, P. A. Mayewski, D. A. Dixon, A. Ekaykin, M. Frezzotti, I. Goodwin, E. Isaksson, S. D. Kaspari, V. I. Morgan, H. Oerter, T. D. Van Ommen, C. J. Van der Veen, and J. Wen (2006), Insignificant Change in Antarctic Snowfall Since the International Geophysical Year, *Science*, *313*, 827–831, doi: 10.1126/science.1128243.

Morlighem, M., H. Seroussi, E. Larour, and E. Rignot (2013), Inversion of basal friction in Antarctica using exact and incomplete adjoints of a higher-order model, *Journal of Geophysical Research (Earth Surface)*, *118*, 1746–1753, doi: 10.1002/jgrf.20125.

Mouginot, J., B. Scheuchl, and E. Rignot (2012), Mapping of Ice Motion in Antarctica Using Synthetic-Aperture Radar Data, *Remote Sensing*, *4*, 2753–2767, doi: 10.3390/rs4092753.

Näslund, J.-O., P. Jansson, J. L. Fastook, J. Johnson, and L. Andersson (2005), Detailed spatially distributed geothermal heat-flow data for modeling of basal temperatures and meltwater production beneath the Fennoscandian ice sheet, *Annals of Glaciology*, *40*, 95–101, doi: 10.3189/172756405781813582.

Nicholls, R. J., and A. Cazenave (2010), Sea-Level Rise and Its Impact on Coastal Zones, *Science*, *328*, 1517, doi: 10.1126/science.1185782.

O'Brien, P., and P. Harris (1996), Patterns of glacial erosion and deposition in prydz bay and the past behaviour of the lambert glacier, in *Papers and Proceedings of the Royal Society of Tasmania*, vol. 130, pp. 79–85.

O'Gorman, P. A., and C. J. Muller (2010), How closely do changes in surface and column water vapor follow Clausius-Clapeyron scaling in climate change simulations?, *Environmental Research Letters*, *5*(2), 025207, doi: 10.1088/1748-9326/5/2/025207.

Pachauri, R. K., M. Allen, V. Barros, J. Broome, W. Cramer, R. Christ, J. Church, L. Clarke, Q. Dahe, P. Dasgupta, et al. (2014), Climate Change 2014: Synthesis Report. Contribution of Working Groups I, II and III to the Fifth Assessment Report of the Intergovernmental Panel on Climate Change.

Parry, M., O. Canziani, J. Palutikof, P. van der Linden, and C. Hanson (2007), IPCC, 2007: climate change 2007: impacts, adaptation and vulnerability. Contribution of working group II to the fourth assessment report of the intergovernmental panel on climate change.

Pattyn, F. (2010), Antarctic subglacial conditions inferred from a hybrid ice sheet/ice stream model, *Earth and Planetary Science Letters*, *295*, 451–461, doi: 10.1016/j.epsl.2010.04.025.

Pattyn, F., A. Huyghe, S. de Brabander, and B. de Smedt (2006), Role of transition zones in marine ice sheet dynamics, *Journal of Geophysical Research (Earth Surface)*, *111*, F02004, doi: 10.1029/2005JF000394.

Pattyn, F., C. Schoof, L. Perichon, R. C. A. Hindmarsh, E. Bueler, B. de Fleurian, G. Durand, O. Gagliardini, R. Gladstone, D. Goldberg, G. H. Gudmundsson, P. Huybrechts, V. Lee, F. M. Nick, A. J. Payne, D. Pollard, O. Rybak, F. Saito, and A. Vieli (2012), Results of the Marine Ice Sheet Model Intercomparison Project, MISMIP, *The Cryosphere*, *6*, 573–588, doi: 10.5194/tc-6-573-2012.

Petit, J. R., J. Jouzel, D. Raynaud, N. I. Barkov, J.-M. Barnola, I. Basile, M. Bender, J. Chappellaz, M. Davis, G. Delaygue, M. Delmotte, V. M. Kotlyakov, M. Legrand,

V. Y. Lipenkov, C. Lorius, L. Pépin, C. Ritz, E. Saltzman, and M. Stievenard (1999), Climate and atmospheric history of the past 420,000 years from the Vostok ice core, Antarctica, *Nature*, *399*, 429–436, doi: 10.1038/20859.

Pittard, M. L., J. L. Roberts, R. C. Warner, B. K. Galton-Fenzi, C. S. Watson, and R. Coleman (2013), Flow of the Amery Ice Shelf and its tributary glaciers, in *18th Australasian Fluid Mechanics Conference*, vol. 1, pp. 605–608.

Pittard, M. L., J. L. Roberts, C. S. Watson, B. K. Galton-Fenzi, R. C. Warner, and R. Coleman (2015), Velocities of the Amery Ice Shelf's primary tributary glaciers, 2004-–12, *Antarctic Science*, *27*, 511–523, doi: 10.1017/S0954102015000231.

Pittard, M. L., B. K. Galton-Fenzi, J. L. Roberts, and C. S. Watson (2016a), Organization of ice flow by localized regions of elevated geothermal heat flux, *Geophysical Research Letters*, *43*, doi: 10.1002/2016GL068436.

Pittard, M. L., J. L. Roberts, B. K. Galton-Fenzi, and C. S. Watson (2016b), Sensitivity of the lambert-amery glacial system to geothermal heat flux, *Annals of Glaciology*, *57*, doi: 10.1017/aog.2016.26.

Pollard, D., R. M. DeConto, and A. A. Nyblade (2005), Sensitivity of Cenozoic Antarctic ice sheet variations to geothermal heat flux, *Global and Planetary Change*, *49*(1–2), 63 – 74, doi: 10.1016/j.gloplacha.2005.05.003.

Pollard, D., R. M. DeConto, and R. B. Alley (2015), Potential Antarctic Ice Sheet retreat driven by hydrofracturing and ice cliff failure, *Earth and Planetary Science Letters*, *412*, 112–121, doi: 10.1016/j.epsl.2014.12.035.

Pritchard, H. D., S. R. M. Ligtenberg, H. A. Fricker, D. G. Vaughan, M. R. van den Broeke, and L. Padman (2012), Antarctic ice-sheet loss driven by basal melting of ice shelves, *Nature*, *484*, 502–505, doi: 10.1038/nature10968.

Rack, W., and H. Rott (2004), Pattern of retreat and disintegration of Larsen B Ice Shelf, Antarctic Peninsula, *Annals of Glaciology*, *39*, 505–510, doi: 10.3189/172756404781814005.

Rignot, E., D. G. Vaughan, M. Schmeltz, T. Dupont, and D. Macayeal (2002), Acceleration of Pine Island and Thwaites Glaciers, West Antarctica, *Annals of Glaciology*, *34*, 189–194, doi: 10.3189/172756402781817950.

Rignot, E., G. Casassa, P. Gogineni, W. Krabill, A. Rivera, and R. Thomas (2004), Accelerated ice discharge from the Antarctic Peninsula following the collapse of Larsen B ice shelf, *Geophysical Research Letters*, *31*, L18401, doi: 10.1029/2004GL020697.

Rignot, E., J. L. Bamber, M. R. van den Broeke, C. Davis, Y. Li, W. J. van de Berg, and E. van Meijgaard (2008), Recent Antarctic ice mass loss from radar interferometry and regional climate modelling, *Nature Geoscience*, *1*, 106–110, doi: 10.1038/ngeo102.

Rignot, E., J. Mouginot, and B. Scheuchl (2011a), Ice Flow of the Antarctic Ice Sheet, *Science*, *333*(6048), 1427–1430, doi: 10.1126/science.1208336.

Rignot, E., J. Mouginot, and B. Scheuchl (2011b), MEaSUREs InSAR-Based Antarctica Ice Velocity Map [900m]. Boulder, Colorado USA: National Snow and Ice Data Center., doi: 10.5067/MEASURES/CRYOSPHERE/nsidc-0484.001.

Rignot, E., J. Mouginot, M. Morlighem, H. Seroussi, and B. Scheuchl (2014), Widespread, rapid grounding line retreat of Pine Island, Thwaites, Smith, and Kohler glaciers, West Antarctica, from 1992 to 2011, *Geophysical Research Letters*, *41*, 3502–3509, doi: 10.1002/2014GL060140.

Ritz, C., T. L. Edwards, G. Durand, A. J. Payne, V. Peyaud, and R. C. A. Hindmarsh (2015), Potential sea-level rise from Antarctic ice-sheet instability constrained by observations, *Nature*, *528*, 115–118, doi: 10.1038/nature16147.

Rogozhina, I., J. M. Hagedoorn, Z. Martinec, K. Fleming, O. Soucek, R. Greve, and M. Thomas (2012), Effects of uncertainties in the geothermal heat flux distribution on the Greenland Ice Sheet: An assessment of existing heat flow models, *Journal of Geophysical Research (Earth Surface)*, *117*, F02025, doi: 10.1029/2011JF002098.

Rott, H., W. Rack, P. Skvarca, and H. De Angelis (2002), Northern Larsen Ice Shelf, Antarctica: further retreat after collapse, *Annals of Glaciology*, *34*(1), 277–282, doi: doi:10.3189/172756402781817716.

Rousseeuw, P., and M. Hubert (1997), Recent developments in progress, in *L1-Statistical Procedures and Related Topics*, vol. 31, edited by Y. Dodge, pp. 201–214, Institute of Mathematical Statistics Lecture Notes-Monograph Series, Hayward, California.

Sandiford, M., and S. McLaren (2002), Tectonic feedback and the ordering of heat producing elements within the continental lithosphere, *Earth and Planetary Science Letters*, *204*(1–2), 133 – 150, doi: 10.1016/S0012-821X(02)00958-5.

Sato, T., and R. Greve (2012), Sensitivity experiments for the Antarctic ice sheet with varied sub-ice-shelf melting rates, *Annals of Glaciology*, *53*, 221–228, doi: 10.3189/2012AoG60A042.

Scambos, T., M. Dutkiewicz, J. Wilson, and R. Bindschadler (1992), Application of image cross-correlation to the measurement of glacier velocity using satellite image data, *Remote Sensing of Environment*, *42*(3), 177–186, doi: 10.1016/0034-4257(92)90101-O.

Scambos, T. A., and R. Bindschadler (1993), Complex ice stream flow revealed by sequential satellite imagery, *Annals of Glaciology*, *17*, 177–182.

Scambos, T. A., C. Hulbe, M. Fahnestock, and J. Bohlander (2000), The link between climate warming and break-up of ice shelves in the Antarctic Peninsula, *Journal of Glaciology*, *46*, 516–530, doi: 10.3189/172756500781833043.

Scambos, T. A., J. A. Bohlander, C. A. Shuman, and P. Skvarca (2004), Glacier acceleration and thinning after ice shelf collapse in the Larsen B embayment, Antarctica, *Geophysical Research Letters*, *31*, L18402, doi: 10.1029/2004GL020670.

Schoof, C. (2007), Ice sheet grounding line dynamics: Steady states, stability, and hysteresis, *Journal of Geophysical Research (Earth Surface)*, *112*, F03S28, doi: 10.1029/2006JF000664.

Schoof, C., and R. C. A. Hindmarsh (2010), Thin-film flows with wall slip: An asymptotic analysis of higher order glacier flow models, *The Quarterly Journal of Mechanics and Applied Mathematics*, doi: 10.1093/qjmam/hbp025.

Shapiro, N. M., and M. H. Ritzwoller (2004), Inferring surface heat flux distributions guided by a global seismic model: particular application to Antarctica, *Earth and Planetary Science Letters*, *223*(1–2), 213 – 224, doi: 10.1016/j.epsl.2004.04.011.

Shepherd, A., D. Wingham, and E. Rignot (2004), Warm ocean is eroding West Antarctic Ice Sheet, *Geophysical Research Letters*, *31*, L23402, doi: 10.1029/2004GL021106.

Shepherd, A., E. R. Ivins, G. A, V. R. Barletta, M. J. Bentley, S. Bettadpur, K. H. Briggs, D. H. Bromwich, R. Forsberg, N. Galin, M. Horwath, S. Jacobs, I. Joughin, M. A. King, J. T. M. Lenaerts, J. Li, S. R. M. Ligtenberg, A. Luckman, S. B. Luthcke, M. McMillan, R. Meister, G. Milne, J. Mouginot, A. Muir, J. P. Nicolas, J. Paden, A. J. Payne, H. Pritchard, E. Rignot, H. Rott, L. S. Sørensen, T. A. Scambos, B. Scheuchl, E. J. O. Schrama, B. Smith, A. V. Sundal, J. H. van Angelen, W. J. van de Berg, M. R. van den Broeke, D. G. Vaughan, I. Velicogna, J. Wahr, P. L. Whitehouse, D. J. Wingham, D. Yi, D. Young, and H. J. Zwally (2012), A Reconciled Estimate of Ice-Sheet Mass Balance, *Science*, *338*, 1183, doi: 10.1126/science.1228102.

Siegert, M. J. (2000), Antarctic subglacial lakes, *Earth-Science Reviews*, *50*(1–2), 29 – 50, doi: http://dx.doi.org/10.1016/S0012-8252(99)00068-9.

Smith, B. E., H. A. Fricker, I. R. Joughin, and S. Tulaczyk (2009), An inventory of active subglacial lakes in Antarctica detected by ICESat (2003–2008), *Journal of Glaciology*, *55*(192), doi: doi:10.3189/002214309789470879.

Solomon, S., D. Qin, M. Manning, M. M. Z. Chen, K. Averyt, M.Tignor, and H. Miller (2007), IPCC, 2007: Climate Change 2007: The Physical Science Basis. Contribution of Working Group I to the Fourth Assessment Report of the Intergovernmental Panel on Climate Change, *Cambridge University Press, Cambridge, United Kingdom and New York, NY, USA*.

Steig, E. J., Q. Ding, D. S. Battisti, and A. Jenkins (2012), Tropical forcing of Circumpolar Deep Water Inflow and outlet glacier thinning in the Amundsen Sea Embayment, West Antarctica, *Annals of Glaciology*, *53*, 19–28, doi: 10.3189/2012AoG60A110.

Taylor, J., M. J. Siegert, A. J. Payne, M. J. Hambrey, P. E. O'Brien, A. K. Cooper, and G. Leitchenkov (2004), Topographic controls on post-Oligocene changes in ice-sheet dynamics, Prydz Bay region, East Antarctica, *Geology*, *32*, 197, doi: 10.1130/G20275.1.

Thoma, M., A. Jenkins, D. Holland, and S. Jacobs (2008), Modelling Circumpolar Deep Water intrusions on the Amundsen Sea continental shelf, Antarctica, *Geophysical Research Letters*, *35*, L18602, doi: 10.1029/2008GL034939.

Thomas, R. (1979), The dynamics of marine ice sheets, *J. Glaciol*, *24*(90), 167–177.

Timmermann, R., A. Le Brocq, T. Deen, E. Domack, P. Dutrieux, B. Galton-Fenzi, H. Hellmer, A. Humbert, D. Jansen, A. Jenkins, A. Lambrecht, K. Makinson, F. Niederjasper, F. Nitsche, O. A. Nøst, L. H. Smedsrud, and W. H. F. Smith (2010), A consistent data set of Antarctic ice sheet topography, cavity geometry, and global bathymetry, *Earth System Science Data*, *2*(2), 261–273, doi: 10.5194/essd-2-261-2010.

Treverrow, A., W. F. Budd, T. H. Jacka, and R. C. Warner (2012), The tertiary creep of polycrystalline ice: experimental evidence for stress-dependent levels of strain-rate enhancement, *Journal of Glaciology*, *58*(208), doi: 10.3189/2012JoG11J149.

Treverrow, A., R. C. Warner, W. F. Budd, T. Jacka, and J. L. Roberts (2015), Modelled stress distributions at the dome summit south borehole, law dome, east antarctica: a comparison of anisotropic ice flow relations, *Journal of Glaciology*, *61*(229), doi: doi:10.3189/2015JoG14J198.

van Wessem, J. M., C. H. Reijmer, M. Morlighem, J. Mouginot, E. Rignot, B. Medley, I. Joughin, B. Wouters, M. A. Depoorter, J. L. Bamber, J. T. M. Lenaerts, W. J. van de Berg, M. R. van den Broeke, and E. van Meijgaard (2014), Improved representation of East Antarctic surface mass balance in a regional atmospheric climate model, *Journal of Glaciology*, *60*, 761–770, doi: 10.3189/2014JoG14J051.

Velicogna, I. (2009), Increasing rates of ice mass loss from the Greenland and Antarctic ice sheets revealed by GRACE, *Geophysical Research Letters*, *36*, L19503, doi: 10.1029/2009GL040222.

Vieli, A., and A. J. Payne (2005), Assessing the ability of numerical ice sheet models to simulate grounding line migration, *Journal of Geophysical Research (Earth Surface)*, *110*, F01003, doi: 10.1029/2004JF000202.

Warner, R. C., and J. L. Roberts (2013), Pine Island Glacier (Antarctica) velocities from Landsat7 images between 2001 and 2011: FFT-based image correlation for images with data gaps, *Journal of Glaciology*, *59*(215), 571–582, doi: 10.3189/2013JoG12J113.

Weertman, J. (1974), Stability of the junction of an ice sheet and an ice shelf, *Journal of Glaciology*, *13*, 3–11.

Wen, J., Y. Wang, J. Liu, K. Jezek, P. . Huybrechts, B. Csathó, K. L. Farness, and B. Sun (2008), Mass budget of the grounded ice in the Lambert Glacier-Amery Ice Shelf system, *Annals of Glaciology*, *48*(1), 193–197, doi: 10.3189/172756408784700644.

Wen, J., Y. Wang, W. Wang, K. C. Jezek, H. Liu, and I. Allison (2010), Basal melting and freezing under the Amery Ice Shelf, East Antarctica, *Journal of Glaciology*, *56*, 81–90, doi: 10.3189/002214310791190820.

White, D. A., D. Fink, and D. B. Gore (2011), Cosmogenic nuclide evidence for enhanced sensitivity of an East Antarctic ice stream to change during the last deglaciation, *Geology*, *39*, 23–26, doi: 10.1130/G31591.1.

Whitehouse, P. L., M. J. Bentley, and A. M. Le Brocq (2012), A deglacial model for Antarctica: geological constraints and glaciological modelling as a basis for a new model of Antarctic glacial isostatic adjustment, *Quaternary Science Reviews*, *32*, 1–24, doi: 10.1016/j.quascirev.2011.11.016.

Winkelmann, R., M. A. Martin, M. Haseloff, T. Albrecht, E. Bueler, C. Khroulev, and A. Levermann (2011), The Potsdam Parallel Ice Sheet Model (PISM-PIK) – Part 1: Model description, *The Cryosphere*, *5*(3), 715–726, doi: 10.5194/tc-5-715-2011.

Winkelmann, R., A. Levermann, M. A. Martin, and K. Frieler (2012), Increased future ice discharge from Antarctica owing to higher snowfall, *Nature*, *492*, 239–242, doi: 10.1038/nature11616.

Wright, A., D. White, D. Gore, and M. Siegert (2008), Chapter 12 Antarctica at the Last Glacial Maximum, Deglaciation and the Holocene, in *Antarctic Climate Evolution*, *Developments in Earth and Environmental Sciences*, vol. 8, edited by F. Florindo and M. Siegert, pp. 531 – 570, Elsevier, doi: 10.1016/S1571-9197(08)00012-8.

Young, N. W., and G. Hyland (2002), Velocity and strain rates derived from InSAR analysis over the Amery Ice Shelf, East Antarctica, *Annals of Glaciology*, *34*, 228–234, doi: 10.3189/172756402781817842.

Yu, J., H. Liu, K. C. Jezek, R. C. Warner, and J. Wen (2010), Analysis of velocity field, mass balance, and basal melt of the Lambert Glacier-Amery Ice Shelf sys-

tem by incorporating Radarsat SAR interferometry and ICESat laser altimetry measurements, *Journal of Geophysical Research (Solid Earth)*, *115*(B14), B11102, doi: 10.1029/2010JB007456.

Zwally, H. J., J. Li, J. W. Robbins, J. L. Saba, D. Yi, and A. C. Brenner (2015), Mass gains of the Antarctic ice sheet exceed losses, *Journal of Glaciology*, *61*(230), 1019–1036, doi: doi:10.3189/2015JoG15J071.